A Novel Multiscale Physics-Based Progressive Damage and Failure Modeling Tool for Advanced Composite Structures

by

Evan Jorge Pineda

A dissertation submitted in partial fulfillment
of the requirements for the degree of
Doctor of Philosophy
(Mechanical Engineering)
in The University of Michigan
2012

Doctoral Committee:

Professor Anthony M. Waas, Chair
Professor Alan S. Wineman
Associate Professor Krishnakumar R. Garikipati
Assistant Professor Veera Sundararaghavan
Brett A. Bednarcyk, NASA Glenn Research Center

To my family

ACKNOWLEDGEMENTS

First I would like to thank my advisor, Professor Anthony Waas, for his guidance throughout my graduate studies. During my years as a Ph.D. student I always felt in complete control of my research, but never did I feel I was completely alone. Your supportive attitude and zeal for innovation made research an extremely exciting and enjoyable endeavor. You instilled a passion for research and a confidence in me that will never extinguish. I owe my technical and professional development to the knowledge I have gained from you.

I would also like to thank the other members on my dissertation committee: Professor Alan Wineman, Professor Krishna Garikipati, Professor Veera Sundararaghavan, and Dr. Brett Bednarcyk. Your technical insights, objective perspectives, and excellent advice regarding my dissertation research were inestimable. I am extremely grateful to have such a knowledgable and encouraging committee.

I owe my gratitude to all of my Professors throughout my entire academic career. I am especially indebted to Professor Werner Goldsmith, at the University of California, Berkeley for giving me my first opportunity to conduct research as a sophomore undergraduate student, and opening the doors for me to this wonderful world. I would also like to specifically thank Professor Panos Papadopoulos and Professor Tarek Zohdi at UC Berkeley and Professor Andrea Goldsmith at Stanford University for their tutelage and support during my undergraduate career. Thank you to Professor Anthony Waas, Professor Alan Wineman, Professor Krishna Garikipati, Professor Veera Sundararaghavan, Professor Ellen Arruda, and Professor Gregory Hulbert for

your superlative instruction which exposed me to the next level of mechanics as a new graduate student.

Thank you to the outstanding administrative and technical staff in the Department of Mechanical Engineering and the Department of Aerospace Engineering at the University of Michigan: Cynthia Quann-White, Michele Mahler, Simmi Isaac, Mike Nazareth, Suzanne Smith, Denise Phelps, Cynthia Enoch, Linda Weiss, Thomas Griffin, Chris Chartier, Eric Kirk, David McLean, and Terry Larrow. Without your cooperation and selflessness completing this dissertation would not have been possible.

To my fellow colleagues at the University of Michigan: Amit Salvi, Dr. Woosoek Ji, Dr. Shiladitya Basu, Dr. Peter Gustafson, Dr. Wei Hoek Ng, Dr. Sam Huang, Dr. Shunjun Song, Dr. Mark Pankow, Dr. Christian Heinrich, Dr. Siva Rudraraju, Scott Stapleton, Paul Davidson, Eugene Kheng, Pavana Prabhakar, Pascal Meyer, Lucas Hansen, Zachary Kier, Royan D'Mello, and Brian Justusson. Access to such a bright and friendly group of young engineers and scientists was a blessing. Your assistance throughout my graduate studies proved invaluable, and your attitudes made the office and lab a very special and pleasant workplace.

I am very grateful for the facilitation of my colleagues at the NASA Glenn Research Center, especially Dr. Steven Arnold for your mentorship and your encouragement to see the light at the end of the tunnel. I am also extremely appreciative for the guidance and patience of Dr. Brett Bednarcyk. Your input, advice, and assistance throughout my entire Ph.D. studies has been beneficial beyond words.

I would also like to acknowledge Collier Research Corporation, especially Craig Collier, Phillip Yarrington, Ivvone Collier, James Ainsworth, Ryan Lucking, and Ginny Taber for their generosity. Additionally, I would like to thank Dr. Philip Bogert, Dr. Alex Tessler, Dr. Arunkumar Satyanarayana, and Kevin Gould at the NASA Langley Research Center for all of their collaboration.

A special thanks to my friends who have stood with me. Gabriel Hernandez, Ethan Daley, Max Conroy, Allison Conroy-Krueger, Graham Mowday, J.R. Lindberg, Tubixas Jones, Joe Igber, Ben Chase, Matt Mitchell, Anna Rossi, Veera Simms, Chris Yee, Dr. Parya Naghipour, Marela Keys, Shirley Chung, Elliot Smith, Tiberius Moran-Lopez, Dr. Dominick Wright, Dr. Chloe Funkhouser, Saron Tesfai, Jacqueline Huerta, Marshall Bronson, Dr. K.C. Liu, Alejandro Ponce, Dr. Chinmaya Danadekar, Claudia Garcia, Monica Orozco, Minjin Baek, Tomas Eggers, Tiffany Parrish, Crystal Lia, and Shirley Payne. I apologize for oftentimes being distant and inaccessible, and I am greatly appreciative of your patience with me and for not forgetting about me. Moreover, I am grateful for all the wonderful experiences we have shared.

Finally, to my amazing family: my mother Linda Pineda, my father Jorge Pineda, my sister Christine Pineda, my grandmother Donna Shire, my grandfather Bert Barber, my grandfather Luis Pineda (Papa Foncho), my uncle Steven Girsback, and my cousins Michael and Stephanie Girsback, my godparents Guillermo and Ana Quinteros, and the whole Quinteros family. My family is everything, and without your unwavering love and support this would not have been possible.

The author would like to acknowledge that this work was funded under a Supersonics NRA contract # NNL07AA29C from the NASA Langley Research Center, under the supervision of Dr. Philip Bogert, via a subcontract # 070311 from the Collier Research Corporation.

TABLE OF CONTENTS

LIST OF FIGURES

Figure

LIST OF TABLES

Table

LIST OF APPENDICES

Appendix

ABSTRACT

A Novel Multiscale Physics-Based Progressive Damage and Failure Modeling Tool for Advanced Composite Structures

by

Evan Jorge Pineda

Chair: Anthony M. Waas

A novel, multiscale mechanics model for predicting the evolution of damage and failure in continuous fiber-reinforced laminates was developed. The thermodynamically-based work potential internal state variable (ISV) theory, Schapery theory (ST), is utilized to model matrix microdamage at the lamina level within a finite element method (FEM) setting. Failure due to transverse cracking and fiber breakage is modeled at the microscale within a repeating unit cell (RUC) using the semi-analytical generalized method of cells (GMC). A multiscale procedure is employed to link the microscale GMC calculations to the macroscale at every integration point in the FEM model. Micromechanics calculations are precluded if the macroscale damage is below some nominal value, increasing the overall computational efficiency of the multiscale scheme. Computational results and predicted failure modes are compared to experimental data of two center-notched, carbon fiber/epoxy panels containing different stacking sequences. A novel, single-scale extension of ST, the enhanced Schapery theory (EST), is also presented. Three additional ISVs are introduced to account for failure via matrix transverse cracking (mode I and mode II) and fiber breakage

(mode I only). These ISVs incorporate a characteristic finite element length scale, and are directly related to the fracture toughnesses of the material. In doing so, the pathological mesh dependency, resulting from the failure degradation scheme that was used in the previous multiscale model is eliminated; however, the explicit influence of the fiber-matrix architecture is lost. The EST model is evaluated against the same center-notched panel data. Finally, a mesh objective, smeared crack band model is implemented into the high-fidelity generalized method of cells (HFGMC) micromechanics theory. This failure model utilizes local fields to resolve the orientation of the crack band locally within the subcells of the RUC. The capabilities of the model are demonstrated using an RUC containing multiple randomly oriented fibers subjected to transverse tension and compression. The results of the model are compared to experimental data, and it is concluded that the newly developed model is viable for mesh objective, multiscale simulations.

CHAPTER I

Introduction

The first known use of composite materials, or materials composed of two or more constituents, in load bearing structures dates back to the people of the Mehrgarh region during the Neolithic Era between 7000 B.C. to 2500 B.C. [*Possehl* (1996)]. The people of the Mehrgarh used mud bricks composed of clay, mud, sand, water and straw to build homes. Composite materials have continued to maintain prevalence in structural designs throughout history, as well as the present.

Although composites, more specifically reinforced concrete, are still used in construction, the applications utilizing composite materials have also become more technologically advanced and can be found in industries such as aerospace, automotive, defense, sporting goods, biomedical, and electronics. The high-level application of composite materials requires high-performance constituents ranging from carbon fibers, glass fibers, polymers, ceramics, metals, and carbon nanotubes. Furthermore, natural fibers like jute and hemp can be used with thermoplastics to yield environmentally safe, biodegradable, composite materials. In addition to constituent selection, the micro-architecture of the composite can take various forms. Typical composite materials utilize chopped, continuous, woven, or braided fibers, or particles in a matrix. Due to the broad composition of composite materials, engineers are afforded considerable flexibility when designing with composite materials, and the multi-faceted

nature of a composite material results in the composite behaving closer to a small-scale structure than a traditional monolithic material. This tailorability ultimately leads to more efficient, cost effective designs. As manufacturing techniques advance, the economic feasibility of producing large scale composite structures will continue to improve. In this regard, textile composite materials are an emerging area [*Pankow* (2010)].

To further advance the efficiency of composite structures, while reducing the expense, virtual testing of materials can be employed to supplement some of the physical testing [*Cox and Yang* (2006)]. While physical material testing will always remain the most important component in the design and certification process of composite structures, virtual testing and simulation can be exploited during early stages of design to consider more design possibilities than is practical with physical testing alone, and it can be used to eliminate unsound designs before time and money is wasted on manufacturing the material to test the design. Moreover, numerical (or analytical) predictions can provide guidance for the physical experiments, especially when large components of full-scale structures are to be tested.

However, to obtain dependable and accurate predictions, robust, physics-based numerical tools must be developed. The heterogeneity responsible for the appeal of composites also contributes to their complex behavior, making numerical modeling of composites a challenging feat. Relating to structural integrity, the numerous constituents and inherent length scales present in a composite material elicit various damage and failure mechanisms in the separate constituents at the different length scales. Thus, the overall, observed response of a composite material is the culmination of and interaction between the damage and failure mechanisms in the constituents and across the length scales.

Not only do emerging numerical tools need to contain the fidelity and detail necessary for accurate predictions, they must also be computationally efficient if any

large scale predictions are desired. Furthermore, the tools must be accessible to the engineers who will be using them if widespread use is sought. The objective in this work is to progress towards this goal for modeling progressive damage and failure in continuous fiber-reinforced laminates (FRLs). The formulation of the theories, development of the frameworks, and examples presented are specific to polymer matrix composites (PMCs). To adapt the models to ceramic matrix composites (CMCs) or metal matrix composites (MMCs), the appropriate damage and failure mechanisms would need to be accounted for.

FRLs are most often comprised of layers of unidirectional fibers that are pre-impregnated with resin (pre-preg). The pre-preg layers are stacked and cured under specific temperature cycles and pressure. The orientation of the individual layers are chosen to customize the directional stiffness, strength, and damage tolerance of the laminate. Thus, the global damage and failure mechanisms that arise in the FRL depend considerably on the lay-up and directionality of the applied loads.

Damage and failure in the individual layers, within the FRL, are also functions of the load orientation relative to the axial direction of the fiber. For instance, axial failure is primarily fiber dominated, while transverse and shear failure are essentially controlled by the behavior of the matrix. Although the nonlinear response of a lamina, due to damage and failure evolution, may be controlled by one constituent or the other, the other constituent still contributes. For instance, fibers impede the growth of matrix cracks during transverse or shear failure, and the matrix surrounding the fibers provide a means to dissipate additional energy, through interfacial friction, during axial failure. Furthermore, the response of a lamina, or laminate, in compression (axial or transverse) can differ vastly from that in tension. Additionally, the damage and failure mechanisms in the constituents are occurring at, and interacting across, multiple length scales. It is because of this complex manner in which the global damage and failure mechanisms in FRLs arise that the correct physics must be accounted

for, at the appropriate scale, to actualize truly predictive models.

1.1 Damage and Failure Mechanisms in Fiber-reinforced Laminates

Initially, for low to moderate load levels, damage manifests in the matrix of the laminae in an FRL as matrix microdamage [*Schapery* (1989); *Sicking* (1992); *Schapery and Sicking* (1995)]. Matrix microdamage consists of all preliminary structural changes in the matrix including shear banding, microcracking, fissuring, fiber-matrix debonding, and micro void growth. Matrix microdamage is a highly distributed phenomenon, and the evolution of these mechanisms manifest as progressive changes in the stiffness of the material. The individual mechanisms associated with microdamage manifest at scales near or below that of the diameter of the fiber, but they are very widespread and encompass a scale well beyond the diameter of the fiber. Matrix microdamage accounts for all time independent nonlinearity (other time dependent, preliminary nonlinearities may be a result of viscoelastic or viscoplastic mechanisms), in the composite up until the onset of more catastrophic matrix, fiber, or interlaminar damage or failure mechanisms. A scanning electron microscope (SEM) image of microcracking in $[\pm 45^\circ]_S$ angle ply laminate is displayed in Figure 1.1. A plethora of microcracks are present spanning the distance between adjacent fibers. Arrays of microcracks extend along the axial fiber direction. Additionally, there is a region of matrix, between two fibers, that has been completely pulverized. This region demonstrates a more catastrophic failure mechanism subsequent to matrix microdamage.

Local states of transverse tension, that may also be combined with shear, produce transverse cracks, or simply matrix cracks, in the matrix phase of the FRL, as shown in Figure 1.2. The effects of these cracks are more significant than the previously

described matrix microdamage, and the progression of individual transverse cracks is more abrupt, rather than progressive. Matrix cracks may be a result of the coalescence of microdamage, as observed in Figure 1.1, or they may nucleate from preexisting flaws in the matrix, not necessarily affiliated with microdamage *Sicking* (1992); *McCartney* (1987). These cracks are very localized and generally span the thickness of a layer and run parallel to the fiber direction. Figure 1.2a shows the localized nature of the individual transverse cracks. It is shown that the local placement of the fibers affects the transverse crack path, and the cracks navigate around the inclusions to reach the boundaries of the ply. A magnified SEM image of a single transverse crack is shown in Figure 1.2b. Figure 1.2b exhibits the coalescence of numerous fiber-matrix debonds into a single transverse crack.

In PMCs, axial ply failure (under tension) involves loss of the load carrying capability of the fibers, which are the primary load bearing members in the composite. Thus, tensile, axial ply failure commonly leads to ultimate failure of the laminate or structure. The integrity of the fiber is jeopardized when the fiber fractures as shown in Figure 1.3. Since the axial response of the composite is dominated by the properties of the fibers, experiments on [0°] unidirectional, PMC laminates yield a load versus displacement response that is linear until the specimen fails suddenly and catastrophically. However, in a multi-angle laminate, fibers from off-axis plies bridge the macroscopic crack (see Figure 1.4) preventing immediate fracture. Furthermore, energy is dissipated through friction between the surfaces of the debonded fibers and matrix as fractured fibers are pulled out of the surrounding matrix [*McCartney* (1992b); *Rudraraju* (2011)].

The compressive response, both axially and transverse, of a fiber-reinforced lamina is drastically different than the tensile response. It is energetically favorable for cracks in monolithic materials, such as the matrix phase of a composite, to advance under mode I (tensile) conditions. However, conditions arise where mode I crack growth is

impossible, such as when constraints are imposed by interfaces or compressive loads. In these cases, the crack progresses under pure mode II, mode III, or mixed-mode conditions. When a FRL layer is subjected to transverse compression, internal Mohr-Coulomb friction in the matrix causes the damage and failure to evolve in shear [*Puck and Schürmann* (1998); *Aragonés* (2007); *Gonzaléz and Llorca* (2007b)]. Figure 1.5 shows the failed state of composite layers subjected to transverse compression. Figure 1.5a exhibits shear band and crack progression through the ply at roughly and angle of 56°. A more magnified SEM image of an additional composite, presented in Figure 1.5b, displays significant shear banding, accompanied by microcracking and fiber-matrix debonding. A great degree of damage bridging between the damage paths is also observed.

Fiber kinking, or microbuckling, is the predominant damage or failure mode under axial compression [*Budiansky and Fleck* (1993); *Schapery* (1995); *Yerramalli and Waas* (2003); *Basu* (2005)]. An SEM image of a kink band is displayed in Figure 1.6. Although it would seem that fiber kinking is dominated by the properties of the fiber, this mechanism depends more on the shear properties of the matrix. As the ply is loaded, slight misalignments in the fiber direction, with respect to the load, lead to rotation of the fibers. This fiber rotation increases the shear strain in the surrounding matrix, which advances matrix microdamage. Increasing matrix microdamage degrades the shear stiffness of the matrix making it easier for the fibers to rotate. This feedback loop eventually leads to a runaway instability, and a fiber kink band forms. Kink bands are also responsible for lowering the compressive strength of notched composites [*Waas et al.* (1990b,a)].

Evolution of damage and failure is not restricted solely to the composite layers. Interlaminar damage and failure can occur through delaminations. Delamination cracks run along the ply interface under mixed mode conditions, and usually result from high transverse shear, or peel, stress near free edges, discontinuities, or intralaminar trans-

verse cracks that have approached a ply interface [*Green et al.* (2007); *Hallett et al.* (2008)]. Figure 1.7 contains a photograph of a FRL failed under three-point bending. A single crack can be seen transitioning from a transverse crack in a layer to a delamination (or *vice versa*).

1.2 Computational Progressive Damage and Failure Analysis

A multitude of different damage and failure theories have been developed over the years that have been utilized for progressive damage and failure analysis (PDFA) of composite structures. These theories range from phenomenological, to physics-based, to based on first principles. Most contemporary PDFA is performed numerically using the finite element method (FEM) to discretize the continuum structure of interest. Within an FEM setting, discretization of the continuum may lead to pathological dependence of the solution on the mesh density. For a predictive model, the numerical results must be mesh objective. Some of the theories and techniques for PDFA are summarized in the following sections. A review of recent PDFA approaches is given in *Tay et al.* (2008); *Tsai* (2009); *Liu and Zheng* (2010)

1.2.1 Mesh Dependency Resulting from Post-Peak Strain Softening

The lack of positive definiteness of the elastic, or inelastic, tangent stiffness tensor leads to imaginary wave speeds in the material. The longitudinal wave speed in an isotropic material is given by

$$c_L = \sqrt{\frac{E(1-\nu)}{\rho(1+\nu)(1-2\nu)}} \tag{1.1}$$

where c_L is the wave velocity, E is the Young's modulus of the material, ν is the Poisson's ratio, and ρ is the material density. A one-dimensional approximation yields

$v = \sqrt{\frac{E}{\rho}}$. The existence of an imaginary wave speed results in a boundary value problem that is ill-posed [*Bažant and Cedolin* (1979); *Pietruszczak and Mroz* (1981); *deBorst* (1987); *Bažant and Cedolin* (1991)]. Physically, a material must possess a positive-definite tangent stiffness tensor, and in fact, at the micro-scale the material tangent stiffness tensor always remains positive-definite. However for practical purposes, engineers must model structures at scales much larger than the flaws in the material, and the homogenized continuum representation of a material with nucleation and propagation of discontinuities, such as cracks or voids, exhibits post-peak strain softening in the macroscopic, homogenized, stress-strain response. This homogenized response is assumed to govern over a suitable volume of the material, appropriate to the microstructure of the material.

Loss of positive-definiteness of the tangent stiffness tensor leads to a material instability which manifests as a localization of damage into the smallest length scale in the continuum problem; in FEM this is a single element[*Bažant and Cedolin* (1991)]. Thus in a numerical setting, the post-peak softening strain energy is dissipated over the volume of the element to which the damage localizes. Since a stress-strain relationship prescribes the energy density (energy per unit volume) dissipated during the failure process, the total amount of energy dissipated in the element decreases as the size of the element is reduced. Figure 1.8 illustrates the load-displacement response of a discretized, tensile bar as the size of the elements is reduced (i.e., as the FEM mesh is refined). For a given element size, the load-displacement response exhibits non-physical snap back, and in the limit as the element size approaches zero, the amount of energy dissipated during the failure also approaches zero.

1.2.2 Mesh Dependent Theories

Numerous PDFA methodologies utilize failure criteria to indicate the initiation of damage or failure. These criteria range from strictly phenomenological to physics-

based and include: maximum stress, maximum strain, Tsai-Hill, Tsai-Wu, Hoffman [*Herakovich* (1998); *Jones* (1999); *Daniel and Ishai* (2006)] Hashin-Rotem [*Hashin and Rotem* (1973)], Puck [*Puck and Schürmann* (1998)], and LaRC [*Pinho et al.* (2005)]. Mesh subjectivity does not arise from the use of a particular failure criterion but is predicated upon the degradation scheme utilized subsequent to initiation through any failure criterion.

Early PDFA tools implemented popular quadratic, multiaxial failure criteria into an FEM framework. Upon satisfaction of a failure criterion, a predetermined penalty is imposed on the corresponding component of the elastic stiffness tensor [*Knight, Jr. et al.* (2001); *Bogert et al.* (2006)]. Unfortunately, it is difficult to obtain a converged solution using static, implicit FEM with this methodology because of the abrupt changes in the stiffness tensor [*Belytschko and Mish* (2001)]. Moreover, this approach fails to capture progressive nonlinearity that may arise in the material response, and furthermore, due to reasons discussed earlier, causes lack of mesh objectivity when implemented within FEM.

Continuum damage mechanics (CDM) (see Chapter II, Section 2.1 for an overview of CDM theories) has also been implemented within an FEM setting to predict the response of composite structures. Damage is typically introduced through one or more internal state variables (ISVs), and damage evolution is either postulated or obtained from experiment, and nonlinear functions are utilized to control the influence of the damage on the components of the stiffness tensor. *Matzenmiller et al.* (1995) employed three scalar damage variables to introduce stiffness degradation, and two separate power law evolution laws, for fiber degradation and matrix degradation, were used in thermodynamically-based damage potentials to control the damage evolution. *Basu et al.* (2006); *Pineda et al.* (2010b) implemented a thermodynamically-based work-potential theory developed by *Schapery* (1989, 1990) into an FEM framework to model matrix microdamage using a single ISV under global compressive and tensile

loading, respectively. The polynomial damage functions relating the ISV to the model can be obtained from experiment [*Sicking* (1992)]. *Schuecker and Pettermann* (2008) utilized separate ISVs for transverse and shear matrix degradation. Exponential functions of stress, which are calibrated to experimental data, control the evolution of the ISVs. These methods work well in predicting the non-linear response of the composite, before the onset of post-peak strain softening, but may utilize numerous non-physical parameters. Furthermore, they are pathologically mesh dependent in the post-peak softening regime because a characteristic length scale is not introduced in the formulation of the damage evolution.

1.2.3 Mesh Objective Theories

The current, industry standard for failure analysis of composites is the use of failure criteria to determine first-ply failure. This method is incredibly efficient and useful for design stages where a multitude of configurations must be evaluated to arrive at a preliminary design. Additionally, this procedure is mesh independent, in as much as the mesh density is sufficient to accurately capture the fields in regions where high stress or strain gradients may be present. However, these analyses severely under predict the ultimate load carrying capability of composite materials, especially when damage initiation is followed by significant nonlinearity before final failure [*Hinton et al.* (2004)].

Bažant and Oh (1983) developed the smeared crack band approach which introduced a characteristic element length into the post-peak softening damage evolution formulation. The tangent slope of the softening stress-strain curve was scaled by the characteristic length to ensure that the total strain energy release rate (SERR) upon complete failure (i.e. zero stress) is always equal to the prescribed fracture toughness, regardless of the element size. In the original formulation, the band was always oriented perpendicular to the direction of maximum principal stress; thus, the

crack band always advanced under pure mode I. *de Borst and Nauta* (1985); *Rots and de Borst* (1987) later reformulated the model to incorporate a fixed crack band that evolved under mixed-mode conditions. Both formulations employ linear degradation schemes. Later, *Camanho et al.* (2007) incorporated more sophisticated initiation criteria to predict the onset of mixed-mode crack bands. All of these smeared crack formulations assume linear elastic behavior up to the initiation of the crack band, followed by immediate post-peak strain softening. However, *Spencer* (2002) coupled pre-peak plasticity with crack band post-peak strain softening in modeling failure of concrete.

Mesh dependent behavior arises because the failure localizes, and all of the energy dissipated via failure is dissipated over a volume that is a function of the discretization. Nonlocal, or gradient, failure theories assuage this dilemma by preventing failure localization [*Eringen* (1966); *Bažant* (1994); *Jirásek* (1998)]. The post-peak, stress-strain behavior of an element is influenced by the field gradients of surrounding elements within a characteristic radius. Thus the localization volume is a function of the assigned characteristic length, which is independent of the mesh size.

Nodal enrichment methods, such as the extended FEM (XFEM) [*Sukumar et al.* (2000); *Belytschko et al.* (2001)], and element enrichment methods, such as the variational multiscale cohesive method (VMCM) [*Garikipati and Hughes* (1998); *Garikipati* (2002); *Rudraraju et al.* (2010)], embed small scale fields into the finite element formulation to model discontinuities in the continuum. The evolution of the small scale fields is based on the behavior of cohesive cracks [*Dugdale* (1960); *Barenblatt* (1962)] which follow traction versus separation laws, ensuring mesh objectivity. By embedding the discontinuity in the formulation of the element, the crack path need not be known ahead of time.

The Arlequin method embeds discontinuities within the finite elements as they arise [*Ben Dia and Rateau* (2005); *Qiao et al.* (2011)]. Essentially, the element is

partitioned into subdomains corresponding to the orientation of the crack, or cracks in the element. Coupling matrices are used to introduce the subdomains into the global FEM problem, and the interfacial behavior of the newly created subdomains behaves as a cohesive crack. It should be noted that discrete crack methods (Arlequin, XFEM, VMCM) are useful for modeling macroscopic fracture in structures; however, they are impractical to use in materials where numerous distributed cracks arise during the loading history. They can, however, be coupled with a CDM theory or one of the continuum failure theories (smeared crack band or nonlocal gradient theories).

If a macroscopic crack path is known *a priori*, e.g. delamination, additional methods can be used to model the crack evolution. The virtual crack closure technique (VCCT), developed by *Krüger et al.* (1993) involves calculating the SERR of the structure if the crack progresses one element length along the predetermined path. If the SERR required for crack advancement is less than the available SERR, the crack is allowed to proceed. An overview of various VCCT methodologies is presented by *Krüger* (2002).

Alternatively, discrete cohesive zone method (DCZM) elements can be placed between potential surfaces along the predetermined crack path [*Xie and Waas* (2006); *Gustafson and Waas* (2009)]. Initially DCZM elements are assigned an incredibly high, fictitious, penalty stiffness, simulating perfect adhesion between the surfaces. Once the cohesive strength of the material is met, the element begins to unload according to the cohesive traction versus separation law. The use of cohesive zone model (CZM) elements has become the standard for modeling delamination in FRLs. It should be mentioned, though, that the fictitious, initial stiffness required prior to decohesion can cause numerical problems [*Turon et al.* (2006); *Ranatunga et al.* (2010b)].

Although delamination contributes significantly to the damage and failure of composite structures under numerous loading scenarios, adequate progress has been made

towards modeling this mechanism; therefore, the computational efforts in this work will focus on development of novel methods for modeling in-plane damage and failure mechanisms. Addition of interfacial DCZM elements is an accessible extension left for future work, and in fact, steps towards that realization have already been presented by *Ji et al.* (2011).

1.3 Micromechanics

Micromechanics techniques can be employed to model the individual constituents within the composite material. Typically a repeating unit cell (RUC) in the composite microstructure is identified, and analysis is performed on that RUC assuming periodic boundary conditions. In addition, representative volume element (RVE) methodologies exist which incorporate applying non-periodic boundary conditions to a subvolume that accurately represents the composite microstructure. Micromechanics can be utilized to provide the homogenized composite stiffness or to model damage and failure within the constituents and provide the resulting homogenized composite response. If utilized for the latter, the global mechanisms can arise through the natural evolution and interaction of the mechanisms in the constituents in the micromechanics model. Numerous micromechanics frameworks exist that encompass analytical, semi-analytical, and numerical techniques. An expansive review of many micromechanics theories is given by *Aboudi et al.* (2012) and *Kanoute et al.* (2009).

The first micromechanics models were used to calculate the elastic stiffness of the composite from the properties of its constituents. The simplest approximations by *Voigt* (1887) and *Reuss* (1929), are commonly referred to as the rule of mixtures and calculate the elastic stiffness, or compliance, tensor, by through a weighted sum of the stiffness (compliance) tensors of the constituents using the volume fraction of the constituents. Work by *Hill* (1952) proved that the actual stiffness tensor was bounded by the Voigt and Ruess approximations. The composite sphere assemblage

(CSA) model for spherical inclusions, and the concentric cylinder assemblage (CCA) model for long cylindrical fibers, provided more accurate estimates on the stiffness of the composite by assuming the composite was composed of a distribution of spheres, or cylinders, containing a inner fiber core and outer matrix shell [*Hashin* (1962); *Christensen and Waals* (1972)]. The homogenized properties of single sphere, or cylinder, can be determined by solving a set boundary value problems (BVPs), and those properties can be averaged over the desired distribution of orientations. The generalized-self consistent scheme assumed the spherical, or cylindrical, fiber and matrix were embedded in an effective medium representing the homogenized composite [*Christensen and Lo* (1979)]. The properties of the effective medium could then be calculated. This method can be used to provide the transverse shear modulus which cannot be calculated using the CSA or CCA.

Mori and Tanaka (1973) originally developed a method for calculating the average fields in a fiber contained in an infinite volume of matrix by assuming the fields in the matrix are equivalent to the applied far fields and calculating concentration matrices for the fields in the fiber. The Eshelby inclusion method provides concentration matrices for calculating the average fields in both of the constituents by assuming the presence of an eigenstrain in an ellipsoidal inclusion [*Eshelby* (1957); *Mura* (1982); *Timoshenko and Goodier* (1970)]. The availability of average, constituent level fields provided by these methods make them amenable for damage and failure modeling by prescribing the appropriate constitutive laws in the constituents. However, these methods neglect the variation of the local fields within the constituent materials.

Approaches developed by *Nemat-Nasser et al.* (1982); *Walker et al.* (1989) discretized an RUC of the composite into a number of subvolumes. Global constitutive laws were formulated in terms of the constitutive behavior of the subvolumes in the form of a set of integral equations. These integral equations were solved approximately using a Green's function approach or a Fourier series approach.

The transformation field analysis (TFA) assumes the fields in a discretized RUC are piecewise uniform [*Dvorak* (1992)]. Furthermore, the local stresses and strains contain contributions from the eigenstrains and eigenstresses, respectively. The eigenfields may include thermal, inelastic ad damage effects. Elastic strain concentration tensors (calculated using other methods) are used to relate the global fields to the local fields for the purely elastic case, and account for the shape and volume fraction of the phases in the RUC. These concentration tensors simply need to be calculated once, and nonlinearity is achieved through the evolution of the local eigenstrains and eigenstresses. Thus, the number of unknowns that need to be solved throughout the problem are reduced considerably. TFA was later extended to non-uniform transformation field analysis (NTFA) by *Michel and Suquet* (2003) to incorporate fully non-uniform local fields.

The method of cells (MOC) developed by *Aboudi* (1991) discretized a rectangular composite RUC into four subvolumes, called subcells. One of the subcells was occupied by the fiber material and the rest were occupied by the matrix. Linear displacement fields were assumed in each of the subcells. Displacement and traction continuity conditions were enforced, in an average integral sense, at the subcell interfaces, along with periodic boundary conditions at the RUC boundaries to derive a set of equations that yield a strain concentration matrix. This could, in turn, be used to obtain the local subcell strains from the applied fields. Following determination of the subcell strains, the subcell stress are readily calculated using the local constitutive laws, and volume averaging can be used to obtain the homogenized thermomechanical properties of the composite. MOC was later extended to the generalized method of cells (GMC) by *Paley and Aboudi* (1992) which accommodated any number of subcells and constituents in two periodic directions. *Aboudi* (1995) adapted the formulation to accommodate triply-periodic materials. Finally, *Aboudi et al.* (2001) developed the high-fidelity generalized method of cells (HFGMC) which

utilized second order displacement field approximations in the subcells, rather than linear. *Aboudi et al.* (2003); *Haj-Ali and Aboudi* (2009) showed the local field accuracy produced by HFGMC corresponded very well to FEM for elastic and inelastic phases. *Bednarcyk et al.* (2004) utilized HFGMC to model fiber-matrix debonding in metal matrix composites (MMCs), and *Bednarcyk et al.* (2010) implemented a multi-axial damage model in HFGMC. Reformulations, of GMC and HFGMC, which reduced the total number of unknowns in the problem were introduced by *Pindera and Bednarcyk* (1999) and *Bansal and Pindera* (2004), respectively.

The semi-analytical methods (Green's function/Fourier series approach, TFA, GMC, HFGMC) offer a distinct advantage over the analytical, mean-field approaches, in that, spatially varying local fields can be determined. This robustness allows for better representation of the damage and failure mechanisms at the constituent scale. Furthermore, their semi-analytical formulations retain a computational advantage over fully numerical methods

However, as computational power increases, detailed fully numerical micromechanics simulations are more feasible. Recent works by *Gonzaléz and Llorca* (2007a); *Totry et al.* (2008, 2010) modeled multiple random fibers using a two-dimensional (2-D) FEM model. The matrix was modeled using plasticity, and the fiber and matrix was allowed to debond using CZM elements at the fiber-matrix interfaces. The response of the RUC was investigated under combinations of transverse compression and transverse shear loading. *Cid Alfaro et al.* (2010) modeled fiber-matrix debonding and matrix cracking under global transverse tension in a single-fiber RUC by including CZM elements between every matrix-matrix or fiber-matrix interface. *Mishnaevsky Jr. and Brønsted* (2007) simulated fiber-matrix pullout in a three-dimensional (3-D) RVE by modeling the fiber-matrix interface as a damaging solid.

1.4 Multiscale Modeling

Multiscale modeling involves sharing information between two or more length and/or time scales often using localization and homogenization techniques. This has been achieved through three different multiscale techniques: hierarchical, concurrent, or synergistic [*Sullivan and Arnold* (2011)]. With hierarchical multiscale modeling, simulations of the separate scales are employed sequentially, and subsequently, information is passed up through homogenization (or down through localization). Concurrent multiscale modeling operates across all of the identified time and length scales simultaneously, and data is shared as fields evolve at all scales. Finally, synergistic multiscale modeling utilizes a combination of concurrent and hierarchical modeling in either the spatial or temporal domains. Various physical models can be employed at the various scales. Often, the coarser-scales adopt continuum models, as is appropriate, but the finer-scales can incorporate other analytical, semi-analytical, or numerical continuum models, or atomistic models, depending on the size of the scale of interest. When modeling FRLs, usually the finest-scale of interest is the fiber-matrix scale; thus, the following overview is limited to multiscale continuum models. A breadth of literature is available relating to this subject as evidenced in numerous review papers and books [*Ladeveze* (2004); *Kwon et al.* (2008); *Fish* (2009); *Kanoute et al.* (2009); *Gilat and Banks-Sills* (2010); *Sullivan and Arnold* (2011); *Aboudi et al.* (2012)]

Many multiscale techniques employ FEM at the fine-scale to determine the response of the RUC or RVE. This method, called FE^2 developed by *Feyel* (1999); *Feyel and Chaboche* (2000), uses the FEM simulation of the RUC or RVE to dictate the constitutive behavior of an integration point in the coarse-scale FEM problem. This technique can be computationally expensive and may require a relatively coarse mesh at the finer scales for feasibility.

Other methodologies utilize micromechanics to reduce the order of the fine scale

problems. Asymptotic field expansion is a widely used multiscale technique that expands the fields into any number of fine-scale fields [*Suquet* (1987); *Fish et al.* (1997, 1999)]. The fine-scale fields are related to the coarse-scale fields through a set of homogenization functions. The homogenization functions are obtained by solving the fine-scale BVPs, either analytically or numerically. *Fish and Yu* (2001) utilized FEM to solve the for the asymptotic fields in the fine-scale problem. *Fish et al.* (1997) used FEM to solve for the fine-scale problem generated from TFA. Finally, *Oskay and Fish* (2007) further improved the efficiency of the fine-scale FEM problem by combining asymptotic field expansion and TFA.

The Voronoi cell method, introduced by *Ghosh and Mukhopadhyay* (1991); *Ghosh et al.* (1995); *Ghosh and Moorthy* (1995); *Ghosh and Liu* (1995) uses Dirichlet tessellation to resolve the composite microstructure into an optimal mesh composed of Voronoi polygons that contain, at most, one inclusion. The Voronoi polygons containing an inclusion were formulated as finite elements used to solve the fine-scale FEM problem. The finite element formulation of the Voronoi cells can be adjusted to include all manner of constitutive nonlinearities.

Wilt (1995) implemented GMC within an FEM framework; wherein, a GMC RUC problem is solved at every integration point using the integration point fields as the far fields in the micromechanics solution. This offers a computational advantage over most of the coupled FE problems because the semi-analytical solution of the GMC problem is less expensive than an FEM solution. *Bednarcyk and Arnold* (2002a, 2006) successfully used a multiscale methodology incorporating GMC to model damage in metal matrix composites

It should be mentioned that *Bažant* (2007) inquires whether multiscale analysis is a viable tool for modeling post-peak strain softening in materials. Several inconsistencies in multiscale methodologies are raised including lack of mesh objectivity due to the inconsistent length across the scales, and inappropriate transfer of the

SERR across the scales. Additionally, *Bažant* (2007) cites the common absence of a localization limiter in the fine-scale problem, and in the case where a fine-scale localization limiter exists, absence of the transfusion of that limiter from the fine-scale to the coarse-scale. As described below, these issues are addressed briefly in this dissertation in Chapter V, Section 5.7.

1.5 Objective and Scope of Dissertation

Throughout this document an intentional distinction between damage and failure is drawn. Damage is defined as the resulting effect of all structural changes in the material that yield pre-peak nonlinearities in the stress strain curve through degradation of the secant stiffness tensor. Failure is characterized as the consequence of structural changes in the material that manifest as post-peak strain softening in the stress-strain response of the material. Although particular mechanisms may manifest as both damage and failure, its influence is predominantly one or the other. Therefore, to minimize confusion in this work, mechanisms are treated as either damage mechanisms or failure mechanisms, but never both. Three major mechanisms applicable to in-plane damage and failure of PMCs are considered: matrix microdamage, transverse cracking, and fiber breakage. Matrix microdamage is categorized as a damage mechanism, whereas, transverse cracking and fiber breakage are considered local failure mechanisms. Fiber kinking is acknowledged in this work; however, evolution of this mechanism is directly related to the shear behavior of the matrix, and thus, it is implicitly accounted for. Furthermore, tension dominated problems are chosen to demonstrate the capabilities of the models because fiber kinking was thoroughly explored by previous authors [*Basu* (2005); *Basu et al.* (2006)]. The main objective of this work is to develop a physics-based numerical tool for modeling these in-plane damage and failure mechanisms in PMC FRLs. The four subsequent chapters and two appendices mark the progress towards this development.

In Chapter II a detailed evaluation of the thermodynamically-based work potential theory, established by *Schapery* (1989, 1990); *Sicking* (1992); *Schapery and Sicking* (1995), for modeling matrix microdamage is performed. The evolution of microdamage is investigated under an expansive combination of transverse tension, transverse compression and in-plane shear loading. Furthermore, the stability of the microdamage evolution equations with respect to perturbations in the microdamage ISV is probed with the intention of determining if loss of stability of the microdamage evolution equations can be used as a criterion for the initiation of more severe matrix failure mechanisms, such as transverse cracking.

A synergistic multiscale framework is developed in Chapter III for modeling matrix microdamage, transverse cracking, and fiber failure. The work potential theory from Chapter II is implemented within FEM and used to model distributed matrix microdamage at the lamina/laminate level, or macroscale. GMC is used to resolve the microstructure and model the fiber-matrix level, or microscale, of the FRL via an RUC at integration points throughout the macroscale domain. The MAC/GMC suite of micromechanics codes, developed at the NASA Glenn Research Center (GRC) is utilized to execute the numerical implementation of GMC [*Bednarcyk and Arnold* (2002b,c)]. The FEAMAC software facilitates communication between the microscale (GMC) and the macroscale (FEM). Localized failure due to transverse cracking and fiber breakage is modeled at the microscale using GMC. Simple failure criteria are employed in the subcells of the RUC to indicate failure of that subcell as a result of transverse cracking or fiber breakage. Subsequent to failure initiation, the elastic properties are severely degraded so that the failed subcell no longer contributes significantly to the overall stiffness of the subcell. It is apparent that this failure degradation procedure bares pathologically mesh dependent results. However, it represents a first attempt to utilize micromechanical fields to mark the termination of macroscale damage in lieu of more catastrophic mechanisms.

The benefits of modeling distributed damage and localized failure at separate scales are two-fold. First, the mechanisms are modeled at more appropriate scales. Matrix microdamage, which is distributed over volumes surpassing the fiber-matrix scale (Figure 1.1), is modeled at the macroscale. Whereas, transverse cracking (Figure 1.2) and fiber fracture (Figure 1.3) are extremely local mechanisms, and they are modeled at the microscale. Second, by modeling microdamage at the macroscale, micromechanics calculations can be foregone if the macroscale microdamage is not above some nominal level. Even if this value is set very low, microscale calculations can be avoided in large domains where there is little to no nonlinear action. This variable fidelity approach vastly improves the computational efficiency of the methodology. The performance of the multiscale model is evaluated against experimental results for two carbon fiber/epoxy center-notched panels (CNPs). These panels were tested under uniaxial tension at the NASA Langley Research Center (LaRC), and the experimental data was presented in Refs. [*Bogert et al.* (2006); *Satyanarayana et al.* (2007)]. Global load versus displacement, local strain gage data, and post-test failure images are compared to results from the computational model.

Chapter IV presents a reformulation of the work potential theory to include additional ISVs for transverse cracking and fiber breakage. Evolution of the new failure ISVs is based upon the fracture toughness of the material and incorporates the characteristic length of the element, ensuring mesh objectivity. However, no microscale analysis is performed and the influence of the composite micro-architecture must be inferred when the failure initiation and evolution laws are formulated. The new capabilities of the single-scale model are demonstrated using the same example as in Chapter III, and the results are compared to the experimental data.

Finally, Chapter V directly remedies the mesh dependence resulting from the failure model implemented in the micromechanics in Chapter III. A variation of the mesh objective, smeared crack band model formulated by *Bažant and Oh* (1983) is

implemented within the HFGMC micromechanics model. The crack band is assumed to always orient in accordance to the direction of the maximum principal stress. If that stress is positive, or tensile, the crack band is oriented perpendicular to the principal stress and the crack band grows under mode I conditions if a maximum stress criterion is achieved. It is not physically realistic for cracks to grow in mode I when the faces of the crack tip are subjected to normal compression. Thus, if the principal stress exhibiting the maximum magnitude is negative, or compressive, it is assumed that the crack band evolves because of internal, Mohr-Coulomb friction, and the crack band is oriented parallel to the plane of maximum shear stress in the matrix subcell. The crack band advances under mode II conditions if a Mohr-Coulomb initiation criterion is satisfied. An RUC containing 13 randomly positioned fibers is subjected to transverse tension and compression. The results are compared to experimental data from *Hinton et al.* (2004). Finally, a novel, consistent, mesh objective multiscale framework is outlined and suggested for needed future work in this research field.

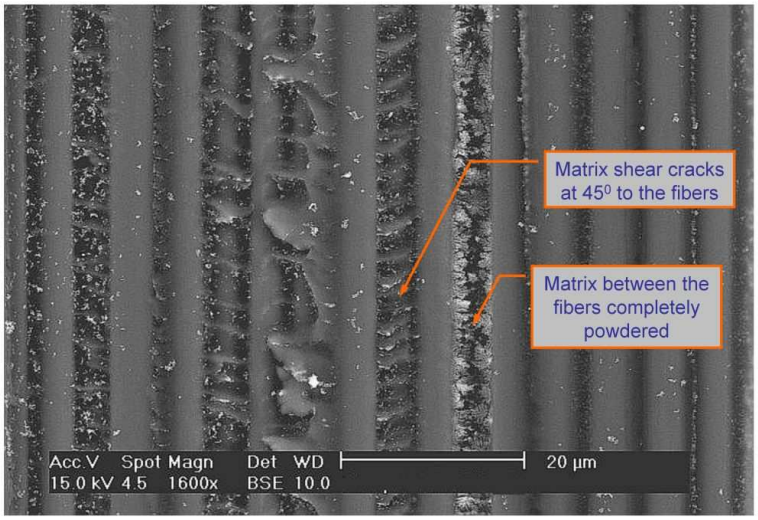

Figure 1.1: Highly distributed Matrix microcracks in $[\pm 45^{\circ}]_S$ carbon fiber/epoxy laminate. Coalescence of microcracks into matrix failure also observed [*Ng et al.* (2010)].

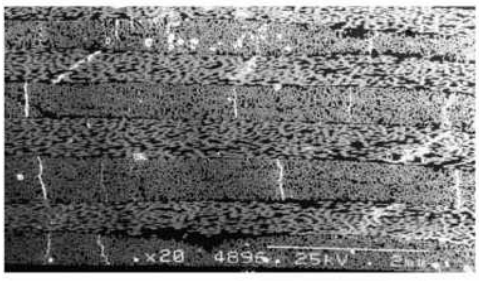

(a) Multiple transverse cracks. [*Roberts* (2000)].

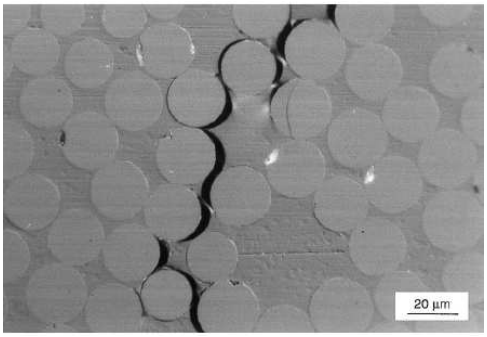

(b) Magnification of a single transverse crack. [*Gamstedt and Sjögren* (1999)].

Figure 1.2: Transverse cracks in glass/epoxy laminates.

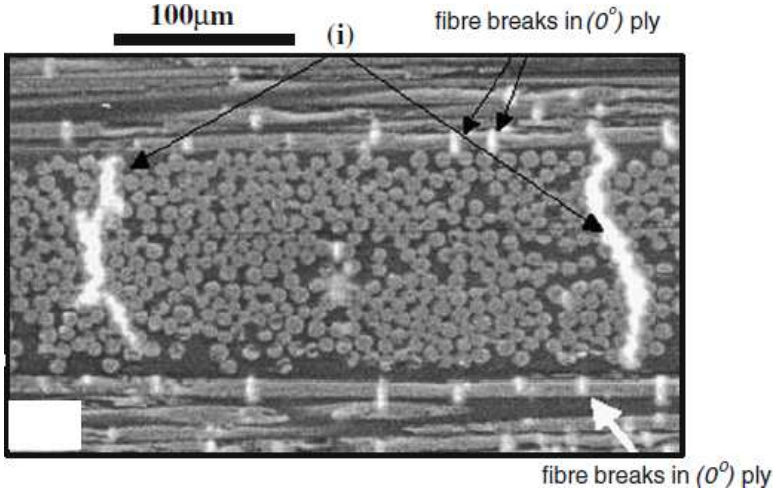

Figure 1.3: Fiber breakage in 0° ply and transverse cracking in 90° ply of cross-ply glass/epoxy laminate [*Beaumont et al.* (2006)].

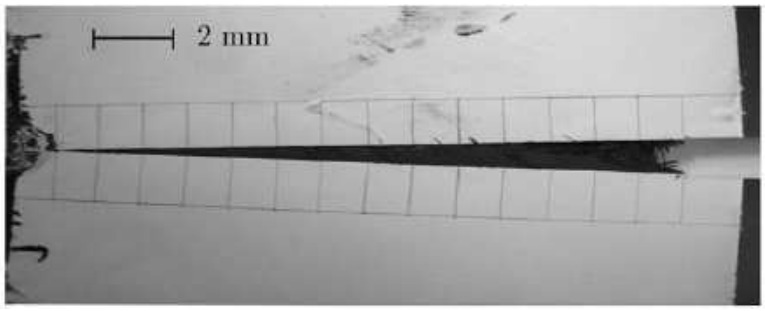

Figure 1.4: Fracture of a quasi-isotropic carbon fiber/epoxy laminate exhibiting significant fiber bridging and fiber-matrix pullout [*Rudraraju et al.* (2010)].

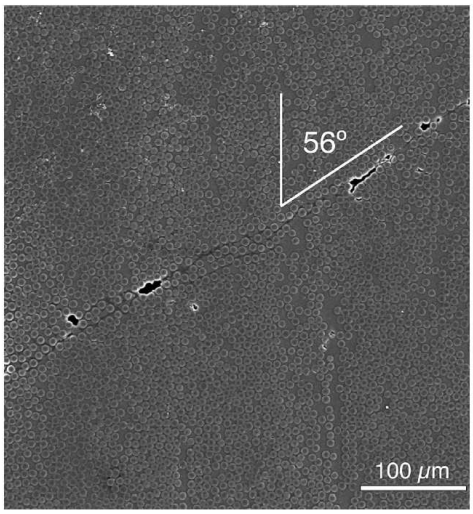

(a) Macroscopic failure [*Aragonés* (2007)].

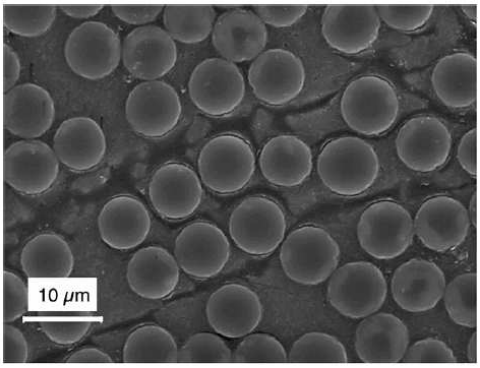

(b) Localized shear bands and cracks [*Gonzaléz and Llorca* (2007b)].

Figure 1.5: Transverse compressive failure of carbon fiber/epoxy laminates. Macroscopic failure path observed at an angle. Magnification illustrates shear banding, cracking and fiber-matrix debonding.

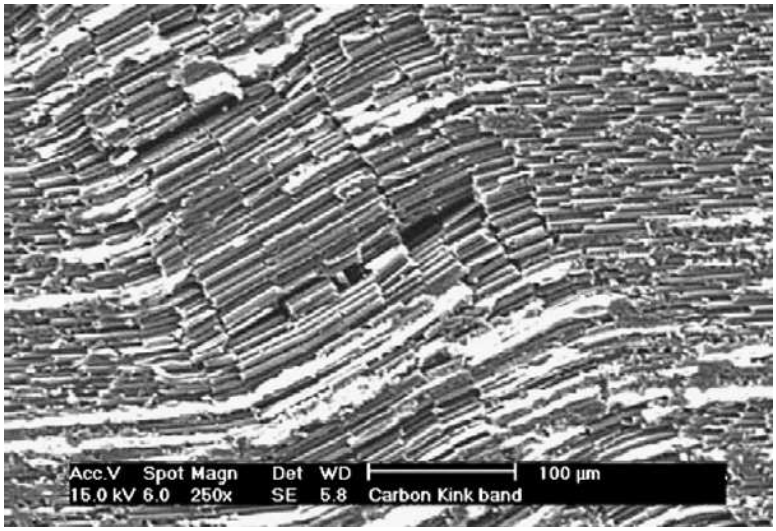

Figure 1.6: Kink band in carbon fiber/epoxy composite under axial compression [*Yerramalli and Waas* (2003)].

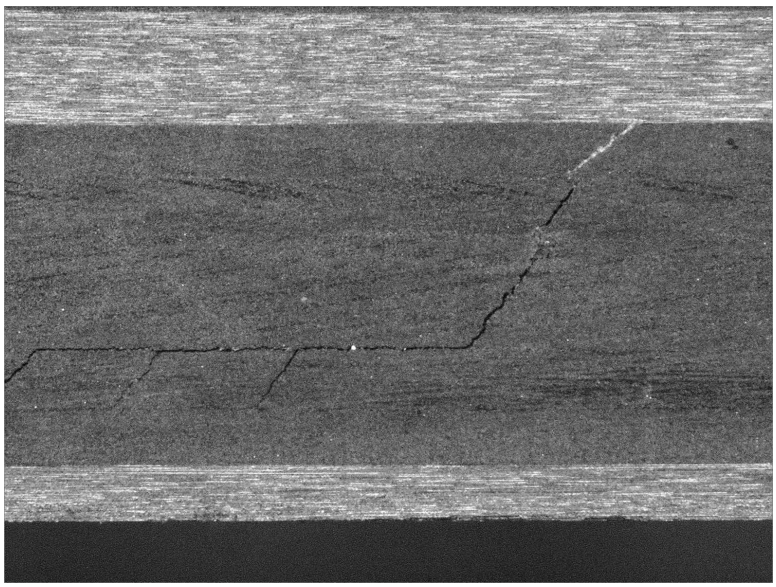

Figure 1.7: Transverse crack/delamination interaction in carbon fiber/epoxy laminate. Photograph courtesy of Dr. Bradley Lerch, NASA GRC.

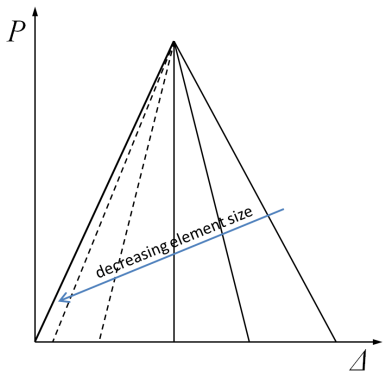

Figure 1.8: Effects of element size on overall load-displacement response for a material exhibiting post-peak softening. Dashed lines indicate non-physical snapback.

CHAPTER II

Modeling Progressive Microdamage in a Unidirectional Composite Lamina using a Thermodynamically-Based Work Potential Theory

2.1 Introduction

Much of the observed nonlinearity in the stress-strain response of polymer matrix, fiber-reinforced composites can be attributed to progressive damage evolution in the matrix phase of the composite. Progressive damage may involve microcracking, transverse cracking, shear banding, micro-fissure growth, micro-void growth, fiber-matrix debonding, and kink band formation, as well as delamination in fiber-reinforced laminates (FRLs). Typically, fiber failure in composite materials is not progressive but rather abrupt. However, when accompanied with fiber bridging and fiber-matrix pullout, the axial failure response of an FRL may be progressive. It is important to capture the underlying physics of the various damage mechanisms to yield accurate predictions of the response of composite structures subjected to service loads.

Continuum damage mechanics (CDM) has emerged as a viable option for predicting the nonlinear behavior of composite structures. The first CDM theory was developed by *Kachanov* (1958, 1986). Subsequently, many publications on this subject were produced, including numerous books [*Talreja* (1985a); *Lemaitre and Chaboche*

(1994); *Lemaitre* (1996); *Krajcinovic* (1996); *Voyiadjis and Kattan* (2005)]. Typically, a set of scalar damage variables, or internal state variables (ISVs), introduce anisotropic damage into the composite constituent behavior by penalizing the components of the material stiffness tensor, and nonlinear functions are used to control the damage evolution. Various authors have used crack density, geometry, strain energy release rate, and other crack features to characterize the damage evolution [*Dvorak et al.* (1985); *Talreja* (1985b); *Laws and Dvorak* (1988); *Lee et al.* (1989); *Nairn* (1989); *Tan and Nuismer* (1989); *Gudmundson and Östlund* (1992); *McCartney* (1992a, 1998)]. Others postulate damage evolution laws and characterize those laws using experiments [*Allen et al.* (1987a,b); *Talreja* (1994); *Paas et al.* (1992); *Matzenmiller et al.* (1995); *Bednarcyk et al.* (2010)]. CDM models must also employ failure criteria to indicate damage initiation. More recently, increasingly sophisticated failure criteria have been developed to better represent the phenomenological behavior of a damaging composite lamina [*Puck and Schürmann* (1998, 2002); *Pinho et al.* (2005)] and are used in conjunction with CDM.

CDM techniques offer computationally efficient and readily implementable means to capture the effects of damage and failure in composite materials. Unfortunately, the majority of the criteria and evolution laws are formulated upon phenomenological observations of the directional dependence of damage evolution, rather than modeling the physics of the actual damage mechanisms. That is, separate damage variables are used to degrade different components of the stiffness tensor (directions) depending on whether the damage is said to accrue in the matrix or fiber constituents of the composite, but the variables do not explicitly distinguish between the separate damage mechanisms. Furthermore, many theories involve a multitude of parameters that are difficult to measure and must be calibrated to correlate with experimental data.

In this chapter, the formulation of a thermodynamically-based work potential theory developed by *Schapery* (1989) is presented for modeling progressive matrix micro-

damage in FRLs, which includes microcracking, micro-fissure growth, shear banding, micro-void growth, and fiber-matrix debonding. Schapery theory (ST) extends the theory developed by *Rice* (1971), which uses internal state variables (ISVs) to control the material nonlinearity, by assuming that damage evolution in composites under combined transverse-shear loading exhibits limited path-dependence [*Lamborn and Schapery* (1988, 1993)]. A single ISV is used to represent the potential needed to drive structural changes in the material associated with microdamage evolution. The derogative effects of the microdamage mechanisms on the stiffness of the composite are related to the ISV associated with energy dissipated via advancement of the mechanisms through a set of measured microdamage functions. *Sicking* (1992) successfully predicted the response of numerous laminated, graphite-epoxy plates using ST. Subsequently, *Basu et al.* (2006); *Basu* (2005) implemented ST in a finite element method (FEM) framework to evaluate the compressive response of edge-notched laminates, and *Pineda et al.* (2009, 2010d) implemented ST in a multiscale framework to investigate the tensile behavior center-notched laminates.

Section 2.2 details the formulation of ST for modeling progressive microdamage in a fiber-reinforced lamina. In Section 2.3, ST is used to predict microdamage evolution in a unidirectional, AS4/3502 (graphite-epoxy) lamina under a range of combined transverse-shear loading. Finally in Section 2.3, the stability of the lamina with respect to small perturbations in the ISV is assessed under the same combined loading conditions to determine if loss of stability can be used to indicate transition between damage mechanisms.

2.2 Thermodynamically-Based Work Potential Theory

2.2.1 Thermodynamic Driving Force

Progressive microdamage in the matrix phase of a composite material is modeled using Schapery theory(*Schapery*, 1989, 1990; *Schapery and Sicking*, 1995). This thermodynamics-based, work potential theory can capture the nonlinear effects of microdamage mechanisms by partitioning the total work potential, W_T, into a recoverable part (elastic), W, and a dissipated portion (free energy available to generate structural changes in the material), W_S.

$$W_T = W + W_S \tag{2.1}$$

Both W and W_S are functions of a set of ISVs, $S_m, (m = 1, 2, M)$. These ISVs account for any nonlinear structural changes in the material. Differentiating W_S with respect to any ISV S_m, assuming limited path-dependence (*Schapery*, 1990), yields the thermodynamic force, f_m, available for advancing structural changes associated with the m^{th} ISV.

$$f_m = \frac{\partial W_s}{\partial S_m} \tag{2.2}$$

It is shown by *Schapery* (1989, 1990) that the total work potential is stationary with respect to each ISV.

$$\frac{\partial W_T}{\partial S_m} = 0 \tag{2.3}$$

Additionally, *Rice* (1971) utilized the second law of thermodynamics to establish the inequality:

$$f_m \dot{S}_m \geq 0 \tag{2.4}$$

which suggests that "healing" is not allowed for a material undergoing structural changes. Equations (2.2), (2.3), and (2.4) form the foundation of a thermodynamically-

based work potential theory for modeling nonlinear structural changes in a material exhibiting limited path-dependence.

2.2.2 Application of ST to Model Progressive Microdamage in Fiber-Reinforced Composites

The irrecoverable potential available to advance structural changes W_S can be a function of any number of state variables. To utilize the work potential model to capture the effects of progressive microdamage in a fiber-reinforced composite, it is assumed that the structural changes which result from microdamage, including matrix microcracking, shear banding, and fiber-matrix debonding, depend on only one ISV: S. It is assumed that S accounts for all microdamage present in the composite, and controls all material nonlinearities, prior to the onset of more catastrophic damage mechanisms such as mesoscopic matrix cracking (transverse cracking) and/or fiber breakage (and/or delamination in laminated composites). It should be noted, that additional ISVs may be included to account for additional damage and failure mechanisms. *Sicking* (1992); *Schapery and Sicking* (1995) used a dual-ISV formulation to capture both microdamage and transverse cracking, and in Chapter IV, ST is extended to account for axial failure, mesoscopic transverse, and shear crack growth.

It can be assumed that W_S is an additive function of the ISVs, $W_S = \sum_i^m W_i(S_i)$. Furthermore, W_i are in one-to-one correspondence with their arguments, so, W_i can be chosen such that $W_i = S_i$. Since, in this case, W_S is a function of only one ISV, $W_S = S$. Therefore, the ISV governing the potential responsible for advancing microdamage and that potential are equivalent. Equation (2.1) can now be recast as,

$$W_T = W + S \tag{2.5}$$

As the material is loaded, a portion of the work potential facilitates structural

changes in the material, such as microdamage, which affect the elastic properties of the material. Energy that is not dissipated is recovered when the structure is unloaded, and the magnitude of energy recovered is contingent upon the degraded, elastic properties at the previously attained maximum strain state. It is assumed, upon subsequent reloading, the material behaves linearly, exhibiting the elastic properties observed during unloading, until the material reaches the preceding maximum strain state. After this state is achieved, structural changes resume, affecting degrading the instantaneous elastic moduli of the material. This process is shown in Figure 2.1. The area above the unloading line represents dissipated potential S, and the shaded, triangular area under is the elastic strain energy density W. It is assumed that the material behaves as a secant material and there is no permanent deformation upon unloading. This a reasonable assumption for FRLs *Sicking* (1992); however, plastic deformation can also be incorporated, if necessary (*Schapery*, 1990). Extension to treat viscoelastic and viscoplastic response is outlined in *Hinterhoelzl and Schapery* (2004).

Differentiating (2.5) with respect to S, and utilizing Equation (2.3) yields:

$$\frac{\partial W}{\partial S} = -1 \tag{2.6}$$

Additionally, combining Equations (2.2) and (2.4) with $W_S = S$ results in

$$\dot{S} \geq 0 \tag{2.7}$$

which is a statement on the inadmissibility of microdamage "healing". Equation (2.7) dictates that the amount of energy dissipated into the progression of microdamage cannot be recovered. The combination of Equations (2.6) and (2.7) represent the evolution equations for microdamage in the matrix of a polymer matrix composite (PMC). If S was a crack length, instead of the energy dissipated through microdamage

evolution, then Equation (2.6) would be the fundamental fracture mechanics condition for crack extension [*Griffith* (1921)].

2.2.3 2-D Plane Stress Constitutive Law for a Unidirectional Fiber-Reinforced Lamina

Plane stress-strain relationships for a FRL can be written in principal material coordinates as:

$$\begin{aligned} \sigma_{11} &= Q_{11}\epsilon_{11} + Q_{12}\epsilon_{22} \\ \sigma_{22} &= Q_{12}\epsilon_{11} + Q_{22}\epsilon_{22} \\ \tau_{12} &= Q_{66}\gamma_{12} \end{aligned} \tag{2.8}$$

where γ_{12} is the engineering shear strain and

$$\begin{aligned} Q_{11} &= \frac{E_{11}}{1 - \nu_{12}\nu_{21}} \\ Q_{22} &= \frac{E_{22}}{1 - \nu_{12}\nu_{21}} \\ Q_{12} &= \nu_{12}Q_{22} \\ Q_{66} &= G_{12} \\ \nu_{21} &= \frac{\nu_{12}E_{22}}{E_{11}} \end{aligned} \tag{2.9}$$

where E_{11} is the axial elastic modulus, E_{22} is the transverse elastic modulus, ν_{12} and ν_{21} are the transverse Poisson's ratios, and G_{12} is the elastic shear modulus. After assuming that the quantity $\nu_{12}\nu_{21} << 1$, Equations (2.9) simplify,

$$\begin{aligned} Q_{11} &= E_{11} \\ Q_{22} &= E_{22} \\ Q_{12} &= \nu_{12}Q_{22} \\ Q_{66} &= G_{12} \end{aligned} \tag{2.10}$$

2.2.4 Determining the Damage State

To calculate the damaged state of the material, a relationship between the stiffness of the lamina and the ISV must be defined. Since the damage mechanisms associated with S accrue only in the matrix of the composite, it is assumed that the moduli affected by this damage are limited to E_{22} and G_{12}. This is a reasonable assumption for the in-plane behavior of PMCs. Experimentally it has been determined that S behaves as the strain cubed (ϵ^3); thus, it is convenient to introduce a reduced damage variable S_r (*Sicking*, 1992).

$$S_r \equiv S^{1/3} \tag{2.11}$$

Furthermore, the use of a reduced ISV transforms the dependence of the moduli on the microdamage variable into polynomial form:

$$E_{22} = E_{220} e_s(S_r) \tag{2.12}$$

$$G_{12} = G_{120} g_s(S_r) \tag{2.13}$$

where E_{220} and G_{120} are the undamaged transverse and shear elastic moduli, and $e_s(S)$ and $g_s(S)$ are polynomial microdamage functions relating the transverse and shear moduli to the reduced microdamage ISV S_r. *Sicking* (1992) provided a procedure for determining e_s and g_s experimentally from three uniaxial coupon tension tests. The stress-strain curve from a $[\pm 45^\circ]_S$ angle-ply laminate yields $g_s(S)$; whereas, a $[15^\circ]$ unidirectional laminate can be used to obtain $e_s(S)$ under transverse tension, and a $[\pm 30^\circ]_S$ angle-ply laminate provides $e_s(S)$ in transverse compression. The experimental curves can then be fit with polynomials (such that, the stiffness values at $S = 0$, are $E_{22} = E_{220}$ and $G_{12} = G_{120}$) and used in Equations (2.12) and (2.13).

The elastic strain energy density W can be written using the plane stress consti-

tutive relationships.

$$W = \frac{1}{2}(E_{11}\epsilon_{11}^2 + E_{22}(S)\epsilon_{22}^2 + G_{12}(S)\gamma_{12}^2) + Q_{12}\epsilon_{11}\epsilon_{22} \tag{2.14}$$

Employing Equation (2.6) with (2.12), (2.13), and (2.14), and assuming the quantity $Q_{12} = \nu_{12}Q_{22}$ is constant (independent of S) yields an ordinary differential equation which can be solved for the damage evolution S.

$$\frac{1}{2}\left(\epsilon_{22}^2 E_{220}\frac{de_s}{dS} + \gamma_{12}^2 G_{120}\frac{dg_s}{dS}\right) = -1 \tag{2.15}$$

Using the reduced ISV the evolution equation, Equation (2.15), becomes

$$\frac{1}{2}\left(\epsilon_{22}^2 E_{220}\frac{de_s}{dS_r} + \gamma_{12}^2 G_{120}\frac{dg_s}{dS_r}\right) = -3S_r^2 \tag{2.16}$$

Once S_r is determined from Equation (2.16), taking into account Equation (2.7), the transverse and shear moduli can be degraded accordingly using Equations (2.12) and (2.13). The above equation indicates that the work of structural change depends only on the strain state, the initial virgin composite moduli (E_{220} and G_{120}), and the microdamage functions ($e_s(S)$, $g_s(S)$). Moreover, the microdamage state is only a function of the current strains and is independent of the loading history. This arises from the postulation of the existence of a work potential and the definition of Equation (2.2). *Lamborn and Schapery* (1988, 1993) demonstrated limited path-dependence experimentally for a graphite/epoxy laminate and deduced that the small amount of path-dependence exhibited is primarily due to rate effects, so long as, the loading is such that the active damage modes change continuously or remain constant. Additionally, unlike most continuum damage theories, Equation (2.16) requires no separate initiation criterion. For low strain levels, S_r will remain near zero, and its effect on the composite moduli will be negligible. However as the strain levels

increase, the rate of evolution of the ISV will also change as dictated by the slope of the microdamage functions $\frac{de_s}{dS_r}$ and $\frac{dg_s}{dS_r}$.

2.3 Microdamage Evolution in a Graphite/Epoxy Lamina

Sicking (1992) measured the microdamage curves for an AS4/3502, graphite/epoxy laminae with virgin, elastic properties listed in Table 2.1. The polynomial coefficients of the microdamage functions of S_r, obtained from $[\pm 45^\circ]_S$ angle-ply, $[15^\circ]$ unidirectional, and $[\pm 30^\circ]_S$ angle-ply laminate coupon tests, are presented here in Table 2.2, and these functions,

$$E_{22} = E_{220}\left(e_{s0} + e_{s1}S_r + e_{s2}S_r^2 + e_{s3}S_r^3 + e_{s4}S_r^4\right) \tag{2.17}$$

$$G_{22} = G_{120}\left(g_{s0} + g_{s1}S_r + g_{s2}S_r^2 + g_{s3}S_r^3 + g_{s4}S_r^4\right) \tag{2.18}$$

are plotted in Figure 2.2. Numerous laminates were tested, but these three laminates achieved the maximum S_r for the given, local loading scenario (shear, transverse tension, or transverse compression) before failing due to transverse cracking.

The AS4/3502 microdamage functions and elastic properties were utilized, and Equation (2.15) was solved numerically for a range of applied transverse and shear strains: -0.04 $\leq \epsilon_{22} \leq$ 0.04 and 0.00 $\leq \gamma_{12} \leq$ 0.05. Only positive shear strain is applied because $g_s(S_r)$, and hence S_r, is independent of the sign of γ_{12}. Depending on the strain state, a maximum S_r was enforced based upon reaching the endpoints of the microdamage functions in Figure 2.2. If no transverse strain was applied, the maximum S_r was limited to 114.7 $\text{Pa}^{\frac{1}{3}}$; if the applied transverse strain was positive, the maximum S_r was 62.13 $\text{Pa}^{\frac{1}{3}}$, and the maximum S_r was set at 97.49 $\text{Pa}^{\frac{1}{3}}$ if the transverse strain was negative. If the calculated S_r was above the predetermined maximum, it was set equal to the maximum, and further damage evolution was not permitted. These endpoints indicate the arrest of microdamage in the experiment

and the initiation of transverse cracking, or other damage mechanisms, which leads to abrupt failure in the angle ply or unidirectional laminates. An additional state variable would be required to damage (or failure) evolution beyond the maximum S_r.

The microdamage curves were obtained by *Sicking* (1992) using numerous different laminate lay-ups. All the lay-ups produced similar microdamage functions; however, the stacking orientation affected the value of S_r at which transverse cracking initiated and the microdamage function ended (i.e. the endpoint of the microdamage functions). The limiting S_r values used here are chosen to be the results from *Sicking* (1992) that reached the largest values of S_r among all the laminates tested.

Figure 2.3 displays a contour surface of S_r as a function of applied ϵ_{22} and γ_{12}. This surface displays that applied shear strain leads to rapid increase in S_r. As the ratio of tensile transverse strain to shear strain increases, the microdamage progression is less rapid but still significant. In the compressive strain regime, microdamage evolution is stagnant, even for relatively low ratios of ϵ_{22} to γ_{12}. It is not until this ratio is below unity, and γ_{12} dominates the applied loading, that the microdamage evolves at a rate similar to that in the tensile transverse strain regime. Thus, microdamage evolution is driven primarily by shear strain, and furthermore, will not accumulate if a compressive transverse strain greater than the shear strain is applied.

The endpoints of the microdamage functions in Figure 2.2 are the maximum attainable microdamage for the lay-ups that were tested ($[\pm 45^\circ]_S$, $[\pm 30^\circ]_S$, and $[15^\circ]$). At those damage levels more catastrophic damage mechanisms initiate, and microdamage progression ceases. It is possible that other configurations could accrue more, or less, microdamage, and in fact, *Sicking* (1992) tested other laminates that failed at lower values of S_r, but the data from all tested laminates coincided with the microdamage curves. Assuming that there is a configuration for which microdamage growth is never superseded by the evolution of other damage mechanisms, the microdamage curves presented in Figure 2.2 were extrapolated to zero in Figure 2.4. The end slope

of the g_s curve in Figure 2.2a was used to linearly extrapolate g_s to zero at $S_r = 132.6$ $\text{Pa}^{\frac{1}{3}}$. Additionally, e_s in tension and in compression were both extrapolated linearly to zero at $S_r = 132.6$ $\text{Pa}^{\frac{1}{3}}$; thus, both the transverse and shear moduli would vanish at the same damage levels. The three extrapolated microdamage functions were fit with fourth order polynomials (see Equations (2.17) and (2.18)); the coefficients are presented in Table 2.3, and they are displayed in Figure 2.5. Reduction of the transverse and shear moduli to zero through microdamage evolution may not be a physical possibility, but it provides mathematical insight into the evolution of S and the stability of the material with respect to progressive microdamage.

Evolution of S_r as a function of ϵ_{22} and γ_{12} is presented in Figure 2.5 using the extrapolated microdamage curves in Figure 2.4. This shows that if microdamage was not limited to 62.13 $\text{Pa}^{\frac{1}{3}}$ when transverse tensile loading is applied, the microdamage would continue to grow until E_{22} and G_{12} reached zero. Additionally, if the compressive transverse strain is between -0.015 and 0.00, the microdamage will progress with increasing shear strain. However, if the compressive transverse strain is below-0.015, and the shear strain is low ($<$0.02), a trend as similar to Figure 2.3 is exhibited; microdamage will not advance. As γ_{12} increases, for this ϵ_{22} level, S_r increases, but reaches a plateau. Under these loading scenarios, the settled value of S_r decreases as the magnitude of the compressive transverse strain is increased. This exemplifies that even if experimental microdamage functions were available for AS4/3502 that contained transverse and shear stiffness data points equal to zero, microdamage is not a dominating mechanism when compressive transverse strains are present.

2.4 Stability of Microdamage Evolution

Microdamage growth is a stable process if the second variation of the total work potential with respect to the ISV is positive (*Schapery*, 1990).

$$\delta_S^2 W_T > 0 \tag{2.19}$$

Taking the second variation of Equation (2.5), while using Equations (2.11) and (2.16) gives an expression for stability of microdamage evolution in a unidirectional, fiber reinforced lamina.

$$\begin{aligned}\delta_S^2 W_T = \frac{\partial^2 W_T}{\partial S^2}(\delta S)^2 = \frac{1}{9S_r^4}\Bigg[\frac{1}{2}\left(\epsilon_{22}^2 E_{220}\frac{d^2 e_s}{dS_r^2} + \gamma_{12}^2 G_{120}\frac{d^2 g_s}{dS_r^2}\right) - \\ \frac{1}{S_r}\left(\epsilon_{22}^2 E_{220}\frac{de_s}{dS_r} + \gamma_{12}^2 G_{120}\frac{dg_s}{dS_r}\right)\Bigg](\delta S)^2 > 0\end{aligned} \tag{2.20}$$

Noting that $S_r \geq 0$ and $S \geq 0$, the condition for stability becomes

$$\begin{aligned}\overline{\delta_S^2 W_T} = &\frac{1}{2}\left(\epsilon_{22}^2 E_{220}\frac{d^2 e_s}{dS_r^2} + \gamma_{12}^2 G_{120}\frac{d^2 g_s}{dS_r^2}\right) - \\ &\frac{1}{S_r}\left(\epsilon_{22}^2 E_{220}\frac{de_s}{dS_r} + \gamma_{12}^2 G_{120}\frac{dg_s}{dS_r}\right) > 0\end{aligned} \tag{2.21}$$

where the overbar indicates that the $\dfrac{1}{9S_r^4}$ and $(\delta S_r)^2$ terms have been divided out. The left hand side of the inequality ($\overline{\delta^2 W_T}$) in Equation (2.21) is evaluated for the same range of ϵ_{22} and γ_{12} used in Section 2.3 and with the properties in Tables 2.1 and 2.3. A contour surface plot is presented in Figure 2.6. The stability condition is satisfied for all values of ϵ_{22} and γ_{12}. For a particular region in quadrant I of the ϵ_{22}-γ_{12} plane where ϵ_{22} and γ_{12} are high, $\overline{\delta^2 W_T} = 0$. However, this corresponds to a regime where there is no change in S_r (i.e. $\delta S_r = 0$); therefore, stability is automatically satisfied. Figure 2.6 indicates that microdamage evolution in AS4/3502 is an unconditionally stable process. Thus, loss of stability pertaining to microdamage cannot be used to

determine the onset of more catastrophic failure mechanisms in the matrix, such as transverse cracking.

2.5 Conclusions

The formulation for the thermodynamically-based, work potential continuum damage theory, Schapery theory, was presented. ST is capable of capturing the effects of progressive matrix microdamage in FRLs by relating the transverse and shear moduli to an ISV associated with the microdamage. Unlike many existing continuum damage theories, ST uses a single damage variable, but degradation of the moduli is controlled by three distinct microdamage functions which are obtained from three uniaxial coupon tests. Additionally, ST requires no initiation criterion.

Microdamage evolution for a range of applied transverse and shear strains was also investigated for an AS4/3502 unidirectional lamina. When positive transverse strains are applied, microdamage growth continues, with increasing transverse and/or shear strains, until the moduli reach a value of zero. However, the actual material, as observed in experiments, exhibits transverse or mesoscopic cracking, leading to rapid failure far before matrix microdamage could degrade the moduli to zero. Under compressive transverse strains, microdamage evolution remains fairly dormant unless a large shear strain is also applied. This indicates that compressive transverse strains constrain microdamage, and another mechanism must be responsible for degradation in transverse compression.

The stability of microdamage evolution in AS4/3502, under a range of applied transverse and shear strains, was calculated. It was shown that microdamage growth is an unconditionally stable process under any transverse-shear strain loading combination. Therefore, loss of stability cannot be used to indicate the initiation of other matrix damage mechanisms, such as transverse cracking, which are ultimately responsible for failure. Moreover, an additional ISV [*Sicking* (1992); *Schapery and*

Sicking (1995)] or separate initiation criteria must be used to predict the onset of more catastrophic mechanisms.

Property	Value
E_{11} (GPa)	125.8
E_{22} (GPa)	9.31
ν_{12}	0.329
G_{12} (GPa)	5.1

Table 2.1: Virgin elastic properties for AS4/3502 (*Sicking*, 1992)

	e_s (Tension)	e_s (Compression)		g_s
e_{s0}	1.00	1.00	g_{s0}	1.00
e_{s1}	-1.91E-3	-2.87E-3	g_{s1}	-3.59E-3
e_{s2}	-2.75E-5	2.23E-4	g_{s2}	-1.20E-4
e_{s3}	-2.48E-7	-3.42E-6	g_{s3}	1.40E-6
e_{s4}	2.51E-9	1.46E-8	g_{s4}	-5.64E-9

Table 2.2: Microdamage polynomial coefficients for AS4/3502 (*Sicking*, 1992)

	e_s (Tension)	e_s (Compression)		g_s
e_{s0}	1.00	1.00	g_{s0}	1.00
e_{s1}	-2.75E-3	-2.08E-3	g_{s1}	-4.02E-3
e_{s2}	3.14E-5	1.32E-4	g_{s2}	-9.45E-5
e_{s3}	-1.24E-6	-1.03E-6	g_{s3}	1.03E-6
e_{s4}	5.57E-9	-2.27E-9	g_{s4}	-3.90E-9

Table 2.3: Extrapolated microdamage polynomial coefficients for AS4/3502

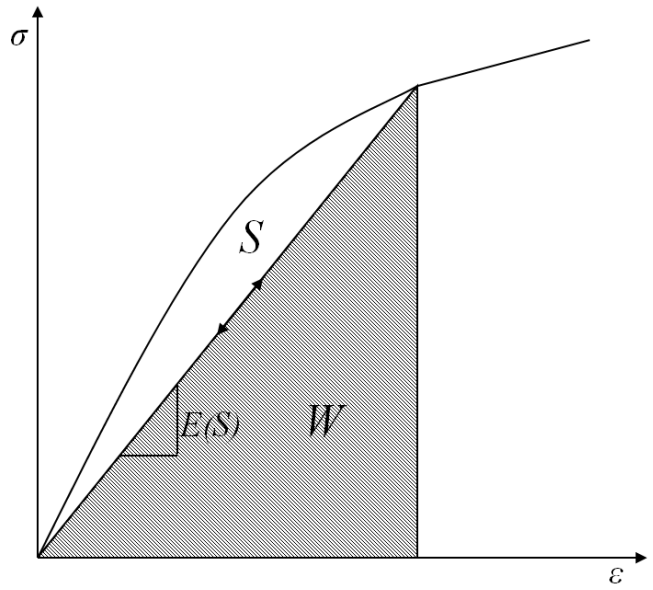

Figure 2.1: Typical stress-strain curve showing the elastic (W) and irrecoverable (S) portions.

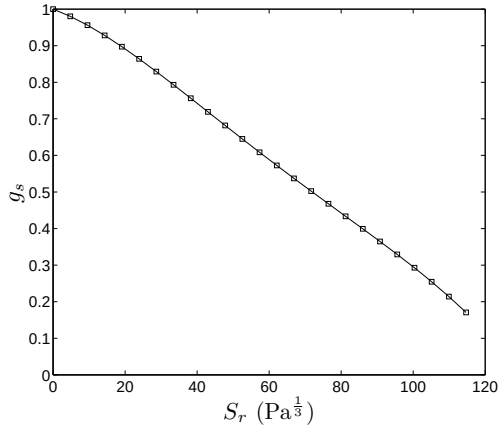

(a) Shear microdamage function obtained from $[\pm 45^\circ]_S$ angle-ply laminate.

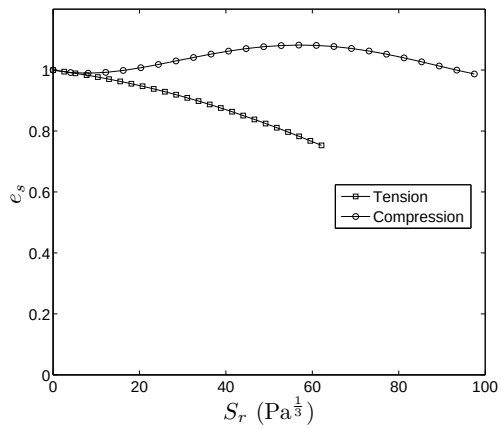

(b) Transverse tension and compression microdamage functions obtained from $[15^\circ]$ unidirectional and $[\pm 30^\circ]_S$ angle-ply laminates, respectively.

Figure 2.2: ST microdamage curves for AS4/3502 (*Sicking*, 1992).

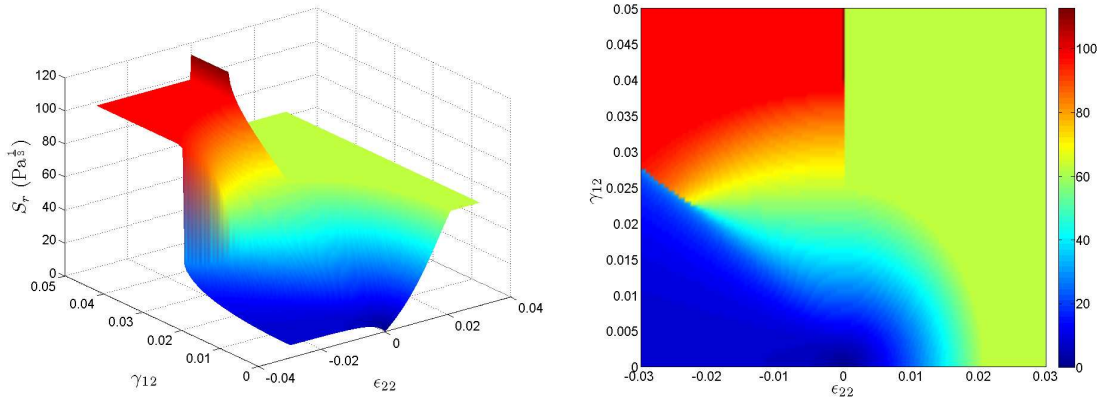

(a) Isometric view.

(b) Top-down view.

Figure 2.3: Microdamage S_r evolution in AS4/3502 as a function of applied ϵ_{22} and γ_{12} using data from *Sicking* (1992).

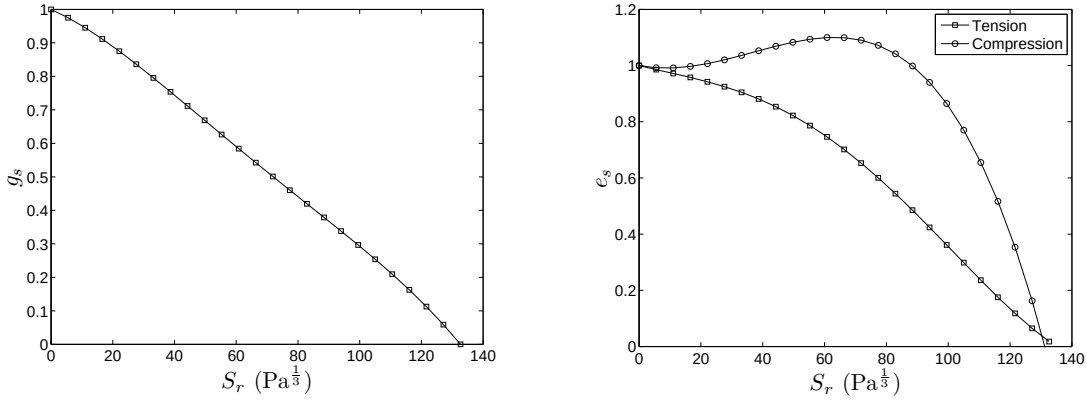

(a) Shear microdamage function obtained from $[\pm 45°]_S$ angle-ply laminate.

(b) Transverse tension and compression microdamage functions obtained from $[15°]$ unidirectional and $[\pm 30°]_S$ angle-ply laminates, respectively.

Figure 2.4: Extrapolated ST microdamage curves for AS4/3502.

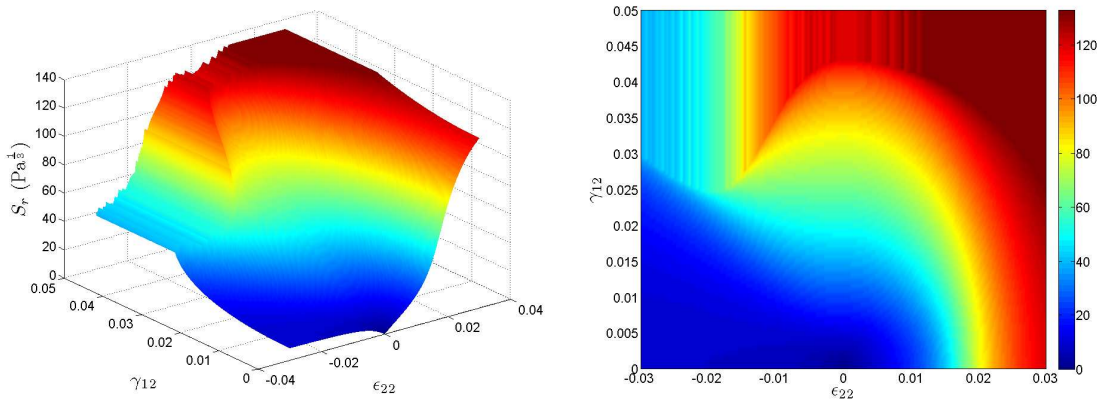

(a) Isometric view.

(b) Top-down view.

Figure 2.5: Microdamage S_r evolution in AS4/3502 as a function of applied ϵ_{22} and γ_{12} using data extrapolated from *Sicking* (1992).

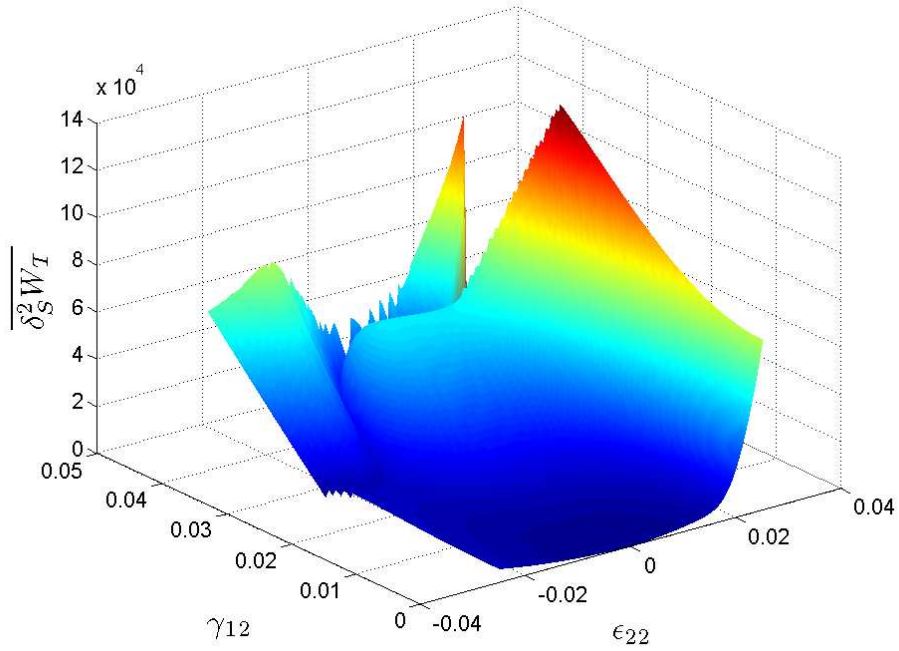

Figure 2.6: Condition for stable microdamage evolution as a function of applied ϵ_{22} and γ_{12} for AS4/3502. $\overline{\delta^2 W_T} > 0$ when $\delta S_r > 0$; therefore, microdamage growth is unconditionally stable.

CHAPTER III

Multiscale Modeling of Progressive Damage and Failure in Fiber-Reinforced Laminates

3.1 Introduction

The complex nature of damage and failure in composite materials arises from their heterogeneity. The separate constituents introduce additional length scales, below the operational, structural length scale, at which damage and failure mechanisms accrue. Thus, the observed, global failure mechanisms of a composite structure are results of the evolution and interaction of damage and failure mechanisms at the subscales. It is in this reciprocative manner that a composite material behaves more like a structure than a material.

The two-scale, multiscale technique (ST-FEAMAC) developed in this chapter utilizes the finite element method (FEM) for the coarse-scale, lamina-level modeling of a fiber-reinforced laminate (FRL). Schapery theory (ST, see Chapter II) is implemented in FEM and used to model progressive matrix microdamage at the macroscale. Conversely in this chapter, micromechanics will be used to mark the localization of damage into failure. The fine-scale, or fiber/matrix microscale, is modeled using the generalized method of cells (GMC)[*Paley and Aboudi* (1992)]. The software implementation of GMC, the MAC/GMC suite of micromechanics codes developed at the

NASA Glenn Research Center (GRC) [*Bednarcyk and Arnold* (2002b,c)], is used to evaluate failure at the microscale.

Within GMC, a repeating unit cell (RUC) is discretized into a number of subcells, each of which is occupied by a particular constituent of the composite. Traction and displacement continuity are enforced, in an average sense, at subcell interfaces in, along with periodic boundary conditions at the boundaries of, the RUC. These conditions can be utilized to calculate a strain concentration matrix which relates the local subcell strains to the globally applied strains. Once the local strains are resolved, the subcell constitutive laws yield the local stresses, and the global stresses and homogenized stiffness of the RUC follow readily. Failure criteria are utilized in each subcell to model the effects of matrix cracking and fiber failure. If a failure criterion is satisfied in a particular subcell, the stiffness of that subcell is greatly reduced and that reduced subcell stiffness is used to calculate the local subcell stresses as well as the homogenized stiffness of the RUC and the global stresses. Thus, the effects of failure at the microscale manifest as a reduction of the global, homogenized stiffness of the composite. This methodology is known as subvolume elimination method [*Aboudi et al.* (2012)].

The FEAMAC software [*Bednarcyk and Arnold* (2006)] is employed to facilitate communication between the MAC/GMC core micromechanics engine and the Abaqus [*Abaqus* (2008)] finite element solver. Integration point strains are applied to the GMC RUC, and GMC is used to calculate the homogenized stiffness tensor of the RUC (accounting for potential subcell failure) and update the integration point stresses. To improve computational efficiency in ST-FEAMAC, micromechanics calculations are precluded unless the lamina-level microdamage is above a predetermined threshold.

The GMC formulation is presented in Section 3.2. Whereas, details on the multiscale ST-FEAMAC methodology developed are given in Section 3.3. Experimental data from two laminated center-notched panels (CNPs), tested at the NASA Lang-

ley Research Center (LaRC) [*Bogert et al.* (2006); *Satyanarayana et al.* (2007)], are compared to ST-FEAMAC in Section 3.4.

3.2 The Generalized Method of Cells

A micromechanical analysis technique, coined the method of cells (MOC), was developed by *Aboudi* (1991); subsequently, *Paley and Aboudi* (1992) expanded MOC into the generalized method of cells, and later *Aboudi et al.* (2001) further increased the robustness of this method with the high-fidelity generalized method of cells (HFGMC). These methods provide semi-closed form solutions for determining global anisotropic composite properties in terms of the constituent materials, as well as, the fully three dimensional (3-D) stresses and strains in each of the constituent subcells. The sophisticated methods (GMC and HFGMC) offer a high degree of accuracy at a relatively low computational cost.

Displacement and traction continuity are enforced in an average, integral sense at the subcell interfaces of a discretized RUC in GMC. These continuity conditions are used to formulate a set of semi-analytical linear algebraic equations that can be solved for the local subcell strains in terms of globally applied strains or stresses. Subsequently, local constitutive laws can be utilized to obtain the local subcell stresses, and a constitutive law for the effective, homogenized composite can be formulated.

It is assumed that a composite microstructure can be represented as a collection of triply periodic RUCs containing a general number of constituents, as shown in Figure 3.1. The RUC is then discretized into N_α x N_β x N_γ parallelepiped subcells, as exhibited in Figure 3.2. Each of these subcells is occupied by one of the constituent materials of the composite. The number of subcells and the materials occupying each subcell are completely general. For a two-phase fibrous composite, any desired micro-architecture can be represented by occupying each subcell with either a matrix or fiber constituent. Since the microstructure does not vary along the axial, fiber-direction,

a unidirectional composite can be modeled using a doubly-periodic RUC (Figure 3.3), where only the x_2-x_3 plane is discretized. Herein, doubly-periodic formulations of both GMC [*Paley and Aboudi* (1992)] and HFGMC [*Aboudi et al.* (2001)] (see Chapter V) will be employed; the reader is referred to *Aboudi et al.* (2012) for the fully 3D formulations.

3.2.1 Definition of subcell strains and stresses

The objective of this method is to determine the average behavior of the composite material; thus, the displacement fields in each subcell are approximated to be linear (HFGMC employs a quadratic displacement approximation). If a local coordinate frame is defined with the origin at the center of each subcell with dimensions h_β x l_γ, as in Figure 3.4, the corresponding displacement field is approximated as:

$$u_i^{(\beta\gamma)} = w_i^{(\beta\gamma)} + \bar{x}_2^{(\beta)}\phi_i^{(\beta\gamma)} + \bar{x}_3^{(\gamma)}\psi_i^{(\beta\gamma)} \quad i = 1, 2, 3 \tag{3.1}$$

where $w_i^{(\beta\gamma)}$ is the displacement at the center of subcell $\beta\gamma$. Microvariables $(\phi_i^{(\beta\gamma)}, \psi_i^{(\beta\gamma)})$ characterize the first-order dependence of the displacement field on the local coordinates $\bar{x}_2^{(\beta)}$ and $\bar{x}_3^{(\gamma)}$. Note that in this doubly-periodic formulation, the displacements are not a function of x_1, but all three displacement components are present.

The components of the strain tensor follow from Equation (3.1) as,

$$\epsilon_{ij}^{(\beta\gamma)} = \frac{1}{2}\left(\partial_i u_j^{(\beta\gamma)} + \partial_j u_i^{(\beta\gamma)}\right) \tag{3.2}$$

where $\partial_1 = \frac{\partial}{\partial x_1}, \partial_2 = \frac{\partial}{\partial \bar{x}_2^{(\beta)}}, \partial_3 = \frac{\partial}{\partial \bar{x}_3^{(\gamma)}}$. Substituting Equation (3.1) into Equation (3.2) results in the six components of the strain tensor $\epsilon_{ij}^{(\beta\gamma)}$ for each subcell in terms

of the microvariables.

$$\begin{aligned}
\epsilon_{11}^{(\beta\gamma)} &= \partial_1 w_1^{(\beta\gamma)} \\
\epsilon_{22}^{(\beta\gamma)} &= \phi_2^{(\beta\gamma)} \\
\epsilon_{33}^{(\beta\gamma)} &= \psi_3^{(\beta\gamma)} \\
2\epsilon_{23}^{(\beta\gamma)} &= \phi_3^{(\beta\gamma)} + \psi_2^{(\beta\gamma)} \\
2\epsilon_{13}^{(\beta\gamma)} &= \psi_1^{(\beta\gamma)} + \partial_1 w_3^{(\beta\gamma)} \\
2\epsilon_{12}^{(\beta\gamma)} &= \phi_1^{(\beta\gamma)} + \partial_1 w_2^{(\beta\gamma)}
\end{aligned} \tag{3.3}$$

A constitutive relationship between the local subcell stresses and strains can be established.

$$\sigma_{ij}^{(\beta\gamma)} = C_{ijkl}^{(\beta\gamma)} \left(\epsilon_{kl}^{(\beta\gamma)} - \epsilon_{kl}^{P(\beta\gamma)} - \epsilon_{kl}^{T(\beta\gamma)} \right) \tag{3.4}$$

where $\epsilon_{ij}^{P(\beta\gamma)}$ and $\epsilon_{ij}^{T(\beta\gamma)}$ are the plastic and thermal strains in subcell $\beta\gamma$, respectively. In this work, plastic and thermal effects are not considered and all material nonlinearity is due to progressive degradation of the components of the elastic stiffness tensor $C_{ijkl}^{(\beta\gamma)}$. Therefore, Equation (3.4) reduces to

$$\sigma_{ij}^{(\beta\gamma)} = C_{ijkl}^{(\beta\gamma)} \epsilon_{kl}^{(\beta\gamma)} \tag{3.5}$$

3.2.2 Displacement continuity conditions

Subcell displacements are required to be continuous at the interfaces between adjacent subcells, as well as at the boundaries between neighboring repeating cells.

$$u_i^{(\beta\gamma)}\Big|_{\bar{x}_2^{(\beta)}=h_\beta/2} = u_i^{(\hat{\beta}\gamma)}\Big|_{\bar{x}_2^{(\hat{\beta})}=-h_{\hat{\beta}}/2} \tag{3.6}$$

$$u_i^{(\beta\gamma)}\Big|_{\bar{x}_3^{(\gamma)}=l_\gamma/2} = u_i^{(\beta\hat{\gamma})}\Big|_{\bar{x}_3^{(\hat{\gamma})}=-l_{\hat{\gamma}}/2} \tag{3.7}$$

where h_β and l_γ are the subcell dimensions shown in Figure 3.4, and the ' $\hat{}$ ' symbol indicates the adjacent subcell.

$$\hat{\beta} = \begin{cases} \beta+1, & \beta > N_\beta \\ 1, & \beta = N_\beta \end{cases} \tag{3.8}$$

$$\hat{\gamma} = \begin{cases} \gamma+1, & \gamma > N_\gamma \\ 1, & \gamma = N_\gamma \end{cases} \tag{3.9}$$

The displacement continuity conditions given in Equations (3.6) and (3.7) are enforced at the interfaces in an average, integral sense.

$$\int_{l_\gamma/2}^{l_\gamma/2} u_i^{(\beta\gamma)}\Big|_{\bar{x}_2^{(\beta)}=h_\beta/2} d\bar{x}_3^{(\gamma)} = \int_{-l_\gamma/2}^{l_\gamma/2} u_i^{(\hat{\beta}\gamma)}\Big|_{\bar{x}_2^{(\hat{\beta})}=-h_{\hat{\beta}}/2} d\bar{x}_3^{(\gamma)} \tag{3.10}$$

$$\int_{h_\beta/2}^{h_\beta/2} u_i^{(\beta\gamma)}\Big|_{\bar{x}_3^{(\gamma)}=l_\gamma/2} d\bar{x}_2^{(\beta)} = \int_{-h_\beta/2}^{h_\beta/2} u_i^{(\beta\hat{\gamma})}\Big|_{\bar{x}_3^{(\hat{\gamma})}=-l_{\hat{\gamma}}/2} d\bar{x}_2^{(\beta)} \tag{3.11}$$

Substituting the displacement field approximation Equation (3.1) into Equations (3.10) and (3.11) yields statements of displacement continuity in terms of the microvariables.

$$w_i^{(\beta\gamma)} + \frac{1}{2}h_\beta \phi_i^{(\beta\gamma)} = w_i^{(\hat{\beta}\gamma)} - \frac{1}{2}h_{\hat{\beta}}\phi_i^{(\hat{\beta}\gamma)} \tag{3.12}$$

$$w_i^{(\beta\gamma)} + \frac{1}{2}l_\gamma \psi_i^{(\beta\gamma)} = w_i^{(\beta\hat{\gamma})} - \frac{1}{2}l_{\hat{\gamma}}\psi_i^{(\beta\hat{\gamma})} \tag{3.13}$$

All field variables are evaluated at the center of each subcell; therefore Taylor expansions of the field variables in Equations (3.12) and (3.13), omitting second order and higher terms, results in

$$w_i^{(\beta\gamma)} - \frac{1}{2}h_\beta\left(\frac{\partial w_i^{(\beta\gamma)}}{\partial x_2} - \phi_i^{(\beta\gamma)}\right) = w_i^{(\hat{\beta}\gamma)} - \frac{1}{2}h_{\hat{\beta}}\left(\frac{\partial w_i^{(\hat{\beta}\gamma)}}{\partial x_2} - \phi_i^{(\hat{\beta}\gamma)}\right) \tag{3.14}$$

$$w_i^{(\beta\gamma)} - \frac{1}{2} l_\gamma \left(\frac{\partial w_i^{(\beta\gamma)}}{\partial x_3} - \psi_i^{(\beta\gamma)} \right) = w_i^{(\beta\hat{\gamma})} - \frac{1}{2} l_{\hat{\gamma}} \left(\frac{\partial w_i^{(\beta\hat{\gamma})}}{\partial x_3} - \psi_i^{(\beta\hat{\gamma})} \right) \tag{3.15}$$

where the field variables are evaluated at the corresponding subcell interface. In order to map the RUC to a single point within an equivalent, homogenous medium, Equations (3.14) and (3.15) must hold for all $\beta = 1, \ldots, N_\beta$ and $\gamma = 1, \ldots, N_\gamma$.

Subtracting Equation (3.12) from (3.14) and Equation (3.13) from (3.14) gives

$$\frac{\partial w_i^{(\beta\gamma)}}{\partial x_2} = \frac{\partial w_i^{(\hat{\beta}\gamma)}}{x_2} \tag{3.16}$$

$$\frac{\partial w_i^{(\beta\gamma)}}{\partial x_3} = \frac{\partial w_i^{(\beta\hat{\gamma})}}{x_3} \tag{3.17}$$

To satisfy Equations (3.16) and (3.17), the displacement field must be such that

$$w_i^{(\beta\gamma)} = w_i, \quad \begin{matrix} \beta = 1, \ldots, N_\beta \\ \gamma = 1, \ldots, N_\gamma \end{matrix} \tag{3.18}$$

it is now clear that w_i represents the average displacements of the multiphase RUC that maps to a single point in an equivalent, homogenous continuum that effectively represents the multiphase composite. As such, the linear terms in the displacement field Equation (3.1) provide the local variations from the average displacements.

Utilizing Equation (3.18) and summing Equations (3.14) and (3.15) over all β and γ, respectively, results in $N_\beta + N_\gamma$ relations between the displacement of the equivalent continuum point and local, subcell microvariables in the RUC

$$\sum_{\beta=1}^{N_\beta} h_\beta \phi_i^{(\beta\gamma)} = H \frac{\partial w_i}{\partial x_2}, \quad \gamma = 1, \ldots, N_\gamma \tag{3.19}$$

$$\sum_{\beta=1}^{N_\beta} l_\gamma \psi_i^{(\beta\gamma)} = L \frac{\partial w_i}{\partial x_3}, \quad \beta = 1, \ldots, N_\beta \tag{3.20}$$

3.2.3 Derivation of the displacement continuity conditions in terms of average subcell strains

Equations (3.19) and (3.20) relate the global, equivalent displacement field of an equivalent continuum w_i to the local, subcell microvariables $\phi_i^{(\beta\gamma)}$ and $\psi_i^{(\beta\gamma)}$. It is possible to recast these equations in terms of the average, local subcell strains $\epsilon_{ij}^{(\beta\gamma)}$.

First, because w_i are the average displacement components of an equivalent continuum, it follows that the average global RUC strains are defined as

$$\bar{\epsilon}_{ij} = \frac{1}{2}\left(\frac{\partial w_i}{\partial x_j} + \frac{\partial w_j}{\partial x_i}\right) \tag{3.21}$$

Substituting the first relation in Equation (3.3) yields

$$\epsilon_{11}^{(\beta\gamma)} = \bar{\epsilon}_{11}, \quad \beta = 1, \ldots, N_\beta, \quad \gamma = 1, \ldots, N_\gamma \tag{3.22}$$

These $N_\beta N_\gamma$ equations are a result of the doubly periodic assumptions and indicate a state of generalized plane strain; i.e., the average strain in x_1-direction of all subcells is uniform and equal to the global strain in the x_1-direction.

Setting $i = 2$ in Equation (3.19) and utilizing the second relationship of Equation (3.3) and Equation (3.21) yields

$$\sum_{\beta=1}^{N_\beta} h_\beta \epsilon_{22}^{(\beta\gamma)} = H\bar{\epsilon}_{22}, \quad \gamma = 1, \ldots, N_\gamma \tag{3.23}$$

Similarly, using Equation (3.20) with $i = 3$, the third relationship of Equation (3.3) and Equation (3.21) gives

$$\sum_{\gamma=1}^{N_\gamma} l_\gamma \epsilon_{33}^{(\beta\gamma)} = L\bar{\epsilon}_{33}, \quad \beta = 1, \ldots, N_\beta \tag{3.24}$$

Two of the shear strain continuity conditions can be derived by adding $H\dfrac{\partial w_2}{\partial x_1}$ to Equation (3.19) with $i = 1$, noting the sixth relation in Equation (3.3) and Equation (3.21),

$$\sum_{\beta=1}^{N_\beta} h_\beta \epsilon_{12}^{(\beta\gamma)} = H\bar{\epsilon}_{12}, \gamma = 1, \ldots, N_\gamma \tag{3.25}$$

and adding $L\dfrac{\partial w_1}{\partial x_2}$ to Equation (3.20) with $i = 1$, using the fifth relation in Equation (3.3) and Equation (3.21).

$$\sum_{\gamma=1}^{N_\gamma} l_\gamma \epsilon_{13}^{(\beta\gamma)} = L\bar{\epsilon}_{13}, \quad \beta = 1, \ldots, N_\beta \tag{3.26}$$

Finally, averaging the local subcell strains to obtain the global composite strain

$$\sum_{\beta=1}^{N_\beta}\sum_{\gamma=1}^{N_\gamma} h_\beta l_\gamma \epsilon_{ij}^{(\beta\gamma)} = HL\bar{\epsilon}_{ij} \tag{3.27}$$

with $i = 2$ and $j = 3$ yields the finally strain continuity condition.

$$\sum_{\beta=1}^{N_\beta}\sum_{\gamma=1}^{N_\gamma} h_\beta l_\gamma \epsilon_{23}^{(\beta\gamma)} = HL\bar{\epsilon}_{23} \tag{3.28}$$

Equations (3.23)-(3.26) and (3.28) represent $2(N_\beta + N_\gamma) + N_\beta N_\gamma + 1$ average strain continuity conditions, and can be written in matrix form as

$$\mathbf{A}_G \boldsymbol{\epsilon}_S = \mathbf{J}\bar{\boldsymbol{\epsilon}} \tag{3.29}$$

where the global, average strain vector is

$$\bar{\boldsymbol{\epsilon}} = [\bar{\epsilon}_{11}, \bar{\epsilon}_{22}, \bar{\epsilon}_{33}, 2\bar{\epsilon}_{23}, 2\bar{\epsilon}_{13}, 2\bar{\epsilon}_{12}]^T \tag{3.30}$$

and the local subcell strain vector is

$$\boldsymbol{\epsilon}_S = \left[\boldsymbol{\epsilon}^{(11)}, \boldsymbol{\epsilon}^{(12)}, \ldots, \boldsymbol{\epsilon}^{(N_\beta N_\gamma)}\right]^T \tag{3.31}$$

where $\boldsymbol{\epsilon}^{(\beta\gamma)}$ are vectors containing the subcell strains in the same order as Equation (3.30).

The displacement continuity conditions can be relaxed to account for interfacial debonding by introducing a displacement jump at the subcell interfaces. The interfacial displacement can then be related to the interfacial traction through appropriate interfacial constitutive law. *Bednarcyk et al.* (2004) utilized the evolving compliant interface (ECI) model to relate traction to separation at fiber/matrix interfaces in titanium matrix composites. A cohesive zone based debonding formulation is presented in Appendix B.

3.2.4 Traction continuity conditions

Traction continuity must also be enforced, on average, at the interface between adjacent subcells, in order to arrive at the correct number of equations needed to solve for the $6N_\beta N_\gamma$ subcell strain unknowns. The traction continuity equations are expressed as,

$$\sigma_{2j}^{(\beta\gamma)} = \sigma_{2j}^{(\hat{\beta}\gamma)} \tag{3.32}$$

$$\sigma_{3j}^{(\beta\gamma)} = \sigma_{3j}^{(\beta\hat{\gamma})} \tag{3.33}$$

After eliminating repeating traction continuity conditions, the following $5N_\beta N_\gamma - 2(N_\beta + N_\gamma) - 1$ independent equations remain:

$$\sigma_{22}^{(\beta\gamma)} = \sigma_{22}^{(\hat{\beta}\gamma)}, \quad \beta = 1, \ldots, N_\beta - 1, \quad \gamma = 1, \ldots, N_\gamma \tag{3.34}$$

$$\sigma_{33}^{(\beta\gamma)} = \sigma_{33}^{(\beta\hat{\gamma})}, \quad \beta = 1, \ldots, N_\beta, \quad \gamma = 1, \ldots, N_\gamma - 1 \tag{3.35}$$

$$\sigma_{23}^{(\beta\gamma)} = \sigma_{23}^{(\hat{\beta}\gamma)}, \quad \beta = 1, \ldots, N_\beta - 1, \quad \gamma = 1, \ldots, N_\gamma \tag{3.36}$$

$$\sigma_{32}^{(\beta\gamma)} = \sigma_{32}^{(\beta\hat{\gamma})}, \quad \beta = N_\beta, \quad \gamma = 1, \ldots, N_\gamma - 1 \tag{3.37}$$

$$\sigma_{21}^{(\beta\gamma)} = \sigma_{21}^{(\hat{\beta}\gamma)}, \quad \beta = 1, \ldots, N_\beta - 1, \quad \gamma = 1, \ldots, N_\gamma \tag{3.38}$$

$$\sigma_{31}^{(\beta\gamma)} = \sigma_{31}^{(\beta\hat{\gamma})}, \quad \beta = 1, \ldots, N_\beta, \quad \gamma = 1, \ldots, N_\gamma - 1 \tag{3.39}$$

These traction conditions can be recast in terms of the average subcell strains using the constitutive relationship, in this case Equation (3.4) or (3.5). The equations can then be written in matrix form.

$$\mathbf{A}_M \boldsymbol{\epsilon}_S = \mathbf{0} \tag{3.40}$$

where ϵ_S is given in Equation (3.31)

Note that the traction continuity conditions require that particular components of the stress tensor must be equal along certain rows or columns of the RUC. For instance, given a particular column of subcells γ, all subcells in that column must have the same $\sigma_{22}^{(\beta\gamma)}$ for all β. *Pindera and Bednarcyk* (1999) used this characteristic to reduce the total number of unknowns by introducing a mixed formulation in terms of local stresses and strains. This reformulation is employed in all numerical GMC simulations provided here, but the reader is referred to *Pindera and Bednarcyk* (1999) for details on the reformulation. It should also be noted that this same feature is an indication of the lack of normal shear coupling (meaning applied normal stress can only induce local normal stresses) in GMC arising from the linear approximation of the displacement fields in the subcells, and the enforcement of the displacement and traction continuity at the subcell interfaces in an average, integral sense.

3.2.5 Determining local subcell fields and global effective composite constitutive relations

Once $\mathbf{A}_G$, $\mathbf{A}_M$, and $\mathbf{J}$ have been determined, the subcell strains can be computed by solving

$$\tilde{\mathbf{A}}\boldsymbol{\epsilon}_S = \mathbf{K}\bar{\boldsymbol{\epsilon}} \tag{3.41}$$

where

$$\tilde{\mathbf{A}} = \begin{bmatrix} \mathbf{A}_M \\ \mathbf{A}_G \end{bmatrix} \tag{3.42}$$

and

$$\mathbf{K} = \begin{bmatrix} \mathbf{0} \\ \mathbf{J} \end{bmatrix} \tag{3.43}$$

The local subcell strains are related to the global composite strains through

$$\boldsymbol{\epsilon}_S = \mathbf{A}\bar{\boldsymbol{\epsilon}} \tag{3.44}$$

where $\mathbf{A}$ is the strain concentration matrix given by

$$\mathbf{A} = \tilde{\mathbf{A}}^{-1}\mathbf{K} \tag{3.45}$$

Once the relationship between local and global strains has been established with Equation (3.44), the local subcell stresses are readily obtained using the local constitutive law, Equation (3.5).

$$\boldsymbol{\sigma}^{(\beta\gamma)} = \mathbf{C}^{(\beta\gamma)}\mathbf{A}^{(\beta\gamma)}\bar{\boldsymbol{\epsilon}} \tag{3.46}$$

where $\mathbf{A}^{(\beta\gamma)}$ is a submatrix of $\mathbf{A}$ that relates the local strain in subcell $\beta\gamma$ to the global composite strains.

$$\boldsymbol{\epsilon}^{(\beta\gamma)} = \mathbf{A}^{(\beta\gamma)}\bar{\boldsymbol{\epsilon}} \tag{3.47}$$

The global, composite stresses can be defined as a standard average of the local, subcell stresses.

$$\bar{\boldsymbol{\sigma}} = \frac{1}{HL}\sum_{\beta=1}^{N_\beta}\sum_{\gamma=1}^{N_\gamma} h_\beta l_\gamma \boldsymbol{\sigma}^{(\beta\gamma)} \tag{3.48}$$

Then, substituting Equation (3.46) into Equation (3.48) yields the global constitutive law.

$$\bar{\boldsymbol{\sigma}} = \mathbf{B}\bar{\boldsymbol{\epsilon}} \tag{3.49}$$

where

$$\mathbf{B} = \frac{1}{HL}\sum_{\beta=1}^{N_\beta}\sum_{\gamma=1}^{N_\gamma} h_\beta l_\gamma \mathbf{C}^{(\beta\gamma)}\mathbf{A}^{(\beta\gamma)} \tag{3.50}$$

3.3 Multiscale Methodology

The multiscale model developed involves linking the GMC micromechanics model to the lamina-level FEM model. A synergistic approach is employed which utilizes concurrent multiscaling in time, but sequential in length [*Sullivan and Arnold* (2011)]. The commercial finite element software, Abaqus [*Abaqus* (2008)], is used as the FEM platform, and the MAC/GMC core micromechanics software [*Bednarcyk and Arnold* (2002b,c)] is used to perform microscale calculations. To tie the scales together, the FEAMAC software implementation [*Bednarcyk and Arnold* (2006)] is used. In the following analyses, damage and failure are separated. Damage is the evolution of mechanisms which result in nonlinear, positive-definite changes in the stiffness tensor of the material while failure is considered to be all structural changes that result in post-peak strain softening within the material. Here matrix microdamage is considered responsible for all damage in the composite lamina. ST (see Chapter II) is implemented at the lamina level within FEM. Intralaminar failure is taken as the evolution of matrix cracks, and fiber breakage. Micromechanics is used to percolate the influence of these failure mechanisms up the scales. Since failure is a highly localized phenomenon, it is hypothesized that the fiber-matrix architecture influences

the evolution of failure. Thus, fiber and matrix failure is initiated at the microscale using the MAC/GMC core engine. If failure does initiate in a GMC subcell, the stiffness of the subcell is severely reduced, and the global stiffness is recalculated and passed to Abaqus using the FEAMAC framework. Both ST and FEAMAC are implemented in Abaqus/Standard with a user material subroutine `UMAT` [*Abaqus* (2008)].

The ST algorithm is displayed in Figure 3.5. The ST evolution equations derived in Chapter II are restated below.

$$\frac{1}{2}\left(\epsilon_{22}^2 E_{220}\frac{de_s}{dS_r} + \gamma_{12}^2 G_{120}\frac{dg_s}{dS_r}\right) = -3S_r^2 \tag{3.51}$$

$$\dot{S}_r \geq 0 \tag{3.52}$$

At the beginning of the analysis, the derivatives of microdamage functions $e_s'(S_r)$ and $g_s'(S_r)$ (where the prime indicates a derivative with respect to S_r) are approximated using linear spline interpolants and the coefficients of the interpolants are saved. Using linear interpolants for the derivatives of the microdamage functions results in a form of Equation (3.51) that is quadratic in S_r, yielding an efficient, analytical solution for S_r. Since the solution of Equation (3.51) is multi-valued, the solution which is closest to S_r from the previous increment is chosen as the correct solution. The value of S_r from the previous solution is used to estimate the appropriate spline regime used in the calculation of the current S_r solution. If the current solution falls outside the applicable range of S_r for those splines, new splines associated with the current solution are used to resolve Equation (3.51). This iteration continues until the solution of S_r and the splines used to obtain the solution correspond. A maximum number of iterations can be set, after which Equation (3.51) is solved using the full polynomial forms of the damage functions by finding the eigenvalues of the complimentary matrix of the polynomial coefficients of the evolution equation.

If S_r increases from the previous increment, the transverse and shear moduli are degraded using the damage functions: Equations (2.12) and (2.13). The new, degraded stiffnesses are used to calculate the stress state. In an Abaqus/Standard analysis the material Jacobian (tangent stiffness matrix) is also calculated.

It is possible to integrate ST directly into the micromechanics through the subcell constitutive relationships by using a 3D extension of ST. Details of a novel, 3DST formulation are presented in Appendix A. However, matrix microdamage is highly distributed and often spans regions beyond the fiber-matrix scale (see Figure 1.1). Conversely, transverse cracking and fiber breakage are highly localized and are on the order of the microscale, as shown in Figures 1.2 and 1.3. Additionally, separating damage from failure and performing all damage calculations at the lamina-scale and all failure calculations at the microscale enables judicious use of the micromechanics calculations. A minimum critical value for the microdamage S_r^* can be chosen, wherein if S_r remains below that value, the micromechanics calculations are foregone. This assumes that failure must follow some degree of damage, but even if S_r^* is chosen as a relatively small value, immense computational savings are achieved by eliminating FEAMAC calculations at integration points that are exhibiting little to no microdamage.

Once the global stresses and Jacobian have been calculated using ST and S_r is above the assigned threshold, FEAMAC is called to evaluate failure criteria locally in the subcells of an RUC using GMC. However, before any micromechanical analysis can be performed, it must be ensured that the homogenized stiffness tensor calculated by GMC, using Equation (3.50), is consistent with the degraded stiffness calculated with ST. To this end, the lamina-level microdamage is taken to be distributed uniformly throughout the matrix phase of the RUC; therefore, the properties of all matrix

subcells are degraded equally according to

$$E_m = E_{m0} e_m(S_r) \tag{3.53}$$

$$G_m = G_{m0} g_m(S_r) \tag{3.54}$$

where E_{m0} and G_{m0} are the virgin matrix Young's and shear modulus, and $e_m(S_r)$ and $g_m(S_r)$ are the matrix microdamage functions. The matrix microdamage functions are determined *a priori* using a series of standalone micromechanics simulations. Equations (2.12) and (2.13) are evaluated for numerous values of S_r. Then for each S_r, E_m and G_m are calibrated such that GMC calculates the same E_{22} and G_{12} as Equations (2.12) and (2.13). The values of E_m and G_m are normalized by E_{m0} and G_{m0} (obtained from $S_r = 0$) and the $(E_m/E_{m0}, S_r)$ and $(G_m/G_{m0}, S_r)$ pairs are fit with polynomials yielding $e_m(S_r)$ and $g_m(S_r)$.

After the consistent matrix properties are calculated, the micromechanics can be executed using FEAMAC. FEAMAC consists of four ABAQUS/Standard user defined subroutines, as well as six subroutines exclusive to the FEAMAC package (see Figure 3.6). The Abaqus/Standard `UMAT` provides the strains, strain increments, and current values of state variables to MAC/GMC through the front end subroutine `FEAMAC`. MAC/GMC then returns a new stiffness and stress state, as well as updated state variables, to the `UMAT` via the `FEAMAC` subroutine. The Abaqus/Standard user subroutine `SDVINI` initializes the state variables used in `UMAT`. The ABAQUS/Standard user subroutine `UEXPAN` is used for thermal analysis by providing the integration point temperature, temperature increment, and current state to MAC/GMC, which in turn, calculates new thermal strains and thermal strain rates. Problem set-up task, initialization, and writing MAC/GMC level output data to files is achieved through the ABAQUS/Standard user subroutine `UEXTERNALDB`, which communicates between ABAQUS/Standard, the `FEAMAC_PRE`, and `FEAMAC_PLOTS` subroutines. The reader is

referred to *Bednarcyk and Arnold* (2006) for further details on the FEAMAC software implementation.

Micro-constituent failure is evaluated within MAC/GMC. Through localization (Equation (3.44)), the local fields in the subcells of the RUC are obtained, and failure criteria are enacted within each subcell. Herein, for the fiber subcells, a maximum strain criterion is used.

$$\frac{\epsilon_{11}^{(\beta^f \gamma^f)}}{X_T^f} = 1 \tag{3.55}$$

where β^f and γ^f are fiber subcell indices, and X_T^f is the axial fiber tensile strain allowable. Softening due to axial compression arises automatically due to fiber rotation; see Chapter IV, Section 4.2.3 [*Basu* (2005)]. A strain-based Tsai-Hill criterion is used to determine failure in the matrix subcells.

$$\begin{aligned} &\frac{\epsilon_{11}^{(\beta^m\gamma^m)^2} + \epsilon_{22}^{(\beta^m\gamma^m)^2} + \epsilon_{33}^{(\beta^m\gamma^m)^2}}{{Y_m}^2} \\ &\quad - \frac{\epsilon_{11}^{(\beta^m\gamma^m)}\epsilon_{22}^{(\beta^m\gamma^m)} + \epsilon_{11}^{(\beta^m\gamma^m)}\epsilon_{33}^{(\beta^m\gamma^m)} + \epsilon_{22}^{(\beta^m\gamma^m)}\epsilon_{33}^{(\beta^m\gamma^m)}}{{Y_m}^2} \\ &\quad + \frac{\epsilon_{23}^{(\beta^m\gamma^m)^2} + \epsilon_{13}^{(\beta^m\gamma^m)^2} + \epsilon_{11}^{(\beta^m\gamma^m)^2}}{Z_m^2} = 1 \end{aligned} \tag{3.56}$$

where β^m and γ^m are matrix subcell indices.

If subcell failure criteria are satisfied, the properties of the failed subcells are severely reduced instantaneously so the stiffness of the failed subcells no longer contribute significantly to the overall stiffness of the RUC. This failure procedure is meant to simulate the localization of damage into matrix cracks or fiber breakage. Equations (3.55) and/or (3.56) mark the initiation of the localization, and the reduction of subcell stiffness simulates the effects of cracking on the RUC. This procedure does not correctly capture the physics of matrix and fiber cracking, but it is computationally efficient and was readily achievable using pre-existing modules within MAC/GMC. Furthermore, the degradation scheme results in mesh dependent solutions [*Bažant*

and Cedolin (1979)]. However, this methodology represents a first attempt to couple micromechanics driven failure with global, distributed, lamina-level damage. Chapter V introduces physics-based failure criteria and evolution schemes into the HFGMC micromechanics frameworks.

It is assumed that strain localizes to a vicinity near the failure within the RUC; therefore, strain relaxes in the surrounding bulk material, and subsequent increases in strain do not advance lamina-level progressive damage any further. Thus, once failure occurs in any subcell, the ST calculations for S_r are circumvented in successive increments at the applicable point in the FEM model. FEAMAC is called immediately at the start of each increment with the matrix subcell properties that were used just prior to first subcell failure, calculated with Equations (3.53) and (3.54).

In order to set up an FEAMAC problem, a standard Abaqus input file is used that includes a user material with a name ending in either "`.mac`" or "`_mac`". These extensions indicate to FEAMAC that the material is a MAC/GMC composite material whose constituent properties and architecture (e.g., fiber volume fraction and fiber arrangement) are defined in a MAC/GMC input file of the same name. The applicable MAC/GMC input file(s) must be located in the same directory as the Abaqus input file. Materials that are not associated with MAC/GMC are also permitted in FEAMAC problems. The Abaqus input file will also typically include an orientation definition (as composite materials are usually anisotropic), while the necessary cards usually associated with a user material must be specified as well. Only one additional card, not typically associated with a user material problem, must be specified in order to trigger certain initialization tasks: `*INITIAL CONDITIONS, TYPE=SOLUTION, USER`. These initialization tasks are executed within the Abaqus/Standard user subroutine `SDVINI`. FEAMAC problem execution is accomplished identically to any problem that utilizes a user material, wherein the FORTRAN source file containing the appropriate user subroutines is specified. The FEAMAC subroutines are compiled in

a static `.lib` library file which is linked to Abaqus/Standard when the FEM job is executed. The location of the `.lib` file is indicated in the `abaqus_v6.env` file. Finally, FEAMAC problem post processing is accomplished identically to any Abaqus problem, as all typical Abaqus output, including the `.odb` file, is available. Constituent level field variables are stored internally within the Abaqus state variable space and are also available for postprocessing.

3.4 Example - Center Notched Panels Subjected to Uniaxial Tension

3.4.1 Experimental Details

Two center-notched panel configurations were tested at NASA LaRC [*Bogert et al.* (2006); *Satyanarayana et al.* (2007)]. The geometrical details of the panel and testing boundary conditions are presented in Figure 3.7. The panels were 3" wide and 11.5" long. Two 3" x 2.75" tabs were placed on both ends of the specimens, leaving a gage section of 3" x 6" which is displayed in Figure 3.7. A central notch was machined in each panel that was 0.75" wide and had a notch tip radius of 0.09375". The end tabs were clamped and a vertical, tensile displacement (in the y-direction) was applied to the top tab using a servo-hydraulic testing machine. The bottom tab was fixed preventing any y-displacement of the bottom boundary of the gage section. The gripped tabs also prevented any displacement in the x-direction at the top and bottom boundaries of the gage section.

The panels were comprised of laminated T800/3900-2 carbon fiber/toughened epoxy composites. Three different lay-up configurations were tested; however one of the configurations exhibited significant delamination. Since the focus of this work is modeling in-plane damage and failure mechanisms, this configuration is not considered here. The two remaining configurations are presented in Table 3.1. The

first lay-up, Laminate-1, consists of 12 0° plies, and the second, Laminate-2, is a symmetric, multi-angle lay-up with 40% |45°|, 40% 0°, and 20% 90° layers.

Several strain gages where affixed to the test panel, labeled Sg-1 through Sg-4 in Figure 3.7. Sg-1 was placed in the center of the panel, 1.5" above the notch. Sg-2 was placed 1.5" above the notch tip. Sg-3 was attached in front of the notch, 0.5" from the free edge, and Sg-4 placed at the notch tip. Global load versus displacement data, and local strain gage data was reported by *Bogert et al.* (2006); *Satyanarayana et al.* (2007), along with a post-test C-Scan of Laminate-1 and photograph of Laminate-2.

3.4.2 Finite Element Model Details

Simulation of the two CNPs were performed using Abaqus/Standard, version 6.10-1 [*Abaqus* (2008)]. The domain was modeled using linear, quadrilateral S4R layered shell elements. The refined finite element mesh, shown in Figure 3.8 was chosen after simulations with coarser meshes indicated locations where the most damage and failure should be expected. The average size of the elements in the refined regions was 0.0469" x 0.0469" and was selected to accommodate two elements per length equal to the notch tip radius in the regions where the greatest non-linearities were expected. Outside of the suspected critical areas the element size was allowed to grow. Elements with an area equal to 0.0254" x 0.0254" were used at the locations of the strain gages shown in Figure 3.7.

The displacement in the x-direction as well as all rotations where prohibited at the nodes along the top and bottom edges, and displacement in $y-$direction was fixed at the nodes on the bottom edge to simulate the gripped boundary conditions present in the experiments. A uniform displacement was applied to all the nodes on the top boundary in the positive y-direction to model tensile loading.

The linear elastic properties of T800/3900-2 used in the FEM models are presented in Table 3.2, and were taken from *Bogert et al.* (2006). The shear microdamage

function g_s utilized in Equation (2.13) was obtained from T800/3900-2 $[45°/\text{-}45°]_{3S}$ angle-ply coupon tests. The $[\pm 30°]_S$ and $[15°]$ laminates needed to determine the transverse tensile and transverse compressive microdamage functions were not available. Therefore, these microdamage functions were inferred by scaling the coefficients of the microdamage curves presented by *Sicking* (1992) for AS4/3502 (see Table 2.2) by the ratio of the virgin transverse modulus of T800/3900-2 to that of AS4/3502. The same procedure described in Section 2.3 was used to extrapolate the microdamage curves to values of zero stiffness. The coefficients of the microdamage curves (Equations (2.17) and (2.18)) are presented in Table 3.3, and the curves are plotted in Figure 3.9.

The multiscale methodology (ST-FEAMAC) described in Section 3.3, is utilized to model the response of the T800/3900-2 laminates. A doubly-periodic, seven subcell by seven subcell RUC shown in Figure 3.3 was chosen to model the composite microstructure, assuming square packing. The 13 blue subcells represent fiber subcells, and the 36 green indicate matrix subcells. The size of the fiber was chosen to maintain a 54% volume fraction. The virgin elastic properties used for the fiber and matrix constituents were calibrated such that the composite stiffness calculated using the seven subcell by seven subcell RUC matched the lamina stiffnesses in Table 3.4. The elastic properties of the constituents are given in Table 3.4. The microdamage functions for the matrix subcells were obtained using the procedure outlined in Section 3.3, the curves are plotted in Figure 3.10.

$$E_m = E_{m0}\left(e_{m0} + e_{m1}S_r + e_{m2}S_r^2 + e_{m3}S_r^3 + e_{m4}S_r^4 + e_{m5}S_r^5\right) \tag{3.57}$$

$$G_m = G_{m0}\left(g_{m0} + g_{m1}S_r + g_{m2}S_r^2 + g_{m3}S_r^3 + g_{m4}S_r^4 + g_{m5}S_r^5\right) \tag{3.58}$$

The strain allowables used in the maximum tensile strain criterion for fiber failure, Equation (3.55), the strain-based Tsai-Hill criterion for matrix failure, Equation

(3.56) are displayed in Table 3.5. These allowables were calibrated using characteristic experimental loads (see Sections 3.4.3 and 3.4.3). Once Equation (3.55) or (3.56) is satisfied, the local moduli of the subcell are reduced by 99.99%.

Displacement was applied to both laminates using the `*DYNAMIC` keyword in Abaqus with the parameter `APPLICATION = QUASI-STATIC`. This implicit dynamic solver is recommended for quasi-static problems exhibiting a high-degree of nonlinearity. This procedure uses numerical damping to stabilize the problem. The numerical damping does not significantly affect the simulation results because the velocities in these simulations are low. For Laminate-1 a total displacement of 0.0236", and for Laminate-2 a displacement of 0.0472", is applied over 1000 seconds. The panels were assigned a representative density of 0.057 lb/in.^{3}. This technique has advantages over traditional static, implicit solvers which have difficulty converging when the material exhibits post-peak softening [*Belytschko et al.* (2000); *Belytschko and Mish* (2001)], and is not limited by a minimum stable time step required with explicit solvers [*Hughes* (2000)].

3.4.3 Results - Laminate-1

Figure 3.11 compares the global load P versus the displacement Δ of a 4" section results from ST-FEAMAC to the experiment. The relationship is initially linear, but at the splitting load, reported as 8,250 lbf. by *Bogert et al.* (2006). ST-FEAMAC captures the global nonlinearity well. The numerical splitting load is inferred from the global load versus local Sg-1 strain gage results in Figure 3.12a as the load at which the strain relaxation begins. The numerical splitting load was 8,490 lbf. The splitting loads from the experiment and simulation are tabulated in Table 3.6. The matrix strain allowables used in Equation (3.56) were calibrated to obtain the best correlation between the numerical results and the experimental data at Sg-1; however, the global load versus displacement and data at the other strain gage locations obtained from the

model are predictions. The results for the other three strain gages are also presented in Figure 3.12. For the gage locate far above the notch, ST-FEAMAC predicts the onset of nonlinearity and the nonlinear trend matches the data reasonably. Both the experiment and ST-FEAMAC exhibit slight nonlinear behavior at Sg-3 which is in front of the notch, near the free edge. For the gage located directly at the notch, the results from ST-FEAMAC are in agreement with the experimental data, although ST-FEAMAC shows a slightly stiffer response.

A C-Scan of the failed Laminate-1 specimen is displayed in Figure 3.13. The C-Scan shows four splitting cracks propagating from the notch in the loading direction towards the free edge. Figure 3.14 shows the normalized microdamage contour predicted by ST-FEAMAC. In Figure 3.14 S_r is normalized by the maximum achievable value, 144.12 $\text{Pa}^{\frac{1}{3}}$, which was obtained from extrapolating the measured damage curves to zero stiffness. At the splitting load, the microdamage pattern mirrors the splitting pattern. The microdamage is more dispersed, but contains localized regions of highly degraded elements. At a load of 16,400 lbf., nearly twice the splitting load, the microdamage splits have nearly progressed to the gripped boundary of the panel, and S_r is 38% of its maximum.

The failure pattern in Figure 3.15 plots the number of subcells that have failed within the RUC at each integration point. An initial single scale simulation containing only ST was used to determine which regions of the panel were most susceptible to failure. To improve computational efficiency, regions that did not exhibit an microdamage were not modeled using the multiscale procedure. These regions are displayed in gray. Black regions indicate no subcells have failed. Blue indicates one subcell has failed. Yellow marks that 36 subcells, or all of the matrix subcells have failed. Red would indicate that every subcell has failed, but there was no fiber failure in this example. The same splitting pattern, observed in Figure 3.13 is observed in Figure 3.15. Subcell failure is localized into a one element wide regions that propagate to-

wards the gripped boundary of the specimen. However, it appears that the tip of the splitting crack progresses discontinuously, in every other element. Scrutiny of the strains just in front of the crack tip revealed that the element adjoined to the splitting crack tip had lower shear and transverse strains than is present two elements in front of the crack tip. Therefore, the splitting failure occurs in every other element as the splitting crack progresses.

3.4.4 Results - Laminate-2

The P versus Δ results obtained from ST-FEAMAC for Laminate-2 are compared against the experimental data in Figure 3.16. The experiment exhibits linear behavior up until the specimen fails catastrophically at 15,300 lbf. The axial strain allowable in Equation (3.55) was calibrated to provide the best correspondence between the ultimate loads from the experiment and the simulation; however, the simulation results at all the strain gage locations are predictions. The ST-FEAMAC simulation produced an ultimate load of 14,740 lbf., but there was some nonlinearity behavior exhibited just before final failure. The load versus local strain gage data, shown in Figure 3.17, predicted by ST-FEAMAC agrees very well the experimental data. However at Sg-4 (Figure 3.17d), just in front of the notch tip, there is a discrepancy in the stiffness from the model and the experiment. This could be result of the very high strain gradients at the notch tip. A very small misalignment in the strain gage from what was reported could yield a significantly different strain state. Secondly, *Bogert et al.* (2006) attributed the nonlinear behavior of Sg-4 to local delamination in the CNP at the notch.

A photograph taken of the failed specimen is presented in Figure 3.18. The photograph shows that two macroscopic cracks initially propagate from the notch tip towards the free edges, perpendicular to the applied load, in a self-similar fashion. Eventually, the cracks turn and proceed towards the free edge at an angle. *Bogert*

et al. (2006) claim, supported by visual image correlation displacement data, that there was some eccentricity in the specimen alignment which results in deviation from self similar crack growth.

Figures 3.19-3.22 present microdamage contours and failure patterns in each of the unique layers in the laminate (i.e. 45°, 0°, -45°, and 90°). The first normalized S_r contour, Figure 3.19, is given at a load of 12,770 lbf. and is right before any fiber failure initiation. At this point, the load-displacement curve (Figure 3.16) from ST-FEAMAC is still nearly linear. The 45° and -45° layers exhibit moderate levels of highly distributed microdamage, whereas, the 0° ply displays localized microdamage around the notch tips. The 90° layer shows a similar pattern as the 0°, but there is some low level microdamage distributed throughout the ply.

The subcell failure pattern at the ultimate load is presented in Figure 3.20. The 45°, -45° and 0° plies all display the same fiber subcell failure pattern (red), and the 90° does not show any fiber subcell failure, but has a region of compete matrix subcell failure (yellow) that matches the fiber subcell failure pattern in the other plies. This indicates that a crack extends through all of the plies in the laminate. It should be noted that doubly-periodic GMC assumes generalized plane strain. Thus, the fiber strain allowable will always be met in all fiber subcells within a given ply simultaneously. The 45° and -45° layers exhibit regions of matrix subcell failure that are biased towards the fiber orientation in the plies. The 0° ply shows extensive matrix subcell failure surrounding the fiber subcell failure path. Numerous elements in the 90° layer exhibit some degree of subcell failure.

The microdamage contours in each unique layer are given at the end of the simulation in Figure 3.21. Widespread microdamage is observed in the 45° and -45° plies. Substantial microdamage surrounds the fiber subcell failure path (Figure 3.22). Moderate microdamage is present on the boundaries of the matrix subcell failure pattern (Figure 3.22b) in the 0° layer. The 90° layer exhibits low levels of microdamage

throughout but moderate levels propagating outward from the notch.

In Figure 3.22 the fiber subcell failure pattern can be seen in the 45°, 0° and -45° plies, and a corresponding region of matrix subcell failure is seen in the 90° ply. Since all stiffness in the direction of the loading is lost in these regions, that failure pattern essentially represents a crack propagating out from the notch in the same fashion as shown in the photograph in Figure 3.18. In all the layers, significant matrix subcell failure surrounds the crack.

3.5 Conclusions

A multiscale methodology, ST-FEAMAC, was presented which models matrix microdamage at the lamina level, or macroscale, and models failure due to transverse cracking and fiber failure at the constituent scale. Matrix microdamage was modeled with the thermodynamically based Schapery theory, presented in the last chapter. The generalized method of cells is the micromechanics framework employed to resolve the local fields at the microscale. Local failure criteria are used to predict failure due to transverse cracking in the matrix subcells, and fiber breakage in the fiber subcells. Results from ST-FEAMAC were compared to global and local experimental data from two center-notched panels, tested at NASA LaRC.

The degradation scheme used at the microscale yields mesh dependent results, but it is readily implemented and ultra-efficient. In the following chapter a single scale model is developed that alleviates the mesh dependency associated with failure. Finally, in Chapter V a mesh objective failure model is implemented at the microscale.

ID	Stacking Sequence	Thickness (in.)
Laminate-1	$[0°]_{12}$	0.078
Laminate-2	$[45°/0°/\text{-}45°/0°/90°]_S$	0.065

Table 3.1: T800/3900-2 lay-up configurations used in CNP tests at NASA LaRC.

Property	T800/3900-2
E_{11} (Msi)	23.2
E_{22} (Msi)	1.3
G_{12} (Msi)	0.9
ν_{12}	0.28

Table 3.2: Linear elastic properties for T800/3900-2 used in FEM models.

$e_s(S_r)$ Coefficients	Tension	Compression	$g_s(S_r)$ Coefficients	
e_{s0}	1.0000	1.0000	g_{s0}	1.0000
e_{s1}	-6.0373E-2	8.4887E-4	g_{s1}	-3.0567E-2
e_{s2}	2.5937E-2	2.8002E-2	g_{s2}	-1.2135E-1
e_{s3}	-1.5789E-2	-6.2122E-3	g_{s3}	3.7438E-2
e_{s4}	2.2571E-3	N/A	g_{s4}	-4.5405E-4
e_{s5}	-1.0440E-4	N/A	g_{s5}	1.9532E-4

Table 3.3: Microdamage function coefficients for T800/3900-2 used in FEM models.

Property	Fiber	Matrix
E_{11} (Msi)	42.27	0.79
E_{22} (Msi)	1.77	0.79
ν_{12}	0.2	0.35
G_{12} (Msi)	17.61	0.29

Table 3.4: Virgin elastic properties for T800 carbon fiber and 3900-2 toughened epoxy matrix used in GMC subcells. These elastic properties were calibrated so that the composite properties of the RUC calculated by GMC corresponded to the elastic lamina properties presented in Table 3.2

Property	Strain Allowable
X_f	0.031
Y_m^T	0.0125
Y_m^C	0.04685
Z_m	0.091

Table 3.5: Strain allowables used in failure criteria implemented in GMC subcells. These allowables were calibrated to provide the best match between the characteristic loads (see Table 3.6) from the experiments and the ST-FEAMAC simulations.

	Type	Experimental	Numerical
Laminate-1	Splitting	8,250 lbf.	8,490 lbf.
Laminate-2	Ultimate	15,300 lbf.	14,740 lbf.

Table 3.6: Characteristic loads obtained from experiment and ST-FEAMAC simulation.

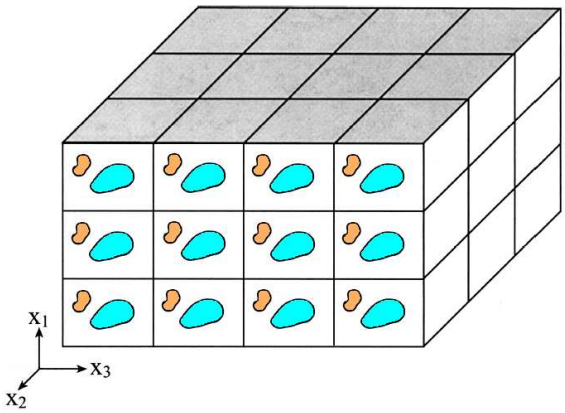

Figure 3.1: Representation of triply-periodic microstructure of a composite material *Bednarcyk et al.* (2010).

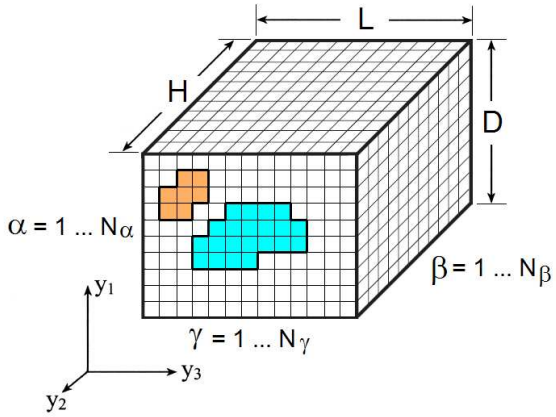

Figure 3.2: Discretization of a 3D, triply-periodic RUC *Bednarcyk et al.* (2010).

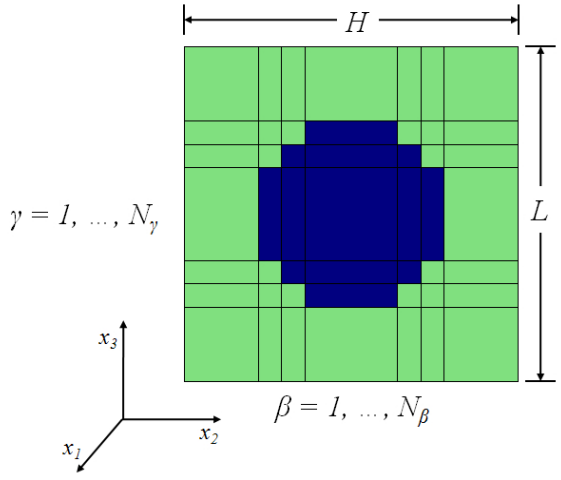

Figure 3.3: Discretization of a 2D, doubly-periodic RUC.

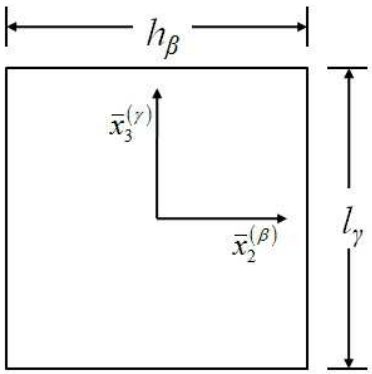

Figure 3.4: 2D GMC/HFGMC subcell with local coordinate frame.

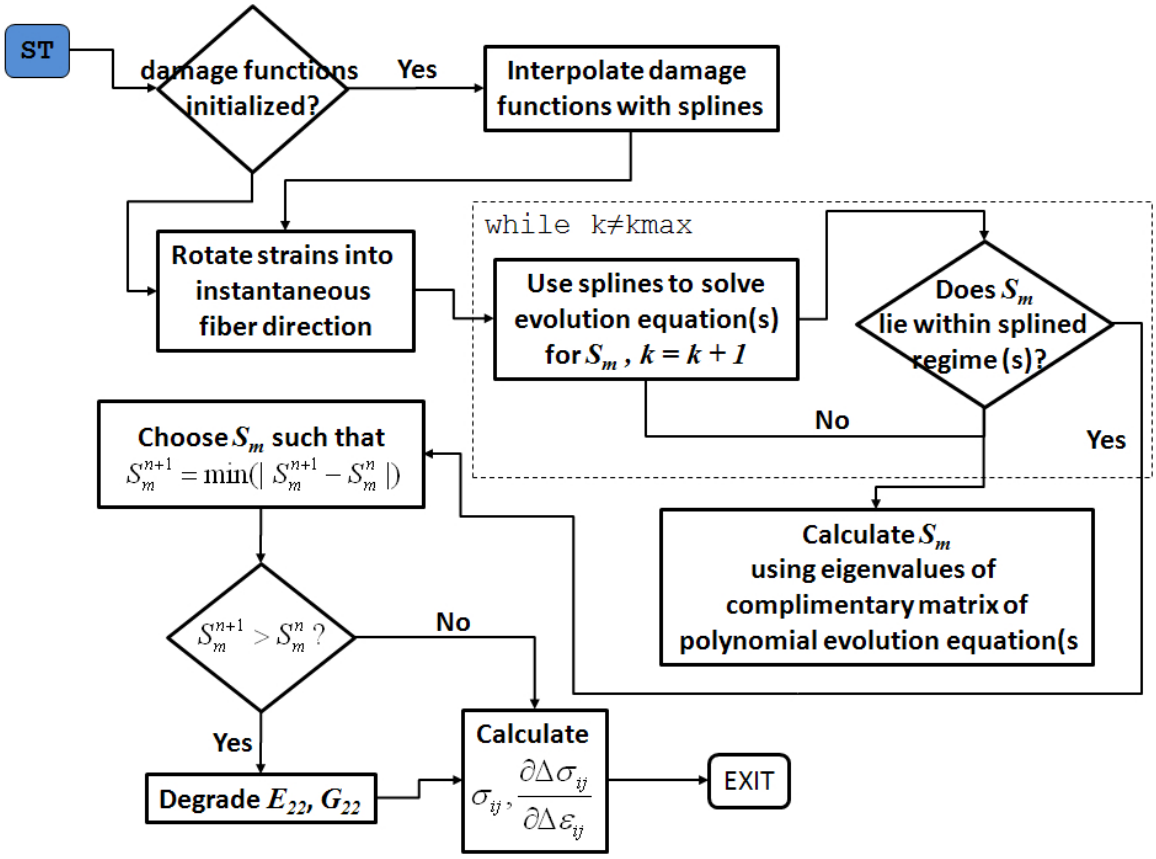

Figure 3.5: ST computer code architecture.

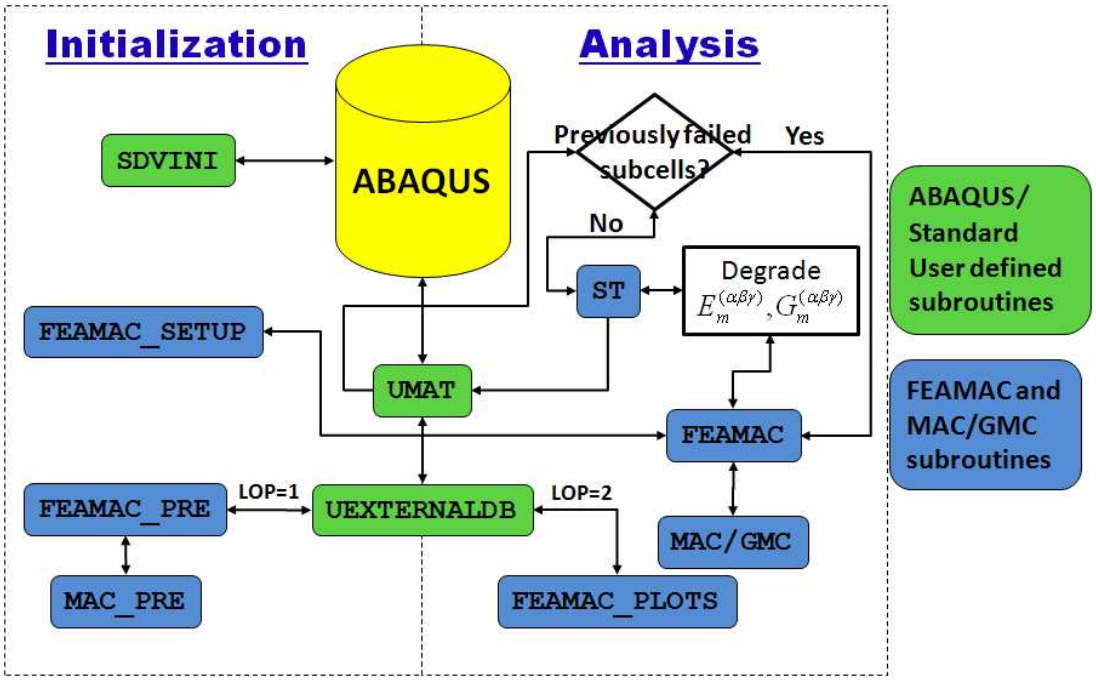

Figure 3.6: Hierarchy of FEAMAC software implementation for use with Abaqus/Standard.

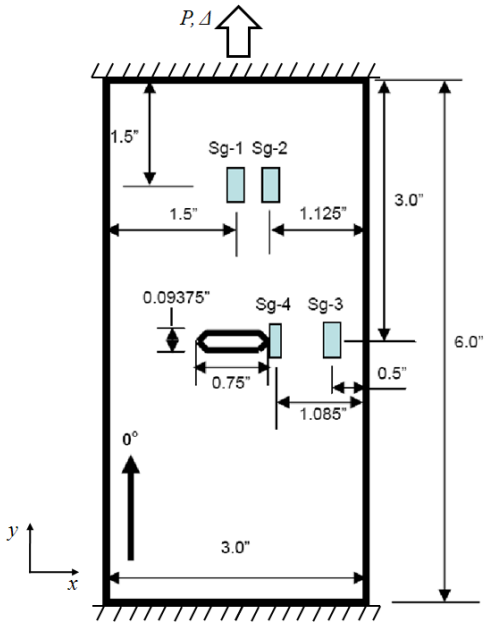

Figure 3.7: Geometry and boundary conditions of CNPs tested at NASA LaRC [*Bogert et al.* (2006)].

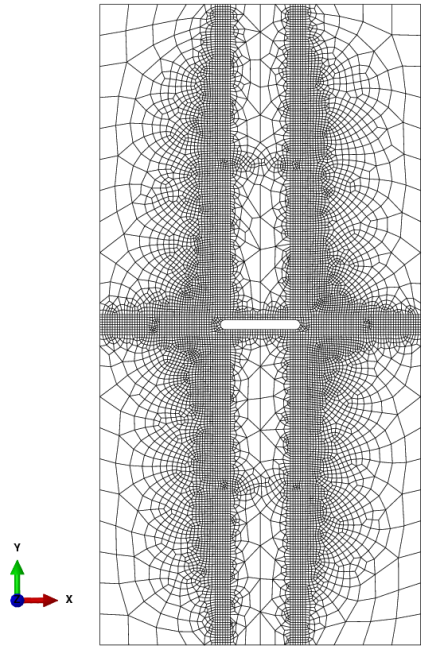

Figure 3.8: FEM mesh used to simulate tensile loading of CNPs.

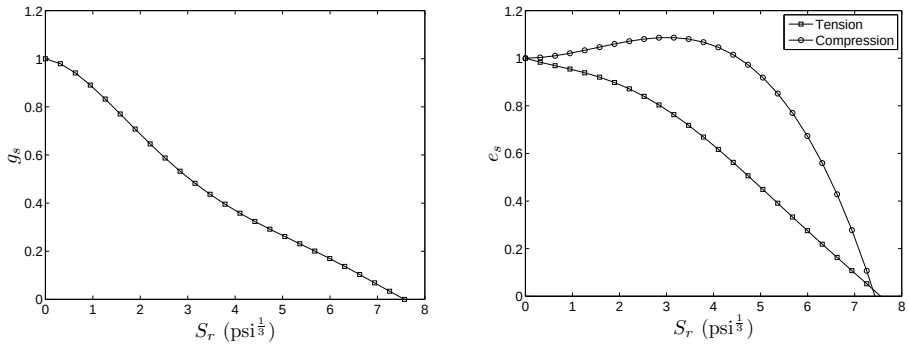

(a) Shear microdamage function obtained from $[\pm 45^\circ]_S$ angle-ply laminate.

(b) Transverse tension and compression microdamage functions obtained by scaling data for AS4/3502 in Ref. [*Sicking* (1992)].

Figure 3.9: Microdamage functions for T800/3900-2 used in FEM models.

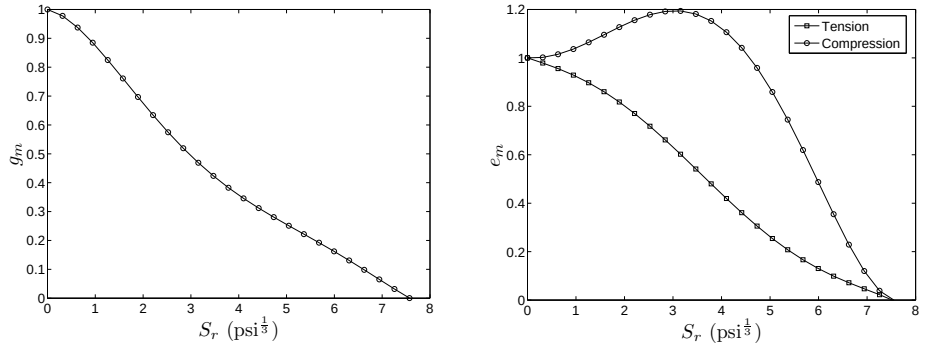

(a) Shear microdamage function for 3900-2 epoxy matrix.

(b) Transverse tension and compression microdamage functions for 3900-2 epoxy matrix.

Figure 3.10: Microdamage functions used in GMC matrix subcells.

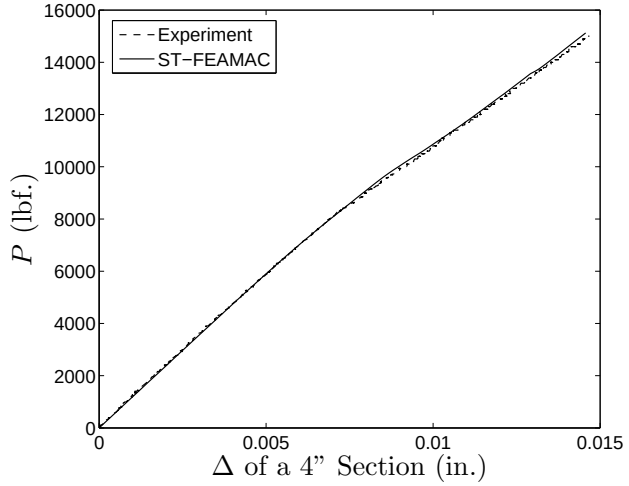

Figure 3.11: Applied load versus displacement of a 4" section for Laminate-1.

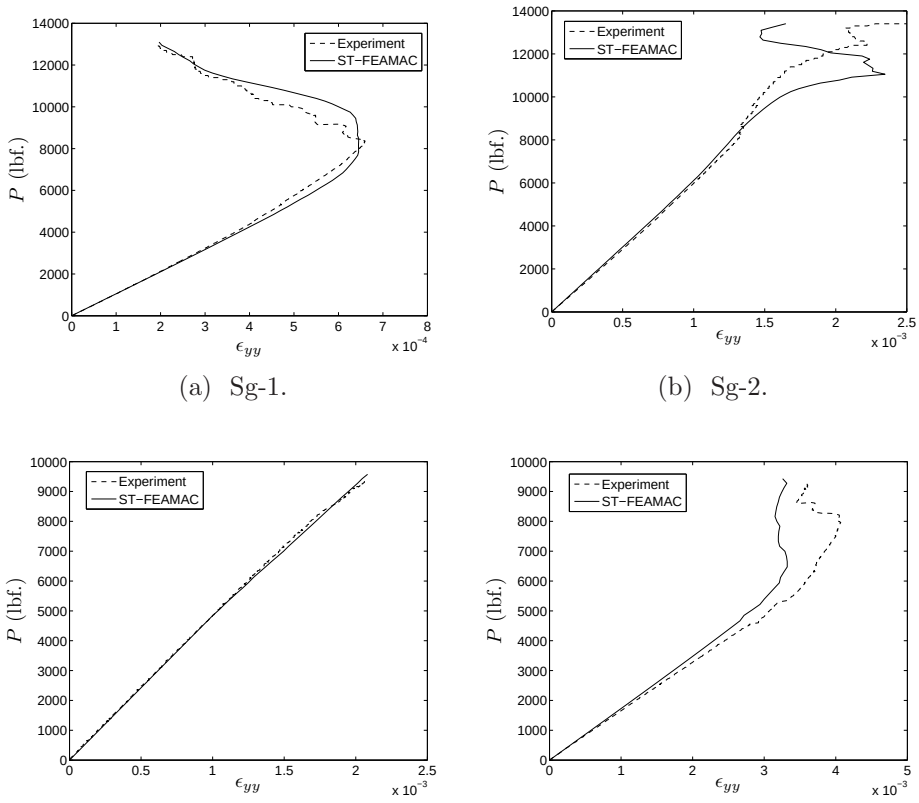

(a) Sg-1. (b) Sg-2.

(c) Sg-3. (d) Sg-4.

Figure 3.12: Applied load versus local strain for Laminate-1.

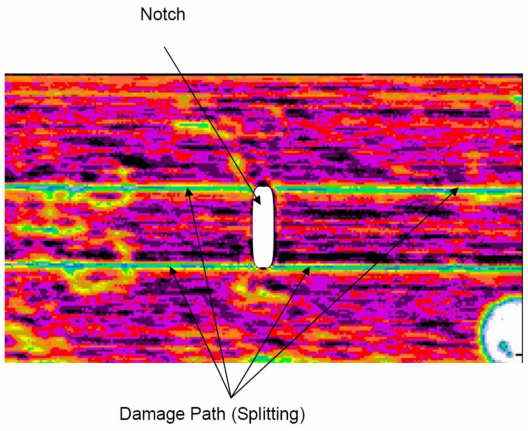

Figure 3.13: C-Scan of failed Laminate-1 specimen [*Bogert et al.* (2006)].

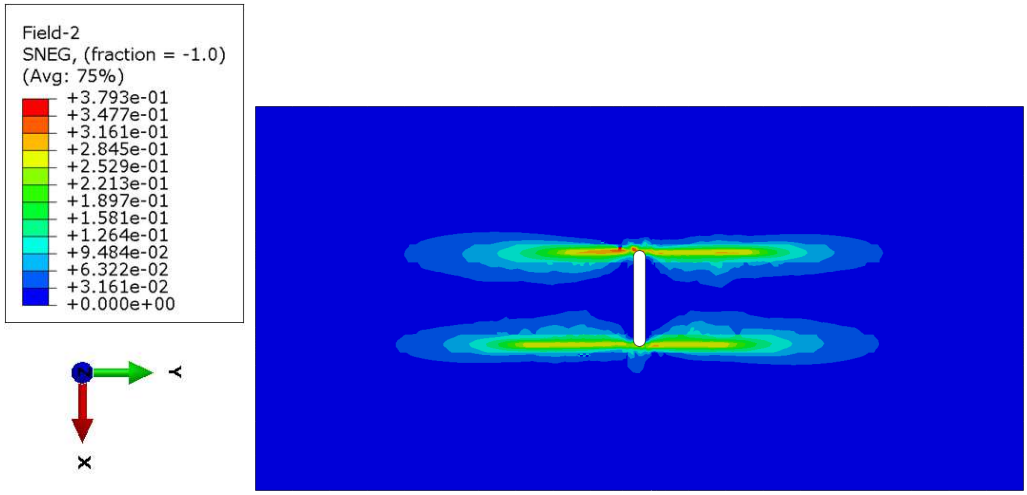

(a) $P = 8{,}490$ lbf.

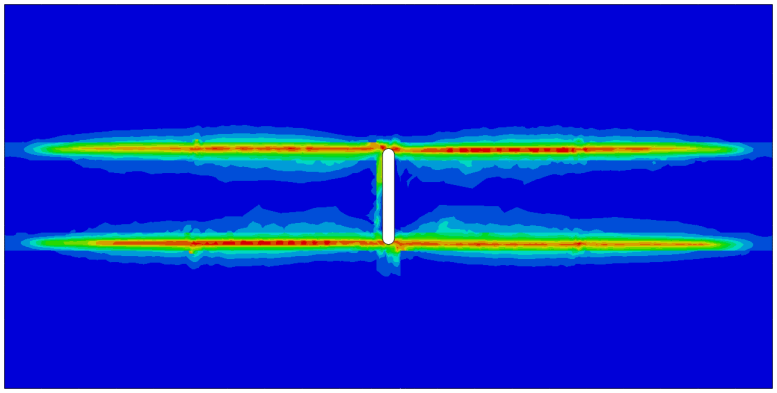

(b) $P = 16{,}400$ lbf.

Figure 3.14: Normalized matrix microdamage contour $\frac{S_r}{S_r^{max}}$ in Laminate-1.

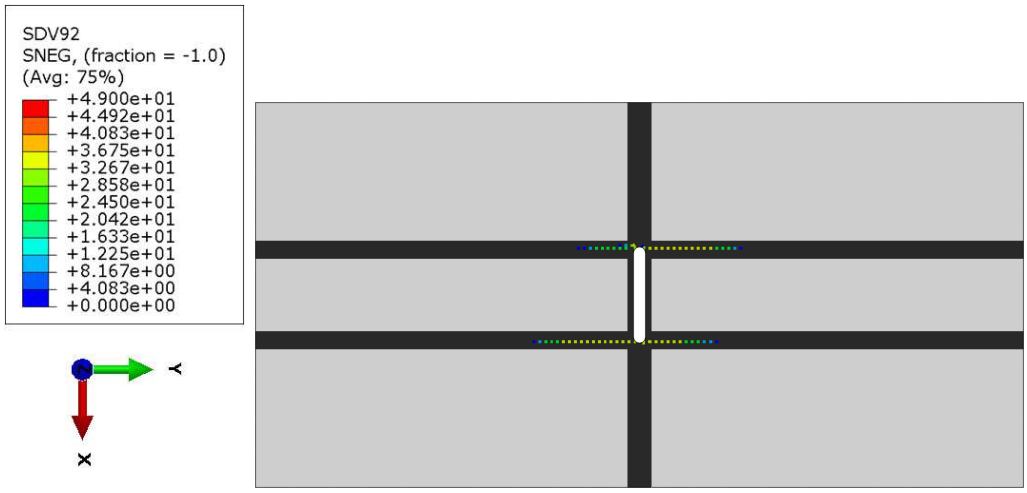

(a) $P = 8{,}490$ lbf.

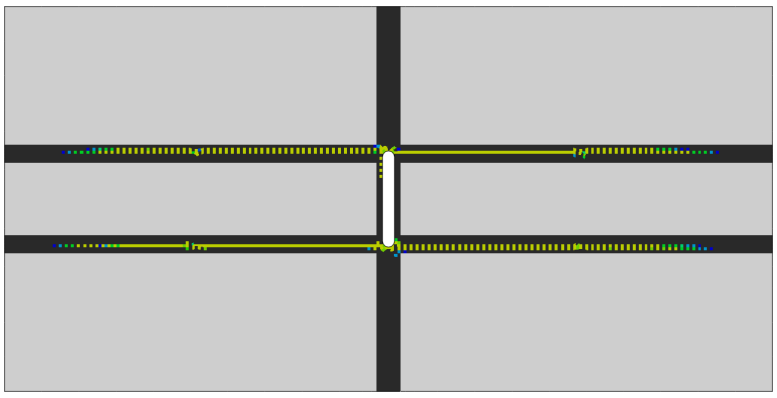

(b) $P = 16{,}400$ lbf.

Figure 3.15: Failed GMC subcells in Laminate-1. Black indicates no failure has occurred; gray indicates failure was not permitted.

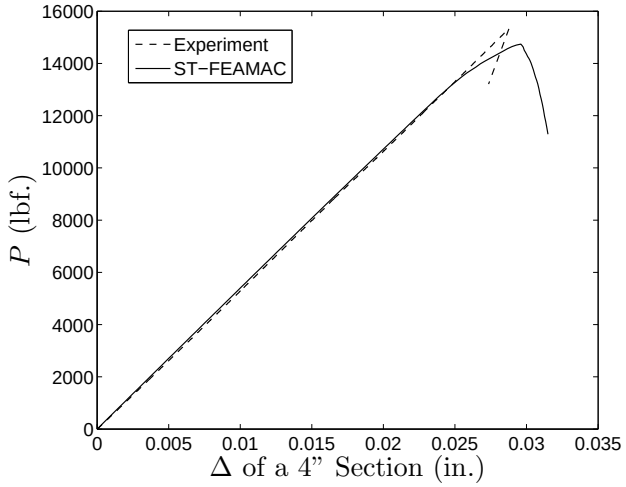

Figure 3.16: Applied load versus displacement of a 4" section for Laminate-2.

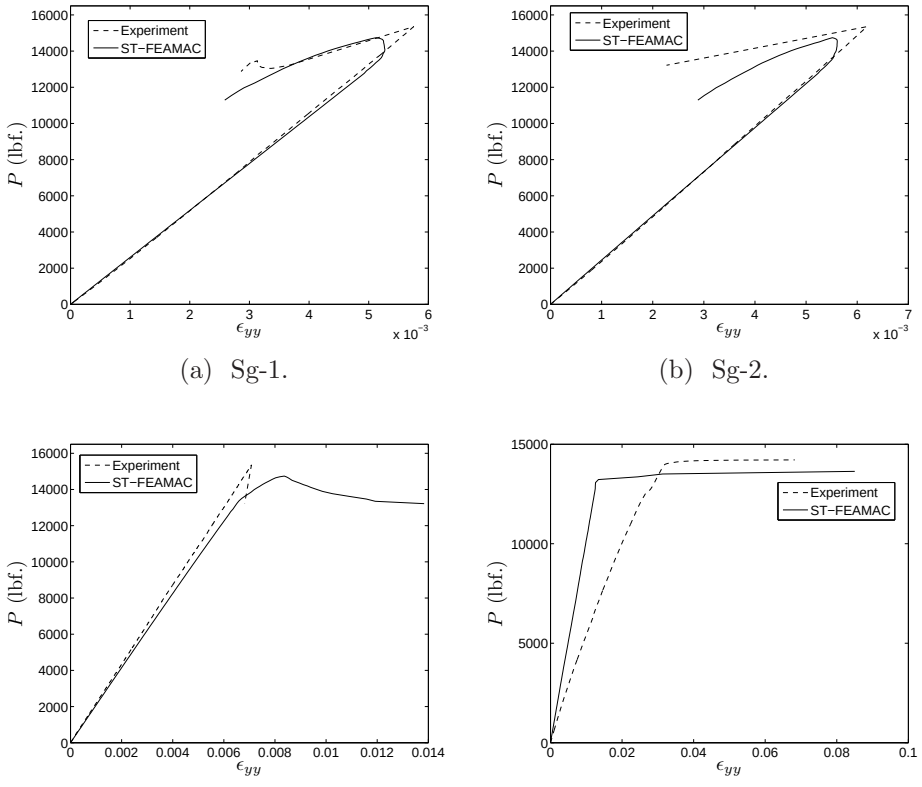

(a) Sg-1. (b) Sg-2.

(c) Sg-3. (d) Sg-4.

Figure 3.17: Applied load versus local strain for Laminate-2.

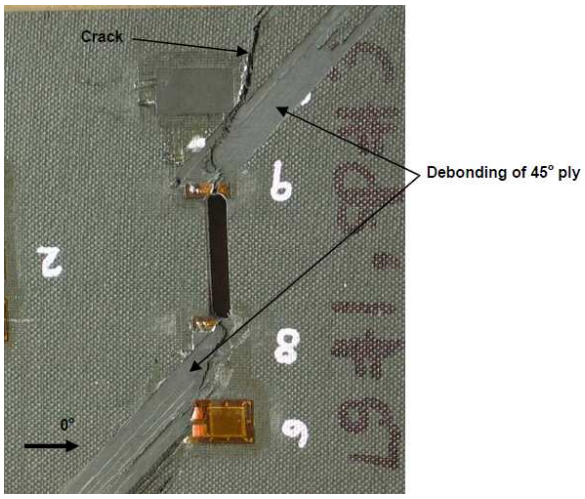

Figure 3.18: Photograph of failed Laminate-2 specimen [*Bogert et al.* (2006)].

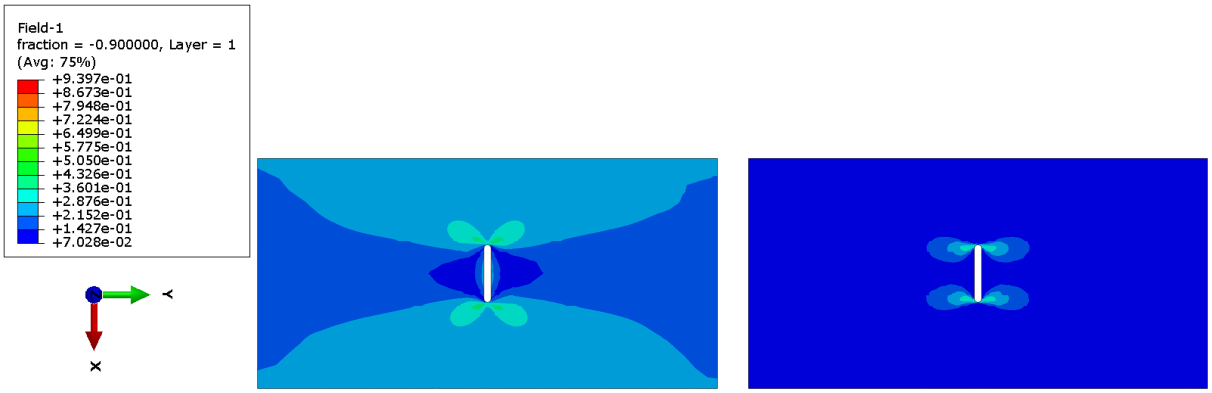

(a) 45° Layer.

(b) 0° Layer.

(c) -45° Layer.

(d) 90° Layer.

Figure 3.19: Normalized matrix microdamage contour $\frac{S_r}{S_r^{max}}$ in Laminate-2 just prior to first axial failure initiation $P = 12{,}770$ lbf.

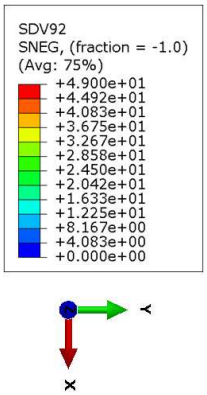

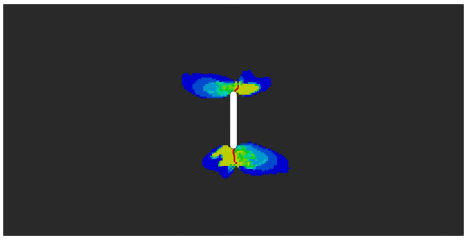

(a) 45° Layer.

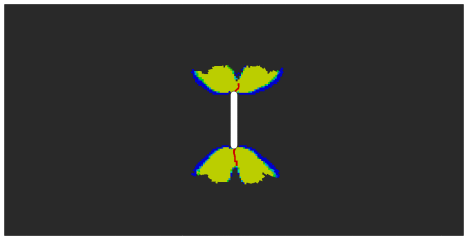

(b) 0° Layer.

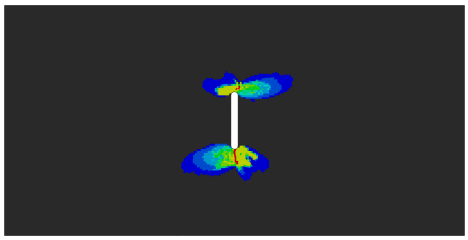

(c) -45° Layer.

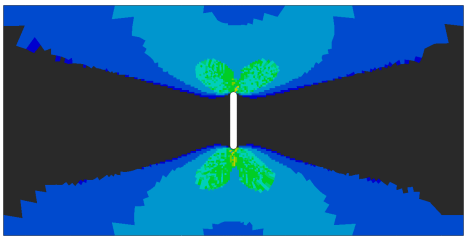

(d) 90° Layer.

Figure 3.20: Failed GMC subcells in Laminate-2 at ultimate load $P = 14{,}740$ lbf. Black indicates no failure has occurred.

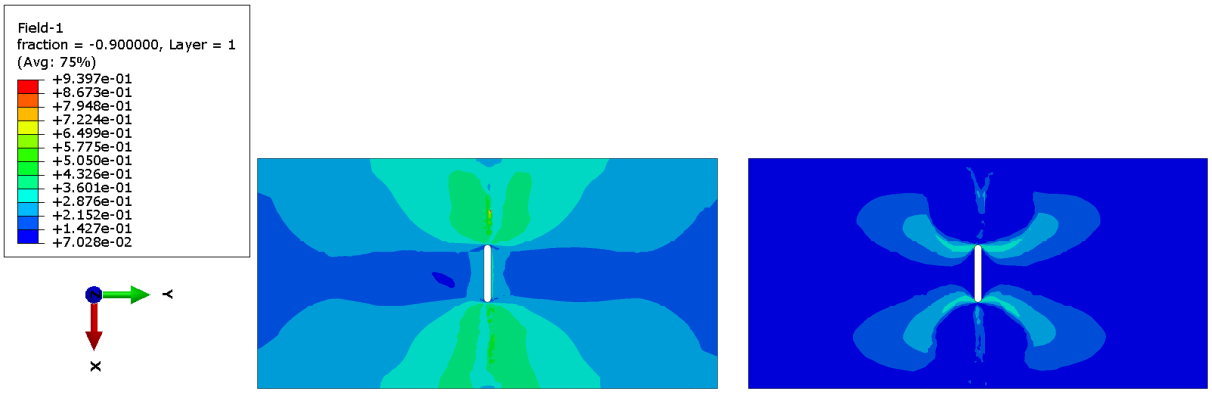

(a) 45° Layer.

(b) 0° Layer.

(c) -45° Layer.

(d) 90° Layer.

Figure 3.21: Normalized matrix microdamage contour $\frac{S_r}{S_r^{max}}$ in Laminate-2 at end of simulation.

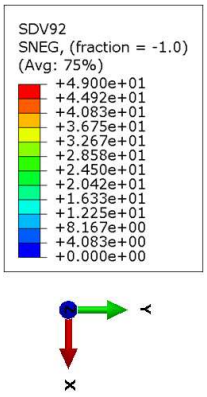

(a) 45° Layer.

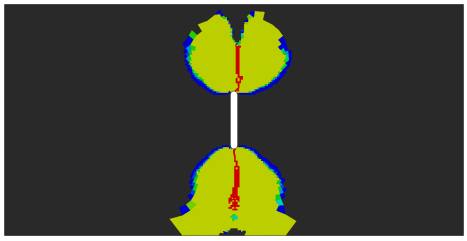

(b) 0° Layer.

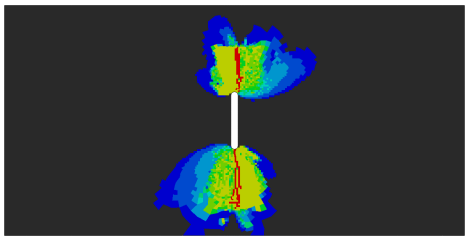

(c) -45° Layer.

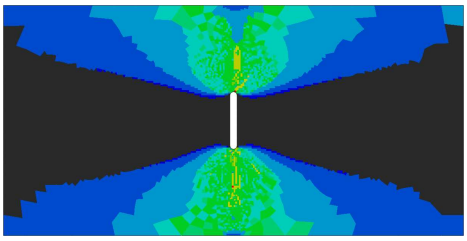

(d) 90° Layer.

Figure 3.22: Failed GMC subcells in Laminate-2 at end of simulation. Black indicates no failure has occurred.

CHAPTER IV

Numerical Implementation of a Multiple-ISV Thermodynamically-Based Work Potential Theory for Modeling Progressive Damage and Failure in Fiber-Reinforced Laminates

4.1 Introduction

Many progressive damage and failure analysis (PDFA) methodologies breakdown when the material enters the post-peak strain softening regime locally within an element. Loss of positive definiteness of the tangent stiffness tensor leads to pathological mesh dependence [*Bažant and Cedolin* (1979); *Pietruszczak and Mroz* (1981)]. To overcome this deficiency, *Bažant* (1982) developed the smeared crack, or crack band, model that introduces a characteristic element length into the formulation of the damage evolution. The original formulation assumed that the mode I crack band always aligns with the principle axes [*Bažant and Oh* (1983)]. *de Borst and Nauta* (1985) altered the formulation to accommodate a fixed crack band under mixed mode conditions. An encompassing overview of smeared crack band models is provided by *Spencer* (2002).

In Chapter II, the thermodynamically-based, work potential theory, Schapery the-

ory (ST), was presented for modeling matrix microdamage in fiber-reinforced laminates (FRLs). *Sicking* (1992) and *Schapery and Sicking* (1995) extended the formulation to include the effects of transverse cracking by adding an additional internal state variable (ISV) and predicted the evolution of microdamage and transverse cracking in coupon laminates analytically. *Pineda et al.* (2010b) implemented this extended formulation in a numerical setting to simulate the failure of a buffer strip-reinforced, center-notched panel (CNP). However, due to the cumbersome nature of the evolution equations, the microdamage and transverse cracking evolution equations were decoupled to arrive at a more efficient implementation. Since no characteristic length was introduced into the formulation, the theory produces mesh dependent results in a computational setting. In the previous chapter, micromechanics was used to resolve the localization due to failure. Unfortunately, the microscale failure degradation scheme utilized also produces mesh dependent results.

In this chapter, the Schapery theory (ST) formulation is modified to the enhanced Schapery theory (EST) to accommodate the effects of macroscopic transverse and shear matrix cracking, as well as fiber breakage, using an approach that differs from Refs. [*Sicking* (1992); *Schapery and Sicking* (1995); *Pineda et al.* (2010b)]. As in the previous chapter, a deliberate distinction between damage and failure is made. Damage is defined as the effects of any structural changes resulting in a nonlinear response that preserves the positive definiteness of the tangent stiffness tensor of the material. Conversely, failure is considered to be the consequence of structural changes that yield post-peak strain softening in the stress versus strain response of the material. Here, matrix microdamage is categorized as a damage mechanism, but macroscopic matrix cracking and fiber breakage are hypothesized to be failure mechanisms resulting from damage localization. The traditional ISV used in Chapter II is maintained to model microdamage. Upon failure initiation, the element domain is no longer considered a continuum, and a smeared crack approach is used to model

the embedded discontinuities. Three new ISVs, which incorporate the characteristic length of the finite element, dictate the evolution of the failure mechanisms. Although the refinement gained in the multiscale model is lost, the EST formulation presented in Section 4.2 offers nonlinear progressive damage coupled with mesh objective, post-peak strain softening.

Mesh objectivity is demonstrated in Section 4.3. In Section 4.4, EST is verified against experimental results for two CNPs. Global load versus deflection data, local strain gage data, as well as observed failure mechanisms obtained from experiments performed at the NASA Langley Research Center (LaRC) [*Bogert et al.* (2006); *Satyanarayana et al.* (2007)] (also presented in Chapter III) are compared to numerical results.

4.2 Enhanced Schapery Theory

The previously developed ST (Chapter II) [*Schapery* (1990, 1995); *Schapery and Sicking* (1995); *Basu et al.* (2006); *Pineda et al.* (2009, 2010b)] is extended to accommodate mesh objective, post-peak strain softening. Separate ISVs are used to govern the evolution of matrix microdamage, transverse (mode I) matrix failure, shear (mode II) matrix failure, and fiber breakage (mode I). The first and second laws of thermodynamics are enforced, establishing thermodynamically consistent evolution laws for progressive matrix microdamage, as well as post-peak failure. The following sections detail the formulation of this work potential theory.

4.2.1 Multiple ISV Formulation of ST to Account for Multiple Damage and Failure Mechanisms

Due to the generality of the thermodynamically-based evolution equations, Equations (2.3) and (2.4) presented in Chapter II, the work potential theory can account for any number and type of structural changes that may occur in a material. This is

especially useful for modeling progressive damage in composites because the heterogeneity of the composite, and multiaxiality of the local fields, enables multiple damage mechanisms to arise during a typical loading history. For instance in the matrix phase alone, microdamage accrues until its effects are superseded by the growth of larger transverse cracks. Microdamage is considered the advancement of microcracks, voids, fissures, shear bands, and other flaws that are present in the matrix of a composite [*Sicking* (1992); *Schapery and Sicking* (1995); *Basu et al.* (2006); *Ng et al.* (2010)]. The size of these flaws is typically on the order of that of the fiber or smaller. Transverse cracks nucleate from preexisting flaws within the matrix but grow parallel to the fibers and span the thickness of the lamina [*Talreja* (1985b); *Allen et al.* (1987a); *Laws and Dvorak* (1988); *Gudmundson and Östlund* (1992); *Yang and Cox* (2005); *Noda et al.* (2006); *Green et al.* (2007)]. Often, the growth of individual transverse cracks is extremely rapid; however, the effects of transverse cracking on the stiffness of a composite laminate can be progressive if multiple cracks form over an extended period of time, and there are adjacent layers in the laminate that can support the additional load that cannot be sustained by the cracking ply. Eventually, transverse cracking is succeeded by more catastrophic damage mechanisms including interlaminar delamination, fiber breakage, pullout and bridging associated with macroscopic laminate fracture [*McCartney* (1992a,b); *Hallett et al.* (2008)].

Here it is assumed that three major intralaminar mechanisms are responsible for all observed non-linearities in the stress-strain curve of a composite lamina: matrix microdamage, matrix macroscopic cracking, and axial fiber failure. Each of these mechanisms can be accommodated by partitioning the total dissipated energy density W_S into portions associated with each mechanism.

Matrix microdamage is the primary cause of observed non-linearity in the stress versus strain response of polymer matrix composites (PMCs) (not including nonlinear elasticity, plasticity or viscous effects) up to localization of microdamage into more

severe failure mechanisms, such as transverse cracking, fiber breakage, kink band formation, or delamination. Microdamage can be considered the combination of matrix microcracking, micro-void growth, shear banding, and fiber-matrix debonding. Figure 2.1 shows a typical uniaxial response of a material exhibiting microdamage evolution, where the recoverable energy potential is given by W and the potential dissipated into evolving structural changes associated with microdamage is given by S.

Typically, matrix microdamage continues to grow until the onset of more catastrophic failure mechanisms initiate. It should be noted that this work explicitly distinguishes between damage and failure in the following manner:

Damage - Structural changes in a material that manifest as pre-peak non-linearity in the stress-strain response of the material through the degradation of the secant moduli.

Failure - Structural changes that result from damage localization in a material and manifest as post-peak strain softening in the stress-strain response of the material.

Here, three major failure mechanisms are considered: transverse (mode I) matrix cracking, shear (mode II) matrix cracking, and axial (mode I) fiber fracture. It is assumed that the evolution of these mechanisms yields an immediate reduction in the load-carrying capability of a local subvolume surrounding the mechanism. Three ISVs are used to account for mode I matrix cracking, mode II matrix cracking, and mode I fiber failure, respectively: S_I^m, S_{II}^m, and S_I^f. These ISVs are defined completely in Section 4.2.2, and are taken to be the potentials required to advance structural changes associated with these failure mechanisms. The uniaxial stress-strain response of a material exhibiting post-peak strain softening is displayed in Figure 4.1. The shaded area above the unloading line represents the total, dissipated potential W_S,

and the triangular area underneath is the total, recoverable, elastic strain energy density W_E.

At any given state the total dissipated energy density W_S can be calculated as a sum of energy dissipated through the aforementioned damage and failure mechanisms, given by the four ISVs.

$$W_S = S + S^m_{IF} + S^m_{IIF} + S^f_I \tag{4.1}$$

According to the first law of thermodynamics, Equation (2.1), the total work potential (ignoring thermal dissipation) is given by the sum of the elastic strain energy density and the potentials associated with each of the damage or failure mechanisms.

$$W_T = W_E + S + S^m_I + S^m_{II} + S^f_I \tag{4.2}$$

where W_E is the elastic strain energy density. Invoking the stationarity principle, Equation (2.3),

$$\begin{aligned} \frac{\partial W_E}{\partial S} &= -1 \\ \frac{\partial W_E}{\partial S^m_I} &= -1 \\ \frac{\partial W_E}{\partial S^m_{II}} &= -1 \\ \frac{\partial W_E}{\partial S^f_I} &= -1 \end{aligned} \tag{4.3}$$

and the second law of thermodynamics, Equation (2.4), gives:

$$\begin{aligned} \dot{S} &\geq 0 \\ \dot{S}^m_{IF} &\geq 0 \\ \dot{S}^m_{IIF} &\geq 0 \\ \dot{S}^f_F &\geq 0 \end{aligned} \tag{4.4}$$

Equations (4.3) and (4.4) constitute the evolution equations for damage and failure in a material experiencing matrix microdamage, matrix cracking, and fiber breakage in tension.

It should be noted, that EST can also account for kink band formation under axial compression [*Schapery* (1995); *Basu* (2005); *Basu et al.* (2006)]; although, the applied loading in the examples presented in Sections 4.3 and 4.4 are tensile, and kink banding does not occur. As the lamina is loaded, the fibers in the composite rotate by some angle ϕ, given by the deformation gradient in the model. To model the kink band mechanism, all calculations are then executed in the instantaneous fiber frame given by ϕ; therefore, fiber rotation induces larger shear strains, γ_{12}. Increased shear strain yields more damage, leading to a reduction in the shear modulus. The increase in shear compliance allows for further progression of the shear strain. Under axial compression, this leads to a runaway instability, and a kink band will form.

4.2.2 Failure Initiation

As stated previously in Chapter II, matrix microdamage requires no initiation criterion. For low strain levels, the microdamage ISV S remains small and its effects on the composite moduli are not apparent. As S evolves, with increased strains,

its effects on the stress-strain response of the composite become more noticeable. However, it is postulated that the evolution of the failure mechanisms immediately yield a negative tangent stiffness; therefore, initiation criteria are required. Furthermore, criteria are required to mark failure initiation because the macroscopic cracks responsible for failure may result from localization of microdamage, or they may nucleate from preexisting flaws in the material not necessarily associated with evolving microdamage.

EST is implemented in homogenized laminae; therefore, phenomenological criteria must be utilized that account for the composite microstructure. The Hashin-Rotem failure criterion incorporates separate equations for matrix failure and fiber failure initiation [*Hashin and Rotem* (1973)]. The matrix failure criterion involves contributions form both the transverse (ϵ_{22}) and shear (γ_{12}) strains.

$$\begin{aligned} \left(\frac{\epsilon_{22}}{Y_T}\right)^2 + \left(\frac{\gamma_{12}}{Z}\right)^2 = 1 \quad \epsilon_{22} \geq 0 \\ \left(\frac{\epsilon_{22}}{Y_C}\right)^2 + \left(\frac{\gamma_{12}}{Z}\right)^2 = 1 \quad \epsilon_{22} < 0 \end{aligned} \tag{4.5}$$

where Y_T is the transverse lamina failure strain in tension, Y_C is the transverse failure lamina strain in compression, and Z is the shear failure strain. The fiber failure criterion only involves the axial strain ϵ_{11}.

$$\left(\frac{\epsilon_{11}}{X_T}\right)^2 = 1 \quad \epsilon_{11} \geq 0 \tag{4.6}$$

where X_T is the maximium allowable axial strain of the lamina. A local, lamina coordinate frame is chosen such that, 1- is the axial direction of the fibers, 2- is the in-plane transverse direction, and 3- is the out-of-plane direction. When Equation (4.5) is satisfied the matrix failure ISVs S_I^m and S_{II}^m are activated, and when Equation (4.6) is satisfied fiber failure evolution S_I^f is permitted; otherwise, S remains the only

active ISV. Upon satisfaction of either Equation (4.5) or Equation (4.6), it is assumed that the more severe failure mechanisms dominate, superseding the effects of matrix microdamage; therefore, $\dot{S} = 0$, and additional microdamage is precluded.

4.2.3 Use of Traction-Separation Relationships to Define the Failure Potentials

Sicking (1992) and *Schapery and Sicking* (1995) used a single ISV to model the effects of transverse cracking on a composite lamina. Similar to microdamage, the transverse and shear moduli were related to transverse crack evolution through a set damage functions obtained from coupon experiments. Predictions of the nonlinear response of numerous laminates were presented assuming a homogenous strain state in the laminates. *Pineda et al.* (2010b) implemented the dual-ISV formulation of ST for predicting microdamage and transverse cracking within FEM to model the response of a center-notched laminate that was reinforced with buffer strips. The original formulation required the solution of two, coupled, bi-variate polynomials, which is computationally intensive in an FEM framework. Thus, *Pineda et al.* (2010b) decoupled the microdamage and transverse cracking evolution equations.

In the aforementioned publications, it was assumed that the transverse cracking affected the relationships between stress and strain. However, the existence of a macroscopic crack invalidates the assumption of a continuum. Here, it is presumed that failure arises from the evolution of cohesive cracks within the continuum, and the ISVs associated with failure (axial, transverse, and shear) influences the relationship between traction on the crack faces and the crack-tip opening displacement. The satisfaction of Equations (4.5) and/or (4.6) indicates the material behavior transitions from that of a damaging continuum to that of a cohesive crack, and the essential fields become traction and separation, rather than stress and strain (see Figure 4.2).

Once a cohesive crack initiates in the continuum, opening of the crack yields a

reduction in traction on the crack faces at the crack tip. If subsequently the crack is closed, it is assumed that traction at the crack tip will unload linearly towards the origin of the traction versus separation law (see Figure 4.3). The strain energy release rate (SERR) G_M^j is taken as the total energy dissipated per unit area of new surface that is created through crack advancement and can be calculated as the area under the traction-separation law (for a given traction and separation pair) minus the energy per area that can potentially be recovered by unloading.

$$G_M^j = \int_0^{\delta_M^j} t_M^j d\delta_M^j - \frac{1}{2} t_M^j \delta_M^j \tag{4.7}$$

where j indicates the material (fiber f or matrix m), M represents the corresponding mode (mode I or mode II), δ_M^j is the crack tip opening displacement in mode M and material j, and t_M^j is the corresponding traction at the crack tip.

Theoretically, the shape of the traction-separation laws for mode I crack growth in the fiber, and mode I and II crack growth in the matrix can take any shape. *Gustafson and Waas* (2009) investigated triangular, trapezoidal, beta distribution, and sinusoidal traction-separation laws in discrete cohesive zone method (DCZM) elements and determined that the shape only affected convergence of the FEM solver, but not the overall results. For simplicity, it is assumed here that all three types of cracks obey triangular traction-separation laws, presented in Figure 4.3. The total area under the traction-separation curves is controlled by the corresponding material fracture toughness in the appropriate mode, where G_{IC}^f is the mode I fracture toughness of the fiber, G_{IC}^m is the mode I fracture toughness of the matrix, and G_{IIC}^m is the mode II fracture toughness of the matrix. The cohesive strengths of the materials t_{IC}^f (mode I fiber strength), t_{IC}^m (mode I matrix strength), and t_{IIC}^m (mode II matrix strength) are given by the stresses in the continuum when Equations (4.5) and/or (4.6) are satisfied. Mode I, normal cracks are not allowed to grow under compres-

sion, but mode II, shear cracks can evolve under normal compression. Therefore, the mode I traction-separation laws for the fiber and matrix (Figures 4.3a and 4.3b) do not accommodate negative crack tip displacements. However under negative mode II displacement (see Figure 4.3c), the traction on the crack faces will increase linearly until the maximum, previously attained displacement magnitude is reached, after which, the crack faces will resume unloading according to the negative portion of the traction-separation law. The traction-separation laws exhibited in Figure 4.3 do not require any initial, fictitious, pre-peak stiffnesses because the cracks are embedded within a continuum. This is an advantage over the use of DCZM elements which do require an initial stiffness because these interfacial elements do not actually represent physical material within the model and must simulate initially perfect bonding between adjacent material domains [*Xie et al.* (2006); *Gustafson* (2008)]. If set incorrectly, these fictitious stiffnesses can cause numerical problems [*Turon et al.* (2006)].

Although no mode I crack can advance under compression, it is possible for post-peak softening to occur under compressive loading situations. For instance a kink band could form under global axial compression, or the matrix could fail in local shear due to internal friction (Mohr-Coulomb) in quasi-brittle materials under transverse compression (see Chapter V) [*Hoek and Bieniawski* (1965)]. Since these failure mechanisms involve local shear at a the fiber/matrix scale which is typically below the operating lamina/laminate scale, it appears that these mechanisms evolve under mode I compression. In a numerical model containing homogenized laminae, there is no subscale shear to drive these compressive failure modes. However, EST could be extended further to incorporate these mechanisms through phenomenological accessions. The methods, developed by *Basu* (2005); *Basu et al.* (2006) and described in Section 4.2.2, can be used to track the instantaneous fiber angle, and a critical fiber angle can be assigned to indicate the initiation of post-peak softening due to

kink band formation. Similarly, a matrix compression criterion, such as the one developed by *Puck and Schürmann* (1998, 2002) could be used to signal the initiation of Mohr-Coulomb compressive failure. The traction-separation laws for mode I fiber compression and mode I transverse matrix compression could be adjusted to include the post-peak softening effects of microbuckling and Mohr-Coulomb matrix failure. These postulated, compressive, mode I traction-separation laws could account for energy released through these subscale failure modes in a homogenous model at the lamina/laminate scale. However, the examples presented in this chapter are tension dominated, and extension of the theory to accommodate apparent mode I compressive failure is left for future work.

Using the traction-separation laws in Figure 4.3, the SERR can be calculated with Equation (4.7).

$$G_I^f = \frac{1}{2} t_{IC}^f \delta_I^f \tag{4.8}$$

$$G_I^m = \frac{1}{2} t_{IC}^m \delta_I^m \tag{4.9}$$

$$G_{II}^m = \frac{1}{2} t_{IIC}^m \delta_{II}^m \tag{4.10}$$

It is assumed that the energy released due to cracking is smeared over the entire element [*Bažant* (1982); *Bažant and Oh* (1983)]. Thus, the dissipation potentials resulting from macroscopic cracking in an element are related to the SERRs using the suitable element dimensions.

$$S_I^f = \frac{G_I^f}{l_e^{(\theta+90^\circ)}} \tag{4.11}$$

$$S_I^m = \frac{G_I^m}{l_e^{(\theta)}} \tag{4.12}$$

$$S_{II}^m = \frac{G_{II}^m}{l_e^{(\theta)}} \tag{4.13}$$

If there is a single integration point in the element, $l_e^{(\theta+90^\circ)}$ is the length of a line

running perpendicular to fiber direction in the element that intersects two edges of the element and the integration point, and $l_e^{(\theta)}$ is the length of a line that is parallel to the fiber direction in the element that intersects two edges of the element and the integration point. If there is more than one integration point in the element, the element can be partitioned into a number of subvolumes equal to the number of integration points, and the lengths $l_e^{(\theta+90^\circ)}$ and $l_e^{(\theta)}$ are lengths of lines that intersect the corresponding integration point as well as two element edges or integration point subvolume boundaries. Incorporating a length scale into the ISVs results in mesh objective, post-peak, softening. This is elaborated upon further in Section 4.4.

4.2.4 EST Evolution Equations for a Fiber-Reinforced Lamina

To arrive at the evolution equations for the four ISVs, the elastic strain energy density must be defined for a material which may contain cohesive cracks. Therefore, the elastic strain energy W_E comprises of a contribution from the continuum W and any possible cohesive cracks W_M^j. The elastic strain energy density in the continuum remains as defined in Equation (2.14), and the elastic strain energy density of the cohesive cracks are defined as the recoverable energy per unit crack surface area smeared over the entire element.

$$W_I^f = \frac{t_I^f \delta_I^f}{2l_e^{(\theta+90^\circ)}} \tag{4.14}$$

$$W_I^m = \frac{t_I^m \delta_I^m}{2l_e^{(\theta)}} \tag{4.15}$$

$$W_{II}^m = \frac{t_{II}^m \delta_{II}^m}{2l_e^{(\theta)}} \tag{4.16}$$

The tractions in Equations (4.14)-(4.16) can be related to the secant stiffness' in the traction-separation laws k_M^j.

$$t_I^f = k_I^f \delta_I^f \tag{4.17}$$

$$t_I^m = k_I^m \delta_I^m \tag{4.18}$$

$$t_{II}^m = k_{II}^m \delta_{II}^m \tag{4.19}$$

Hence, the total elastic strain energy density in the continuum is given by

$$\begin{aligned} W_E =& \frac{1}{2}\left(E_{11}\epsilon_{11}^2 + E_{22}(S)\epsilon_{22}^2 + G_{12}(S)\gamma_{12}^2\right) + Q_{12}\epsilon_{11}\epsilon_{22} \\ &+ \frac{k_I^f(S_I^f)}{2l_e^{(\theta+90^\circ)}}\delta_I^{f\,2} + \frac{k_I^m(S_I^m)}{2l_e^{(\theta)}}\delta_I^{m\,2} + \frac{k_{II}^m(S_{II}^m)}{2l_e^{(\theta)}}\delta_{II}^{m\,2} \end{aligned} \tag{4.20}$$

Substituting Equation (4.20) into Equations (4.3) gives the ISV evolution equations.

$$\frac{1}{2}\left(\epsilon_{22}^2 E_{220}\frac{de_s}{dS_r} + \gamma_{12}^2 G_{120}\frac{dg_s}{dS_r}\right) = -3S_r^2 \tag{4.21}$$

which is unchanged from Equation (2.16); keeping in mind Equations (2.11)-(2.13).

$$\frac{1}{2l_e^{(\theta+90^\circ)}}\frac{dk_I^f}{dS_I^f}\delta_I^{f\,2} = -1 \tag{4.22}$$

$$\frac{1}{2l_e^{(\theta)}}\frac{dk_I^m}{dS_I^m}\delta_I^{m\,2} = -1 \tag{4.23}$$

$$\frac{1}{2l_e^{(\theta)}}\frac{dk_{II}^m}{dS_{II}^m}\delta_{II}^{m\,2} = -1 \tag{4.24}$$

Using the chain rule and minding that

$$\frac{dS_I^f}{d\delta_I^f} = \frac{t_{IC}^f}{2l_e^{(\theta+90^\circ)}} \tag{4.25}$$

$$\frac{dS_I^m}{d\delta_I^m} = \frac{t_{IC}^m}{2l_e^{(\theta)}} \tag{4.26}$$

$$\frac{dS_{II}^m}{d\delta_{II}^m} = \frac{t_{IIC}^m}{2l_e^{(\theta)}} \tag{4.27}$$

by Equations (4.8)-(4.13), the cohesive secant stiffnesses are determined.

$$k_I^f = -\int \frac{t_{IC}^f}{{\delta_I^f}^2} d\delta_I^f \tag{4.28}$$

$$k_I^m = -\int \frac{t_{IC}^m}{{\delta_I^m}^2} d\delta_I^m \tag{4.29}$$

$$k_{II}^m = -\int \frac{t_{IIC}^m}{{\delta_{II}^m}^2} d\delta_{II}^m \tag{4.30}$$

Evaluating the integrals in Equations (4.28)-(4.30), while enforcing $k_M^j = 0$ when $\delta_M^j = \dfrac{2G_{MC}^j}{t_{MC}^j}$ results in expressions for k_M^j in terms of δ_M^j.

$$k_I^f = t_{IC}^f \left(\frac{1}{\delta_I^f} - \frac{t_{IC}^f}{2G_{IC}^f} \right) \tag{4.31}$$

$$k_I^m = t_{IC}^m \left(\frac{1}{\delta_I^m} - \frac{t_{IC}^m}{2G_{IC}^m} \right) \tag{4.32}$$

$$k_{II}^m = t_{IIC}^m \left(\frac{1}{\delta_{II}^m} - \frac{t_{IIC}^m}{2G_{IIC}^m} \right) \tag{4.33}$$

Note that the thermodynamically consistent stiffnesses derived in Equations (4.31)-(4.33) can also be derived directly from the traction-separation laws using geometry.

Finally, it is assumed that following failure initiation the strains are related to the crack tip opening displacements by

$$l_e^{(\theta+90^\circ)} \epsilon_{11} = l_e^{(\theta+90^\circ)} \epsilon_{11}^C + \delta_I^f \tag{4.34}$$

$$l_e^{(\theta)} \epsilon_{22} = l_e^{(\theta)} \epsilon_{22}^C + \delta_I^m \tag{4.35}$$

$$l_e^{(\theta)} \gamma_{12} = l_e^{(\theta)} \gamma_{12}^C + 2\delta_{II}^m \tag{4.36}$$

where ϵ_{11}^C, ϵ_{22}^C, and γ_{12}^C are the strains when Equations (4.5) and/or (4.6) are satisfied. Equations (4.34)-(4.36) imply that the strain in the continuum remains at the values

obtained when failure initiates, and that any incremental change in the global strain after failure initiation is used wholly to advance the crack tip opening displacement. To account for changes in the continuum strain after failure initiates, it can be assumed that the stress state in the cracked body is homogenous and the tractions on the crack tip faces are equal to the stresses in the continuum. Then, the strains in Equation (4.20) can be formulated in terms of the cohesive secant stiffnesses and the crack tip opening displacement. However, it is believed that the evolution of strain in the continuum is negligible once cohesive cracks form. Equations (4.34)-(4.36) can be utilized in Equations (4.31)-(4.33) to obtain k_M^j as functions of the global strain at an integration point.

$$k_I^f = t_{IC}^f \left[\frac{1}{l_e^{(\theta+90^\circ)} \left(\epsilon_{11} - \epsilon_{11}^C\right)} - \frac{t_{IC}^f}{2G_{IC}^f} \right] \tag{4.37}$$

$$k_I^m = t_{IC}^m \left[\frac{1}{l_e^{(\theta)} \left(\epsilon_{22} - \epsilon_{22}^C\right)} - \frac{t_{IC}^m}{2G_{IC}^m} \right] \tag{4.38}$$

$$k_{II}^m = t_{IIC}^m \left[\frac{2}{l_e^{(\theta)} \left(\gamma_{12} - \gamma_{12}^C\right)} - \frac{t_{IIC}^m}{2G_{IIC}^m} \right] \tag{4.39}$$

Once failure initiates, it is assumed the effects of failure supersede the effects of microdamage and evolution of S_r ceases. The cohesive stiffness in a cracked element is calculated using Equations (4.37)-(4.39) for a given strain state; then, Equations (4.17)-(4.19) and (4.34)-(4.36) are used to calculate the tractions on the crack tip faces and the crack tip opening displacement. It is assumed that the stress state in the element is homogenous, and the tractions on the crack tip faces are equal to the stresses in the element. Lastly, the axial, transverse, and shear moduli of the element

can be calculated [*Bažant and Oh* (1983)].

$$E_{11} = \left\{ \frac{1}{E_{110}} - \frac{\epsilon_{11} - \epsilon_{11}^{C}}{t_{IC}^{f} \left[1 + \frac{l_e^{(\theta+90^\circ)} t_{IC}^{f}}{2G_{IC}^{f}} \left(\epsilon_{11} - \epsilon_{11}^{C} \right) \right]} \right\}^{-1} \tag{4.40}$$

$$E_{22} = \left\{ \frac{1}{E_{22}^{*}} - \frac{\epsilon_{22} - \epsilon_{22}^{C}}{t_{IC}^{m} \left[1 + \frac{l_e^{(\theta)} t_{IC}^{m}}{2G_{IC}^{m}} \left(\epsilon_{22} - \epsilon_{22}^{C} \right) \right]} \right\}^{-1} \tag{4.41}$$

$$G_{12} = \left\{ \frac{1}{G_{12}^{*}} - \frac{\gamma_{12} - \gamma_{12}^{C}}{2t_{IIC}^{m} \left[1 + \frac{l_e^{(\theta)} t_{IIC}^{m}}{4G_{IIC}^{m}} \left(\gamma_{12} - \gamma_{12}^{C} \right) \right]} \right\}^{-1} \tag{4.42}$$

where E_{110} is the elastic axial modulus, and E_{22}^{*} and G_{12}^{*} are the degraded transverse and shear moduli, due to microdamage, when Equation (4.5) is met.

For visualization purposes in the FEM simulations, degradation parameters are defined which relate the current, degraded stiffnesses to their original values upon failure initiation.

$$D_I^f = 1 - \frac{E_{11}}{E_{11}^{*}} \tag{4.43}$$

$$D_I^m = 1 - \frac{E_{22}}{E_{22}^{*}} \tag{4.44}$$

$$D_{II}^m = 1 - \frac{G_{12}}{G_{12}^{*}} \tag{4.45}$$

The degradation parameter can have a minimum value of zero, which indicates that no degradation has occurred, or a maximum value of one, signaling that the corresponding modulus has been completely diminished.

The negative tangent stiffness of the stress-strain curve necessary for post-peak strain softening to occur imposes a restriction the maximum allowable element size,

as shown by *Bažant and Oh* (1983).

$$l_e^{(\theta+90^\circ)} < \frac{2G_{IC}^f E_{11}}{{t_{IC}^f}^2} \tag{4.46}$$

$$l_e^{(\theta)} < \min\left\{\frac{2G_{IC}^m E_{22}^*}{{t_{IC}^m}^2}, \frac{2G_{IIC}^m G_{12}^*}{{t_{IIC}^m}^2}\right\} \tag{4.47}$$

The analyst must be careful to ensure the dimensions of any failing elements are smaller than the conditions given in Equations (4.46) and (4.47).

In summary, Equations (4.5) and (4.6) mark the transition from evolving microdamage to failure via macroscopic cracking. Prior to failure initiation, Equation (4.21) is used to calculate the microdamage reduced ISV S_r, and the failure ISVs S_I^f, S_I^m, and S_{II}^m remain zero. Equations (2.12) and (2.13) are used to calculate the degraded transverse and shear moduli. Subsequent to matrix failure initiation, microdamage growth is precluded, and S_r remains at S_r^*, the value of S_r when Equation (4.5) was satisfied. The degeneration of the transverse and shear moduli, resulting from matrix transverse and shear cracking, is calculated using Equations (4.41) and (4.42). Finally if Equation (4.6) is satisfied, the axial modulus is calculated using Equations (4.40) as fiber breakage evolves in the element. Once the material moduli have been calculated using the appropriate evolution equations, the stresses can be updated accordingly using Equations (2.10).

4.3 Mesh Objectivity

The theory outlined in Section 4.2 solves the mesh dependency ill-posedness when the elements enter the post-peak softening regime by introducing a characteristic length into the formulation. The total SERR dissipated during the evolution of the discontinuity is equal to the prescribed fracture toughness and is independent of the element size. This approach, commonly referred to as the smeared crack approach,

or crack band model, has been used to alleviate mesh dependency in FEM since it was first developed by *Bažant* (1982) for post-peak strain softening in concrete.

To exhibit the mesh objectivity of EST, a simple example is presented in this section. One quarter of a 200 mm x 100 mm panel is modeled with finite elements using the Abaqus, version 6.10-1 finite element software **?**. The panel contains a hole with a radius of $r_h = 5$ mm in the center. The left edge of the panel is constrained in the x-direction to simulate symmetry. Similarly, the bottom edge is constrained in the y-direction. A uniform displacement is applied to all the nodes on the top edge of the panel in y-direction. Details on the panel geometry and boundary conditions are displayed in Figure 4.4. The panel is composed of a generic composite $[90^o]$ lamina with the fiber angle measured with respect to the y-axis; thus, the applied displacement is perpendicular to the fiber direction in the panel. EST is used to model damage and failure in the panel.

Four different meshes are used to evaluate the effect of mesh size on the response of the panel. All four meshes consist of two-dimensional (2-D), plane stress, quadrilateral, S4R shell elements. The elements are linear, reduced integration elements and contain four nodes and one integration point each. The density of the four meshes, shown in Figure 4.5, increases within a region near the central hole. Average element sizes equal $0.5r_h$, $0.2r_h$, $0.1r_h$, and $0.04r_h$ are used in the four different meshes. Coarser elements are used away from the hole to improve computation time. The four meshes are subjected to the same boundary conditions and loading, and are composed of the same material properties. The same elastic, damage and failure parameters are also used in all four simulations.

The resultant, applied tensile stress (given by two times the sum of the reaction forces at the nodes on the top edge divided by the cross-sectional area) normalized by the critical strain times the axial Young's modulus $\bar{\sigma}$ is plotted versus the applied displacement normalized by the radius of the hole $\bar{\Delta}$ for the four different meshes in

Figure 4.6. It can be seen that the mesh density has a minimal effect on the load-deflection results. The small discrepancy in the results between the four meshes can be attributed to the increased accuracy in the fields as the mesh is refined. Moreover, the total energy dissipated is preserved from mesh to mesh.

Figure 4.7 displays contours of the normalized, reduced microdamage ISV S_r immediately before failure initiation in the four different meshes. S_r is normalized by the maximum S_r obtained in all four simulations which is 27% of the maximum allowable S_r required to bring the moduli to zero. The four meshes exhibit similar microdamage contours, but as the mesh is refined, the microdamage is contained in the vicinity of the hole. Additionally, the global stress at which failure initiates reduces as the mesh is refined; this supports the previous speculation that the discrepancies in the stress-displacement responses were a facet of increasing field accuracy with mesh refinement.

The transverse matrix failure degradation parameter D_I^m is plotted for all four meshes in Figure 4.8. Figures 4.8a-4.8d show the failure pattern at the ultimate, global load. The coarsest mesh shows that a crack has grown at the intersection of the hole and the bottom symmetric boundary and is propagating towards the free edge, while moving away from the bottom boundary when the specimen ultimate load is achieved. In the finer meshes, the crack path is different. In Figures 4.8b-4.8c the crack initiates at the hole slightly above the bottom boundary and propagates towards the free edge while approaching the bottom boundary. Since crack band initiation is governed by the quadratic H-R failure criterion (Equation (4.5)), both the transverse and shear strains are contributing to the initiation leading to crack band initiation at the hole boundary away from the symmetric, horizontal edge where the transverse strain is not the maximum. Any failure criterion, in theory, could be used to govern crack band initiation, and if a maximum strain criterion was used, the crack band would always initiate at the hole boundary at the symmetric edge of

the model, which is the location of the maximum transverse strain. The finest mesh, Figure 4.8d, exhibits multiple cracks near the hole, but only one of the cracks grows significantly. Moreover, Figures 4.8c and 4.8d show some crack beginning to initiate at the free edge and propagate inwards. Figures 4.8e-4.8h display the transverse crack pattern once the specimen has lost all load carrying capability. The solution for the simulation with the finest mesh $0.04r_h$ diverged before all the load carrying capability was lost; so, Figure 4.8h presents the crack path at the final converged state, which is still far below the ultimate load state. In Figures 4.8e-4.8h the same crack patterns that developed in Figures 4.8a-4.8d are evident, except those cracks have saturated to maximum degradation: $D_I^m = 1$. Additionally, the cracks advancing from the free edge observed in Figures 4.8c and 4.8d have progressed further. However, this is well after the specimens reached their ultimate load; therefore, it is assumed that those cracks did not influence the load carrying capability of the panels. The discrepancy in crack path observed for the different meshes indicate that the crack path is dictated by the accuracy of the fields surrounding the leading boundary of the crack path.

4.4 Example - Center Notched Panels Subjected to Uniaxial Tension

The same examples used to demonstrate the capabilities of ST-FEAMAC in the previous chapter are used here to exhibit the performance of the EST. The experimental details of the two center-notched laminates are given in Chapter III, Section 3.4.1. Similarly, details on the FEM modeling of the panels is presented in Chapter III, Section 3.4.2.

To increase computational efficiency, the first derivatives of the higher order microdamage polynomials are approximated using linear spline interpolants. Thus, the microdamage evolution equation, Equation (4.21) is always a second order in S_r,

yielding a very efficient, analytical solution. Since the value of S_r from the previous increment is used to estimate which spline regime should be used to solve for S_r in the current increment, the solution is checked to ensure that it falls within the applicable range of the spline that was used. If it falls outside of the range of S_r that are valid for the splines, the solution is calculated again using splines that accord to the solution of the previous iteration. This procedure continues until the solution of Equation (4.21) falls within the relevant range of S_r for the splines used in Equation (4.21). A maximum number of iterations can be set, after which Equation (4.21) is solved using the full polynomial forms of the damage functions by finding the eigenvalues of the complimentary matrix of the polynomial coefficients of the evolution equation.

The axial mode I, transverse mode I, and shear mode II critical cohesive strains, and fracture toughness' are given in Table 4.1. The matrix mode I and mode II parameters were calibrated using the Sg-1 data from Laminate-1, but this laminate did not exhibit any axial failure; so, the fiber mode I parameters were calibrated using the global load-deflection data from Laminate-2.

Displacement was applied to both laminates using the `*DYNAMIC` command in Abaqus with the parameter `APPLICATION = QUASI-STATIC`. This implicit dynamic solver is recommended for quasi-static problems exhibiting a high-degree of nonlinearity. This procedure uses numerical damping to stabilize the problem. The numerical damping does not significantly affect the simulation results because the velocities in these simulations are low. For Laminate-1 a total displacement of 0.0236", and for Laminate-2 a displacement of 0.0472", is applied over 1000 seconds. The panels were assigned a generic density of 0.057 lb/in.^{3}. This technique has advantages over traditional static, implicit solvers which have difficulty converging when the material exhibits post-peak softening [*Belytschko et al.* (2000); *Belytschko and Mish* (2001)], and is not limited by a minimum stable time step required with explicit solvers [*Hughes* (2000)].

4.4.1 Results - Laminate-1

Global load P versus displacement Δ of a 4" section of Laminate-1 is compared to results from the EST simulation in Figure 4.9. Very good agreement between the model and the experimental results is achieved. The response of the specimen appears to be linear until near 8,000 lbf., where the specimen begins deforming non-linearly. The EST simulation captures the initiation and progression of the global nonlinearity accurately. This panel was not loaded until catastrophic failure; hence, the data presented in Figure 4.9 represents load versus displacement data prior to the ultimate load of the specimen.

Local strain gage data (global load P versus local y-direction strain ϵ_{yy}) from Laminate-1 is plotted with the results from the EST FEM model in Figure 4.10; please refer to Figure 3.7 for locations of strain gages. Strain relaxation is observed in the gage farthest away from the notch: Sg-1, shown in Figure 4.10a. The mode I and mode II matrix failure parameters in EST where calibrated such that the model demonstrates the same transition into strain relaxation at this location and at a similar global applied load. This load, taken as the splitting load, is 8,250 lbf. in experiment and 8,210 lbf. in the model (summarized in Table 4.2). The transition to strain relaxation is more abrupt in the experiment as evidenced by the sharp knee in the load-strain curve, whereas, the transition in the model is more gradual. Prior to strain relaxation at this point, the experiment displayed slight stiffening not observed in the model. Additionally, the model response is much smoother than that of the experiment in the strain relaxation regime. Even though the global loading is quasi-static, local events, such as cracking, may be dynamic; therefore, the discrepancy in the strain relaxation portion of the load-strain curves could be a result of dynamic matrix crack growth and arrest in the test specimen. Local crack dynamics were not accounted for in the model. Additionally, the jaggedness of the experimental data may be a facet of the stochastics related to the local microstructure of the composite

that are not included in the model. The data from the experiment and simulation for Sg-2, which is located 1.5" directly above the notch, are presented in Figure 4.10b. The model predicts less strain at Sg-2, for a given load, than the experiment, but the non-linear trends are very similar. This gage lies directly in front of the splitting crack path, shown in Figure 3.7, and it is not realistic to expect perfect agreement in areas experiencing high levels of damage and failure because of idealizations used to model the evolution of cracks in the simulations. Figure 4.10c displays data for Sg-3, located in front of the notch near the free edge. Very good agreement between the experimental and simulation results are exhibited. The model accurately captures the nonlinear evolution of strain, away from the highly damaged regions, as a function of applied load. Finally, results for Sg-4 (located directly at the notch tip) are given in Figure 4.10d. Both the experiment and simulation display axial strain relaxation. As with Sg-2, Sg-4 shows less strain for a given applied load. However, the load at which the strain at Sg-4 relaxes in both the experiment and model correlate well, in accordance with the splitting load. Again, the relaxation response of the experiment is discontinuous, but the model exhibits continuous behavior.

A C-Scan of the failed Laminate-1 specimen is displayed in Figure 3.13. Four splitting cracks can be observed propagating outward from the notch tip, parallel to the loading direction, towards the gripped edges. Contour plots of the normalized microdamage obtained from the simulation are presented in Figure 4.11 at the splitting load 8,200 lbf. and at 16,400 lbf. In these plots, S_r is normalized by the maximum achievable value, $S_r^{max} = 7.57$ psi$^{\frac{1}{3}}$, obtained from Figure 3.9. In Laminate-1, S_r reached a maximum value equal to $0.171 S_r^{max}$. At the splitting load, the regions of maximum damage are localized to small regions, along the same crack path observed in Figure 3.13, embedded in a more widespread domain exhibiting less severe microdamage. A similar microdamage contour is observed at $P = 16{,}400$ lbf., except the localized damage region has nearly proceeded to the fixed boundaries of the panel.

Figure 4.12 shows the shear failure degradation factor D_{II}^m at the splitting load and 16,400 lbf. The shear failure localizes into crack bands that are a single element wide and progress equivalently to the cracks observed in the experiment. At the splitting load (Figure 4.12a), the crack bands have progressed less than half of the way between the notch and the panel boundary on either side of the notch. In Figure 4.12b, the crack bands have nearly reached the fixed grip boundaries. Additionally, Figure 4.12b displays some irregularity in the crack path. In these regions, the mesh is not uniform because it needed to accommodate larger elements used to represent the strain gages (see Figure 3.8). No axial failure was observed in this simulation. The shear crack path was in a state of transverse compressions, and according to the traction-separation relations used in Figure 4.3b, transverse failure does not progress under compressive conditions. Thus, contours of D_I^f and D_I^m are not shown.

4.4.2 Results - Laminate-2

Numerical results for applied load versus displacement of a 4" section of Laminate-2 are presented in Figure 4.13. The experimental ultimate load 15,300 lbf. correlates well (axial failure parameters were calibrated to obtain an ultimate load the most closely matched the experimental data) with the ultimate load obtained from the model, also 15,300 lbf., and is summarized with the splitting load from the Laminate-1 analysis in Table 4.2. The global response up to failure is nearly linear and failure occurs suddenly and catastrophically.

Figure 4.14 compares the applied load versus strain gage results from the model to the data from the experiment. Sg-1 and Sg-2 exhibited similar behavior; the strain increases until the ultimate load is obtained, after which the strain relaxes abruptly. The experimental data and numerical results both display this behavior. The model exhibits slightly more strain, for a given load, prior to ultimate failure. At Sg-3, the model predicts strain localization after the ultimate load is achieved.

The gage data shows a slight reduction in strain as the load drops; however, the gage was placed directly in the crack path and may have been damaged when the panel failed. The model results and experimental data for Sg-4 exhibit similar trends, but the strain gage shows a large degree of nonlinearity at the notch tip. *Bogert et al.* (2006) attributed this observed nonlinearity to local interlaminar stresses near the notch free edge which caused some local delaminations. Since the focus of this work was modeling in-plane damage mechanisms, these effects are not captured; however, the model could be easily extended to incorporate delamination by placing DCZM elements between continuum shell layers [*Satyanarayana et al.* (2007)].

In the experiment, the gages measure the strain over a continuous area associated with the size of the gage, but in the model, the strain is taken at the integration point of an element; thus, these measures should not be expected to correspond exactly. In areas where there are large gradients present, such as near a notch tip (Sg-4) or near cracks (Laminate-1, Sg-2 or Laminate-2, Sg-3), it becomes even more difficult to relate the strain gage data to numerical strains from a discretized continuum. This may contribute to some of the discrepancies between the local gage data and the model results in Figures 4.10 and 4.14.

A photograph taken of the failed, Laminate-2 specimen is presented in Figure 3.18. The photograph shows that two macroscopic cracks initially propagate from the notch tip towards the free edges, perpendicular to the applied load, in a self-similar fashion. Eventually, the cracks turn and proceed towards the free edge at an angle. *Bogert et al.* (2006) claim, supported by visual image correlation displacement data, that there was some eccentricity in the specimen alignment, which resulted in deviation from self similar crack growth.

Normalized microdamage contours just prior to the ultimate load are presented for the outermost 45°, 0°, -45°, and 90° plies in Figure 4.15. Similar microdamage patterns are evident in the 45° and -45° layers. Microdamage propagates outward,

toward the free edge, from the notch tip in petal-like patterns. The microdamage in these layers is highly distributed throughout the plies. The 0° ply displays a more contained microdamage pattern along the lines of the microdamage contours associated with axial splitting shown in Figure 4.11. A moderate level of microdamage is also displayed in the 90° layer, but a low degree of microdamage is distributed throughout most of the layer.

Figure 4.16 shows the axial failure degradation parameter D_I^f at the ultimate load for the four unique layers. A small amount of axial failure in the 45°, 0°, and -45° layers can be observed at the notch tips. It appears that more failure occurs at one notch tip than the other. This can be attributed to numerical imperfections resulting from dissimilar meshes at the opposite notch tips, that is the mesh is not symmetric about the y-axis. No axial failure is observed in the 90° layer. Contours of the transverse, mode I, failure degradation parameter D_I^m at the ultimate load are plotted in Figure 4.17. The failure patterns are similar in the 45° and -45° plies in Figures 4.17a and 4.17c and are comparable to the microdamage contours in Figures 4.15a and 4.15c, except the failure is restricted to regions on either side of the notch. Furthermore, small, highly degraded domains can be observed propagating from the notch tip at an angle corresponding to the fiber direction in the ply. The 90° layer exhibits some moderate degradation in a localized region around the notch tips, and the 0° layer does not exhibit much D_I^m. Contours of the shear, mode II, failure degradation parameter D_{II}^m are presented at the ultimate load in Figure 4.18. Very similar failure paths can be seen in the 45° and -45° layers and the patterns are nearly symmetric across both centerlines of the panel. This is expected because as Figure 4.3c indicates, the sign of the local shear strain does not affect the failure degradation. D_{II}^m in the 0° and 90° is limited to very small regions surrounding the notch tips.

Contours representing the microdamage in the four unique layers are presented in Figure 4.19 after the panel has completely failed and lost all of its load carrying

capability. Although further matrix microdamage evolution is prohibited in elements that have failed (transverse/shear or axial), in the other elements that have not failed, matrix microdamage evolution continues. Nearly the entire 45° and -45° layers reach a microdamage level of $0.18S_r^{max}$. The 0° and 90° plies exhibit similar microdamage patterns; however, low levels of microdamage are more widespread in the 90° ply. Figure 4.20 shows the fiber failure path once the specimen has completely failed. All the layers, except the 90° layer, show self similar cracks propagating from the notch tips towards the free edges of the panel. The angled crack path shown in Figure 3.18 was not reproduced because the eccentric loading (suspected in the test) was not introduced into the simulation; therefore, the crack growth remained self-similar. A high degree of transverse matrix failure can be seen in the axial crack path in the 45°, -45°, and 90° plies in Figure 4.21. In the 0° layer, some transverse failure is observed surrounding the fiber failure, as well as away from the axial failure path, which resulted from a stress wave reflecting off the free edges when the axial crack band reaches the boundary. Finally, D_{II}^m is presented after the specimen has failed in Figure 4.22. Similar failure to Figures 4.18a and 4.18c in the 45° and -45° is exhibited, but a highly degraded region has localized in the axial crack path. Figures 4.22b and 4.22d show fairly extensive regions containing a high degree of shear matrix failure surrounding the axial failure path.

4.5 Conclusions

A thermodynamically-based, work potential theory for damage and failure in composite materials, EST, was developed. A marked distinction between damage and failure was introduced. Damage was considered the evolution of mechanisms that cause structural changes in the material such that the non-linear tangent stiffness tensor remains positive definite. Failure was taken to be the effect of structural changes in the material which result in loss of positive definiteness of the tangent stiffness matrix

and post-peak strain softening. Separate ISVs were used to account for damage and failure mechanisms.

Matrix microdamage, which includes matrix microcracking, shear banding, and microvoid growth, is responsible for all damage in a composite lamina and was accounted for with a single ISV, along the lines of the original ST formulation. The relationship between the transverse and shear moduli of the lamina were related to the ISV through a pair of experimentally obtainable microdamage functions.

Three major, in-plane failure mechanisms were identified: mode I matrix cracks, mode II matrix cracks, and fiber breakage. A failure initiation criterion was used to mark the transition from a damaging continuum to a damaged continuum with an embedded discontinuity. After failure initiation, microdamage evolution ceases and separate ISVs are introduced incorporate the effects of the three major failure mechanisms. Evolution of the failure ISVs is based upon traction-versus separation laws (which are a functions of the appropriate fracture toughness') and a characteristic element length. Typically, the existence of a non-positive definite stiffness tensor would result in pathologically mesh dependent solutions; however in EST, mesh objectivity is ensured by incorporating a characteristic length scale into the failure evolution.

In Section 4.3 mesh objectivity is demonstrated. A unidirectional composite plate with a central hole obeying EST is loaded in transverse tension and the response is calculated using four different, increasingly refined, meshes. The global stress versus strain response remained unaffected by the change in mesh, save for the effects from increased accuracy of local fields in the vicinity of the hole with denser meshing.

Two CNPs, with different lay-ups, composed of T800-3900-2 were tested under tensile loading at NASA LaRC. Global load versus displacement and global load versus local, strain gage strain data was compared to results obtained from an FEM models utilizing EST in Section 4.4. Quantitatively, very good correlation was achieved for both laminates. Furthermore, damage and failure paths predicted by the models

matched the experimental results.

Property	T800/3900-2
X_T	0.021
Y_T	0.0048
Y_C	0.0119
Z	0.0075
G_I^f	1026 $\frac{\text{lbf.-in.}}{\text{in.}^2}$
G_I^m	170.0 $\frac{\text{lbf.-in.}}{\text{in.}^2}$
G_{II}^m	13.54 $\frac{\text{lbf.-in.}}{\text{in.}^2}$

Table 4.1: Failure parameters for T800/3900-2. The transverse and shear parameters were calibrated using the Sg-1 experimental data from Laminate-1. The axial parameters were calibrated using the global load versus displacement data from Laminate-2.

	Type	Experimental	Numerical
Laminate-1	Splitting	8,250 lbf.	8,210 lbf.
Laminate-2	Ultimate	15,300 lbf.	15,300 lbf.

Table 4.2: Critical experimental and simulation loads for Laminate-1 and Laminate-2.

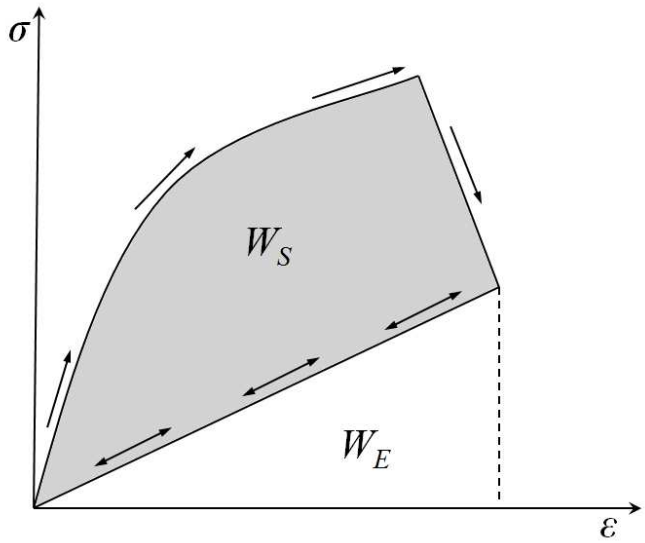

Figure 4.1: Typical stress-strain curve showing the total elastic (W_E) and total dissipated (W_S) potentials.

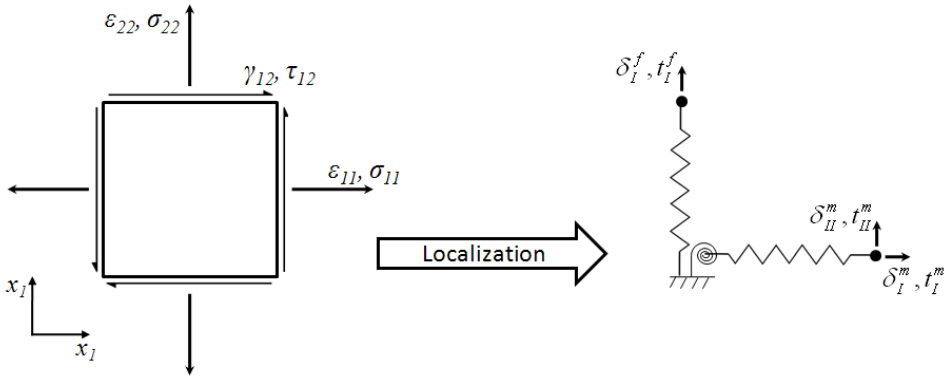

Figure 4.2: Schematic showing the transition form a continuum to a cohesive zone due to the initiation of macroscopic cracks. The essential, constitutive variables switch from stress and strain to traction and separation.

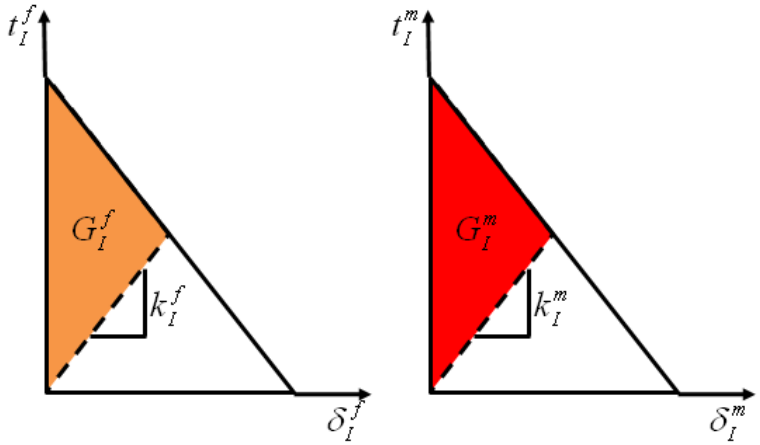

(a) Mode I fiber fracture. (b) Mode I matrix fracture.

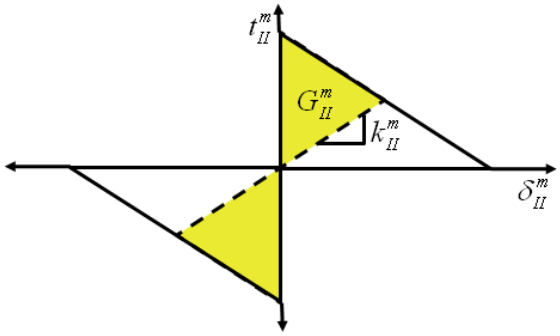

(c) Mode II matrix fracture.

Figure 4.3: Triangular traction versus separation which dictates the behavior of cohesive cracks embedded in the continuum. The total area under the traction-separation law represents the material fracture toughness G_{mC}^j. The area above the unloading line for a given traction-separation state is the strain energy release rate G_m^j.

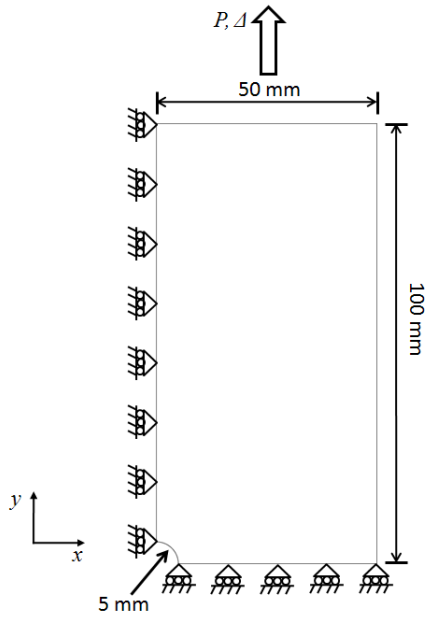

Figure 4.4: Example problem used to demonstrate mesh objectivity of EST. One quarter of a 200 mm x 100 mm containing a central hole with a radius of 5 mm is loaded in tension with symmetric boundary conditions on the bottom and left boundaries.

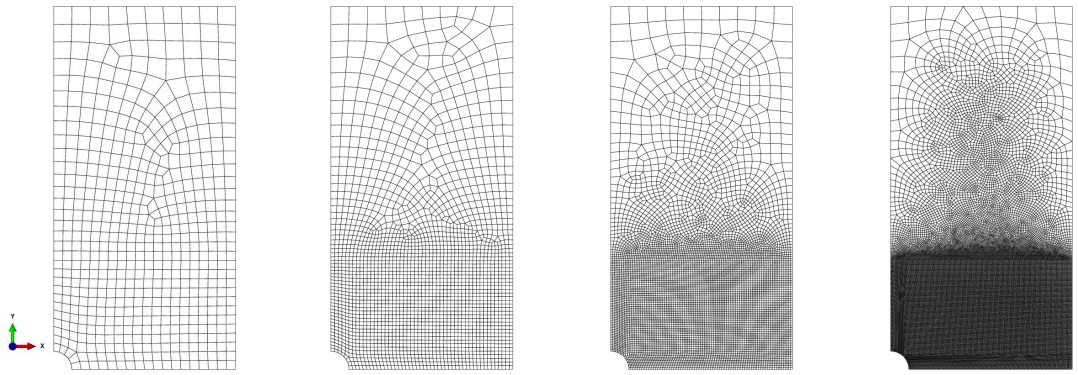

(a) $0.5r_h$. (b) $0.2r_h$. (c) $0.1r_h$. (d) $0.04r_h$.

Figure 4.5: Four mesh densities used to demonstrate the mesh objectivity of EST.

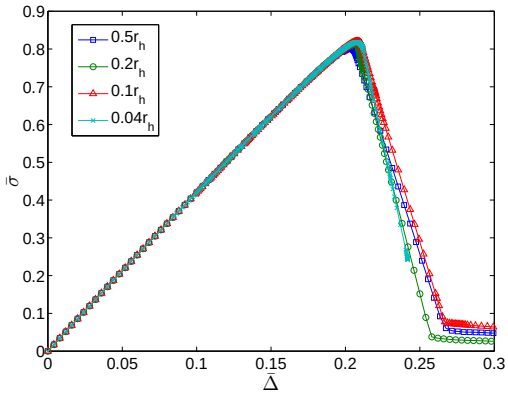

Figure 4.6: Reaction stress normalized by critical axial strain times axial Young's modulus verse applied displacement normalized by hole radius for four different mesh densities.

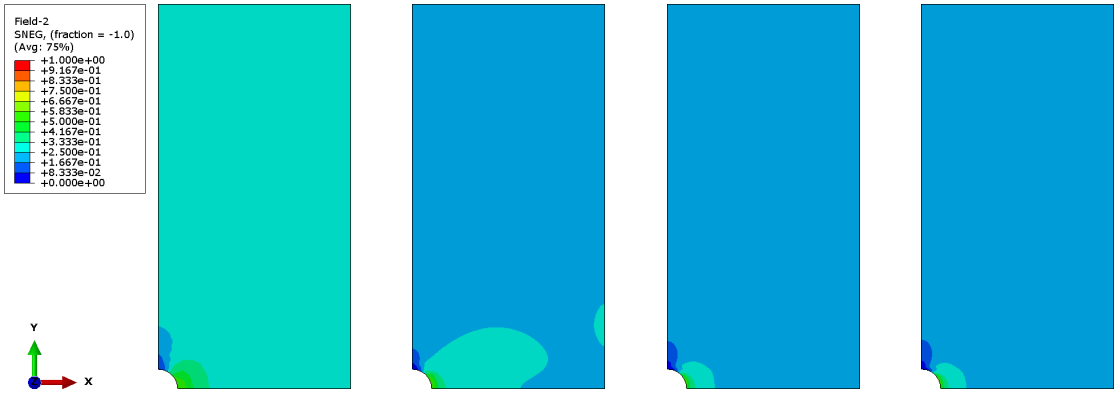

(a) $0.5r_h$, $\bar{\sigma} = 0.50$. (b) $0.2r_h$, $\bar{\sigma} = 0.42$. (c) $0.1r_h$, $\bar{\sigma} = 0.37$. (d) $0.04r_h$, $\bar{\sigma} = 0.36$.

Figure 4.7: Contours of the reduced microdamage ISV S_r, normalized by the maximum S_r obtained from all simulations, immediately prior to failure initiation for four different mesh densities.

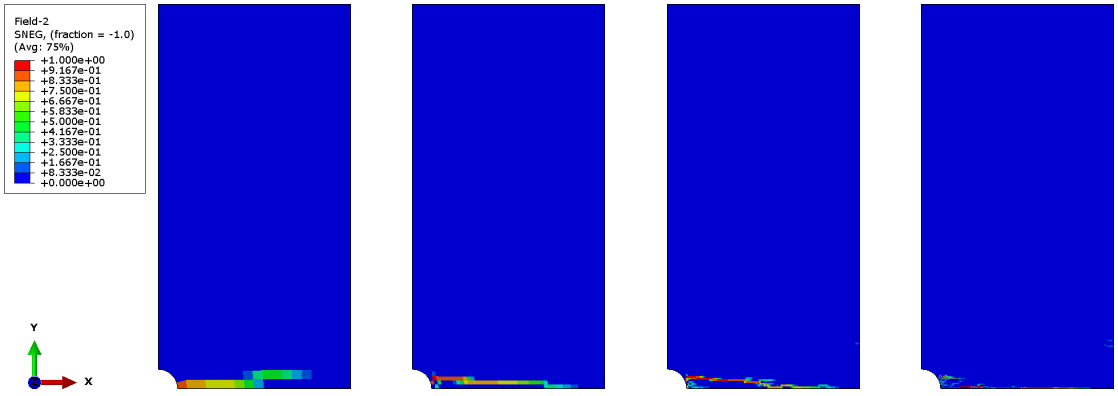

(a) $0.5r_h$, $\bar{\sigma} = 0.80$. (b) $0.2r_h$, $\bar{\sigma} = 0.81$. (c) $0.1r_h$, $\bar{\sigma} = 0.82$. (d) $0.04r_h$, $\bar{\sigma} = 0.82$.

(e) $0.5r_h$, $\bar{\sigma} = 0.030$. (f) $0.2r_h$, $\bar{\sigma} = 0.018$. (g) $0.1r_h$, $\bar{\sigma} = 0.042$. (h) $0.04r_h$, $\bar{\sigma} = 0.242$.

Figure 4.8: Contours of the transverse degradation parameter D_I^m, indicative of the transverse crack path in the specimens. The contours are presented at the ultimate load achieved by the specimens and after the specimens have lost their load carrying capability.

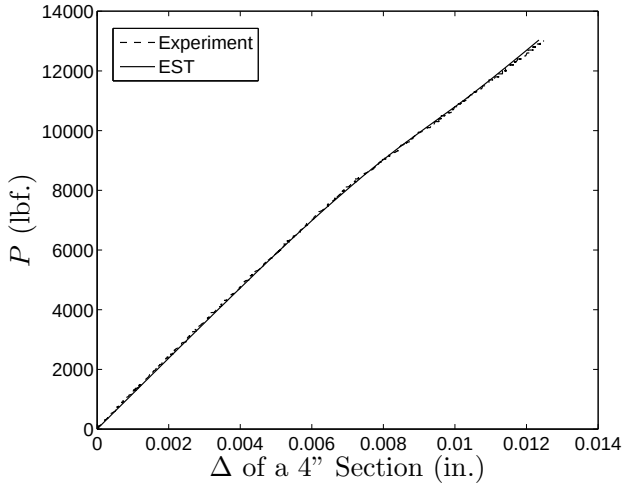

Figure 4.9: Applied load versus displacement of a 4" section for Laminate-1.

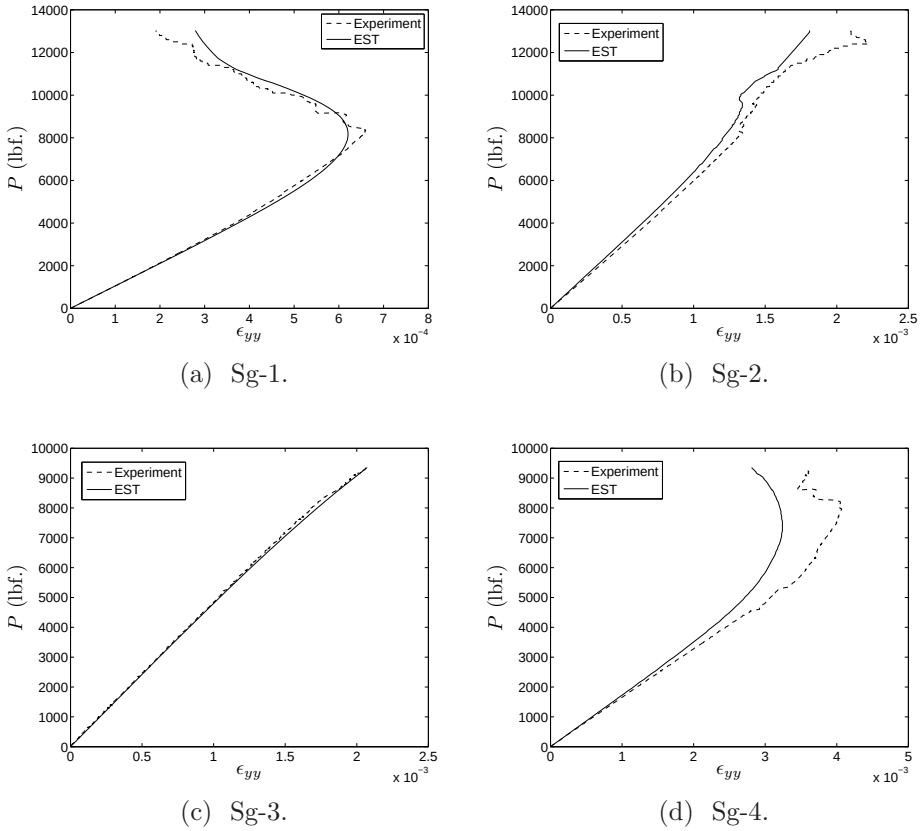

(a) Sg-1. (b) Sg-2.

(c) Sg-3. (d) Sg-4.

Figure 4.10: Applied load versus local strain for Laminate-1.

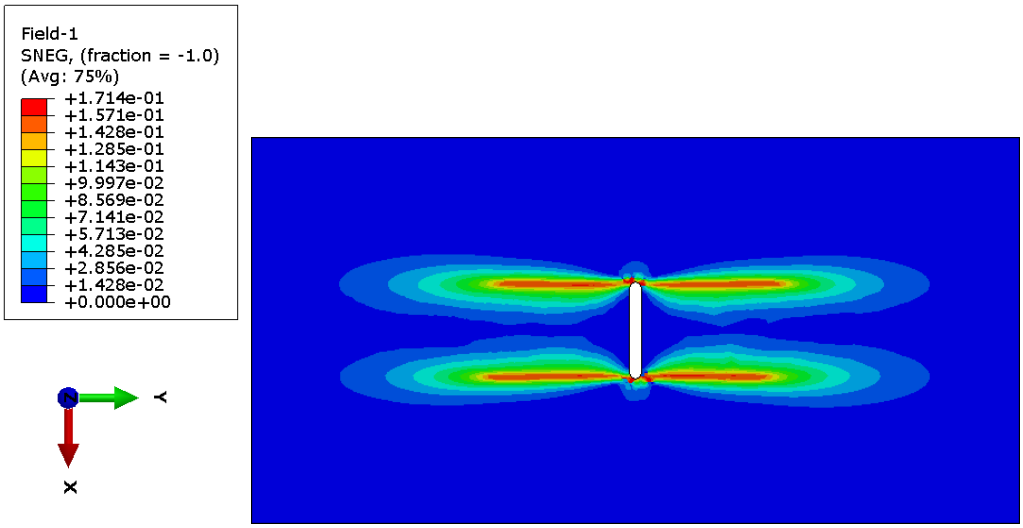

(a) $P = 8{,}210$ lbf.

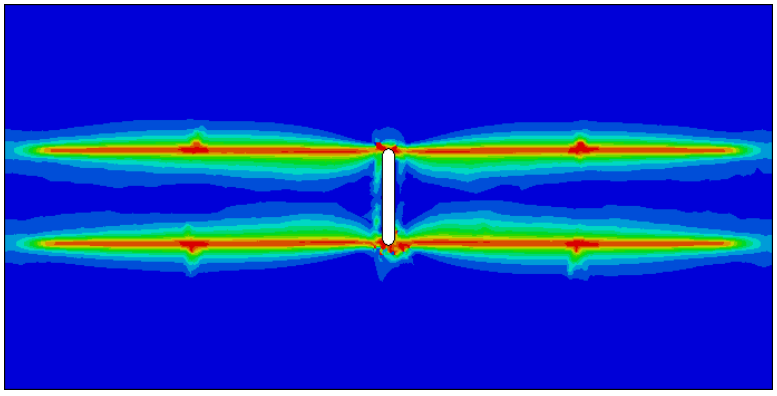

(b) $P = 16{,}400$ lbf.

Figure 4.11: Normalized matrix microdamage contour $\frac{S_r}{S_r^{max}}$ in Laminate-1.

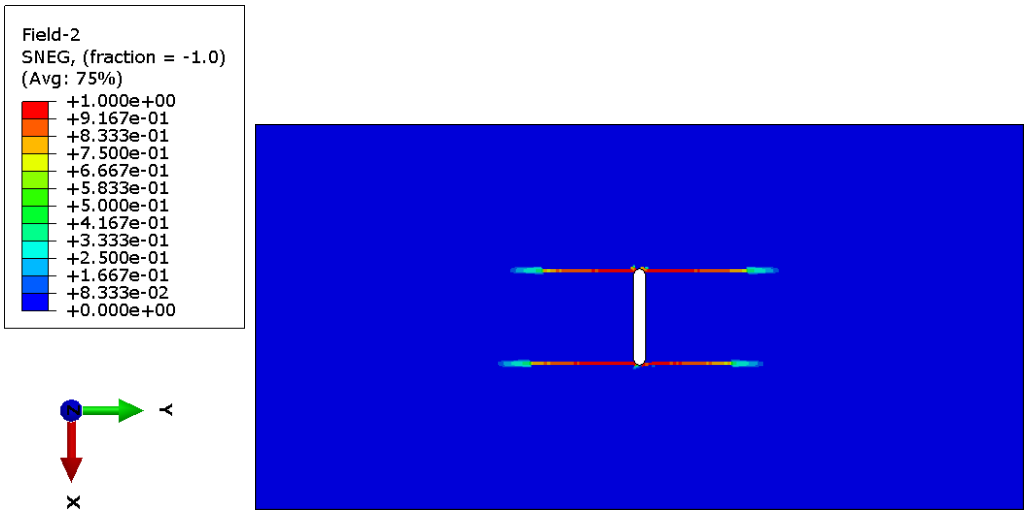

(a) $P = 8{,}210$ lbf.

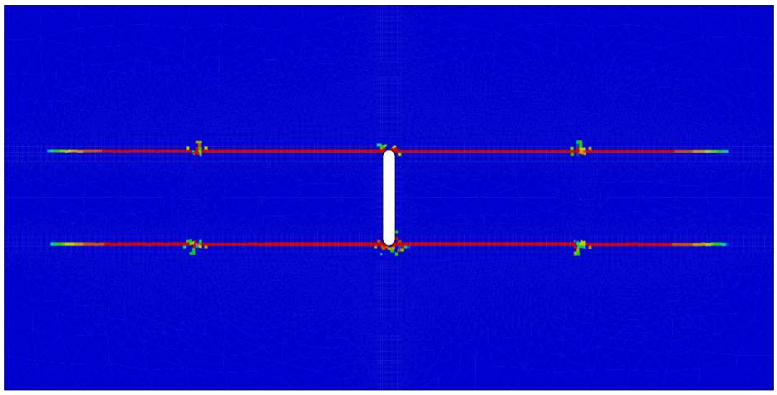

(b) $P = 16{,}400$ lbf.

Figure 4.12: Matrix shear failure degradation D_{II}^m in Laminate-1.

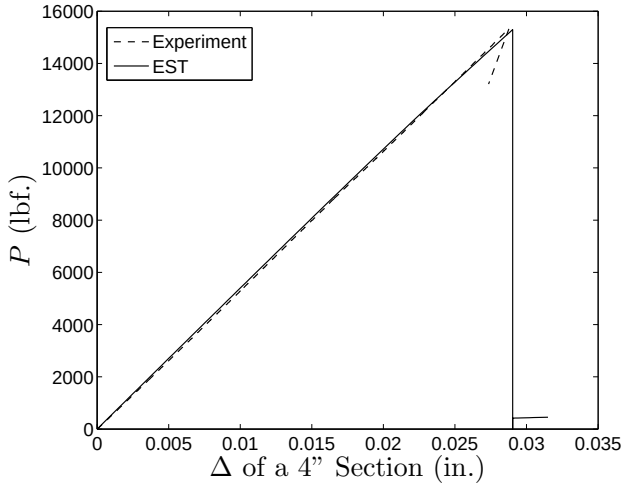

Figure 4.13: Applied load versus displacement of a 4" section for Laminate-2.

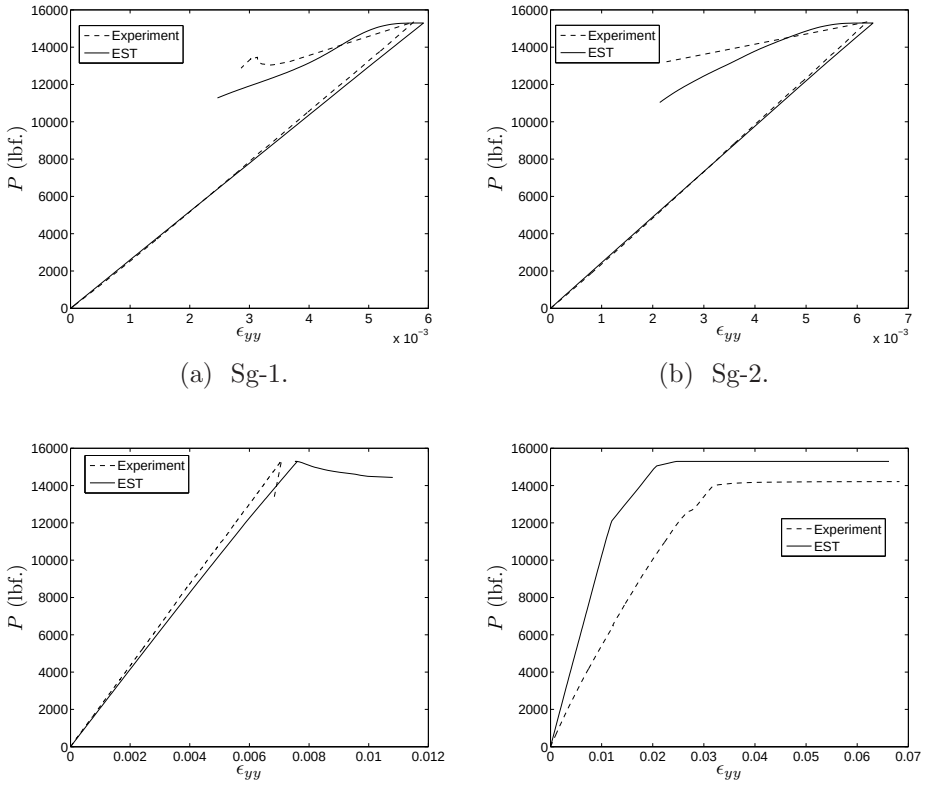

(a) Sg-1. (b) Sg-2.

(c) Sg-3. (d) Sg-4.

Figure 4.14: Applied load versus local strain for Laminate-2.

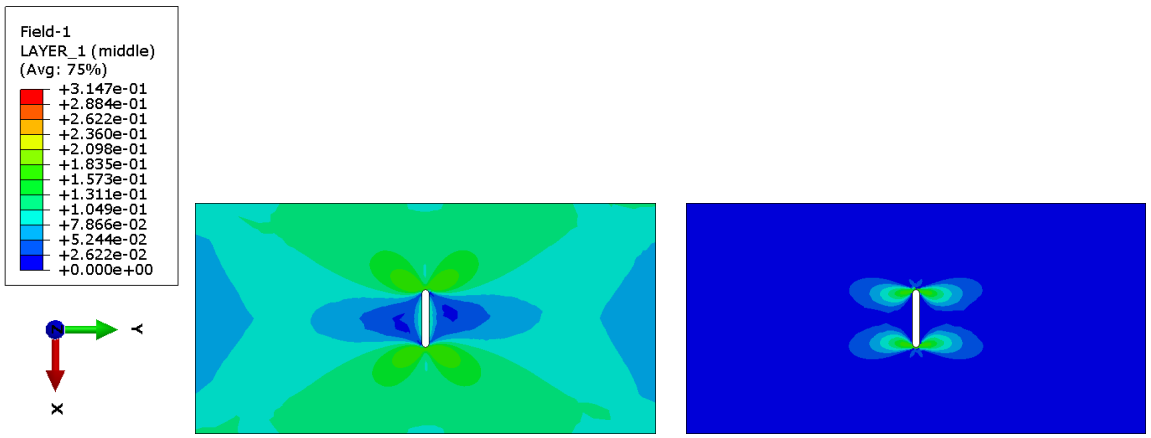

(a) 45° Layer.

(b) 0° Layer.

(c) -45° Layer.

(d) 90° Layer.

Figure 4.15: Normalized matrix microdamage contour $\frac{S_r}{S_r^{max}}$ in Laminate-2 just prior to first axial failure initiation $P = 8{,}640$ lbf.

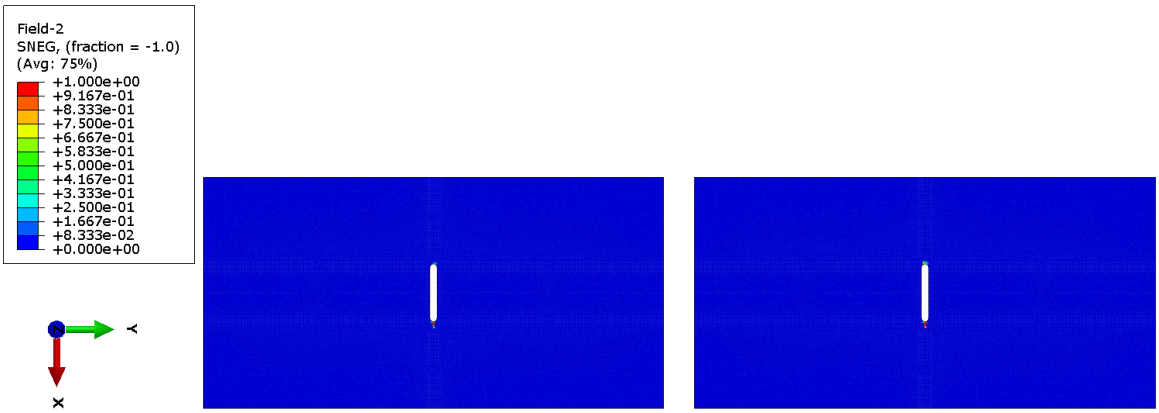

(a) 45° Layer. (b) 0° Layer.

(c) -45° Layer. (d) 90° Layer.

Figure 4.16: Fiber failure degradation D_I^f in Laminate-2 at ultimate load $P = 15{,}300$ lbf.

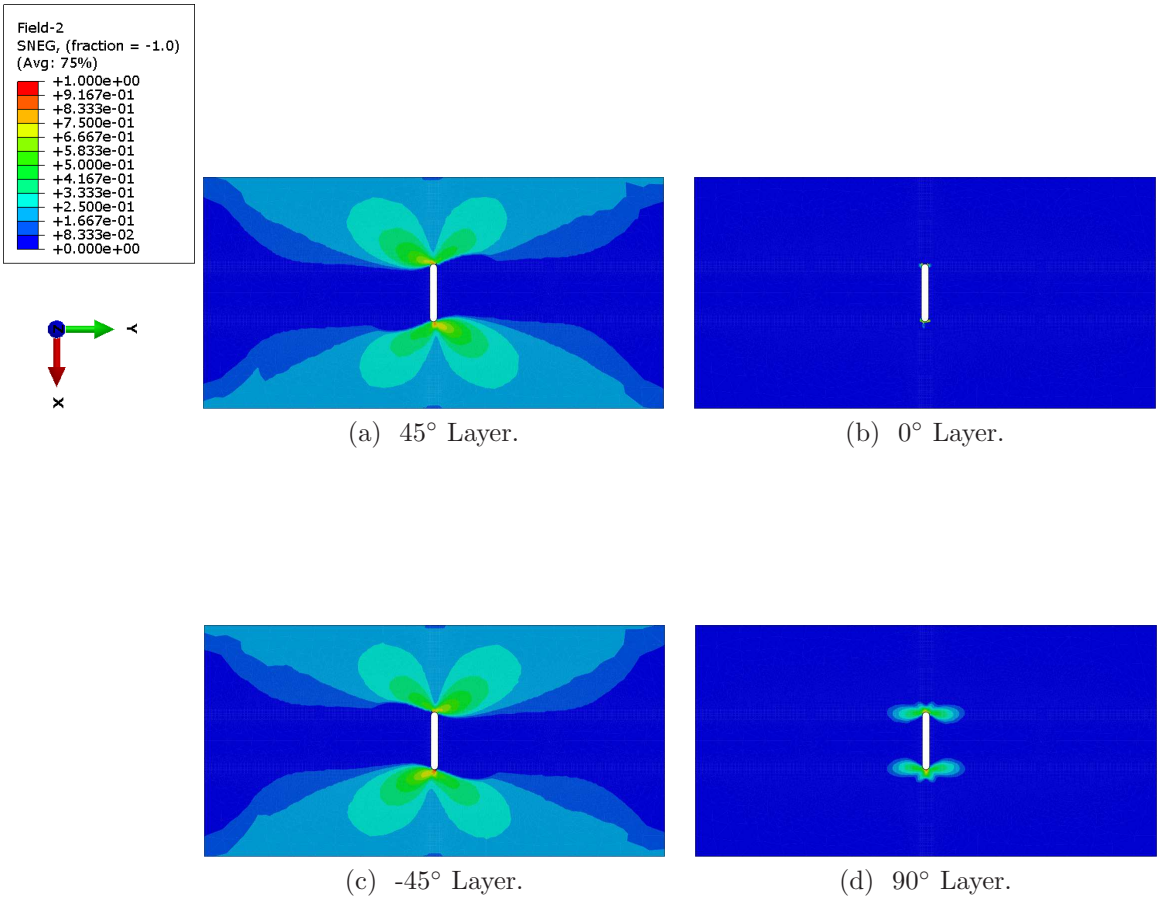

(a) 45° Layer. (b) 0° Layer.

(c) -45° Layer. (d) 90° Layer.

Figure 4.17: Transverse matrix failure degradation D_I^m in Laminate-2 at ultimate load $P = 15{,}300$ lbf.

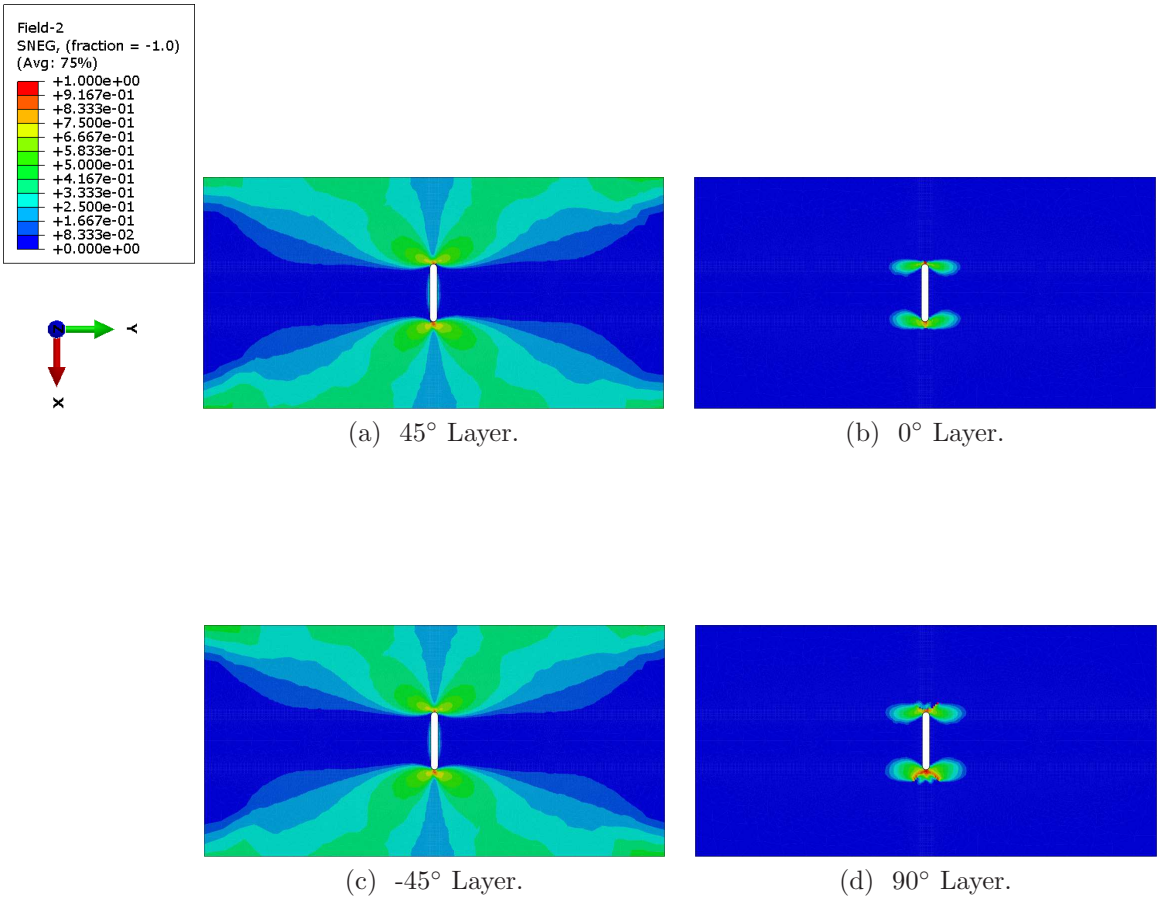

(a) 45° Layer. (b) 0° Layer.

(c) -45° Layer. (d) 90° Layer.

Figure 4.18: Shear matrix failure degradation D_{II}^{m} in Laminate-2 at ultimate load P = 15,300 lbf.

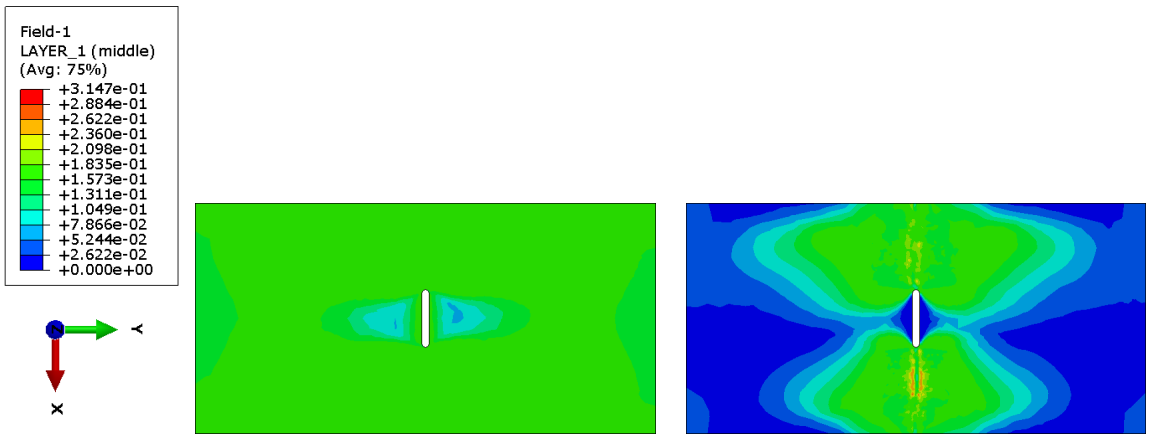

(a) 45° Layer.

(b) 0° Layer.

(c) -45° Layer.

(d) 90° Layer.

Figure 4.19: Normalized matrix microdamage contour $\frac{S_r}{S_r^{max}}$ in Laminate-2 after specimen has lost load carrying capability.

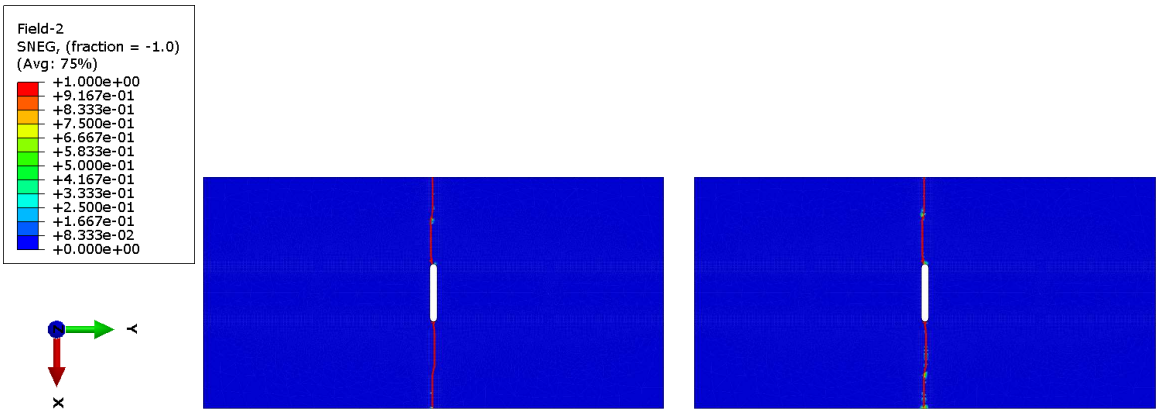

(a) 45° Layer. (b) 0° Layer.

(c) -45° Layer. (d) 90° Layer.

Figure 4.20: Fiber failure degradation D_I^f in Laminate-2 after specimen has lost load carrying capability.

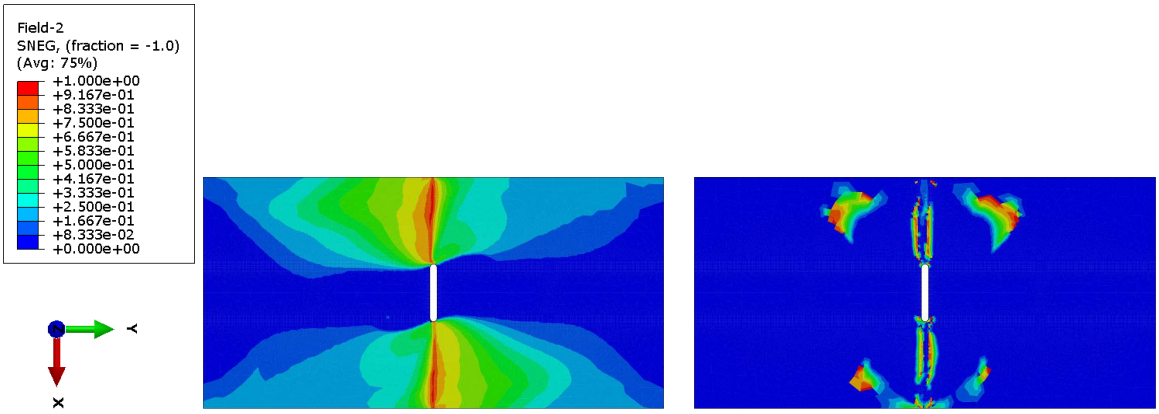

(a) 45° Layer.

(b) 0° Layer.

(c) -45° Layer.

(d) 90° Layer.

Figure 4.21: Transverse matrix failure degradation D_I^m in Laminate-2 after specimen has lost load carrying capability.

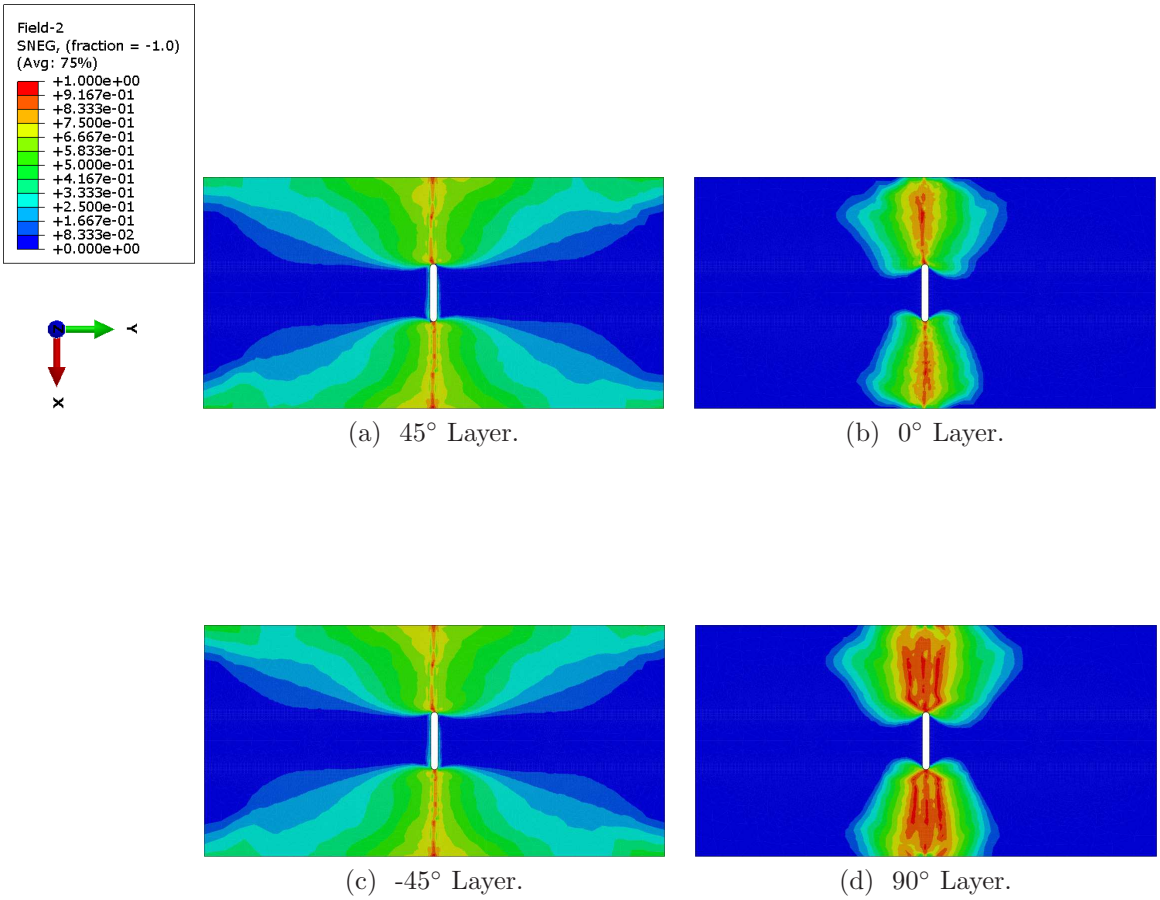

(a) 45° Layer. (b) 0° Layer.

(c) -45° Layer. (d) 90° Layer.

Figure 4.22: Shear matrix failure degradation D_{II}^{m} in Laminate-2 after specimen has lost load carrying capability.

CHAPTER V

Implementation of a Smeared Crack Band Model in a Micromechanics Framework

5.1 Introduction

A multiscale model for progressive damage and failure was developed in Chapter III. One of the shortcomings of the model was the inherent discretization dependent behavior of the model resulting from the post-peak softening degradation scheme that was employed. This issue is addressed in this chapter.

Progressive failure within the subcells of an RUC is modeled using a variation of the crack band model developed by *Bažant and Oh* (1983) for concrete structures. The crack band model uses SERR to dictate the softening behavior of the material; thus, it is completely objective to the discretization of the RUC, beyond that necessary to resolve the local stress and strains accurately.

In this chapter, the focus is restricted to the microscale to evaluate the capabilities of the smeared crack band model to predict progressive failure evolution within a composite microstructure. Thus, a detailed, multiple-fiber RUC is chosen to demonstrate these capabilities. HFGMC is utilized as the micromechanics platform because the level of fidelity required to accurately model detailed failure evolution in a complex microstructure is not provided by GMC.

In Section 5.2 the formulation for HFGMC is given, followed by the implementation of the smeared crack band model in Section 5.3. Two scenarios are considered to determine the mode in which the cracks within the crack band grow. If the principal stress that has the highest magnitude is tensile, it is assumed that it is more energetically favorable for the crack band to form perpendicular to the maximum principal stress and for the cracks within the band to advance under mode I conditions. Conversely, if the magnitude of a compressive principal stress is higher than the other principal stresses, the cracks within the crack band evolve under mode II conditions (due to internal, Mohr-Coulomb friction) and are oriented with the plane of maximum shear stress. In Section 5.4 the objectivity of the post-peak softening behavior of the model with respect to the subcell mesh is shown. An example is presented in Section 5.5 that consists of an RUC composed of 13, randomly placed fibers that is subjected to transverse tension and compression. The model is verified against experimental data in Section 5.6.

The motivation behind the following developments is to arrive at a failure methodology that is capable of accurately capturing localization in a multiscale model without any spurious dependencies. This intention of this chapter is to verify a model for such an application. In Section 5.7 a multiscale methodology is introduced that ensures mesh objectivity and addresses the issues presented by *Bažant* (2007).

5.2 The High-Fidelity Generalized Method of Cells

HFGMC, first introduced by *Aboudi et al.* (2001) resolves some the shortcomings of the original GMC. The biggest of these is the lack of normal-shear coupling in GMC which results from the enforcement of displacement and traction continuity in an average, integral sense and a linear approximation of the displacement fields in each subcell. HFGMC employs quadratic displacement approximations. However, this requires more equations than can be produced using displacement and traction

continuity. Thus, the zeroth, first, and second moments of equilibrium are used to solve the problem. The original, doubly-periodic formulation of HFGMC contained in *Aboudi et al.* (2001) is outlined in this section. The reader is referred to **?** for a more efficient reformulation, as well as the 3D formulation.

5.2.1 Governing Equations

The 3D equilibrium equations for subcell $\beta\gamma$ (see Figure 3.4) in a doubly-periodic RUC (Figure 3.3) are given by

$$\partial_1 \sigma_{1i}^{(\beta\gamma)} + \partial_2 \sigma_{2i}^{(\beta\gamma)} + \partial_3 \sigma_{3i}^{(\beta\gamma)} = 0 \tag{5.1}$$

Since there is no variation in the x_1-direction for a doubly-periodic material, $\partial_1 = \partial/\partial x_1 = 0$. Therefore Equation (5.1) becomes

$$\partial_2 \sigma_{2i}^{(\beta\gamma)} + \partial_3 \sigma_{3i}^{(\beta\gamma)} = 0 \tag{5.2}$$

Averaging Equation (5.2) over the volume of the subcell yields

$$J_{2i(00)}^{(\beta\gamma)} + K_{3i(00)}^{(\beta\gamma)} = 0 \tag{5.3}$$

where

$$J_{2i(00)}^{(\beta\gamma)} = \frac{1}{h_\beta}\left[{}^{(2)}t_i^{+(\beta\gamma)} - {}^{(2)}t_i^{-(\beta\gamma)}\right] \tag{5.4}$$

and

$$K_{3i(00)}^{(\beta\gamma)} = \frac{1}{l_\gamma}\left[{}^{(3)}t_i^{+(\beta\gamma)} - {}^{(3)}t_i^{-(\beta\gamma)}\right] \tag{5.5}$$

The surface tractions are given by

$${}^{(2)}t_i^{\pm(\beta\gamma)} = \frac{1}{l_\gamma}\int_{-l_\gamma/2}^{l_\gamma/2} \sigma_{2i}^{(\beta\gamma)}\left(\bar{x}_2^{(\beta)} = \pm\frac{h_\beta}{2}\right) d\bar{x}_3^{(\gamma)} \tag{5.6}$$

$$ {}^{(3)}t_i^{\pm(\beta\gamma)} = \frac{1}{h_\beta}\int_{-h_\beta/2}^{h_\beta/2} \sigma_{3i}^{(\beta\gamma)} \left(\bar{x}_3^{(\gamma)} = \pm\frac{l_\gamma}{2}\right) d\bar{x}_2^{(\beta)} \tag{5.7} $$

where "(2)" and "(3)" are superscripts that indicate the applicable normal direction to the subcell surface and "±" indicates the sign of the normal. Similarly, the first moment of equilibrium can also be averaged over the subcell volume resulting in

$$ J_{2i(10)}^{(\beta\gamma)} - S_{2i(00)}^{(\beta\gamma)} = 0 \tag{5.8} $$

and

$$ K_{3i(01)}^{(\beta\gamma)} - S_{3i(00)}^{(\beta\gamma)} = 0 \tag{5.9} $$

where $S_{ij(mn)}^{(\beta\gamma)}$ is an average stress quantity, and

$$ J_{2i(10)}^{(\beta\gamma)} = \frac{1}{2}\left[{}^{(2)}t_i^{+(\beta\gamma)} + {}^{(2)}\,t_i^{-(\beta\gamma)}\right] \tag{5.10} $$

$$ K_{3i(01)}^{(\beta\gamma)} = \frac{1}{2}\left[{}^{(3)}t_i^{+(\beta\gamma)} + {}^{(3)}\,t_i^{-(\beta\gamma)}\right] \tag{5.11} $$

$$ S_{ij(mn)}^{(\beta\gamma)} = \frac{1}{h_\beta l_\gamma}\int_{-h_\beta/2}^{h_\beta/2}\int_{-l_\gamma/2}^{l_\gamma/2} \sigma_{ij}^{(\beta\gamma)} (\bar{x}_2^{(\beta)})^m (\bar{x}_3^{(\gamma)})^n d\bar{x}_2^{(\beta)} d\bar{x}_3^{(\gamma)} \tag{5.12} $$

Finally, the second moment of equilibrium can be averaged over the subcell volume, then utilizing integration by parts leads to

$$ \frac{h_\beta^2}{4} J_{2i(00)}^{(\beta\gamma)} + \frac{h_\beta^2}{12} K_{3i(00)}^{(\beta\gamma)} - 2S_{2i(10)}^{(\beta\gamma)} = 0 \tag{5.13} $$

and

$$ \frac{l_\gamma^2}{12} J_{2i(00)}^{(\beta\gamma)} + \frac{l_\gamma^2}{4} K_{3i(00)}^{(\beta\gamma)} - 2S_{3i(01)}^{(\beta\gamma)} = 0 \tag{5.14} $$

Substituting Equations (5.13) and (5.14) into Equation (5.3) gives

$$ J_{2i(00)}^{(\beta\gamma)} = \frac{12}{h_\beta^2} S_{2i(10)}^{(\beta\gamma)} \tag{5.15} $$

$$K^{(\beta\gamma)}_{3i(00)} = \frac{12}{l^2_\gamma} S^{(\beta\gamma)}_{3i(01)} \tag{5.16}$$

Utilizing Equations (5.15) and (5.16) in Equation (5.14):

$$\frac{1}{h^2_\beta} S^{(\beta\gamma)}_{2i(10)} + \frac{1}{l^2_\gamma} S^{(\beta\gamma)}_{3i(01)} = 0 \tag{5.17}$$

Equation (5.17) represents the average form, in HFGMC, of the equilibrium equations, Equation (5.2), of subcell $\beta\gamma$ within a doubly-periodic composite RUC.

5.2.2 Second Order Displacement Approximation

Contrary to GMC, HFGMC employs a quadratic expansion of the subcell displacements

$$\begin{aligned} u^{(\beta\gamma)}_i = \bar{\epsilon}_{ij} x_j + W^{(\beta\gamma)}_{i(00)} + \bar{x}^{(\beta)}_2 W^{(\beta\gamma)}_{i(10)} + \bar{x}^{(\gamma)}_3 W^{(\beta\gamma)}_{i(01)} + \\ \frac{1}{2}\left(3\bar{x}^{(\beta)^2}_2 - \frac{h^2_\beta}{4}\right) W^{(\beta\gamma)}_{i(20)} + \frac{1}{2}\left(3\bar{x}^{(\gamma)^2}_3 - \frac{l^2_\gamma}{4}\right) W^{(\beta\gamma)}_{i(02)} \end{aligned} \tag{5.18}$$

where $\bar{\epsilon}_{ij}$ are, as in GMC, the average global strain components, and $W^{(\beta\gamma)}_{i(mn)}$ are microvariables describing the spatial variation of the displacement field and are determined by enforcing interfacial and periodic conditions.

5.2.3 Constitutive Relations

The local strains in subcell $\beta\gamma$ are related to the global strains and local displacement fields through

$$\epsilon^{(\beta\gamma)}_{ij} = \bar{\epsilon}_{ij} + \frac{1}{2}\left(\partial_i u^{(\beta\gamma)}_j + \partial_j u^{(\beta\gamma)}_i\right) \tag{5.19}$$

Employing the local constitutive law,

$$\sigma^{(\beta\gamma)}_{ij} = C^{(\beta\gamma)}_{ijkl} \epsilon^{(\beta\gamma)}_{kl} \tag{5.20}$$

ignoring plastic and thermal effects (for HFGMC formulation with plasticity and thermal strains please see Ref. [*Aboudi et al.* (2003)]) in Equation (5.12) along with Equations (5.18) and (5.19), the relationship between zeroth order stress components and the microvariables is determined to be:

$$\begin{aligned} S^{(\beta\gamma)}_{11(00)} &= C^{(\beta\gamma)}_{11}\bar{\epsilon}_{11} + C^{(\beta\gamma)}_{12}\left(W^{(\beta\gamma)}_{2(10)} + \bar{\epsilon}_{22}\right) + C^{(\beta\gamma)}_{13}\left(W^{(\beta\gamma)}_{3(01)} + \bar{\epsilon}_{33}\right) \\ &+ C^{(\beta\gamma)}_{14}\left(W^{(\beta\gamma)}_{2(01)} + W^{(\beta\gamma)}_{3(10)} + 2\bar{\epsilon}_{23}\right) + C^{(\beta\gamma)}_{15}\left(W^{(\beta\gamma)}_{1(01)} + 2\bar{\epsilon}_{13}\right) \\ &+ C^{(\beta\gamma)}_{16}\left(W^{(\beta\gamma)}_{1(10)} + 2\bar{\epsilon}_{12}\right) \end{aligned} \tag{5.21}$$

$$\begin{aligned} S^{(\beta\gamma)}_{22(00)} &= C^{(\beta\gamma)}_{12}\bar{\epsilon}_{11} + C^{(\beta\gamma)}_{22}\left(W^{(\beta\gamma)}_{2(10)} + \bar{\epsilon}_{22}\right) + C^{(\beta\gamma)}_{23}\left(W^{(\beta\gamma)}_{3(01)} + \bar{\epsilon}_{33}\right) \\ &+ C^{(\beta\gamma)}_{24}\left(W^{(\beta\gamma)}_{2(01)} + W^{(\beta\gamma)}_{3(10)} + 2\bar{\epsilon}_{23}\right) + C^{(\beta\gamma)}_{25}\left(W^{(\beta\gamma)}_{1(01)} + 2\bar{\epsilon}_{13}\right) \\ &+ C^{(\beta\gamma)}_{26}\left(W^{(\beta\gamma)}_{1(10)} + 2\bar{\epsilon}_{12}\right) \end{aligned} \tag{5.22}$$

$$\begin{aligned} S^{(\beta\gamma)}_{33(00)} &= C^{(\beta\gamma)}_{13}\bar{\epsilon}_{11} + C^{(\beta\gamma)}_{23}\left(W^{(\beta\gamma)}_{2(10)} + \bar{\epsilon}_{22}\right) + C^{(\beta\gamma)}_{33}\left(W^{(\beta\gamma)}_{3(01)} + \bar{\epsilon}_{33}\right) \\ &+ C^{(\beta\gamma)}_{34}\left(W^{(\beta\gamma)}_{2(01)} + W^{(\beta\gamma)}_{3(10)} + 2\bar{\epsilon}_{23}\right) + C^{(\beta\gamma)}_{35}\left(W^{(\beta\gamma)}_{1(01)} + 2\bar{\epsilon}_{13}\right) \\ &+ C^{(\beta\gamma)}_{36}\left(W^{(\beta\gamma)}_{1(10)} + 2\bar{\epsilon}_{12}\right) \end{aligned} \tag{5.23}$$

$$\begin{aligned} S^{(\beta\gamma)}_{44(00)} &= C^{(\beta\gamma)}_{14}\bar{\epsilon}_{11} + C^{(\beta\gamma)}_{24}\left(W^{(\beta\gamma)}_{2(10)} + \bar{\epsilon}_{22}\right) + C^{(\beta\gamma)}_{34}\left(W^{(\beta\gamma)}_{3(01)} + \bar{\epsilon}_{33}\right) \\ &+ C^{(\beta\gamma)}_{44}\left(W^{(\beta\gamma)}_{2(01)} + W^{(\beta\gamma)}_{3(10)} + 2\bar{\epsilon}_{23}\right) + C^{(\beta\gamma)}_{45}\left(W^{(\beta\gamma)}_{1(01)} + 2\bar{\epsilon}_{13}\right) \\ &+ C^{(\beta\gamma)}_{46}\left(W^{(\beta\gamma)}_{1(10)} + 2\bar{\epsilon}_{12}\right) \end{aligned} \tag{5.24}$$

$$\begin{aligned} S^{(\beta\gamma)}_{55(00)} &= C^{(\beta\gamma)}_{15}\bar{\epsilon}_{11} + C^{(\beta\gamma)}_{25}\left(W^{(\beta\gamma)}_{2(10)} + \bar{\epsilon}_{22}\right) + C^{(\beta\gamma)}_{35}\left(W^{(\beta\gamma)}_{3(01)} + \bar{\epsilon}_{33}\right) \\ &+ C^{(\beta\gamma)}_{45}\left(W^{(\beta\gamma)}_{2(01)} + W^{(\beta\gamma)}_{3(10)} + 2\bar{\epsilon}_{23}\right) + C^{(\beta\gamma)}_{55}\left(W^{(\beta\gamma)}_{1(01)} + 2\bar{\epsilon}_{13}\right) \\ &+ C^{(\beta\gamma)}_{56}\left(W^{(\beta\gamma)}_{1(10)} + 2\bar{\epsilon}_{12}\right) \end{aligned} \tag{5.25}$$

$$
\begin{aligned}
S^{(\beta\gamma)}_{66(00)} = {} & C^{(\beta\gamma)}_{16}\bar{\epsilon}_{11} + C^{(\beta\gamma)}_{26}\left(W^{(\beta\gamma)}_{2(10)} + \bar{\epsilon}_{22}\right) + C^{(\beta\gamma)}_{36}\left(W^{(\beta\gamma)}_{3(01)} + \bar{\epsilon}_{33}\right) \\
& + C^{(\beta\gamma)}_{46}\left(W^{(\beta\gamma)}_{2(01)} + W^{(\beta\gamma)}_{3(10)} + 2\bar{\epsilon}_{23}\right) + C^{(\beta\gamma)}_{56}\left(W^{(\beta\gamma)}_{1(01)} + 2\bar{\epsilon}_{13}\right) \\
& + C^{(\beta\gamma)}_{66}\left(W^{(\beta\gamma)}_{1(10)} + 2\bar{\epsilon}_{12}\right)
\end{aligned} \tag{5.26}
$$

where the contracted notation for the stiffness tensor components $C^{(\beta\gamma)}_{ij}$ is used. Similarly the first stress moments are

$$
S^{(\beta\gamma)}_{11(10)} = \frac{h^2_\beta}{4}\left[C^{(\beta\gamma)}_{12}W^{(\beta\gamma)}_{2(20)} + C^{(\beta\gamma)}_{14}W^{(\beta\gamma)}_{3(20)} + C^{(\beta\gamma)}_{16}W^{(\beta\gamma)}_{1(20)}\right] \tag{5.27}
$$

$$
S^{(\beta\gamma)}_{11(01)} = \frac{l^2_\gamma}{4}\left[C^{(\beta\gamma)}_{13}W^{(\beta\gamma)}_{3(02)} + C^{(\beta\gamma)}_{14}W^{(\beta\gamma)}_{2(02)} + C^{(\beta\gamma)}_{15}W^{(\beta\gamma)}_{1(02)}\right] \tag{5.28}
$$

$$
S^{(\beta\gamma)}_{22(10)} = \frac{h^2_\beta}{4}\left[C^{(\beta\gamma)}_{22}W^{(\beta\gamma)}_{2(20)} + C^{(\beta\gamma)}_{24}W^{(\beta\gamma)}_{3(20)} + C^{(\beta\gamma)}_{26}W^{(\beta\gamma)}_{1(20)}\right] \tag{5.29}
$$

$$
S^{(\beta\gamma)}_{22(01)} = \frac{l^2_\gamma}{4}\left[C^{(\beta\gamma)}_{23}W^{(\beta\gamma)}_{3(02)} + C^{(\beta\gamma)}_{24}W^{(\beta\gamma)}_{2(02)} + C^{(\beta\gamma)}_{25}W^{(\beta\gamma)}_{1(02)}\right] \tag{5.30}
$$

$$
S^{(\beta\gamma)}_{33(10)} = \frac{h^2_\beta}{4}\left[C^{(\beta\gamma)}_{23}W^{(\beta\gamma)}_{2(20)} + C^{(\beta\gamma)}_{34}W^{(\beta\gamma)}_{3(20)} + C^{(\beta\gamma)}_{36}W^{(\beta\gamma)}_{1(20)}\right] \tag{5.31}
$$

$$
S^{(\beta\gamma)}_{33(01)} = \frac{l^2_\gamma}{4}\left[C^{(\beta\gamma)}_{33}W^{(\beta\gamma)}_{3(02)} + C^{(\beta\gamma)}_{34}W^{(\beta\gamma)}_{2(02)} + C^{(\beta\gamma)}_{35}W^{(\beta\gamma)}_{1(02)}\right] \tag{5.32}
$$

$$
S^{(\beta\gamma)}_{44(10)} = \frac{h^2_\beta}{4}\left[C^{(\beta\gamma)}_{24}W^{(\beta\gamma)}_{2(20)} + C^{(\beta\gamma)}_{44}W^{(\beta\gamma)}_{3(20)} + C^{(\beta\gamma)}_{46}W^{(\beta\gamma)}_{1(20)}\right] \tag{5.33}
$$

$$
S^{(\beta\gamma)}_{55(01)} = \frac{l^2_\gamma}{4}\left[C^{(\beta\gamma)}_{35}W^{(\beta\gamma)}_{3(02)} + C^{(\beta\gamma)}_{45}W^{(\beta\gamma)}_{2(02)} + C^{(\beta\gamma)}_{55}W^{(\beta\gamma)}_{1(02)}\right] \tag{5.34}
$$

$$
S^{(\beta\gamma)}_{66(10)} = \frac{h^2_\beta}{4}\left[C^{(\beta\gamma)}_{26}W^{(\beta\gamma)}_{2(20)} + C^{(\beta\gamma)}_{46}W^{(\beta\gamma)}_{3(20)} + C^{(\beta\gamma)}_{66}W^{(\beta\gamma)}_{1(20)}\right] \tag{5.35}
$$

$$
S^{(\beta\gamma)}_{66(01)} = \frac{l^2_\gamma}{4}\left[C^{(\beta\gamma)}_{36}W^{(\beta\gamma)}_{3(02)} + C^{(\beta\gamma)}_{46}W^{(\beta\gamma)}_{2(02)} + C^{(\beta\gamma)}_{56}W^{(\beta\gamma)}_{1(02)}\right] \tag{5.36}
$$

5.2.4 Displacement Continuity

The unknown microvariables (the volume-averaged displacement vector $W^{(\beta\gamma)}_{i(00)}$ and the higher order terms $W^{(\beta\gamma)}_{i(mn)}$) can be calculated from the governing equation, Equation (5.17), subcell interfacial continuity conditions, and periodicity conditions.

The periodic boundary conditions for an RUC are given by

$$u_i|_{x_2=0} = u_i|_{x_2=H} \tag{5.37}$$

$$\sigma_{2i}|_{x_2=0} = \sigma_{2i}|_{x_2=H} \tag{5.38}$$

$$u_i|_{x_3=0} = u_i|_{x_3=L} \tag{5.39}$$

$$\sigma_{3i}|_{x_3=0} = \sigma_{3i}|_{x_3=L} \tag{5.40}$$

The displacement continuity conditions are enforced, as in GMC, in an average (integral) sense, yielding:

$$\int_{-l_\gamma/2}^{l_\gamma/2} \left[u_i^{(1\gamma)}\Big|_{\bar{x}_2^{(1)}=-h_1/2} \right] d\bar{x}_3^{(\gamma)} = \int_{-l_\gamma/2}^{l_\gamma/2} \left[u_i^{(N_\beta\gamma)}\Big|_{\bar{x}_2^{(N_\beta)}=h_{N_\beta}/2} \right] d\bar{x}_3^{(\gamma)}, \quad \gamma = 1, \ldots, N_\gamma \tag{5.41}$$

$$\int_{-h_\beta/2}^{h_\beta/2} \left[u_i^{(\beta 1)}\Big|_{\bar{x}_3^{(1)}=-l_1/2} \right] d\bar{x}_2^{(\beta)} = \int_{-h_\beta/2}^{h_\beta/2} \left[u_i^{(\beta N_\gamma)}\Big|_{\bar{x}_3^{(N_\gamma)}=l_{N_\gamma}/2} \right] d\bar{x}_2^{(\beta)}, \quad \beta = 1, \ldots, N_\beta \tag{5.42}$$

Using the definition of the subcell displacements, Equation (5.18), in the average displacement continuity conditions, Equations (5.41) and (5.42), gives:

$$W_{i(00)}^{(1\gamma)} - \frac{h_1}{2} W_{i(10)}^{(1\gamma)} - \frac{h_1^2}{4} W_{i(20)}^{(1\gamma)} = W_{i(00)}^{(N_\beta\gamma)} - \frac{h_{N_\beta}}{2} W_{i(10)}^{(N_\beta\gamma)} - \frac{h_{N_\beta}^2}{4} W_{i(20)}^{(N_\beta\gamma)}, \quad \gamma = 1, \ldots, N_\gamma \tag{5.43}$$

$$W_{i(00)}^{(\beta 1)} - \frac{l_1}{2} W_{i(01)}^{(\beta 1)} - \frac{l_1^2}{4} W_{i(02)}^{(\beta 1)} = W_{i(00)}^{(\beta N_\gamma)} - \frac{l_{N_\gamma}}{2} W_{i(01)}^{(\beta N_\gamma)} - \frac{l_{N_\gamma}^2}{4} W_{i(02)}^{(\beta N_\gamma)}, \quad \beta = 1, \ldots, N_\beta \tag{5.44}$$

Equations (5.43) and (5.44) represent the displacement continuity conditions necessary to enforce periodicity of the RUC. Similar relations can be derived to enforce

displacement continuity across adjacent subcell boundaries,

$$W_{i(00)}^{(\beta\gamma)} + \frac{h_\beta}{2} W_{i(10)}^{(\beta\gamma)} + \frac{h_\beta^2}{4} W_{i(20)}^{(\beta\gamma)} = W_{i(00)}^{(\beta+1\gamma)} + \frac{h_{\beta+1}}{2} W_{i(10)}^{(\beta+1\gamma)} + \frac{h_{\beta+1}^2}{4} W_{i(20)}^{(\beta+1\gamma)}, \quad \beta = 1, \ldots, N_\beta - 1, \quad \gamma = 1, \ldots, N_\gamma \tag{5.45}$$

$$W_{i(00)}^{(\beta\gamma)} + \frac{l_\gamma}{2} W_{i(01)}^{(\beta\gamma)} + \frac{l_\gamma^2}{4} W_{i(02)}^{(\beta\gamma)} = W_{i(00)}^{(\beta\gamma+1)} + \frac{l_{\gamma+1}}{2} W_{i(01)}^{(\beta\gamma+1)} + \frac{l_{\gamma+1}^2}{4} W_{i(02)}^{(\beta\gamma+1)}, \quad \beta = 1, \ldots, N_\beta, \quad \gamma = 1, \ldots, N_\gamma - 1 \tag{5.46}$$

Note that Equations (5.43)-(5.44) can be relaxed to incorporate the effects of local, interfacial debonding [*Bednarcyk et al.* (2004)].

5.2.5 Traction Continuity

Using Equations (5.6) and (5.7), the average implementation of the stress periodicity conditions (Equations (5.38) and (5.40)) is

$${}^{(2)}t_i^{+(1\gamma)} = {}^{(2)}\, t_i^{+(N_\beta\gamma)}, \quad \gamma = 1, \ldots, N_\gamma \tag{5.47}$$

$${}^{(3)}t_i^{+(\beta 1)} = {}^{(3)}\, t_i^{+(\beta N_\gamma)}, \quad \beta = 1, \ldots, N_\beta \tag{5.48}$$

Using Equations (5.4) and (5.5) with Equations (5.10) and (5.11) gives

$${}^{(2)}t_i^{\pm(\beta\gamma)} = J_{2i(10)}^{(\beta\gamma)} \pm \frac{h_\beta}{2} J_{2i(00)}^{(\beta\gamma)}, \quad \beta = 1, \ldots, N_\beta, \quad \gamma = 1, \ldots, N_\gamma \tag{5.49}$$

$${}^{(3)}t_i^{\pm(\beta\gamma)} = K_{3i(01)}^{(\beta\gamma)} \pm \frac{l_\gamma}{2} K_{3i(00)}^{(\beta\gamma)}, \quad \beta = 1, \ldots, N_\beta, \quad \gamma = 1, \ldots, N_\gamma \tag{5.50}$$

Substituting Equations (5.8), (5.9), (5.15), and (5.16)

$${}^{(2)}t_i^{\pm(\beta\gamma)} = S_{2i(00)}^{(\beta\gamma)} \pm \frac{6}{h_\beta} S_{2i(10)}^{(\beta\gamma)}, \quad \beta = 1, \ldots, N_\beta, \quad \gamma = 1, \ldots, N_\gamma \tag{5.51}$$

$$^{(3)}t_i^{\pm(\beta\gamma)} = S_{3i(00)}^{(\beta\gamma)} \pm \frac{6}{l_\gamma} S_{3i(01)}^{(\beta\gamma)}, \quad \beta = 1, \ldots, N_\beta, \quad \gamma = 1, \ldots, N_\gamma \tag{5.52}$$

Thus, the average stress periodicity conditions, Equations (5.47) and (5.48), become

$$S_{2i(00)}^{(1\gamma)} - \frac{6}{h_1} S_{2i(10)}^{(1\gamma)} = S_{2i(00)}^{(N_\beta\gamma)} - \frac{6}{h_{N_\beta}} S_{2i(10)}^{(N_\beta\gamma)}, \quad \gamma = 1, \ldots, N_\gamma \tag{5.53}$$

$$S_{3i(00)}^{(\beta 1)} - \frac{6}{l_1} S_{3i(01)}^{(\beta 1)} = S_{3i(00)}^{(\beta N_\gamma)} - \frac{6}{l_{N_\gamma}} S_{3i(01)}^{(\beta N_\gamma)}, \quad \beta = 1, \ldots, N_\beta \tag{5.54}$$

Equations (5.53) and (5.54) represent the stress continuity conditions at the boundaries of the RUC necessary to enforce periodicity. Similarly, traction continuity between adjacent subcells is given by:

$$S_{2i(00)}^{(\beta\gamma)} - \frac{6}{h_\beta} S_{2i(10)}^{(\beta\gamma)} = S_{2i(00)}^{(\beta+1\gamma)} - \frac{6}{h_{\beta+1}} S_{2i(10)}^{(\beta+1\gamma)}, \quad \beta = 1, \ldots, N_\beta - 1, \quad \gamma = 1, \ldots, N_\gamma \tag{5.55}$$

$$S_{3i(00)}^{(\beta\gamma)} - \frac{6}{l_\gamma} S_{3i(01)}^{(\beta\gamma)} = S_{3i(00)}^{(\beta\gamma+1)} - \frac{6}{l_{\gamma+1}} S_{3i(01)}^{(\beta\gamma+1)}, \quad \beta = 1, \ldots, N_\beta, \quad \gamma = 1, \ldots, N_\gamma - 1 \tag{5.56}$$

5.2.6 Summary of Global Equations

The number of unknown microvariables in the displacement expansion, Equation (5.18), is $15N_\beta N_\gamma$. The governing equations, Equation (5.17) provide $3N_\beta N_\gamma$ relations for the unknown microvariables while Equations (5.43) and (5.44) provide $3(N_\beta + N_\gamma)$ relations, Equations (5.45) and (5.46) provide $3[(N_\beta - 1)N_\gamma + N_\beta(N_\gamma - 1)]$ relations, Equations (5.53) and (5.54) provide $3(N_\beta + N_\gamma)$ relations, and Equations (5.55) and (5.56) provide $3[(N_\beta - 1)N_\gamma + N_\beta(N_\gamma - 1)]$ relations, which yields a total of $15N_\beta N_\gamma$ linear equations for the unknown microvariables.

This system of equations can be expressed as

$$\mathbf{KU} = \mathbf{f} \tag{5.57}$$

where $\mathbf{K}$, the structural stiffness matrix, contains geometric and mechanical constitutive information from each of the subcells in the RUC. The displacement vector $\mathbf{U}$ contains the unknown displacement microvariables for each subcell.

$$\mathbf{U} = [\mathbf{U}^{(\mathbf{11})}, \ldots, \mathbf{U}^{(\mathbf{N}_\beta \mathbf{N}_\gamma)}] \tag{5.58}$$

and

$$\mathbf{U}^{(\beta\gamma)} = [\mathbf{W}^{(\beta\gamma)}_{(\mathbf{00})}, \mathbf{W}^{(\beta\gamma)}_{(\mathbf{10})}, \mathbf{W}^{(\beta\gamma)}_{(\mathbf{01})}, \mathbf{W}^{(\beta\gamma)}_{(\mathbf{20})}, \mathbf{W}^{(\beta\gamma)}_{(\mathbf{02})}] \tag{5.59}$$

where the vectors $\mathbf{W}^{(\beta\gamma)}_{(\mathbf{mn})}$ contain the three components of that displacement microvariable for that particular subcell

$$\mathbf{W}^{(\beta\gamma)}_{(\mathbf{mn})} = \left[W^{(\beta\gamma)}_{1(mn)}, W^{(\beta\gamma)}_{2(mn)}, W^{(\beta\gamma)}_{3(mn)}\right] \tag{5.60}$$

The force vector $\mathbf{f}$ contains details of the applied average strains $\bar{\epsilon}_{ij}$. To prevent rigid body motion, the displacement of the corners of the RUC are pinned and those equations are eliminated from Equation (5.57).

Solving Equation (5.57) yields a strain concentration matrix that relates the local, average subcell strains to the global, applied, average strains.

$$\bar{\boldsymbol{\epsilon}}^{(\boldsymbol{\beta\gamma})} = \mathbf{A}^{(\beta\gamma)}_{\mathbf{HF}} \bar{\boldsymbol{\epsilon}} \tag{5.61}$$

Once the local strains are obtained, the local stresses are readily determined through the local constitutive laws, Equation (5.20). The average global stresses are simply the volume average of the local stresses.

$$\bar{\boldsymbol{\sigma}} = \frac{1}{HL} \sum_{\beta=1}^{N_\beta} \sum_{\gamma=1}^{N_\gamma} h_\beta l_\gamma \bar{\boldsymbol{\sigma}}^{(\boldsymbol{\beta\gamma})} \tag{5.62}$$

where $\bar{\boldsymbol{\sigma}}^{(\boldsymbol{\beta\gamma})}$ are the average subcell stresses.

The global, composite constitutive relationship is taken to be

$$\bar{\boldsymbol{\sigma}} = \boldsymbol{C}^{*}\bar{\boldsymbol{\epsilon}} \tag{5.63}$$

Thus, the effective elastic stiffness matrix for the composite is given by substituting Equations (5.61) and (5.62) into Equation (5.63).

$$\mathbf{C}^{*} = \frac{1}{HL}\sum_{\beta=1}^{N_\beta}\sum_{\gamma=1}^{N_\gamma} h_\beta l_\gamma \mathbf{C}^{(\beta\gamma)}\mathbf{A}_{\mathbf{HF}}^{(\beta\gamma)} \tag{5.64}$$

It should be noted that HFGMC was reformulated using the displacement continuity conditions to reduce the overall number of unknown microvariables, thus reducing computer memory requirements and computational cost. The reader is referred to [*Bansal and Pindera* (2004); *Aboudi et al.* (2012)] for details on this reformulation.

5.3 Modeling Constituent-Level Post-Peak Strain Softening with the Smeared Crack Band Approach

HFGMC is an efficient, useful tool for modeling intricate details of the microstructure of a composite material. Additionally, it is readily amenable for implementation into a multiscale framework. Although, physics-based, discretization objective, progressive failure constitutive models must be in place for the constituents of the composite to accurately predict the response of a structure that is a damaging. For pre-peak loading (i.e. positive-definite tangent stiffness tensor), there are a multitude of non-linear elasticity, plasticity, continuum damage mechanics, and visoelastic/plastic theories available that can predict the evolution of the appropriate mechanisms in the composite. However when the local fields enter the post-peak regime of the stress-strain laws, most of these theories breakdown in a numerical setting and display pathological mesh dependence [*Bažant and Cedolin* (1979); *Pietruszczak and Mroz*

(1981)]. See Chapter I, Section 1.2.2 for more on pathological mesh dependence.

A simple way to remedy this non-physical behavior in a numerical setting is to judiciously scale the post-peak softening slope of the stress-strain constitutive law. Then, the failure energy density dissipated becomes a function of the characteristic length of discretized continuum. *Bažant* (1982); *Bažant and Oh* (1983) first proposed a crack band model in which post-peak softening damage (herein referred to as failure) in the material was assumed to occur within a band. The post-peak slope of the material constitutive law was scaled by the characteristic length of the finite element exhibiting failure; such that, the total strain energy release rate in the element, upon reaching a state of zero stress, and the material fracture toughness were coincident. In this reference, equivalence between this smeared crack approach and a line crack approach is presented. Subsequently, *Bažant and Cedolin* (1983) exhibited propagation of a crack band not aligned with the mesh bias. In this chapter, the crack band model is implemented within the HFGMC framework, in the MAC/GMC suite of micromechanics codes developed at the NASA Glenn Research Center [*Bednarcyk and Arnold* (2002b,c)], and used to analyze crack band growth in composite RUCs. The following subsections provide theoretical details on the crack band model.

5.3.1 Physical Behavior of Crack band

The smeared crack band model is meant to capture the behavior of a region of a material wherein numerous microcracks have initiated and now coalesce to form a larger crack. Figure 5.2 displays a crack band of width w_c embedded in a continuum. The domain of the crack band is denoted as Ω' and the remaining continuum as Ω. The crack band is oriented within the continuum such that, for a given point within the crack band, the unit vector normal to the crack band is $\boldsymbol{n}$.

The total energy dissipated during the failure process is dissipated over Ω', and the size w_c of Ω' is a material property directly related to the material fracture toughness

[*Bažant and Oh* (1983)].

$$w_c = \frac{2\mathcal{G}_C}{\sigma_C^2}\left(\frac{1}{E} - \frac{1}{E_T}\right)^{-1} \tag{5.65}$$

where σ_C is the critical stress for initiation of the post-peak regime in the 1D material stress-strain law (given in Figure 5.3a), and E_T is the negative tangent slope in that regime. The fracture toughness $\mathcal{G}_C$, or critical strain energy release rate, of the material is given by the area under the 1D traction-separation law (Figure 5.3b) which governs the cohesive response of the separation of crack faces as a crack propagates in the material. The energy density dissipated during failure W_F is related to the material fracture toughness by the characteristic length in the material.

$$\mathcal{G}_C = w_c W_F \tag{5.66}$$

5.3.2 Numerical Implementation of Crack Band Model in GMC/HFGMC

The crack band model is implemented in the HFGMC micromechanical framework. The local subcell fields are used to govern crack brand evolution in the constituents of the composite. Figure 5.4 shows the discretization of the continuum displayed in Figure 5.2. A magnified view of the crack band embedded in a single subcell is also displayed in Figure 5.4. Since the all of the energy dissipated in the crack band is smeared over the subcell volume, the subcell must be large enough to contain the crack band of width w_C. Note that Figure 5.4 shows a 2D geometry for illustrative purposes, but the crack bands can also evolve in a general 3D space.

5.3.2.1 Mode I Crack Band Growth Under Tensile Principal Stress

The orientation of the crack band in subcell $\beta\gamma$ is given by the vector $\boldsymbol{n_1^{(\beta\gamma)}}$ (see Figure 5.4) and is determined from the local principal stress state $(\bar{\sigma}_1^{(\beta\gamma)}, \bar{\sigma}_2^{(\beta\gamma)}, \bar{\sigma}_3^{(\beta\gamma)})$. In a monolithic material, cracks orient such that the crack tips are always subjected to pure mode I (opening mode) conditions unless there are constraints that

limit the crack orientation. In a micromechanical analysis the composite material is composed of separate, monolithic constituents; thus, in the matrix, the crack band runs perpendicular to $\bar{\sigma}_1^{(\beta\gamma)}$, the principal stress with the largest magnitude, $|\bar{\sigma}_1^{(\beta\gamma)}| > |\bar{\sigma}_2^{(\beta\gamma)}| > |\bar{\sigma}_3^{(\beta\gamma)}|$, if $\bar{\sigma}_1^{(\beta\gamma)} \geq 0$ (tensile). Under these conditions, a crack oriented as such, is subjected to pure mode I loading, locally. Although, the resulting global behavior may appear to be mixed mode because of the influence of the fibers on the matrix crack band path. Crack orientation and evolution is determined differently if $\bar{\sigma}_1^{(\beta\gamma)} < 0$ as described in 5.3.2.2. The characteristic length of the subcell $l_C^{(\beta\gamma)}$ is determined as the dimension of the subcell running parallel to $\boldsymbol{n_1^{(\beta\gamma)}}$. Crack band initiation is determined using a very simple, but physical, maximum stress criterion.

$$\frac{\bar{\sigma}_1^{(\beta\gamma)}}{\sigma_C^{(\beta\gamma)}} = 1, \qquad \bar{\sigma}_1^{(\beta\gamma)} \geq 0 \tag{5.67}$$

where $\sigma_C^{(\beta\gamma)}$ is the cohesive strength of the crack band. Once the crack band has initiated, the crack band orientation is fixed as time evolves.

Once the crack band orientation has been calculated, the subcell compliance is rotated into the principle frame using the transformation matrix.

$$\boldsymbol{T} = [\boldsymbol{n_1^{(\beta\gamma)}} \boldsymbol{n_2^{(\beta\gamma)}} \boldsymbol{n_3^{(\beta\gamma)}}][\boldsymbol{e_1} \boldsymbol{e_2} \boldsymbol{e_3}] \tag{5.68}$$

where $\boldsymbol{n_1^{(\beta\gamma)}}$, $\boldsymbol{n_2^{(\beta\gamma)}}$, and $\boldsymbol{n_3^{(\beta\gamma)}}$ are the principal stress directions, and $\boldsymbol{e_1}$, $\boldsymbol{e_2}$, and $\boldsymbol{e_3}$ are the unit basis vectors. All material degradation due to crack band evolution is imposed on the rotated compliance $\bar{\boldsymbol{S}}^{(\beta\gamma)}$, the components of which are given by:

$$\bar{S}_{ijkl}^{(\beta\gamma)} = T_{pi} T_{qj} S_{pqrs}^{(\beta\gamma)} T_{kr} T_{ls} \tag{5.69}$$

The strain energy released during the formation of new surfaces corresponding to the growth of cracks within the crack band is assumed to be dissipated over the

entire subcell volume. Therefore, the post-peak softening slope $E_{IT}^{(\beta\gamma)}$, and the strain at which a the principle stress state is zero, is calculated using the characteristic length of the subcell $l_C^{(\beta\gamma)}$ and the material fracture toughness $\mathcal{G}_{IC}^{(\beta\gamma)}$ (see Figure 5.3a).

$$\epsilon_F^{(\beta\gamma)} = \frac{2\mathcal{G}_{IC}^{(\beta\gamma)}}{\sigma_C^{(\beta\gamma)} l_C^{(\beta\gamma)}} \tag{5.70}$$

$$E_{IT}^{(\beta\gamma)} = \left(\frac{1}{\bar{E}_{110}} - \frac{\epsilon_F^{(\beta\gamma)}}{\sigma_C^{(\beta\gamma)}} \right)^{-1} \tag{5.71}$$

where $\bar{E}_{110}$ is the undamaged, axial Young's modulus in the principle frame. It should be noted that $E_{IT}^{(\beta\gamma)}$ must be less than zero; therefore, by Equations (5.70) and (5.71), a restriction is placed on the maximum allowable subcell size.

$$l_C^{(\beta\gamma)} < \frac{2\mathcal{G}_{IC}^{(\beta\gamma)} \bar{E}_{110}}{\sigma_C^{(\beta\gamma)}} \tag{5.72}$$

The local, rotated, subcell strain state $\bar{\epsilon}_i^{(\beta\gamma)}$

$$\left\{ \begin{array}{c} \bar{\epsilon}_1^{(\beta\gamma)} \\ \bar{\epsilon}_2^{(\beta\gamma)} \\ \bar{\epsilon}_3^{(\beta\gamma)} \end{array} \right\} = \left\{ \begin{array}{c} T_{1i}^{(\beta\gamma)} \bar{\epsilon}_{ij}^{(\beta\gamma)} T_{1j}^{(\beta\gamma)} \\ T_{2i}^{(\beta\gamma)} \bar{\epsilon}_{ij}^{(\beta\gamma)} T_{2j}^{(\beta\gamma)} \\ T_{3i}^{(\beta\gamma)} \bar{\epsilon}_{ij}^{(\beta\gamma)} T_{3j}^{(\beta\gamma)} \end{array} \right\} \tag{5.73}$$

is used to degrade the rotated compliance components. The scalar damage factor $D^{(\beta\gamma)}$ is calculated using the rotated strain corresponding to $\bar{\sigma}_1^{(\beta\gamma)}$.

$$D^{(\beta\gamma)} = 1 + \frac{E_{IT}^{(\beta\gamma)} \left(\epsilon_C^{(\beta\gamma)} - \bar{\epsilon}_1^{(\beta\gamma)} \right)}{\bar{E}_{110} \bar{\epsilon}_1^{(\beta\gamma)}} \tag{5.74}$$

where $\epsilon_C^{(\beta\gamma)}$ is the value of $\bar{\epsilon}_1^{(\beta\gamma)}$ when the initiation criterion, Equation (5.67), is satisfied. If $D^{(\beta\gamma)}$ is less than zero, no damage occurs, and a maximum damage level of one corresponds to a zero stress state on the softening stress-strain curve. Also,

damage healing is inadmissable.

$$\dot{D}^{(\beta\gamma)} \geq 0 \tag{5.75}$$

Components of the rotated compliance matrix are degraded with the damage factor.

$$\bar{\boldsymbol{S}}^{(\boldsymbol{\beta\gamma})} = \begin{bmatrix} \frac{\bar{S}^{0(\beta\gamma)}_{1111}}{(1-D^{(\beta\gamma)})} & \bar{S}^{(\beta\gamma)}_{1122} & \bar{S}^{(\beta\gamma)}_{1133} & 0 & 0 & 0 \\ \bar{S}^{(\beta\gamma)}_{1122} & \bar{S}^{(\beta\gamma)}_{2222} & \bar{S}^{(\beta\gamma)}_{2233} & 0 & 0 & 0 \\ \bar{S}^{(\beta\gamma)}_{1133} & \bar{S}^{(\beta\gamma)}_{2233} & \bar{S}^{(\beta\gamma)}_{3333} & 0 & 0 & 0 \\ 0 & 0 & 0 & \bar{S}^{(\beta\gamma)}_{2323} & 0 & 0 \\ 0 & 0 & 0 & 0 & \frac{\bar{S}^{0(\beta\gamma)}_{1313}}{(1-D^{(\beta\gamma)})} & 0 \\ 0 & 0 & 0 & 0 & 0 & \frac{\bar{S}^{0(\beta\gamma)}_{1212}}{(1-D^{(\beta\gamma)})} \end{bmatrix} \tag{5.76}$$

Since the crack band orientation is fixed upon initiation, the $\bar{S}^{(\beta\gamma)}_{1313}$ and $\bar{S}^{(\beta\gamma)}_{1212}$ shear compliances in the rotated frame are degraded, as well as the $\bar{S}^{(\beta\gamma)}_{1111}$ compliance, so that the crack band faces normal to $\boldsymbol{n_1^{(\beta\gamma)}}$ are free of normal and shear tractions when all of the crack band energy has been dissipated (i.e. $l_C^{(\beta\gamma)} W_F^{(\beta\gamma)} = \mathcal{G}_{IC}^{(\beta\gamma)}$). Once the compliance in the rotated frame is degraded, the compliance is transformed back to the global frame to yield the new subcell compliance.

$$S^{(\beta\gamma)}_{ijkl} = T^{-1}_{pi} T^{-1}_{qj} \bar{S}^{(\beta\gamma)}_{pqrs} T^{-1}_{kr} T^{-1}_{ls} \tag{5.77}$$

Note that, damage introduced in the principal frame, through Equation (5.76), can induce normal-shear coupling in the global frame.

5.3.2.2 Mode II Crack Band Growth Under Compressive Principal Stress

Crack band growth under pure mode I conditions are energetically favorable; however, conditions arise, under which, mode I crack growth is not possible. For instance, the crack cannot grow under in mode I if the normal traction at the crack tip is compressive. This occurs when the principal stress with the maximum magnitude is compressive ($\bar{\sigma}_1^{(\beta\gamma)} < 0$). However, experimental data shows that monolithic materials subjected to global compression will eventually fracture.

In brittle and quasi-brittle materials, it has been shown that local, internal friction results in shear (mode II) fracture when the monolithic material is subjected to compressive stresses [*Hoek and Bieniawski* (1965); *Horii and Nemat-Nasser* (1986); *Ashby and Sammis* (1990); *Chen and Ravichandran* (2000)]. Consequently, if $\bar{\sigma}_1^{(\beta\gamma)} < 0$ it is assumed that the crack band is aligned with plane of maximum shear stress $\bar{\tau}^{(\beta\gamma)}$ in the matrix subcell and a Mohr-Coulomb failure criterion will be used to indicate crack band initiation under maximum principal compression.

$$\frac{\bar{\tau}_E^{(\beta\gamma)}}{\tau_C^{(\beta\gamma)}} = 1, \qquad \bar{\sigma}_1^{(\beta\gamma)} < 0 \tag{5.78}$$

where $\tau_C^{(\beta\gamma)}$ is the cohesive shear strength of the matrix, and $\bar{\tau}_E^{(\beta\gamma)}$ is an effective shear stress that includes the influence of the traction normal to the crack band $\bar{\sigma_n}^{(\beta\gamma)}$.

$$\bar{\tau}_E^{(\beta\gamma)} = |\bar{\tau}^{(\beta\gamma)}| + \mu_i \bar{\sigma_n}^{(\beta\gamma)} \tag{5.79}$$

where μ_i is the internal friction coefficient and must lie between $0 < \mu_i \leq 1.5$ to obtain physically reasonable surface friction coefficient [*Chen and Ravichandran* (2000)]. Since the principal stress with the largest magnitude is compressive, the traction normal to the maximum shear stress plane $\bar{\sigma_n}^{(\beta\gamma)}$ must also be compressive. Hence, in Equation (5.79), an increase in the normal compressive stress will yield a reduction

in the effective shear stress and an increase in apparent shear strength. *Taliercio and Sagramoso* (1995) derived relationships between internal friction coefficient, shear strength, the tensile strength and compressive strength of the material, yielding an expression for μ_i in terms of $\sigma_C^{(\beta\gamma)}$ and $\tau_C^{(\beta\gamma)}$.

$$\mu_i = \tan\left\{\sin^{-1}\left[\frac{\left(2\tau_C^{(\beta\gamma)}\right)^2 - \sigma_C^{(\beta\gamma)^2}}{\left(2\bar{\tau}^{(\beta\gamma)}\right)^2 + \sigma_C^{(\beta\gamma)^2}}\right]\right\} \tag{5.80}$$

Similar criteria are used for shear failure under compressive loading in homogenized composite materials [*Puck and Schürmann* (1998, 2002); *Pinho et al.* (2005)]. In these theories, the orientation of the crack is not aligned with the plane of maximum shear stress because of the influence of the fibers on the crack path, but rather, orientation is an input to the theories obtained from experimental data. Since the influence of the fibers are explicitly accounted for in the present methodology, the crack may remain oriented with the maximum shear stress plane and the local stress in the matrix will drive the crack path.

Subsequent to mode II crack band initiation via Equation (5.78), the compliance tensor of the subcell is rotated into the maximum shear stress frame using Equations (5.68) and (5.69), where $\boldsymbol{n_1^{(\beta\gamma)}}$ is a unit-vector perpendicular to the plane of maximum shear stress. Features of the post-peak softening shear stress-shear strain curve, such as the endpoint and post-peak tangent stiffness, can be calculated from the mode II fracture parameters.

$$\gamma_F^{(\beta\gamma)} = \frac{2\mathcal{G}_{IC}^{(\beta\gamma)}}{\tau_C^{(\beta\gamma)} l_C^{(\beta\gamma)}} \tag{5.81}$$

$$E_{IIT}^{(\beta\gamma)} = \left(\frac{1}{\bar{G}_{120}} - \frac{\gamma_F^{(\beta\gamma)}}{\tau_C^{(\beta\gamma)}}\right)^{-1} \tag{5.82}$$

where $\bar{G}_{120}$ is the undamaged, axial shear modulus in the maximum shear stress frame. Again the tangent stiffness $E_{IIT}^{(\beta\gamma)}$ must be less than zero; therefore, Equations

(5.81) and (5.82) place a restriction is on the maximum allowable subcell size.

$$l_C^{(\beta\gamma)} < \frac{2\mathcal{G}_{IC}^{(\beta\gamma)}\bar{G}_{120}}{\tau_C^{(\beta\gamma)}} \tag{5.83}$$

The shear strain corresponding to the maximum shear stress $\bar{\gamma}^{(\beta\gamma)}$ is obtained by rotating the strain tensor.

$$\bar{\gamma}^{(\beta\gamma)} = T_{1i}^{(\beta\gamma)}\bar{\epsilon}_{ij}^{(\beta\gamma)}T_{2j}^{(\beta\gamma)} \tag{5.84}$$

An effective shear strain $\bar{\gamma}_E^{(\beta\gamma)}$ can be defined that is work conjugate with the effective shear stress $tEbg$.

$$\bar{\tau}_E^{(\beta\gamma)}d\bar{\gamma}_E^{(\beta\gamma)} = \bar{\tau}^{(\beta\gamma)}d\bar{\gamma}^{(\beta\gamma)} + \bar{\sigma_n}^{(\beta\gamma)}d\bar{\epsilon_n}^{(\beta\gamma)} \tag{5.85}$$

where $\bar{\tau}^{(\beta\gamma)}$ and $\bar{\sigma_n}^{(\beta\gamma)}$ are the shear and normal tractions acting on the crack faces oriented parallel to the plane of maximum shear stress, and $\bar{\gamma}^{(\beta\gamma)}$ and $\bar{\epsilon_n}^{(\beta\gamma)}$ are the apparent shear and normal strains with respect to the maximum shear orientation in the subcell, including the effects of crack tip opening displacement. Taking the derivative of Equation (5.85) with respect to $\bar{\tau}^{(\beta\gamma)}$ yields

$$\frac{\partial\bar{\tau}_E^{(\beta\gamma)}}{\partial\bar{\tau}^{(\beta\gamma)}}d\bar{\gamma}_E^{(\beta\gamma)} = d\bar{\gamma}^{(\beta\gamma)} \tag{5.86}$$

and along with the derivative of Equation (5.79) with respect to $\bar{\tau}^{(\beta\gamma)}$

$$\frac{\partial\bar{\tau}_E^{(\beta\gamma)}}{\partial\bar{\tau}^{(\beta\gamma)}} = 1 \tag{5.87}$$

finally, after integrating, gives:

$$\bar{\gamma}_E^{(\beta\gamma)} = \bar{\gamma}^{(\beta\gamma)} \tag{5.88}$$

which states that the shear strain in the rotated, maximum shear stress frame and the effective shear strain that is work conjugate to the effective, Mohr-Coulomb shear stress are equivalent.

Thus, $\bar{\gamma}^{(\beta\gamma)}$ is used to degrade the rotated compliance components. The damage factor $D^{(\beta\gamma)}$ is calculated using $\bar{\gamma}$.

$$D^{(\beta\gamma)} = 1 + \frac{E_{IIT}^{(\beta\gamma)}\left(\gamma_C^{(\beta\gamma)} - \bar{\gamma}^{(\beta\gamma)}\right)}{\bar{G}_{120}\bar{\gamma}^{(\beta\gamma)}} \tag{5.89}$$

where $\gamma_C^{(\beta\gamma)}$ is the value of $\bar{\gamma}^{(\beta\gamma)}$ when the initiation criterion, Equation (5.78), is satisfied. In the case of mode II fracture, only the shear moduli are degraded. The normal direction is subjected to compression, and thus, retains its stiffness.

$$\bar{\boldsymbol{S}}^{(\boldsymbol{\beta\gamma})} = \begin{bmatrix} \bar{S}_{1111}^{(\beta\gamma)} & \bar{S}_{1122}^{(\beta\gamma)} & \bar{S}_{1133}^{(\beta\gamma)} & 0 & 0 & 0 \\ \bar{S}_{1122}^{(\beta\gamma)} & \bar{S}_{2222}^{(\beta\gamma)} & \bar{S}_{2233}^{(\beta\gamma)} & 0 & 0 & 0 \\ \bar{S}_{1133}^{(\beta\gamma)} & \bar{S}_{2233}^{(\beta\gamma)} & \bar{S}_{3333}^{(\beta\gamma)} & 0 & 0 & 0 \\ 0 & 0 & 0 & \bar{S}_{2323}^{(\beta\gamma)} & 0 & 0 \\ 0 & 0 & 0 & 0 & \dfrac{\bar{S}_{1313}^{0(\beta\gamma)}}{(1-D^{(\beta\gamma)})} & 0 \\ 0 & 0 & 0 & 0 & 0 & \dfrac{\bar{S}_{1212}^{0(\beta\gamma)}}{(1-D^{(\beta\gamma)})} \end{bmatrix} \tag{5.90}$$

Then, the compliance tensor is rotated back to the global frame using Equation (5.77).

5.4 Subcell Mesh Objectivity

The key advantage of using the smeared crack band approach is that it has been verified to provide mesh objective results within an FEM setting; this can also be said for implementation of this model within HFGMC. To illustrate this, a uniform, uni-

axial, tensile displacement u was applied to monolithic, doubly-periodic, unit square RUCs in the x_3-direction. As shown in Figure 5.5, the levels of subcell refinement ranged from: 35 subcells x 35 subcells, 45 subcells x 45 subcells, 55 subcells x 55 subcells, to 65 subcells x 65 subcells. The elastic properties were chosen to match data for in-situ MY750/HY917/DY063 epoxy matrix [*Hinton et al.* (2004)]. The fracture properties were chosen such that the problem would demonstrate significant post-peak energy dissipation. All properties are given in Table 5.1. A single subcell, colored red in Figure 5.5, was given a 10% lower initiation strain then the rest of the domain. Additionally, only the subcells that lie along a horizontal line running through the weaker subcell were allowed to fail because as the damaged region grows, the opposite ends of the damaged region would interact with each other (due to periodicity), as a result of the periodic boundary conditions, altering the damage path and resulting in damage growth that is not self-similar. Restricting the damage path ensures that only subcell dimensions would influence the results from case to case.

The resulting load P in the x_3-direction is plotted in Figure 5.6 against the applied displacement for the four different levels of subcell refinement. It is clear that the total strain energy release rate dissipated in the system, and the ultimate load, is insensitive to the dimension of the subcell size. Of course, in more complicated RUCs, a certain level of subcell refinement is necessary to capture the local fields accurately; however, that behavior is not pathological subcell mesh dependence because the solution is bounded.

5.5 Details of Numerical Models

The smeared crack band model, presented in Section 5.3.2, is implemented within HFGMC, and it is used to investigated the progression of post-peak softening damage within a unidirectional fiber-reinforced composite RUC. The main objective was to capture the failure evolution of a composite RUC under transverse tension and com-

pression. In tension, the lamina is susceptible to transverse cracking, as evidenced by Figure 1.2. The behavior of this mechanism is observed to be quite brittle, as is evidenced by tension tests on 90° coupon laminates. However, in compression a network of shear bands develop, accompanied by some matrix cracking and fiber-matrix debonding (see Figure 1.5) and the stress-strain response if much more ductile. To emulate these failure modes, a doubly-periodic HFGMC RUC of the 2-3 plane of the composite was created (see Figure 5.7). This RUC was subjected to global tensile and compressive, transverse, uniaxial strains: $\pm\bar{\epsilon}_{22}$. The constitutive behavior of the matrix subcells follows linear elasticity, coupled with the crack band model for post-peak strain softening formulated earlier. This model is verified against experimental data in Section 5.6.

A representation of the 2-3 plane of a typical composite lamina (where the 1-axis runs in the longitudinal direction of the fibers and the 2- and 3-axes span the plane of transverse isotropy) was produced to examine the evolution of transverse cracks within the composite. The blueprint for the discrete model is created by randomly placing thirteen circular fibers with a diameter of 5 μm in a square box. The domain was then discretized into a number of subcells. The considered formulation of HFGMC only admits rectangular subcells in doubly-periodic models (parallelepiped in triply-periodic models); so, some of the fiber domains would overlap or lie directly adjacent to one another. An isoparametric formulation of HFGMC has been recently developed by *Haj-Ali and Aboudi* (2010). Mesh objective, subcell interfacial debonding has been formulated for GMC (see Appendix B, also *Pineda et al.* (2010a,c)) but has not been fully developed within the HFGMC framework. As a result, thin matrix channels were inserted between any adjacent fibers to avoid arrest of the crack band for non-physical reasons such as the inability of two adjacent fiber to separate. The final architecture and discretization is shown in Figure 5.7, which contains 81 subcells x 85 subcells. The blue subcells indicate fiber material and the green represent the matrix.

The dimensions of the RUC (21.25 μm x 21.25 μm) were chosen such that the final fiber volume fraction in Figure 5.7 would be preserved at 58%, corresponding to the experimental data provided in *Hinton et al.* (2004).

The elastic properties for a Silenka E-glass/MY750/HY917/DY063 lamina were taken from data from the world wide failure exercise (WWFE) [*Hinton et al.* (2004)]. Elastic properties for Silenka E-glass fiber and MY750/HY917/DY063 epoxy matrix used are given in Table 5.2. Note that the matrix properties were correlated to represent the in-situ properties of the matrix, which differ significantly from those of the neat material [*Ng et al.* (2010)], and match the global properties of the composite. As a result of this calibration, the isotropic relationship between the shear modulus and the Young's modulus and Poisson's ratio of the matrix is not maintained. The fracture properties (also Table 5.2) were calibrated to produce and ultimate transverse tensile stress of 40 MPa, and the compressive properties were calibrated to match transverse compression data, reported in *Hinton et al.* (2004).

5.6 Results

5.6.1 Transverse Tension

A comparison between the tensile results obtained from the HFGMC model and the experiment is provided in Figure 5.8. Only one data point is given in *Hinton et al.* (2004), implying that the tensile response is linear until ultimate failure. The first peak in the $\bar{\sigma}_{22}$-$\bar{\epsilon}_{22}$ obtained from HFGMC at $\bar{\sigma}_{22}$ = 39.76 MPa and $\bar{\epsilon}_{22}$ = 0.00244 was calibrated to match the experimental data, and thus, correlates well. Subsequent to the first peak, the model exhibits a sudden drop in the global stress; however, the RUC then continues to reload in a nonlinear manner. A second peak is achieved at an applied transverse strain of 0.00308 and a transverse stress of 37.97 MPa, which is slightly less than the stress at the first peak. After the second peak, the load carrying

capability of the RUC is severely diminished.

The evolution of the tensile crack band in the RUC is presented in Figure 5.9. At $\bar{\sigma}_{22} = 37.84$ MPa a crack band initiates near the top of the RUC between two fibers (please refer back to Figure 5.7 for the fiber-matrix architecture). At the ultimate stress 39.76 MPa, the initial crack band has grown significantly into a fully developed crack band that propagated across the periodic boundary into the bottom of the RUC. The tips of the initial crack band are arrested in lower stress, matrix rich regions. At $\bar{\sigma}_{22} = 35.09$ MPa, after the ultimate stress has been achieved and the RUC is reloading, A new crack band initiates between two adjacent fibers. When the second peak is reached, the subcells composing the second crack band have degraded significantly, and the original crack band has extended further. As the stress drops, Figure 5.9e, a third crack band initiates. The newest crack band develops rapidly, and the second crack band becomes stagnant. When the RUC has completely failed and can no longer sustain any load, the first and third crack band have bridged to form a nearly continuous crack that has maneuvered around the fiber inclusions and spans the entire height of the RUC. This failure path closely resembles the SEM image of a transverse crack in the glass/epoxy composite shown in Figure 1.2b, and although the model does not account for fiber-matrix debonding, the model exhibits appreciable matrix failure in matrix subcells adjacent to fiber subcells.

5.6.2 Transverse Compression

The same HFGMC RUC is loaded in transverse compression and the stress-strain response is compared to the experimental data in Figure 5.10. The nonlinear behavior of the model and experiment correlate well until the model exhibits catastrophic failure at -104.8 MPa, which is well below the reported ultimate compressive strength of 145 MPa.

Investigations into the failure progression within the RUC reveal the cause of

the premature ultimate failure. Figure 5.11 shows the progression of mode II failure (D_C), resulting from maximum, compressive principal stresses (left column), mode I failure (D_T), resulting from maximum, tensile principal stress (middle column), and the superposition of mode I and mode II failure ($D_T + D_C$, right column) as the RUC is loaded in global, transverse compression. The first failure initiation occurs between two fibers near the top of the RUC under mode II conditions at a global stress of -65.68 MPa. As the applied strain increases, many mode II crack bands form in angular matrix regions between closely packed fibers. This is exhibited in Figures 5.11b and 5.11c. When the global stress reaches -92.88 MPa, a mode I crack band initiates in the top-right corner of the RUC. At the ultimate stress, Figure 5.11f both the mode I and mode II crack band have evolved. In Figure 5.11g, shortly after the ultimate stress was reached, a network of angular mode II crack bands has formed. These mode II crack bands are bridged by a horizontal, mode I crack band forming one continuous crack band that has progressed throughout the RUC. When the global stress has dropped severely, in Figure 5.11h, there is substantial matrix degradation resulting from mode II crack band propagation. Furthermore, one fiber is completely surrounded by crack bands. Comparing Figure 5.11h to an SEM image of a compressively failed carbon fiber/epoxy laminate in Figure 1.5b, displays closely resembling failure patterns, indicating that the qualitative failure mode was captured accurately, despite the quantitative discrepancy.

The development of mode I crack bands corresponded to a drop in global stress shortly thereafter. Thus, to determine if the mode I crack bands were responsible for the premature failure of the RUC, the simulation was re-executed but mode I crack band growth was prohibited. The global $\bar{\sigma}_{22}$-$\bar{\epsilon}_{22}$ response is presented in Figure 5.10, along with the previous results and experimental data. It can be observed that ultimate failure is delayed considerably until the $\bar{\sigma}_{22}$ = -146.4 MPa, which corresponds well to the strength reported in Ref. [*Hinton et al.* (2004)] although the ultimate

failure strain 16% higher. Moreover, the majority of the stress-strain response of the RUC matches the experimental data. This indicates that, in the model, the mode II crack bands are responsible for the observed nonlinearity; whereas, the mode I crack bands are responsible for the early onset of ultimate failure, as the mode I fracture toughness is an order of magnitude lower than mode II.

Extending this observation to the behavior of actual composite would suggest that its non-linearity is controlled by shear band evolution, and the ultimate failure is due to progression of tensile cracks and fiber-matrix debonding. It may be that the size of the RUC (i.e. number of fibers included in the RUC) was too small to get an accurate representation of the quantitative response of the composite under compression, and the growth of the tensile crack band made an unrealistically large impact on the response of the RUC. Further studies evaluating the influence of fiber-matrix architecture on the compressive response of composites needs to be performed. Additionally, adjacent constraining plies with different local architectures, present in the experiment, may have helped to diminish the effect of formation of tensile cracks, which is an effect not captured in this analysis.

The mode II crack band progression, produced by the simulation in which mode I crack band growth was disabled, is displayed in Figure 5.12. Prior to the initiation of the mode I crack band in Figure 5.11, Figures 5.11 and 5.12 are identical. However as the stress continues beyond the ultimate stress observed in the original simulation, more angular, distributed, mode II crack bands arise, as shown in Figure 5.12i at the ultimate stress of the simulation with mode I crack band preclusion. Upon ultimate failure, the expansive array of mode II crack bands is almost entirely adjoined and nearly all of the matrix subcells in the RUC have failed. The SEM image, Figure 1.5b, does not display such extensive failure. This further supports that the failure mode predicted with both mode I and mode II crack bands is more physically correct, and other factors are influencing the discrepancy between the response of the model

and the experiment.

5.7 Conclusions

A mesh objective, smeared crack band model was implemented at the matrix subcell level within the HFGMC micromechanics framework. Mode I crack bands were allowed to propagate normal to the maximum principal stress when the principal stress component with the maximum magnitude was tensile, and the associated strain exceeded a critical value. If the principal stress component with the maximum magnitude was compressive, however, it was assumed that mode I cracks within the crack band could not evolve, and instead, they grew in mode II as a result of Mohr-Coulomb friction, upon satisfaction of a Mohr-Coulomb failure criterion. The mode II crack bands were aligned with the plane of maximum shear stress. Interfacial debonding was not considered in this analysis; however, a cohesive zone-based debonding model, formulated in Appendix B has been implemented within GMC and is currently being verified. Future efforts will be focused towards implemented the same debonding model in HFGMC.

An RUC containing 13, randomly distributed fibers was simulated under global transverse tension and compression. The results for both cases were compared to experimental data. The tensile response correlated extremely well with the test results. Furthermore, the predicted failure mode mirrored SEM images of composites failed in tension. Under compression, the micromechanics model predicted failure well below the reported compressive strength. This was attributed to the formation of tensile, mode I crack bands in the matrix which exhibit very low fracture toughness. A simulation wherein mode I crack band evolution was restricted, provided quantitative results that more closely agreed with the experiment. However, the failure mode exhibited by the simulation allowing for both mode I and mode II crack bands more closely resembled an SEM image of a compressively failed composite compared to

the latter simulation. This indicates that a sensitivity study on the size and level of refinement of the RUC should be enacted. Future studies will determine the number of fibers in the RUC required to achieve convergence of the stiffness and the failure progression.

Additionally, the response of the RUC to applied intralaminar shear strain $\bar{\gamma}_{12}$ was not enacted. As seen in the SEM image presented in Figure 1.1 of shear microcracking in a composite lamina, numerous cracks form between fibers along the fiber direction. This 3-D effect results in the composite exhibiting a very ductile response in shear. To capture these 3-D, geometric effects with the proposed model, a very complex, 3-D RUC is required.

The RUC examples that were provided are far too computationally expensive for a multiscale analysis. However, insight gained from the micromechanics analysis can be utilized to formulate traction-separation laws, or to postulate fracture toughnesses that include the geometric effects and can be implemented into simpler, more computationally feasible RUCs. To preserve the stress-strain response a consistent strain energy density must exist across the scales. However, the mesh objectivity gained by utilizing the smeared crack band model at the microscale is lost if the SERR is not also preserved across the scales. To accomplish this, a consistent length must be used at both scales. Thus, the volume of the microscale RUC and the volume associated with the corresponding macroscale integration point must be equivalent.

Property	Value
E (GPa)	3.7
ν	0.35
ϵ_C	0.0135
ϵ_C (weak)	0.01215
$\mathcal{G}_{IC}$ (N/mm)	750

Table 5.1: Elastic and fracture properties used in mesh objectivity study.

Property	Value
E_f (GPa)	74.000
ν_f	0.200
E_m (GPa)	4.65
ν_m	0.350
$\mathcal{G}_m$	1.4
$\epsilon_C^{(\beta\gamma)}$	0.0167
$\gamma_C^{(\beta\gamma)}$	0.0256
$\mathcal{G}_{IC}^{(\beta\gamma)}$ (N/mm)	0.00076
$\mathcal{G}_{IC}^{(\beta\gamma)}$ (N/mm)	0.00435

Table 5.2: Elastic and fracture properties used in RUC simulation of 2-3 plane of a Silenka E-Glass/MY750/HY917/DY063 composite lamina. The fracture properties were calibrated to provide the best correlation with experimental data.

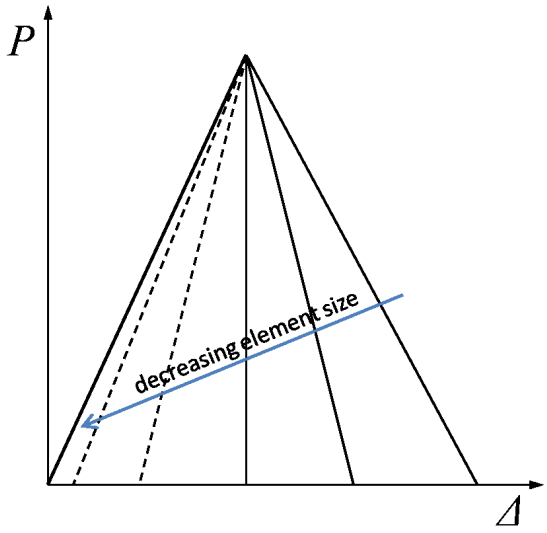

Figure 5.1: Effects of mesh refinement on overall load-displacement response for a material exhibiting post-peak softening. Dashed lines indicate non-physical snapback.

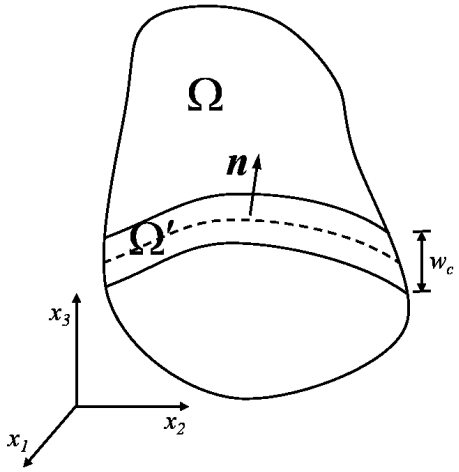

Figure 5.2: Crack band domain Ω' of width w_c oriented normal to vector $\boldsymbol{n}$ within a continuum Ω.

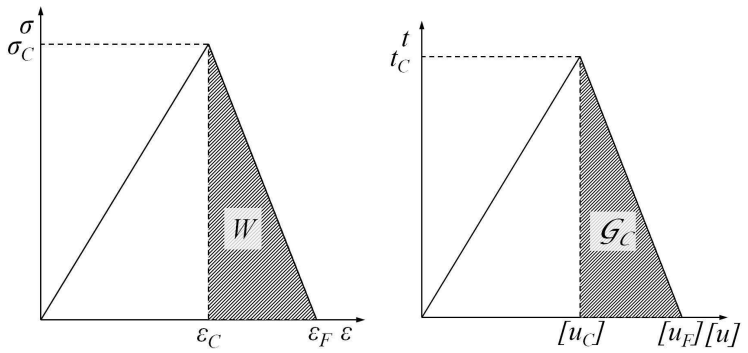

Figure 5.3: Stress-strain (a) and traction-separation (b) laws governing material behavior. Failure energy density W_F is related to fracture toughness $\mathcal{G}_C$ through the characteristic length.

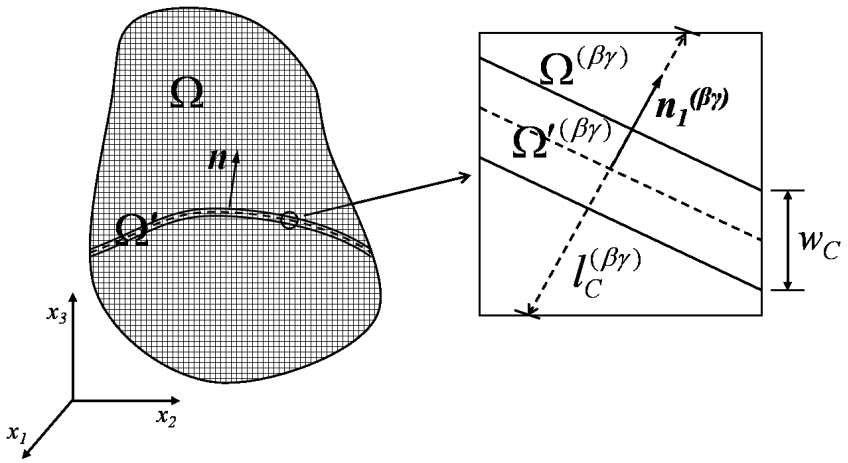

Figure 5.4: Crack band embedded in discretized continuum. Magnified subcell displays crack band orientation within subcell as well as characteristic length of subcell.

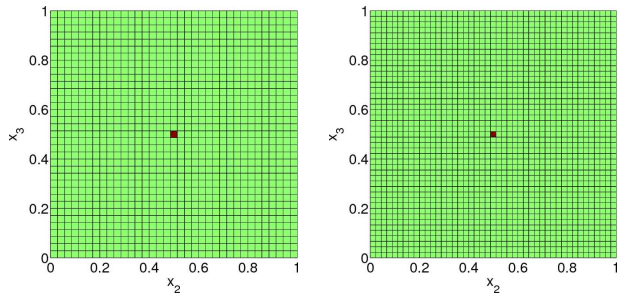

(a) 35 subcells x 35 subcells.

(b) 45 subcells x 45 subcells.

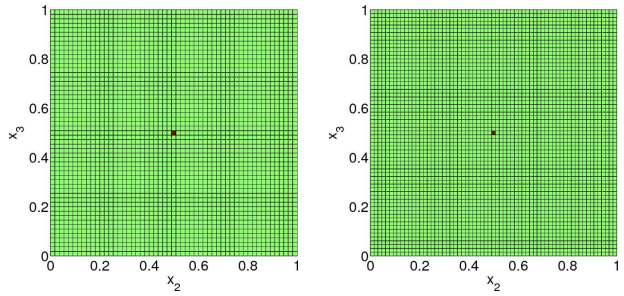

(c) 55 subcells x 55 subcells.

(d) 65 subcells x 65 subcells.

Figure 5.5: Four subcell meshes used in mesh objectivity study. Red subcell was given a lower crack band initiation strain than others.

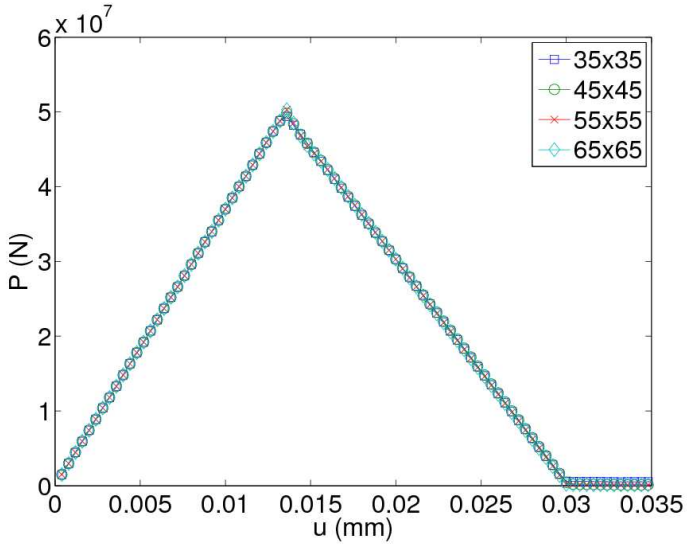

Figure 5.6: Load versus displacement for four different subcell meshes. Total strain energy release rate and ultimate load are unaffected by mesh refinement.

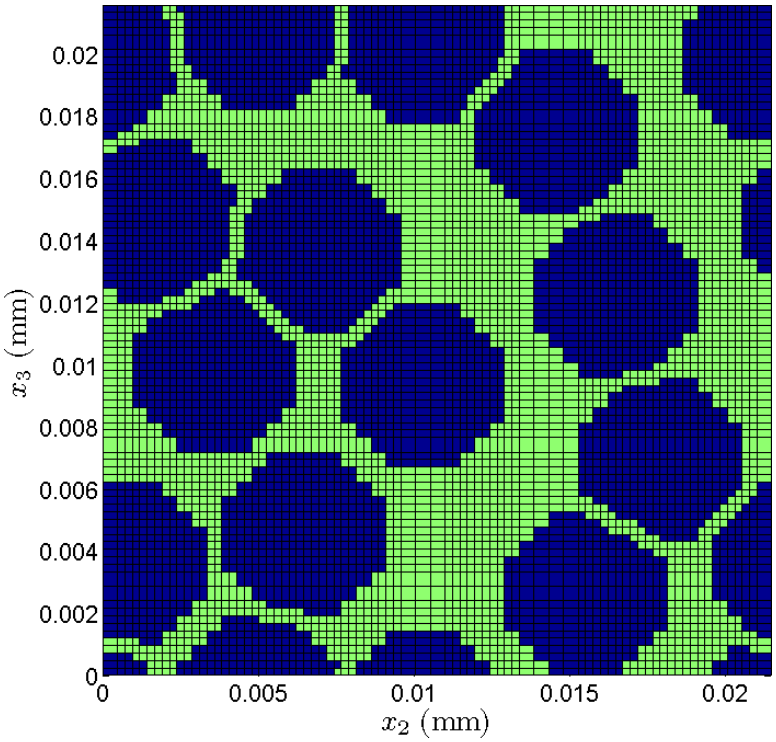

Figure 5.7: GMC/HFGMC and FEM mesh used in simulations of RUC in 2-3 plane of lamina containing 13 fibers and a fiber volume fraction of 58%. Subcells/elements occupied by fibers are colored blue, and subcells/elements occupied by matrix are colored green.

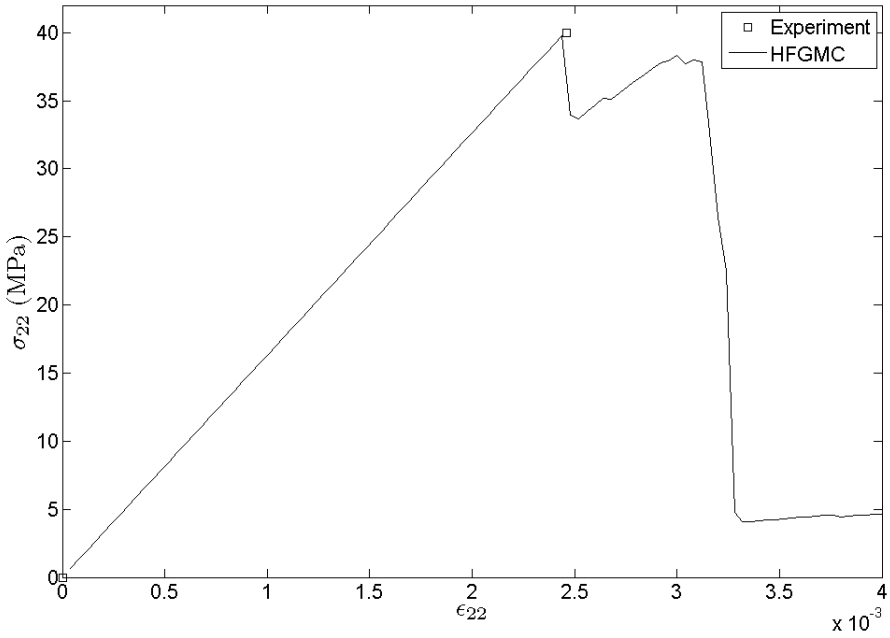

Figure 5.8: Transverse tensile stress versus transverse strain of E-glass/Epoxy composite from experiment compared to HFGMC micromechanics model.

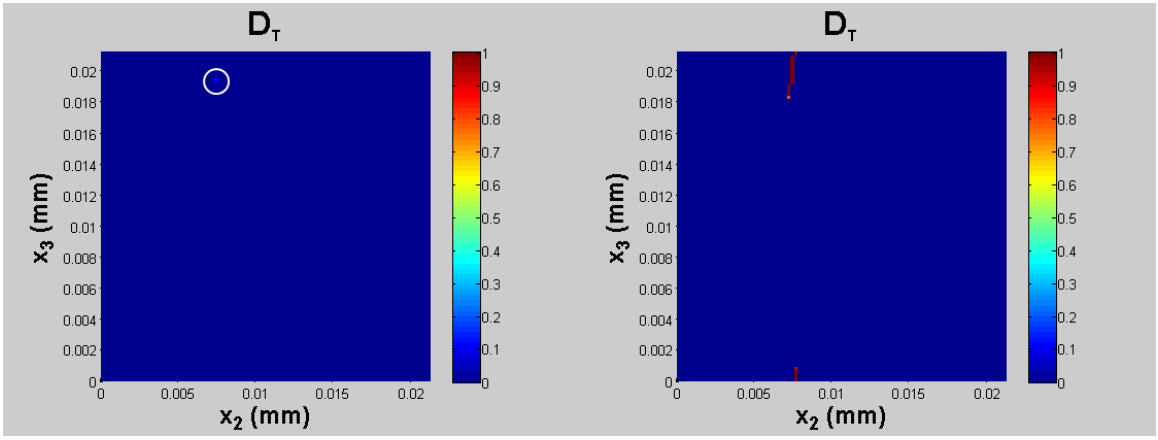

(a) $\epsilon_{22} = 0.00232$, $\sigma_{22} = 37.84$ MPa.

(b) $\epsilon_{22} = 0.00248$, $\sigma_{22} = 39.76$ MPa (First peak stress).

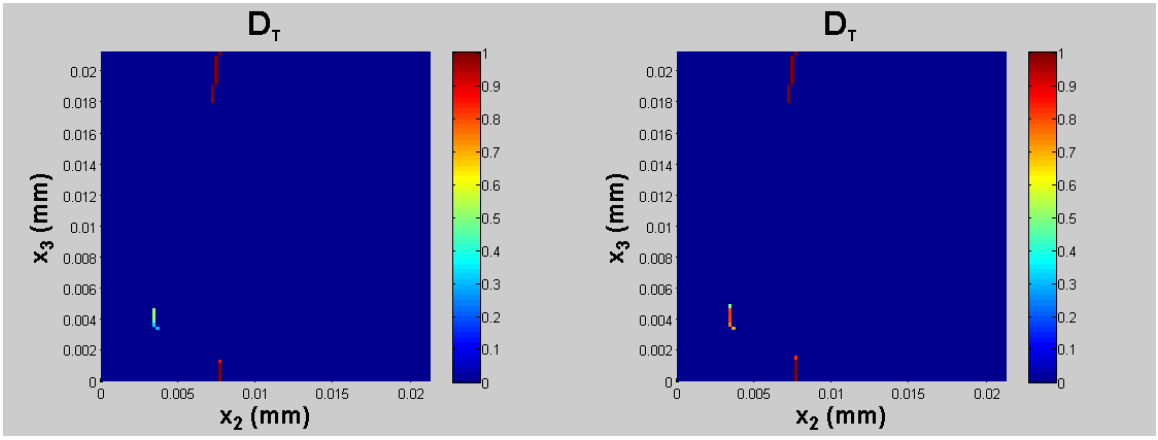

(c) $\epsilon_{22} = 0.00268$, $\sigma_{22} = 35.09$ MPa.

(d) $\epsilon_{22} = 0.00300$, $\sigma_{22} = 38.35$ MPa (Second peak stress).

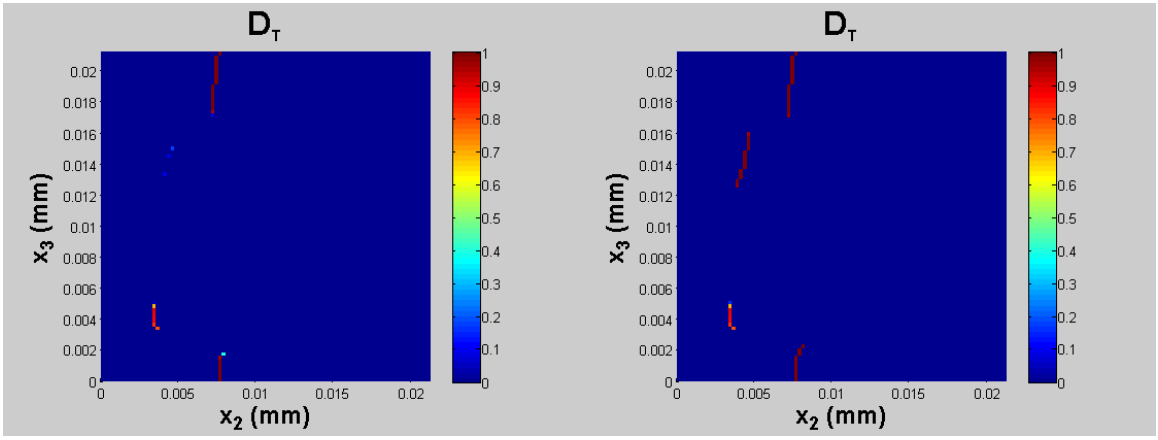

(e) $\epsilon_{22} = 0.00308$, $\sigma_{22} = 37.88$ MPa.

(f) $\epsilon_{22} = 0.00316$, $\sigma_{22} = 32.68$ MPa.

Figure 5.9: Evolution of mode I crack band in RUC subjected to applied transverse tensile strain.

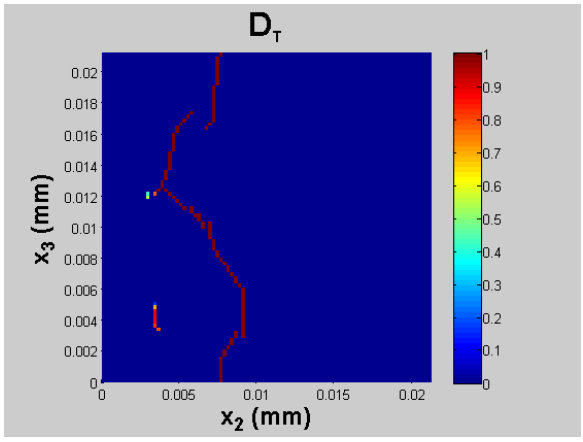

(g) $\epsilon_{22} = 0.00336$, $\sigma_{22} = 4.11$ MPa.

Figure 5.9: Evolution of mode I crack band in RUC subjected to applied transverse tensile strain.

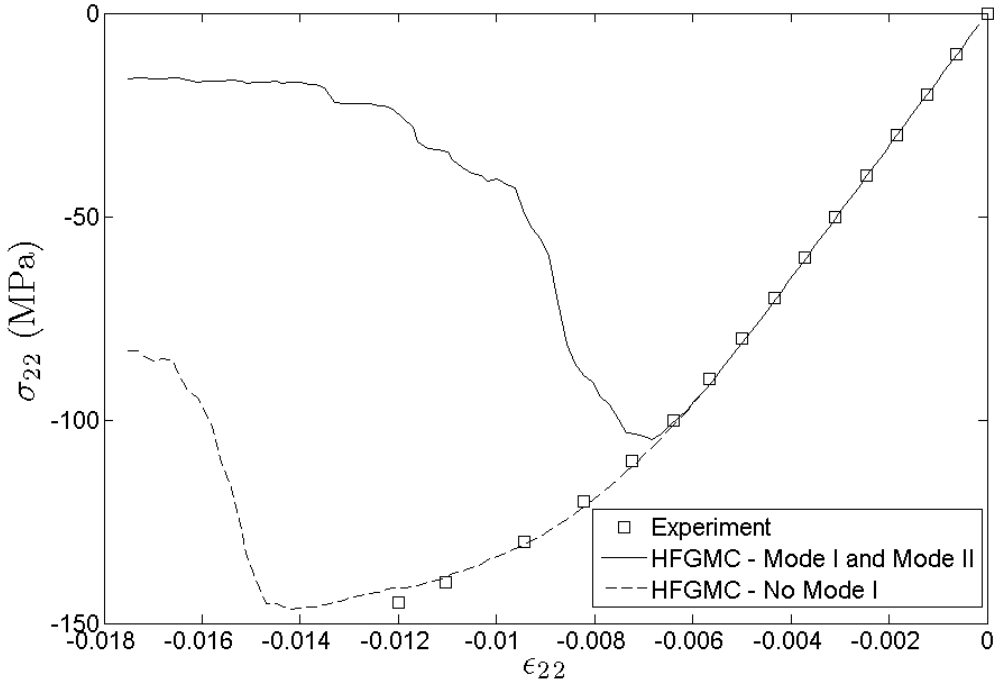

Figure 5.10: Compressive Transverse stress versus transverse strain of E-glass/Epoxy composite from experiment compared to HFGMC micromechanics model.

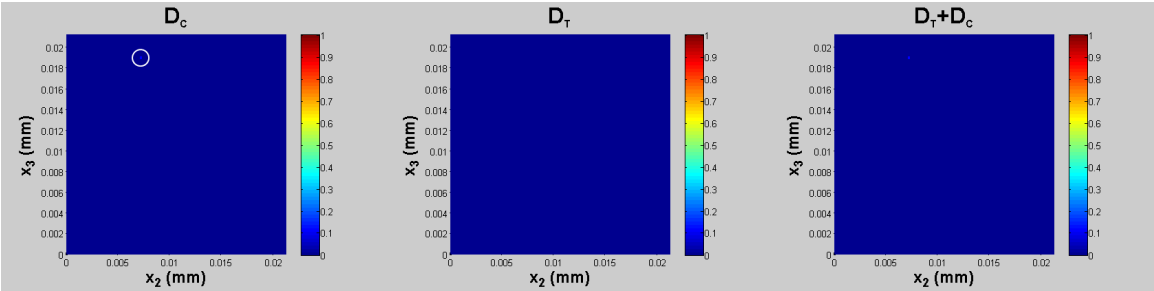

(a) ϵ_{22} = -0.00403, σ_{22} = -65.68 MPa.

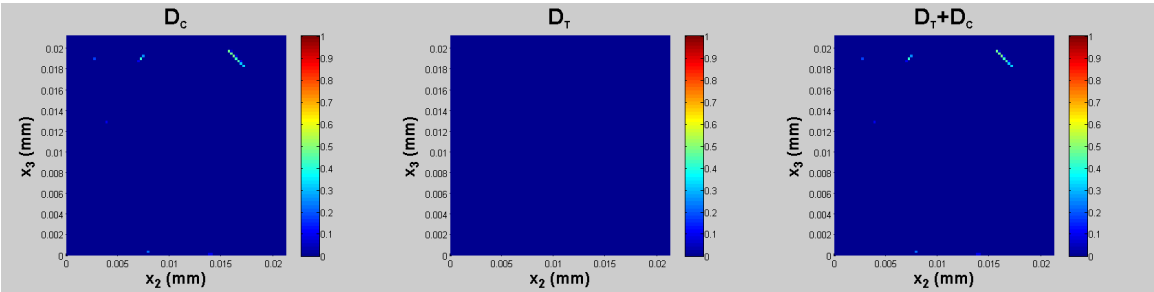

(b) ϵ_{22} = -0.00490, σ_{22} = -79.66 MPa.

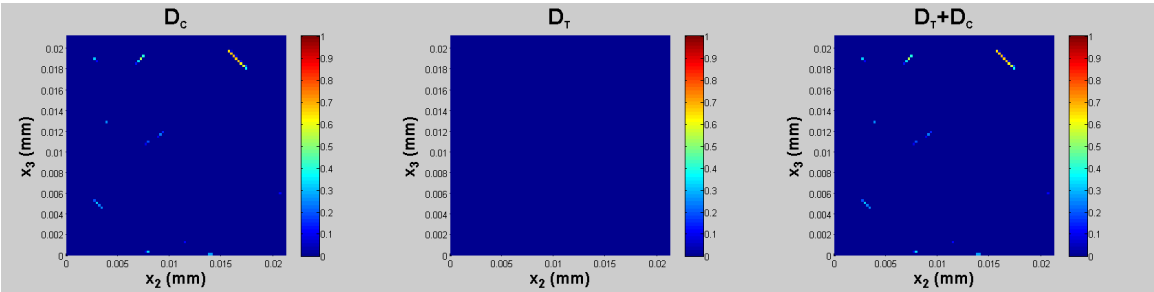

(c) ϵ_{22} = -0.00543, σ_{22} = -87.71 MPa.

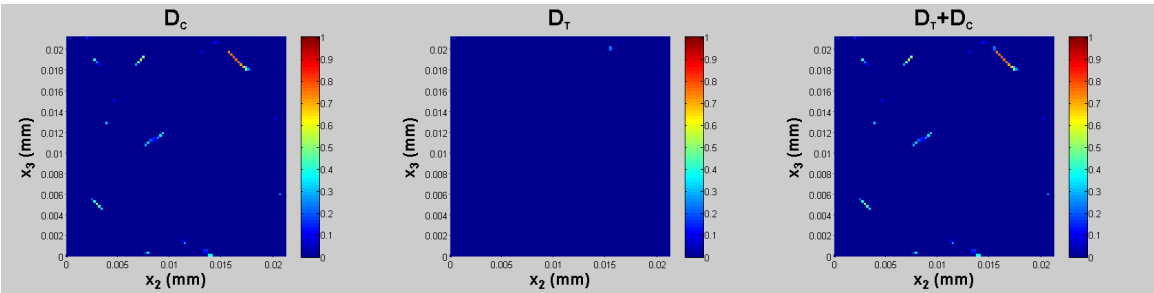

(d) ϵ_{22} = -0.00578, σ_{22} = -92.88 MPa.

Figure 5.11: Evolution of mode I (left), mode II (middle), and superposition of mode I and mode II (right) crack band in RUC subjected to applied transverse compressive strain.

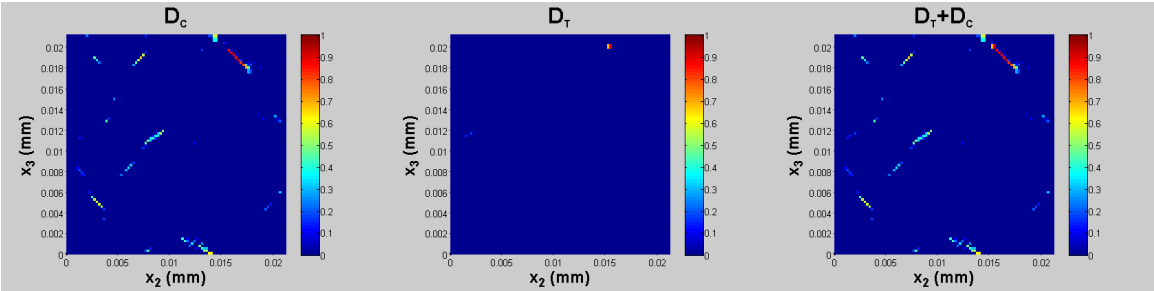

(e) ϵ_{22} = -0.00630, σ_{22} = -99.56 MPa.

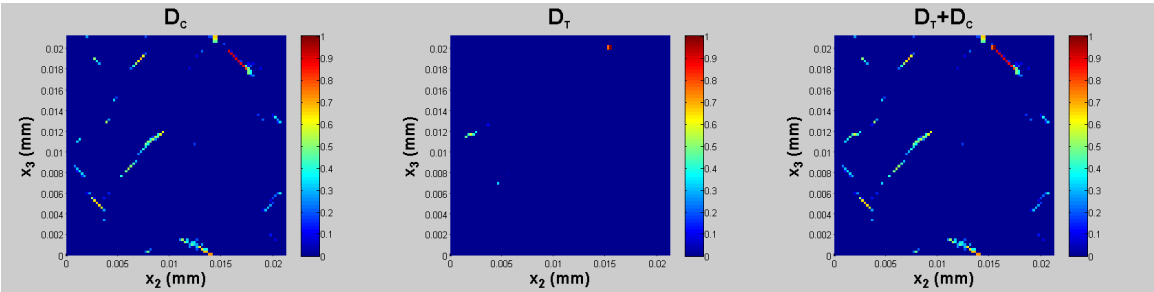

(f) ϵ_{22} = -0.00683, σ_{22} = -104.78 MPa (ultimate stress).

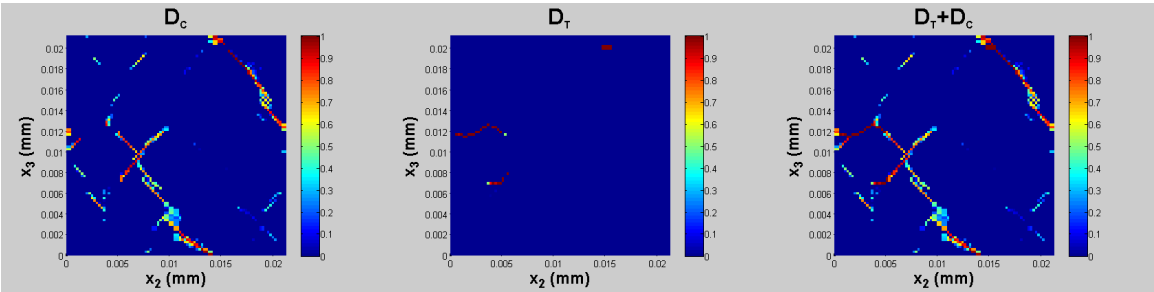

(g) ϵ_{22} = -0.00770, σ_{22} = -96.37 MPa.

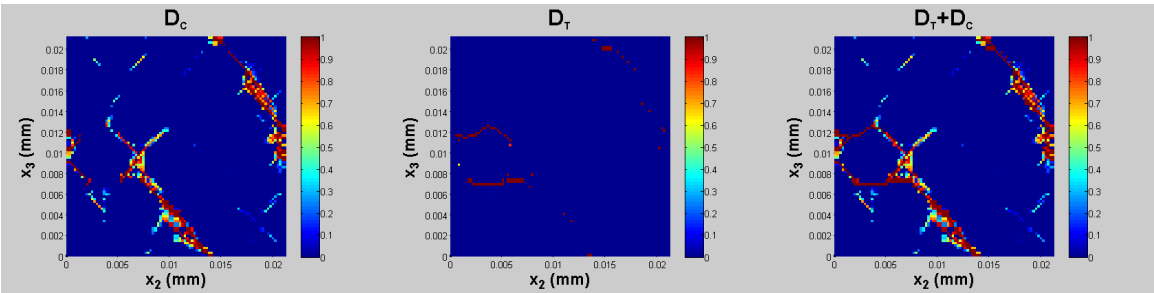

(h) ϵ_{22} = -0.01750, σ_{22} = -16.06 MPa.

Figure 5.11: Evolution of mode I (left), mode II (middle), and superposition of mode I and mode II (right) crack band in RUC subjected to applied transverse compressive strain.

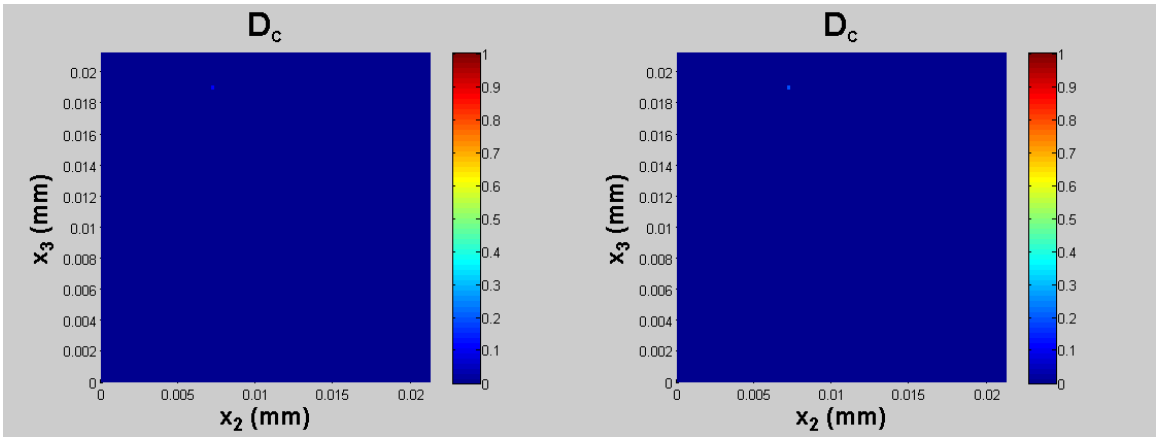

(a) ϵ_{22} = -0.00403, σ_{22} = -65.68 MPa.

(b) ϵ_{22} = -0.00420, σ_{22} = -68.53 MPa.

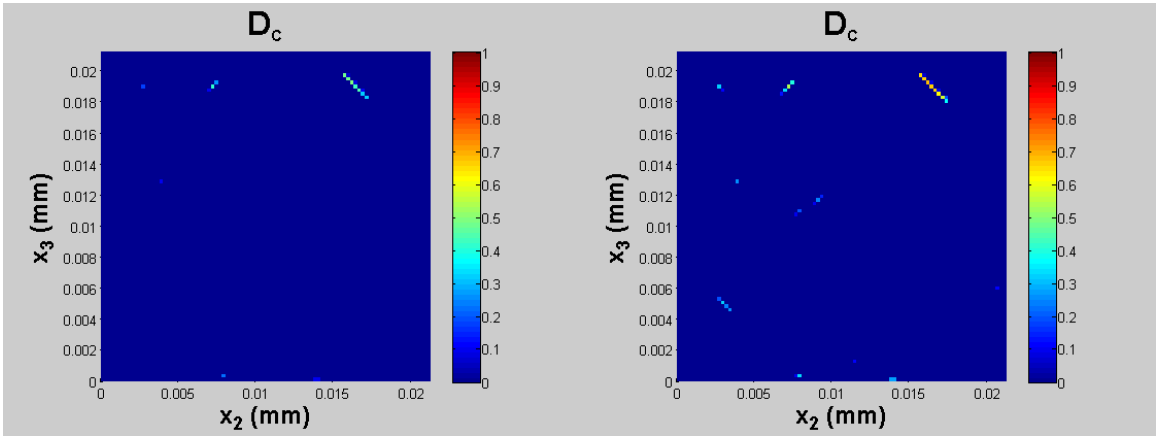

(c) ϵ_{22} = -0.00490, σ_{22} = -79.66 MPa.

(d) ϵ_{22} = -0.00543, σ_{22} = -87.71 MPa.

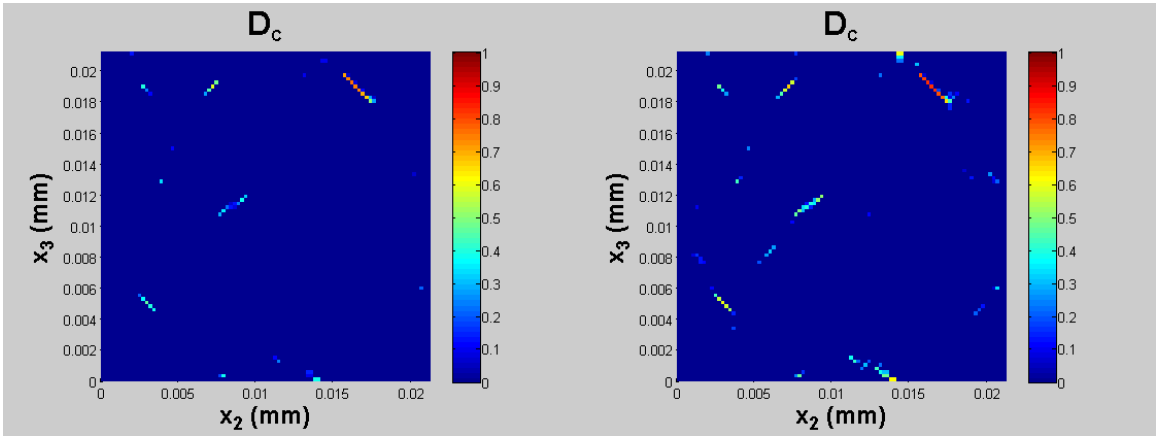

(e) ϵ_{22} = -0.00578, σ_{22} = -92.88 MPa.

(f) ϵ_{22} = -0.00630, σ_{22} = -100.15 MPa.

Figure 5.12: Evolution of mode II crack band in RUC subjected to applied transverse compressive strain if mode I crack band evolution is suppressed.

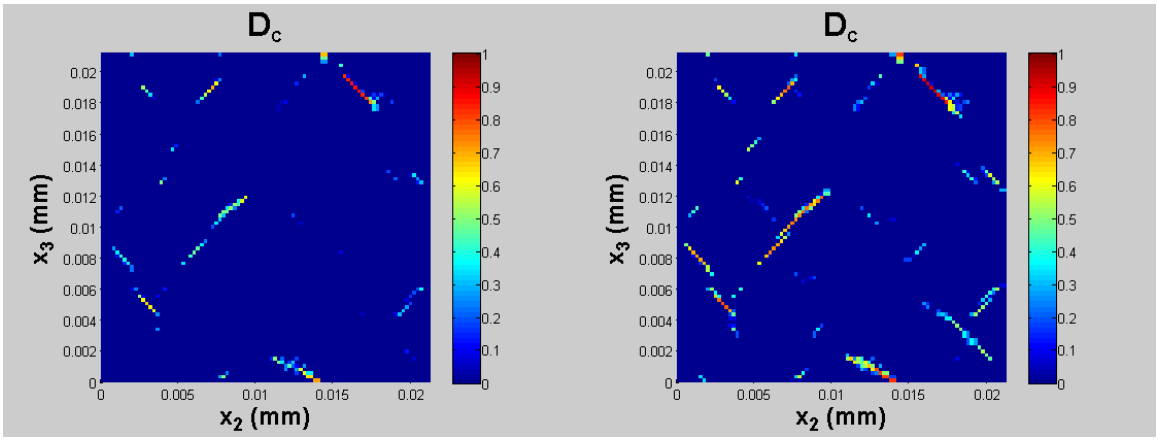

(g) ϵ_{22} = -0.00683, σ_{22} = -106.75 MPa.

(h) ϵ_{22} = -0.00770, σ_{22} = -116.36 MPa.

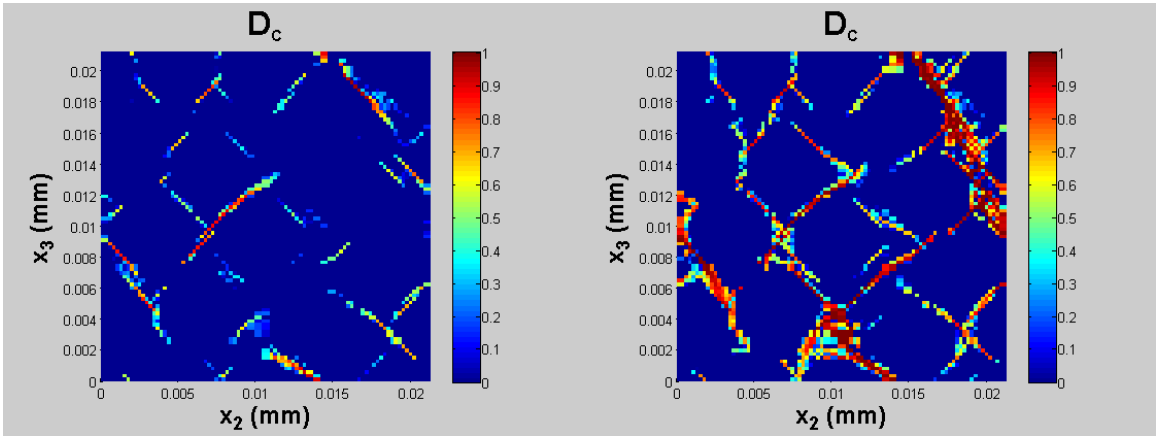

(i) ϵ_{22} = -0.01420, σ_{22} = -146.43 MPa (ultimate stress).

(j) ϵ_{22} = -0.01750, σ_{22} = -82.87 MPa.

Figure 5.12: Evolution of mode II crack band in RUC subjected to applied transverse compressive strain if mode I crack band evolution is suppressed.

CHAPTER VI

Concluding Remarks

6.1 Conclusions

The focus of this dissertation was to develop multiscale analysis tools that capture as much of the physics of intralaminar damage and failure in polymer matrix composite fiber-reinforced laminates (FRLs) as possible while remaining suitable for use in engineering. Several models were developed to meet these requirements, and their capabilities were evaluated against experimental data. One theme used throughout this work was the separation of damage and failure. Damage was defined as the evolution of distributed structural changes in the material that manifest as pre-peak nonlinearities in the stress-strain response of the material. Conversely, failure was defined as effects of structural changes in the material that yield post-peak strain softening, which results in degradation localization. If not handled properly, failure results in discretization dependent solutions in a numerical setting. By separating damage and failure, the appropriate measures can be enacted to reformulate the evolution of failure, by incorporating a characteristic length, such that pathological mesh dependence is eliminated.

In Chapter II, the thermodynamically-based work potential theory, Schapery theory (ST) was presented. ST utilizes the stationarity of the total work potential with respect to internal state variables (ISVs) to arrive at evolution equations for the ISVs.

A single ISV was employed to model the effects of lamina level matrix microdamage in the FRL. The evolution of microdamage was investigated under a wide range of combined transverse and shear loading. It was determined that transverse, compressive strains impede microdamage growth while shear strain promotes it. Additionally, the stability of the work potential with respect to perturbations in the ISV was investigated to determine if the loss of stability could be used to mark the initiation of more catastrophic failure mechanism, such as transverse matrix cracking. The results indicated that the total work potential was unconditionally stable with respect to perturbations in the ISV; thus, explicit criteria are required to signal the onset of failure.

In Chapter III micromechanics was used to predict failure in the constituents of the composite in a numerical multiscale framework. ST was retained to model matrix microdamage at the macroscale, or lamina level. The micromechanics method, the generalized method of cells (GMC), was used model the localization of failure, at the appropriate scale, by employing failure criteria, meant to capture the effects of transverse cracking and fiber breakage, in the matrix and fiber of a repeating unit cell (RUC). Upon satisfaction of a criterion, the stiffness of the corresponding subcell was immediately diminished. The effects of the fiber-matrix architecture on the failure response of the composite were percolated up the scales through the homogenized stiffness of the RUC. Modeling distributed microdamage at the macroscale improved the computational efficiency of the model by avoiding function calls to the micromechanics subroutines unless the microdamage was above some nominal value. The multiscale model, ST-FEAMAC, was evaluated through comparison to global and local experimental data for two center-notched panels (CNPs) with different ply stacking orientations. Very good agreement between the model and experimental data was achieved, and the correct, global failure modes were predicted. One major drawback of this methodology was that the degradation scheme used at the microscale

was inherently mesh dependent. However, the demonstrated technique provided utilized intricate details of the composite microstructure while remaining computational feasibly and readily implemented.

The fourth and fifth chapters sought to remedy the mesh dependence of the failure methodology utilized in Chapter III. In Chapter IV, the multiscale approach was omitted, and instead, both damage and failure were accounted for at the macroscale. ST was reformulated as the enhanced Schapery theory (EST) by adding additional ISVs to account for failure due to transverse cracking and fiber breakage. The evolution of these ISVs was based upon the fracture toughness of the material, and it incorporated the characteristic length of the finite element, ensuring mesh objectivity. The evolution equations for the ISVs were derived within the thermodynamical consistent framework presented in Chapter II. Since the micromechanics was no longer used to incorporate the influence of the fiber and matrix in the laminae, assumptions were made on how the ISVs affected the stiffness tensor of a lamina. Additionally, separate ISVs had to be included for mode I and mode II transverse cracking. The performance of EST in an FEM setting was assessed by comparing the results of the numerical models of the same CNPs used in Chapter IV to the experimental data. The model results correlated well with the experimental data, and the globally observed failure modes in both specimens were predicted. Although EST requires more parameters to characterize the material failure than ST-FEAMAC (strengths and fracture toughnesses in the axial, transverse, and shear directions as compared to critical fiber strength, and transverse and shear strengths for the matrix), the failure parameters can be obtained from coupon level tests. Whereas, designing experiments for measuring in-situ matrix strengths is more difficult.

Finally, Chapter V revisited the micromechanics, and implemented a mesh objective, smeared crack band model into the HFGMC framework. The model utilized the principal stresses to determine the orientation of the crack bands in the subcells of the

RUC. It was assumed that the cracks within the band evolved under opening, mode I conditions perpendicular to the direction of maximum principal stress magnitude. However, if the principal stress component with maximum magnitude is compressive, it was assumed that the cracks inside the band grow under mode II conditions and are aligned with the plane of maximum shear stress. An RUC with 13, randomly placed fibers was loaded in transverse tension and compression. Global stress-strain results were compared to experimental data and exhibited good agreement. It was discovered that under global, transverse compression, mode II crack band evolution led to the observed non-linearities in the stress-strain response of the RUC, but it was tensile, mode I crack bands that dictated the ultimate failure of the RUC. This model can be utilized in future studies to determine the effects of the RUC size and geometry on the predictions of failure evolution in a composite lamina. Moreover, Chapter V presented a suitable micromechanics methodology that is capable of modeling the localization of failure objectively, at the microscale, and is suitable for implementation within a multiscale framework.

APPENDICES

APPENDIX A

Three-Dimensional Thermodynamically-Based Work Potential Theory for Orthotropic Microdamage Growth

Provided in this appendix are developments by the author to extend the thermodynamically-based work potential theory developed *Schapery and Sicking* (1995) for modeling progressive microdamage in two-dimensional (2D), plane stress, transversely isotropic solids to three-dimensional (3D), isotropic materials. The intention of this development is to use new theory to predict damage growth in the constituents of a composite material at the microscale, where, locally, plane stress assumptions are no longer valid. This microscale may then be tied to the macroscale via multiscale modeling [*Pineda et al.* (2008); *Gilat and Banks-Sills* (2010)].

Here, it is assumed that the matrix constituent of the composite is initially isotropic. Microdamage accrues within the solid; however, this damage growth is not necessarily isotropic. In fact, since induced microdamage in homogeneous materials is due to microcracking, damage will be dependent on the orientation of the microcracks. Thus, as microdamage evolves, the material will not behave isotropically, but rather will respond in a generally anisotropic manner.

A.1 Formulation of Three-Dimensional Thermodynamically-Based Work Potential Theory

A.1.1 Formulation of ST for Microdamage Growth in a 3D Isotropic Solid

In this section, the previously outlined work potential theory, Schapery theory (ST), will be specified for a 3D, isotropic solid exhibiting microdamage growth (3DST). As in ST, it is assumed in 3DST that the secant properties of the damaged material are related to the ISVs through a set of microdamage functions. Three functions are needed to characterize the material: normal tensile response function $e_S^T(W_S)$, normal compressive response function $e_S^C(W_S)$, and shear response function $g_S(W_S)$. Although there are only three microdamage functions, damage evolves through six different ISVs associated with the six, generally anisotropic moduli.

$$W_S = \tilde{S}_1 + \tilde{S}_2 + \tilde{S}_3 + \tilde{S}_4 + \tilde{S}_5 + \tilde{S}_6 \tag{A.1}$$

Even though all Young's moduli, and all shear moduli, depend on the same normal, or shear, microdamage functions, the arguments of those functions are different for each moduli

$$\begin{aligned} E_{11} &= E_0 e_S^n(\tilde{S}_1) \qquad G_{23} = G_0 g_S(\tilde{S}_4) \\ E_{22} &= E_0 e_S^n(\tilde{S}_2) \qquad G_{13} = G_0 g_S(\tilde{S}_5) \\ E_{33} &= E_0 e_S^n(\tilde{S}_3) \qquad G_{12} = G_0 g_S(\tilde{S}_6) \end{aligned} \tag{A.2}$$

where n is either tension (T) or compression (C). If all six ISVs were not independent, then damage growth would be independent of direction, and thus, would be more representative of spherical void growth, than microcrack growth. Utilizing the definition of the six state variables in the evolution equations, Equations (2.3) and

(2.4) yields six evolution equations for a 3D solid.

$$\frac{\partial W_T}{\partial \tilde{S}_i} = 0, \quad i = 1 \ldots 6 \tag{A.3}$$

$$\tilde{S}_i \geq 0, \quad i = 1 \ldots 6 \tag{A.4}$$

A.1.2 Reduction to a Single ISV Using Damage Directionality

The 3DST evolution equations presented in Equation (A.3) involve the solution of six equations for six ISVs. In a computational setting, where these evolution equations would needed to be solved a multitude of times, the solution process can be cumbersome. Here, the notion of directional damage and crack orientation will be used to reduce the number of independent ISVs to one, thus significantly reducing the computational intensity of the formulation.

It is assumed that microcracks grow in the material such that the crack surface normal is parallel to the direction of maximum principal strain $\mathbf{p}$. Figure A.1 shows an array of microcracks in a material oriented with the principal strains ($\epsilon_1 \geq \epsilon_2$). The components of the maximum principal strain vector in the basis frame are:

$$\mathbf{p} = \left\{ \begin{array}{c} p_1 \\ p_2 \\ p_3 \end{array} \right\} \tag{A.5}$$

Using the components of $\mathbf{p}$, the six ISVs $\tilde{S}_i$ can be related to a single ISV S,

$$\left\{ \begin{array}{c} \tilde{S}_1 \\ \tilde{S}_2 \\ \tilde{S}_3 \\ \tilde{S}_4 \\ \tilde{S}_5 \\ \tilde{S}_6 \end{array} \right\} = \left\{ \begin{array}{c} p_1^2 \\ p_2^2 \\ p_3^2 \\ p_2^2 + p_3^2 \\ p_1^2 + p_3^2 \\ p_1^2 + p_2^2 \end{array} \right\} \frac{S}{3} \tag{A.6}$$

where S is a scalar measure of the total energy dissipated through all the directional damage variables $\tilde{S}_i$. Thus (and from Equation (A.6)),

$$\sum_{i=1}^{6} \tilde{S}_i = S \tag{A.7}$$

The vector on the right-hand side of Equation (A.6) was postulated such that the normal damage components ($\tilde{S}_1$, $\tilde{S}_2$, and $\tilde{S}_3$) only evolve if the maximum principal strain contains components that lie in the i-direction, and the shear damage components ($\tilde{S}_4$, $\tilde{S}_5$, and $\tilde{S}_6$) only evolve if the maximum principal strain contains components that lie in the plane on which the shear modulus, associated the evolving shear damage component, operates. Note that no damage will accrue in direction i if $p_i = 0$; therefore, the presence of microcracks oriented such that the normals to the crack faces are perpendicular to i will not affect the stiffness in the i-direction. The postulation of Equation (A.6) reduces Equation (A.1) to a function of a single ISV.

$$W_S = S \tag{A.8}$$

Utilizing Equations (2.1) and (A.9) in Equation (2.3) yields a single evolution

equation for S.

$$\frac{\partial W}{\partial S} = -1 \tag{A.9}$$

Once S is determined Equation (A.7) can be used, along with $\mathbf{p}$, to determine $\tilde{S}_i$. Note that Equation (A.7) cannot be used to reduce Equation (A.4) to a single expression; thus, inadmissability of healing must be enforced for each of the original ISVs individually.

The elastic strain energy density function can be defined.

$$\begin{aligned} W = \frac{1}{2}\left(C_{11}\epsilon_{11}^2 + C_{22}\epsilon_{22}^2 + C_{33}\epsilon_{33}^2 + C_{44}\gamma_{23}^2 + C_{55}\gamma_{13}^2 + C_{66}\gamma_{12}^2\right) \\ + C_{12}\epsilon_{11}\epsilon_{22} + C_{13}\epsilon_{11}\epsilon_{33} + C_{23}\epsilon_{22}\epsilon_{33} \end{aligned} \tag{A.10}$$

Where C_{ij} are the orthotropic stiffness constants which can be represented with the moduli given in Equation (A.2) [*Jones* (1999)]. The elastic stiffness tensor is orthotropic because microdamage can induce orthotropy; therefore, isotropy cannot be assumed. Substituting the 3D, orthotropic definition of W into Equation (A.9) yields the evolution equation that must be solved for the ISV S,

$$\begin{aligned} \frac{1}{2}\left(\epsilon_{11}^2\frac{\partial C_{11}}{\partial S} + \epsilon_{22}^2\frac{\partial C_{22}}{\partial S} + \epsilon_{33}^2\frac{\partial C_{33}}{\partial S}\ \gamma_{23}^2\frac{\partial C_{44}}{\partial S} + \gamma_{13}^2\frac{\partial C_{55}}{\partial S} + \gamma_{12}^2\frac{\partial C_{66}}{\partial S}\right) \\ + \epsilon_{11}\epsilon_{22}\frac{\partial C_{12}}{\partial S} + \epsilon_{11}\epsilon_{33}\frac{\partial C_{13}}{\partial S} + \epsilon_{22}\epsilon_{33}\frac{\partial C_{23}}{\partial S} + 1 = 0 \end{aligned} \tag{A.11}$$

keeping in mind Equations (A.4). The partial derivatives in Equation (A.11) are functions of S and the components of $\mathbf{p}$ given by Equations (A.2) and (A.6).

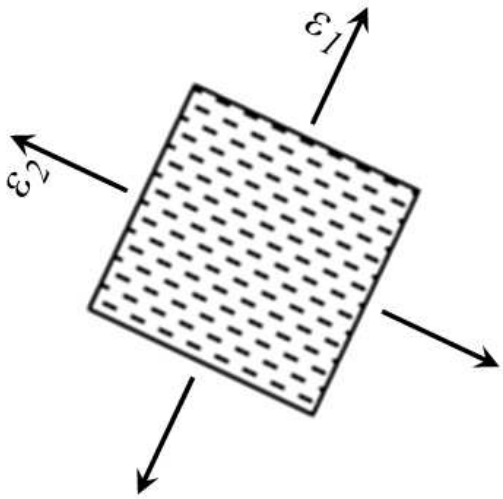

Figure A.1: Array of microcracks in material element oriented with principal strain frame.

APPENDIX B

Cohesive Zone-Based Debonding in the Generalized Method of Cells

B.1 Formulation of Cohesive Zone-Based Interfacial Debonding

B.1.1 Displacement Continuity Conditions

The generalized method of cells (GMC) employs displacement and traction continuity at the boundaries of all subcells in, and the periodic boundaries of, the repeating unit cell (RUC), shown in Figure 3.2. Debonding can modeled at these interfaces by including a displacement jump in the interfacial displacement continuity relations. These six conditions, which admit interfacial displacement discontinuities and replace Equations (3.22)-(3.26) and (3.28), are given by *Aboudi et al.* (2012)

$$\bar{\epsilon}_{11} = \frac{1}{d}\sum_{\alpha=1}^{N_\alpha}\left(d_\alpha \epsilon_{11}^{(\alpha\beta\gamma)} + [u_{11}]^{(\alpha\beta\gamma)}\right), \qquad \begin{matrix}\beta = 1,\ldots,N_\beta \\ \gamma = 1,\ldots,N_\gamma\end{matrix} \tag{B.1}$$

$$\bar{\epsilon}_{22} = \frac{1}{h}\sum_{\alpha=1}^{N_\alpha}\left(h_\beta \epsilon_{22}^{(\alpha\beta\gamma)} + [u_{22}]^{(\alpha\beta\gamma)}\right), \qquad \begin{matrix}\alpha = 1,\ldots,N_\alpha \\ \gamma = 1,\ldots,N_\gamma\end{matrix} \tag{B.2}$$

$$\bar{\epsilon}_{33} = \frac{1}{\ell}\sum_{\alpha=1}^{N_\alpha}\left(l_\gamma \epsilon_{33}^{(\alpha\beta\gamma)} + [u_{33}]^{(\alpha\beta\gamma)}\right), \qquad \begin{matrix}\alpha = 1,\ldots,N_\alpha \\ \beta = 1,\ldots,N_\beta\end{matrix} \tag{B.3}$$

$$\bar{\epsilon}_{23} = \frac{1}{h\ell}\sum_{\beta=1}^{N_\beta}\sum_{\gamma=1}^{N_\gamma}\left[h_\beta l_\gamma \epsilon_{23}^{(\alpha\beta\gamma)} + \frac{1}{2}\left([u_{23}]^{(\alpha\beta\gamma)} + [u_{32}]^{(\alpha\beta\gamma)}\right)\right], \quad \alpha = 1,\ldots,N_\alpha \tag{B.4}$$

$$\bar{\epsilon}_{13} = \frac{1}{d\ell}\sum_{\beta=1}^{N_\beta}\sum_{\gamma=1}^{N_\gamma}\left[d_\alpha l_\gamma \epsilon_{13}^{(\alpha\beta\gamma)} + \frac{1}{2}\left([u_{13}]^{(\alpha\beta\gamma)} + [u_{31}]^{(\alpha\beta\gamma)}\right)\right], \quad \beta = 1,\ldots,N_\beta \tag{B.5}$$

$$\bar{\epsilon}_{12} = \frac{1}{dh}\sum_{\beta=1}^{N_\beta}\sum_{\gamma=1}^{N_\gamma}\left[d_\alpha h_\beta \epsilon_{12}^{(\alpha\beta\gamma)} + \frac{1}{2}\left([u_{12}]^{(\alpha\beta\gamma)} + [u_{21}]^{(\alpha\beta\gamma)}\right)\right], \quad \gamma = 1,\ldots,N_\gamma \tag{B.6}$$

where d, h, and ℓ are the RUC dimensions in the x_1-, x_2-, and x_3-directions (Figure 3.2). Similarly, d_α, h_β, and l_γ are the subcell dimensions and α, β, and γ are the subcell numbers in the x_1-, x_2-, and x_3-directions, respectively. The average, global, tensorial strains are represented with $\bar{\epsilon}_{ij}$, and $\epsilon_{ij}^{(\alpha\beta\gamma)}$ are the strains in each subcell. The interfacial discontinuity $[u_{Ij}]^{(\alpha\beta\gamma)}$ is the displacement jump in the j-direction across interface with unit normal in the I-direction. Note that Equations (B.1)-(B.6) represent the displacement continuity conditions for a triply-periodic RUC (see Figure 3.2), whereas, Equations (3.22)-(3.26) and (3.28) are for a doubly-periodic RUC (see Figure 3.3).

B.1.2 Relationship Between Interfacial Displacement Jump and Traction

The displacement jump across the interface is related to the traction at the interface through a scaling parameter, first proposed by *Jones and Whittier* (1967).

$$[u_{Ij}]^{(\alpha\beta\gamma)} = R_{Ij}^{(\alpha\beta\gamma)}\sigma_{Ij}^{(\alpha\beta\gamma)}; \qquad f_{DB_I}^{(\alpha\beta\gamma)} \geq 1; \tag{B.7}$$

where $\sigma_{Ij}^{(\alpha\beta\gamma)}$ is the traction in subcell $\alpha\beta\gamma$ at interface I. Thus, Equation (B.7) is a traction-separation law for the interfaces. Note that, Einstein notation is not being used; here, repeated indices do not indicate a summation. Interfacial debonding is precluded (i.e. $R_{Ij}^{(\alpha\beta\gamma)} = 0$, and the interface is perfectly bonded) if the value of interfacial strength criterion $f_{DB_I}^{(\alpha\beta\gamma)}$ remains below unity. This strength criterion is completely general and can involve stresses or strains. Compliance of the interface is represented with $R_{ij}^{(\alpha\beta\gamma)}$, and can take numerous forms. In the *Jones and Whittier* (1967) flexible interface model, the compliance of the interface is taken to be a constant. The flexible interface model was originally implemented into the method of cells (MOC) by *Aboudi* (1987) and GMC by *Sankurathri et al.* (1996). Debonding was restricted if the interface was subjected to compression by *Achenbach and Zhu* (1989). The flexible interface model was further extended by *Bednarcyk and Arnold* (2000, 2002a); *Bednarcyk et al.* (2004) with the evolving compliant interface (ECI) model. The ECI model utilized a time dependent compliance, altering Equation (B.7).

$$[u_{Ij}]^{(\alpha\beta\gamma)} = R_{Ij}^{(\alpha\beta\gamma)}(t)\,\sigma_{Ij}^{(\alpha\beta\gamma)}; \qquad f_{DB_I}^{(\alpha\beta\gamma)} \geq 1; \tag{B.8}$$

where the interfacial compliance is explicitly related to time.

$$R_{Ij}^{(\alpha\beta\gamma)}(t) = \Lambda_{Ij}^{(\alpha\beta\gamma)}\left[\exp\left(\frac{t - t_{DB}}{B_{Ij}^{(\alpha\beta\gamma)}}\right) - 1\right]; \qquad t \geq t_{DB}, \tag{B.9}$$

where t_{DB} is the time at which debonding occurs, and $\Lambda_{Ij}^{(\alpha\beta\gamma)}$ and $B_{Ij}^{(\alpha\beta\gamma)}$ are parameters that characterize the relationship between the evolving interfacial compliance and time. The ECI model was used in GMC and the high-fidelity generalized method of cells (HFGMC) to study fiber-matrix debonding in titanium matrix composites. *Ranatunga et al.* (2009, 2010a) used ECI and GMC in a multiscale framework to investigate delamination and in-plane fracture, and compared the results to DCZM finite elements, the virtual crack closure technique (VCCT), and the extended finite

element method (XFEM). *Pineda et al.* (2010a) used ECI to model matrix cracking in very simple GMC RUCs.

The current work focuses on using the Jones and Whittier traction-separation relationship to model fracture within polymer-matrix composite (PMC) RUCs. Fracture can occur not only at a fiber-matrix interface, but also within the bulk matrix surrounding the fibers. To incorporate the physics of fracture, by relating the evolution of the interfacial compliance to measurable quantities using a cohesive zone model, the form of the interfacial compliance is such that the incremental change in the interfacial compliance takes the form

$$\begin{aligned} dR_{Ij}^{(\alpha\beta\gamma)} &= \frac{A_{Ij}^{(\alpha\beta\gamma)}}{\mathcal{G}_{C_{Ij}}^{(\alpha\beta\gamma)} - \mathcal{G}_{Ij}^{(\alpha\beta\gamma)}}, \\ dR_{Ij}^{(\alpha\beta\gamma)} &= 0, \qquad \text{if } d\mathcal{G}_{Ij}^{(\alpha\beta\gamma)} < 0 \\ dR_{Ij}^{(\alpha\beta\gamma)} &= 0, \qquad \begin{array}{c}\text{if j=I, and} \\ \sigma_{Ij}^{(\alpha\beta\gamma)} < 0\end{array} \end{aligned} \tag{B.10}$$

where $\mathcal{G}_{Ij}^{(\alpha\beta\gamma)}$ is the strain energy release rate (SERR) of the interface,

$$\mathcal{G}_{Ij}^{(\alpha\beta\gamma)} = \int \sigma_{Ij}^{(\alpha\beta\gamma)} d\left[u_{Ij}\right]^{(\alpha\beta\gamma)}, \text{ no sum on } I, j \tag{B.11}$$

If $I = j$ the interface undergoes mode I (normal) fracture. Under mode I conditions, if the traction is compressive, the interface is treated as perfectly bonded, and the crack cannot grow in mode I. If $I \neq j$ then the interface is subjected to mode II (shearing) or mode III (twisting) fracture [*Sanford* (2002)]. See Figure B.1 for diagrams exhibiting the three modes of fracture. Additionally, if the interface unloads ($d\mathcal{G}_{Ij}^{(\alpha\beta\gamma)} < 0$), it unloads along the secant stiffness from the previous increment; thus, there is no change in the compliance. **?** introduced cohesive-zone based debonding to MOC by

including five additional subcells between the original fiber-matrix and matrix-matrix interfaces. The micromechanics equations were reformulated incrementally, and the behavior of the five additional subcells was governed by traction-separation laws.

In Equation (B.10), $\mathcal{G}_{C_{Ij}}^{(\alpha\beta\gamma)}$ is the critical fracture energy of the debonding interface. As $\mathcal{G}_{Ij}^{(\alpha\beta\gamma)}$ approaches $\mathcal{G}_{C_{Ij}}^{(\alpha\beta\gamma)}$, $R_{Ij}^{(\alpha\beta\gamma)} \to \infty$, and the interface cannot carry any traction. Thus, the form of Equation (B.10) ensures that the area under the traction versus separation curve is always equal to the critical fracture energy upon complete fracture of the interface (i.e., the interface loses all load carrying capability), as is common with tractions-separation laws (TSLs) used in discrete cohesive zone models (DCZMs) [*Xie et al.* (2006); *Xie and Waas* (2006); *Gustafson and Waas* (2009)], and nodally enriched finite elements (FEs) [*Garikipati* (1996); *Rudraraju et al.* (2008, 2009)]. A triangular TSL, typically used in FE applications, is displayed in Figure B.1; however, the TSL can take any applicable shape as long as the area under the curve is equal to the critical fracture energy [*Gustafson and Waas* (2008, 2009); *Wang* (2010)].

Crack growth initiates when the interfacial traction exceeds strength $\sigma_{C_{Ij}}^{(\alpha\beta\gamma)}$ (or σ_C in Figure B.1), or when the interfacial tractions satisfy some mixed-mode initiation criterion. If the interface subsequently unloads along the arrowed line in Figure B.1, then the purple area under the TSL curve is the SERR. The total area under the curve (both the purple and orange areas) is the critical fracture energy. If the interface is reloaded and the displacement discontinuity across the interfaces reaches δ_f, the interface has completely fractured, the traction at the interface is zero, and the SERR is equal to the critical fracture energy. In Equation (B.10), the denominator preserves the critical fracture energy, but the parameter $A_{Ij}^{(\alpha\beta\gamma)}$ controls the shape of the TSL. This parameter can be calculated to ensure the slope of the TSL is equal to $K_{T_{Ij}}^{(\alpha\beta\gamma)}$, or K_T in Figure B.1, and the law is triangular.

If it is desirable to capture micromechanical crack growth in a composite RUC, all fiber-matrix and matrix-matrix interfaces can be modeled using cohesive zones with

the form of the interfacial compliance increment given by Equation (B.10). Additionally, the fracture parameters ($\mathcal{G}_{C_{Ij}}^{(\alpha\beta\gamma)}, \sigma_{C_{Ij}}^{(\alpha\beta\gamma)}$) used at the different interfaces need not be the same. Furthermore, crack evolution in bulk, composite materials, or monolithic materials, can be investigated by using an RUC containing a single constituent, where every subcell has properties equal to the homogenized properties of the composite, or the monolithic material. The fracture properties of the RUC interfaces will be equal to the fracture properties of the bulk material. This type of analysis is suitable for investigating interlaminar, as well as through-thickness, crack growth. A demonstration of crack growth in the two different types of RUCs is shown in Figure B.2.

B.1.3 Mixed-Mode Crack Initiation and Fracture

Interfacial debonding does not occur (the interfacial compliance is zero and the interface is perfectly bonded) until a damage initiation criterion is satisfied; $f_{DB_I}^{(\alpha\beta\gamma)} \geq 1$ at interface I. The criterion can be a simple, maximum stress criterion

$$f_{DB_I}^{(\alpha\beta\gamma)} = \begin{cases} \dfrac{\left\langle \sigma_{Ij}^{(\alpha\beta\gamma)} \right\rangle}{\sigma_{C_{Ij}}^{(\alpha\beta\gamma)}} & \text{if } j \neq I, \text{ or if } j = I \text{ and } \sigma_{Ij}^{(\alpha\beta\gamma)} \geq 0 \\ 0 & \text{if } j = I \text{ and } \sigma_{Ij}^{(\alpha\beta\gamma)} < 0 \end{cases} \tag{B.12}$$

where $\sigma_{C_{Ij}}^{(\alpha\beta\gamma)}$ is strength of interface I in the j-direction. Equation (B.12) must be satisfied for a particular mode if debonding is to occur in that mode, and j is the direction associated with the crack tip opening displacement needed to advance a crack under that mode. If $j = I$, the interface is subjected to mode I traction, and $\sigma_{Ij}^{(\alpha\beta\gamma)}$ must be greater than zero for crack initiation. If $\sigma_{Ij}^{(\alpha\beta\gamma)} < 0$ the interface is under compressions, and the crack cannot advance.

One disadvantage of using a maximum value initiation criterion, such as Equation

(B.12), is that debonding can initiate in one mode but the interface remains perfectly bonded in the other two modes, which is not consistent with the physics of fracture. A quadratic, stress criterion can be used to obtain more realistic crack initiation conditions.

$$f_{DB_I}^{(\alpha\beta\gamma)} = \left(\frac{\left\langle \sigma_{Ii}^{(\alpha\beta\gamma)} \right\rangle}{\sigma_{C_{Ii}}^{(\alpha\beta\gamma)}} \right)^2 + \left(\frac{\sigma_{Ij}^{(\alpha\beta\gamma)}}{\sigma_{C_{Ij}}^{(\alpha\beta\gamma)}} \right)^2 + \left(\frac{\sigma_{Ik}^{(\alpha\beta\gamma)}}{\sigma_{C_{Ik}}^{(\alpha\beta\gamma)}} \right)^2, \quad i = I, j \neq i, \text{and } k \neq i \neq j \tag{B.13}$$

where i is the direction associated with normal mode I fracture along interface I, and j and k are the directions corresponding to the two shearing modes (modes II and III). Note that the mode I stress $\sigma_{iI}^{(\alpha\beta\gamma)}$ is contained in Macaulay brackets signifying that only tensile, mode I stresses contribute to crack initiation. If the interface is subjected to mode I compression, mode I cracks cannot nucleate.

In addition to interfacial crack initiation, crack evolution must also be defined. Similar to Equation (B.12), an uncoupled damage evolution law can be used based on the SERR and critical fracture energy.

$$\frac{\mathcal{G}_{Ij}^{(\alpha\beta\gamma)}}{\mathcal{G}_{C_{Ij}}^{(\alpha\beta\gamma)}} = 1 \tag{B.14}$$

When Equation (B.14) is satisfied, the interface has fractured completely in the mode associated with the displacement in the j-direction, and the traction $\sigma_{Ij}^{(\alpha\beta\gamma)}$ is equal to zero.

Equation (B.14) does not introduce energy dissipation interaction between the different modes. Therefore, it is common practice to use a mixed-mode, energetic, power law for fracture evolution,

$$\left(\frac{\mathcal{G}_{Ii}^{(\alpha\beta\gamma)}}{\mathcal{G}_{C_{Ii}}^{(\alpha\beta\gamma)}} \right)^m + \left(\frac{\mathcal{G}_{Ij}^{(\alpha\beta\gamma)}}{\mathcal{G}_{C_{Ij}}^{(\alpha\beta\gamma)}} \right)^n + \left(\frac{\mathcal{G}_{Ik}^{(\alpha\beta\gamma)}}{\mathcal{G}_{C_{Ik}}^{(\alpha\beta\gamma)}} \right)^p = 1 \tag{B.15}$$

where m, n, and p are experimentally correlated parameters, for a given material system [*Johnson and Mangalgiri* (1985)]. When Equation (B.15) is satisfied, the interface has fractured completely in all three modes, and the tractions associated with those modes are zero. It should be noted that Equations (B.13) and (B.15) are simply empirical fits to experimental observations. To arrive at true mixed-mode initiation and evolution conditions, atomistic investigations into fracture are required.

B.1.4 Introducing Cohesive Zone-Based Interfacial Debonding into GMC

The traction-separation relationships, Equation (B.8), can be used in the displacement continuity equations, Equations (B.1)-(B.6).

$$\bar{\epsilon}_{11} = \frac{1}{d}\sum_{\alpha=1}^{N_\alpha}\left(d_\alpha \epsilon_{11}^{(\alpha\beta\gamma)} + R_{11}^{(\alpha\beta\gamma)}\sigma_{11}^{(\alpha\beta\gamma)}\right), \qquad \begin{matrix}\beta = 1,\ldots,N_\beta \\ \gamma = 1,\ldots,N_\gamma\end{matrix} \tag{B.16}$$

$$\bar{\epsilon}_{22} = \frac{1}{h}\sum_{\beta=1}^{N_\beta}\left(h_\beta \epsilon_{22}^{(\alpha\beta\gamma)} + R_{22}^{(\alpha\beta\gamma)}\sigma_{22}^{(\alpha\beta\gamma)}\right), \qquad \begin{matrix}\alpha = 1,\ldots,N_\alpha \\ \gamma = 1,\ldots,N_\gamma\end{matrix} \tag{B.17}$$

$$\bar{\epsilon}_{33} = \frac{1}{\ell}\sum_{\gamma=1}^{N_\gamma}\left(l_\gamma \epsilon_{33}^{(\alpha\beta\gamma)} + R_{33}^{(\alpha\beta\gamma)}\sigma_{33}^{(\alpha\beta\gamma)}\right), \qquad \begin{matrix}\alpha = 1,\ldots,N_\alpha \\ \beta = 1,\ldots,N_\beta\end{matrix} \tag{B.18}$$

$$\bar{\epsilon}_{23} = \frac{1}{h\ell}\sum_{\beta=1}^{N_\beta}\sum_{\gamma=1}^{N_\gamma}\left[h_\beta l_\gamma \epsilon_{23}^{(\alpha\beta\gamma)} + \frac{1}{2}\left(l_\gamma R_{23}^{(\alpha\beta\gamma)}\sigma_{23}^{(\alpha\beta\gamma)} + h_\beta R_{32}^{(\alpha\beta\gamma)}\sigma_{32}^{(\alpha\beta\gamma)}\right)\right], \qquad \alpha = 1,\ldots,N_\alpha \tag{B.19}$$

$$\bar{\epsilon}_{13} = \frac{1}{d\ell}\sum_{\alpha=1}^{N_\alpha}\sum_{\gamma=1}^{N_\gamma}\left[d_\alpha l_\gamma \epsilon_{13}^{(\alpha\beta\gamma)} + \frac{1}{2}\left(l_\gamma R_{13}^{(\alpha\beta\gamma)}\sigma_{13}^{(\alpha\beta\gamma)} + d_\alpha R_{31}^{(\alpha\beta\gamma)}\sigma_{31}^{(\alpha\beta\gamma)}\right)\right], \qquad \beta = 1,\ldots,N_\beta \tag{B.20}$$

$$\bar{\epsilon}_{12} = \frac{1}{dh}\sum_{\alpha=1}^{N_\alpha}\sum_{\beta=1}^{N_\beta}\left[d_\alpha h_\beta \epsilon_{12}^{(\alpha\beta\gamma)} + \frac{1}{2}\left(h_\beta R_{12}^{(\alpha\beta\gamma)}\sigma_{12}^{(\alpha\beta\gamma)} + d_\alpha R_{21}^{(\alpha\beta\gamma)}\sigma_{21}^{(\alpha\beta\gamma)}\right)\right], \qquad \gamma = 1,\ldots,N_\gamma \tag{B.21}$$

Written in matrix form, the displacement continuity equations become

$$(\mathbf{A_G} + \mathbf{A_R})\,\boldsymbol{\epsilon_s} = \mathbf{J}\bar{\boldsymbol{\epsilon}} \tag{B.22}$$

where $\mathbf{A_G}$ and $\mathbf{J}$ remain unchanged from the GMC formulation with perfect bonding, and $\mathbf{A_R}$ contains the debonding information. If there is no debonding, $\mathbf{A_R} = \mathbf{0}$. Local, subcell strains are contained in the vector $\boldsymbol{\epsilon_s}$.

$$\boldsymbol{\epsilon_s} = \left\{\boldsymbol{\epsilon}^{(111)}, \ldots, \boldsymbol{\epsilon}^{(N_\alpha N_\beta N_\gamma)}\right\} \tag{B.23}$$

where

$$\bar{\boldsymbol{\epsilon}}^{(\alpha\beta\gamma)} = \left\{\epsilon_{11}^{(\alpha\beta\gamma)}, \epsilon_{22}^{(\alpha\beta\gamma)}, \epsilon_{33}^{(\alpha\beta\gamma)}, 2\epsilon_{23}^{(\alpha\beta\gamma)}, 2\epsilon_{13}^{(\alpha\beta\gamma)}, 2\epsilon_{12}^{(\alpha\beta\gamma)}\right\} \tag{B.24}$$

The vector $\bar{\boldsymbol{\epsilon}}$ houses the average, global strains.

$$\bar{\boldsymbol{\epsilon}} = \{\bar{\epsilon}_{11}, \bar{\epsilon}_{22}, \bar{\epsilon}_{33}, 2\bar{\epsilon}_{23}, 2\bar{\epsilon}_{13}, 2\bar{\epsilon}_{12}\} \tag{B.25}$$

After including the traction continuity conditions, the overall relationship between the global strains and the local, subcell strains becomes

$$\tilde{\mathbf{A}}\boldsymbol{\epsilon_s} = \mathbf{K}\bar{\boldsymbol{\epsilon}} \tag{B.26}$$

where

$$\tilde{\boldsymbol{A}} = \begin{bmatrix} \boldsymbol{A_M} \\ \boldsymbol{A_G} + \boldsymbol{A_R} \end{bmatrix} \tag{B.27}$$

and

$$\boldsymbol{K} = \begin{bmatrix} \mathbf{0} \\ \boldsymbol{J} \end{bmatrix} \tag{B.28}$$

Equation (B.26) can be solved for the subcell strains

$$\boldsymbol{\epsilon_s} = \boldsymbol{A}\bar{\boldsymbol{\epsilon}} \tag{B.29}$$

where **A** is the strain concentration matrix, containing the interfacial compliances, given by

$$\mathbf{A} = \tilde{\mathbf{A}}^{-1}\mathbf{K} \tag{B.30}$$

B.1.5 Solving for the Interfacial Compliance Scaling Parameter

The shape of the TSL curve at a debonding interface is controlled by the scaling parameter $A_{Ij}^{(\alpha\beta\gamma)}$ in the interfacial compliance evolution relationship, Equation (B.10). To obtain a triangular TSL, the appropriate $A_{Ij}^{(\alpha\beta\gamma)}$ can be determined from the traction continuity equations. It should be noted that, for a given strain increment, $A_{Ij}^{(\alpha\beta\gamma)}$ can remain constant due to the form of Equation (B.7), which ensures that the area under the TSL is equal to the critical fracture energy. Upon debonding initiation, a particular $A_{Ij}^{(\alpha\beta\gamma)}$ will results in an initial interfacial compliance increment

$$dR_{0_{Ij}}^{(\alpha\beta\gamma)} = \frac{A_{Ij}^{(\alpha\beta\gamma)}}{\mathcal{G}_{C_{Ij}}^{(\alpha\beta\gamma)}} \tag{B.31}$$

noting that, initially, there is no displacement jump across the interface; therefore, $[u_{Ij}]^{(\alpha\beta\gamma)} = 0$, and thus, $\mathcal{G}_{Ij}^{(\alpha\beta\gamma)} = 0$. If this interfacial compliance increment produces subsequent traction and separation increments,

$$\frac{d\sigma_{Ij}^{(\alpha\beta\gamma)}}{d\left[u_{Ij}\right]^{(\alpha\beta\gamma)}} = K_{T_{Ij}}^{(\alpha\beta\gamma)} \tag{B.32}$$

where $K_{T_{Ij}}^{(\alpha\beta\gamma)}$ is the tangent slope of the TSL. If

$$K_{T_{Ij}}^{(\alpha\beta\gamma)} = -\frac{{\sigma_{C_{Ij}}^{(\alpha\beta\gamma)}}^2}{2\mathcal{G}_{C_{Ij}}^{(\alpha\beta\gamma)}} \tag{B.33}$$

then the shape of the TSL is triangular because Equation (B.32) is equal to the slope of the hypotenuse of a right triangle with an area of $\mathcal{G}_{C_{Ij}}^{(\alpha\beta\gamma)}$. The form of Equation (B.10) requires that the area under the TSL is equal to the critical fracture energy. Therefore, if the initial slope of the TSL is given by Equation (B.33), $K_{T_{Ij}}^{(\alpha\beta\gamma)}$ will not need to change for the area under the TSL to be equal to $\mathcal{G}_{C_{Ij}}^{(\alpha\beta\gamma)}$. If $A_{Ij}^{(\alpha\beta\gamma)}$ is chosen such that the initial traction and separation increments do not satisfy Equation (B.33), then the slope of the TSL will adjust accordingly as debonding evolves, yielding a TSL that is not triangular in shape, but still has an area that is equal to $\mathcal{G}_{C_{Ij}}^{(\alpha\beta\gamma)}$.

For normal debonding in the x_1-direction at interfaces with unit normals in the x_1-direction, Equation (B.16) can be re-written in incremental form. To solve for $A_{11}^{(\alpha\beta\gamma)}$, the incremental form of Equation (B.16) only needs to be solved upon initial debonding, therefore $R_{11}^{(\alpha\beta\gamma)} = 0$.

$$d\bar{\epsilon}_{11} = \frac{1}{\bar{d}} \sum_{\alpha=1}^{N_\alpha} \left(d_\alpha d\epsilon_{11}^{(\alpha\beta\gamma)} + dR_{0_{11}}^{(\alpha\beta\gamma)} \sigma_{11}^{(\alpha\beta\gamma)} \right), \qquad \begin{matrix} \beta = 1, \ldots, N_\beta \\ \gamma = 1, \ldots, N_\gamma \end{matrix} \tag{B.34}$$

where, for notational clarity, $\bar{d}$ is now the RUC dimension in the x_1-direction, and d represents an increment in the adjacent variable. The local subcell strain increments can are related to the local subcell stress increments through the subcell constitutive properties.

$$d\epsilon_{11}^{(\alpha\beta\gamma)} = S_{11}^{(\alpha\beta\gamma)} d\sigma_{11}^{(\alpha\beta\gamma)} + S_{12}^{(\alpha\beta\gamma)} d\sigma_{22}^{(\alpha\beta\gamma)} + S_{13}^{(\alpha\beta\gamma)} d\sigma_{33}^{(\alpha\beta\gamma)}, \qquad \begin{matrix} \alpha = 1, \ldots, N_\alpha \\ \beta = 1, \ldots, N_\beta \\ \gamma = 1, \ldots, N_\gamma \end{matrix} \tag{B.35}$$

Equation (B.35) assumes that the elastic properties of the subcells do not change due to strain induced damage ($dS_{Ij}^{(\alpha\beta\gamma)} = 0$). If subcell damage is desired, the strain increment (Equation (B.35) can be recalculated assuming $dS_{Ij}^{(\alpha\beta\gamma)} \neq 0$. Substituting Equation (B.35) into Equation (B.34) and introducing a new global strain measure

$$d\hat{\epsilon}_{11} = d\bar{\epsilon}_{11} - \frac{1}{\bar{d}} \sum_{\alpha=1}^{N_\alpha} d_\alpha \left(S_{12}^{(\alpha\beta\gamma)} d\sigma_{22}^{(\alpha\beta\gamma)} + S_{13}^{(\alpha\beta\gamma)} d\sigma_{33}^{(\alpha\beta\gamma)} \right), \quad \begin{matrix} \beta = 1, \ldots, N_\beta \\ \gamma = 1, \ldots, N_\gamma \end{matrix} \tag{B.36}$$

yields

$$d\hat{\epsilon}_{11} = \frac{1}{\bar{d}} \sum_{\alpha=1}^{N_\alpha} \left(d_\alpha S_{11}^{(\alpha\beta\gamma)} d\sigma_{11}^{(\alpha\beta\gamma)} + dR_{0_{11}}^{(\alpha\beta\gamma)} \sigma_{11}^{(\alpha\beta\gamma)} \right), \quad \begin{matrix} \beta = 1, \ldots, N_\beta \\ \gamma = 1, \ldots, N_\gamma \end{matrix} \tag{B.37}$$

Equation (B.37) can be utilized in Equation (B.1), and Equation (B.1) can be differentiated with respect to $d\hat{\epsilon}_{11}$.

$$1 = \frac{1}{\bar{d}} \sum_{\alpha=1}^{N_\alpha} \left(d_\alpha S_{11}^{(\alpha\beta\gamma)} \frac{\partial \sigma_{11}^{(\alpha\beta\gamma)}}{\partial \hat{\epsilon}_{11}} + \frac{\partial \left[u_{11} \right]^{(\alpha\beta\gamma)}}{\partial \hat{\epsilon}_{11}} \right), \quad \begin{matrix} \beta = 1, \ldots, N_\beta \\ \gamma = 1, \ldots, N_\gamma \end{matrix} \tag{B.38}$$

Using the chain rule,

$$\frac{\partial \sigma_{11}^{(\alpha\beta\gamma)}}{\partial \hat{\epsilon}_{11}} = \frac{\partial \sigma_{11}^{(\alpha\beta\gamma)}}{\partial \left[u_{11} \right]^{(\alpha\beta\gamma)}} \frac{\partial \left[u_{11} \right]^{(\alpha\beta\gamma)}}{\partial \hat{\epsilon}_{11}}, \quad \begin{matrix} \alpha = 1, \ldots, N_\alpha \\ \beta = 1, \ldots, N_\beta \\ \gamma = 1, \ldots, N_\gamma \end{matrix} \tag{B.39}$$

and realizing Equation(B.32), yields

$$\frac{\partial \left[u_{11} \right]^{(\alpha\beta\gamma)}}{\partial \hat{\epsilon}_{11}} = \frac{1}{K_{T_{11}}^{(\alpha\beta\gamma)}} \frac{\partial \sigma_{11}^{(\alpha\beta\gamma)}}{\partial \hat{\epsilon}_{11}}, \quad \begin{matrix} \alpha = 1, \ldots, N_\alpha \\ \beta = 1, \ldots, N_\beta \\ \gamma = 1, \ldots, N_\gamma \end{matrix} \tag{B.40}$$

If subcell $(\alpha\beta\gamma)$ is not debonding at interface $I = 1$ in the x_1-direction the interface is perfectly bonded; therefore $K_{T_{11}}^{(\alpha\beta\gamma)} = \infty$ and $\partial \left[u_{11}\right]^{(\alpha\beta\gamma)} / \partial \hat{\epsilon}_{11} = 0$. Due to the traction continuity conditions and the linear displacement fields used in GMC, for a given β and γ, $\sigma_{11}^{(\alpha\beta\gamma)}$ are equal for any α; thus, $\sigma_{11}^{(\alpha\beta\gamma)}$ is independent of α.

$$\sigma_{11}^{(\alpha\beta\gamma)} = \sigma_{11}^{(\beta\gamma)}, \qquad \begin{matrix} \beta = 1, \ldots, N_\beta \\ \gamma = 1, \ldots, N_\gamma \end{matrix} \tag{B.41}$$

Substituting Equations (B.40) and (B.41) into Equation (B.38), results in

$$\frac{\partial \sigma_{11}^{(\beta\gamma)}}{\partial \hat{\epsilon}_{11}} = \left[\frac{1}{\bar{\bar{d}}} \sum_{\alpha=1}^{N_\alpha} \left(d_\alpha S_{11}^{(\alpha\beta\gamma)} + \frac{1}{K_{T_{11}}^{(\alpha\beta\gamma)}} \right) \right]^{-1}, \qquad \begin{matrix} \beta = 1, \ldots, N_\beta \\ \gamma = 1, \ldots, N_\gamma \end{matrix} \tag{B.42}$$

Equation (B.42) is similar to the expression for the length of the cohesive zone [*Turon et al.* (2006)]:

$$l_{cz} = ME\frac{G_C}{\sigma_C^2} \tag{B.43}$$

where l_{cz} is the length of the cohesive zone in front of the crack tip, E is the stiffness of the material surrounding the crack, G_C is the critical fracture energy, σ_C is the cohesive strength, and M is a scaling parameter close to unity. The length associated with Equation (B.42) is the dimension of the RUC perpendicular to any cohesive zones, for a given β, and γ. Equation (B.42) implies that this dimension is related to the length of the cohesive zone in front of the crack tip. Therefore, the dimension of the RUC perpendicular to the length of the crack must be approximately less than twice the length of the cohesive zone.

Equations (B.31) and (B.42) can be used in Equation (**??**) to determine $A_{11}^{(\alpha\beta\gamma)}$ in

terms known quantities.

$$\frac{\sigma_{11}^{(\beta\gamma)}}{\bar{d}} \sum_{\alpha=1}^{N_\alpha} \frac{A_{11}^{(\alpha\beta\gamma)}}{\mathcal{G}_{C_{11}}^{(\alpha\beta\gamma)}} = \frac{d\hat{\epsilon}_{11} \sum_{\alpha=1}^{N_\alpha} \frac{1}{K_{T_{11}}^{(\alpha\beta\gamma)}}}{\sum_{\alpha=1}^{N_\alpha} \left(d_\alpha S_{11}^{(\alpha\beta\gamma)} + \frac{1}{K_{T_{11}}^{(\alpha\beta\gamma)}} \right)}, \qquad \begin{matrix} \beta = 1, \ldots, N_\beta \\ \gamma = 1, \ldots, N_\gamma \end{matrix} \tag{B.44}$$

However, additional relationships must be established because Equation (B.44) represents $N_{\tilde{\beta}} \times N_{\tilde{\gamma}}$ equation for $N_{\tilde{\alpha}} \times N_{\tilde{\beta}} \times N_{\tilde{\gamma}}$ unknown values of $A_{11}^{(\alpha\beta\gamma)}$, where $N_{\tilde{\alpha}}$, $N_{\tilde{\beta}}$, and $N_{\tilde{\gamma}}$ are the number of debonded subcells in each direction. Utilizing Equation (B.41) and the chain rule gives

$$\frac{\partial \sigma_{11}^{(\beta\gamma)}}{\partial \left[u_{11}\right]^{(\alpha\beta\gamma)}} d\left[u_{11}\right]^{(\alpha\beta\gamma)} = \frac{\partial \sigma_{11}^{(\beta\gamma)}}{\partial \left[u_{11}\right]^{(\hat{\alpha}\beta\gamma)}} d\left[u_{11}\right]^{(\hat{\alpha}\beta\gamma)}, \qquad \begin{matrix} \alpha = 1, \ldots, N_\alpha \\ \beta = 1, \ldots, N_\beta \\ \gamma = 1, \ldots, N_\gamma \\ \hat{\alpha} \neq \alpha \end{matrix} \tag{B.45}$$

Equations (B.32) and (B.33) can be substituted into Equation (B.45) resulting in

$$K_{T_{11}}^{(\alpha\beta\gamma)} d\left[u_{11}\right]^{(\alpha\beta\gamma)} = K_{T_{11}}^{(\hat{\alpha}\beta\gamma)} d\left[u_{11}\right]^{(\hat{\alpha}\beta\gamma)}, \qquad \begin{matrix} \alpha = 1, \ldots, N_\alpha \\ \beta = 1, \ldots, N_\beta \\ \gamma = 1, \ldots, N_\gamma \\ \hat{\alpha} \neq \alpha \end{matrix} \tag{B.46}$$

Taking the increment of Equation (B.7) gives a new form of Equation (B.46)

$$K_{T_{11}}^{(\alpha\beta\gamma)}\left(R_{11}^{(\alpha\beta\gamma)}d\sigma_{11}^{(\alpha\beta\gamma)}+dR_{11}^{(\alpha\beta\gamma)}\sigma_{11}^{(\alpha\beta\gamma)}\right)=K_{T_{11}}^{(\hat{\alpha}\beta\gamma)}\left(R_{11}^{(\hat{\alpha}\beta\gamma)}d\sigma_{11}^{(\hat{\alpha}\beta\gamma)}+dR_{11}^{(\hat{\alpha}\beta\gamma)}\sigma_{11}^{(\hat{\alpha}\beta\gamma)}\right), \quad \begin{matrix}\alpha=1,\ldots,N_\alpha\\ \beta=1,\ldots,N_\beta\\ \gamma=1,\ldots,N_\gamma\\ \hat{\alpha}\neq\alpha\end{matrix} \tag{B.47}$$

Since $A_{11}^{(\alpha\beta\gamma)}$ only needs to be determined upon initial debonding, Equation (B.47) becomes (making use of Equation (B.41))

$$\frac{K_{T_{11}}^{(\alpha\beta\gamma)}}{\mathcal{G}_{C_{11}}^{(\alpha\beta\gamma)}}A_{11}^{(\alpha\beta\gamma)}=\frac{K_{T_{11}}^{(\hat{\alpha}\beta\gamma)}}{\mathcal{G}_{C_{11}}^{(\hat{\alpha}\beta\gamma)}}A_{11}^{(\hat{\alpha}\beta\gamma)}, \quad \begin{matrix}\alpha=1,\ldots,N_\alpha\\ \beta=1,\ldots,N_\beta\\ \gamma=1,\ldots,N_\gamma\\ \hat{\alpha}\neq\alpha\end{matrix} \tag{B.48}$$

which relates each all $A_{11}^{(\alpha\beta\gamma)}$ for a given β and γ.

Using Equation (B.48) in Equation (B.44) gives $N_\alpha \times N_\beta \times N_\gamma$ equations for determining $A_{11}^{(\alpha\beta\gamma)}$.

$$A_{11}^{(\alpha\beta\gamma)}=\frac{\bar{d}\mathcal{G}_{C_{11}}^{(\alpha\beta\gamma)}d\hat{\epsilon}_{11}}{\sigma_{11}^{(\beta\gamma)}K_{T_{11}}^{(\alpha\beta\gamma)}\sum_{\hat{\alpha}=1}^{N_\alpha}\left(d_{\hat{\alpha}}S_{11}^{(\hat{\alpha}\beta\gamma)}+\dfrac{1}{K_{T_{11}}^{(\hat{\alpha}\beta\gamma)}}\right)}, \quad \begin{matrix}\alpha=1,\ldots,N_\alpha\\ \beta=1,\ldots,N_\beta\\ \gamma=1,\ldots,N_\gamma\end{matrix} \tag{B.49}$$

Note that if $I=1$ of subcell $(\alpha\beta\gamma)$ is bonded in mode I, $K_{T_{11}}^{(\alpha\beta\gamma)}=\infty$, and therefore, $A_{11}^{(\alpha\beta\gamma)}=0$. If the denominator of Equation (B.49) is less than zero, the increment in the interfacial compliance will be negative, resulting in a stiffer interface as debonding evolves. Additionally, as the denominator of Equation (B.49) approaches zero,

$dR_{11}^{(\alpha\beta\gamma)} \rightarrow \infty$. Both of these situations result in non-physical values for $dR_{11}^{(\alpha\beta\gamma)}$; thus, the denominator of Equation (B.49) must remain well above zero. This imposes a restriction on the subcell and overall RUC dimensions for given TSL slope, fracture and elastic properties. Conversely, for a particular geometry, there is a limit on the steepness of the TSL, potentially making it impossible for the area under the curve to be equal to the critical fracture energy.

$$\sum_{\alpha=1}^{N_\alpha} d_\alpha S_{11}^{(\alpha\beta\gamma)} << -\sum_{\alpha=1}^{N_\alpha} \frac{1}{K_{T_{11}}^{(\alpha\beta\gamma)}}, \qquad \begin{matrix} \alpha = 1, \ldots, N_\alpha \\ \beta = 1, \ldots, N_\beta \\ \gamma = 1, \ldots, N_\gamma \end{matrix} \tag{B.50}$$

If the traction separation law is triangular, the slope is dictated by Equation (B.32) and Equations (B.49) and (B.50) become

$$A_{11}^{(\alpha\beta\gamma)} = \frac{2\bar{d}\bar{\mathcal{G}}_{C_{11}}^{(\alpha\beta\gamma)^2} d\hat{\epsilon}_{11}}{\sigma_{11}^{(\beta\gamma)} \sigma_{C_{11}}^{(\alpha\beta\gamma)^2} \sum_{\hat{\alpha}=1}^{N_\alpha} \left(\frac{2\mathcal{G}_{C_{11}}^{(\hat{\alpha}\beta\gamma)}}{\sigma_{C_{11}}^{(\hat{\alpha}\beta\gamma)^2}} - d_{\hat{\alpha}} S_{11}^{(\hat{\alpha}\beta\gamma)} \right)}, \qquad \begin{matrix} \alpha = 1, \ldots, N_\alpha \\ \beta = 1, \ldots, N_\beta \\ \gamma = 1, \ldots, N_\gamma \end{matrix} \tag{B.51}$$

and

$$\sum_{\alpha=1}^{N_\alpha} d_\alpha S_{11}^{(\alpha\beta\gamma)} << \sum_{\alpha=1}^{N_\alpha} \frac{2\mathcal{G}_{C_{11}}^{(\alpha\beta\gamma)}}{\sigma_{C_{11}}^{(\alpha\beta\gamma)^2}}, \qquad \begin{matrix} \beta = 1, \ldots, N_\beta \\ \gamma = 1, \ldots, N_\gamma \end{matrix} \tag{B.52}$$

If debonding has not initiated in subcell $(\alpha\beta\gamma)$ on interface 1 in the x_1-direction, $A_{11}^{(\alpha\beta\gamma)} = 0$. Also, only $\sigma_{C_{11}}^{(\alpha\beta\gamma)}$ and $\mathcal{G}_{C_{11}}^{(\alpha\beta\gamma)}$ of debonded interfaces contribute to Equations (B.51) and (B.52).

A similar procedure can be used to formulate $A_{Ij}^{(\alpha\beta\gamma)}$ for the shear debonding modes $(j \neq I)$. If interfaces $I = 1$ and $I = 2$ are subjected to shear tractions $\sigma_{12}^{(\alpha\beta\gamma)}$ and $\sigma_{21}^{(\alpha\beta\gamma)}$, respectively, then upon initial debonding the incremental form of Equation

(B.21) is

$$d\bar{\epsilon}_{12} = \frac{1}{\bar{dh}} \sum_{\alpha=1}^{N_\alpha} \sum_{\beta=1}^{N_\beta} \left[d_\alpha h_\beta d\epsilon_{12}^{(\alpha\beta\gamma)} + \frac{1}{2} \left(h_\beta dR_{0_{12}}^{(\alpha\beta\gamma)} \sigma_{12}^{(\alpha\beta\gamma)} + d_\alpha dR_{0_{21}}^{(\alpha\beta\gamma)} \sigma_{21}^{(\alpha\beta\gamma)} \right) \right], \quad \gamma = 1, \ldots, N_\gamma \tag{B.53}$$

The constitutive equations of each subcell yield

$$\begin{aligned} d\epsilon_{12}^{(\alpha\beta\gamma)} &= \frac{1}{2} S_{66}^{(\alpha\beta\gamma)} d\sigma_{12}^{(\alpha\beta\gamma)} \qquad & \alpha &= 1, \ldots, N_\alpha \\ & & \beta &= 1, \ldots, N_\beta \\ d\epsilon_{21}^{(\alpha\beta\gamma)} &= \frac{1}{2} S_{66}^{(\alpha\beta\gamma)} d\sigma_{21}^{(\alpha\beta\gamma)} \qquad & \gamma &= 1, \ldots, N_\gamma \end{aligned} \tag{B.54}$$

assuming the elastic compliance of the subcell does not change. Using the constitutive relationship Equation (B.54) in Equation (B.53) gives

$$\begin{aligned} d\bar{\epsilon}_{12} = \frac{1}{\bar{dh}} \sum_{\alpha=1}^{N_\alpha} \sum_{\beta=1}^{N_\beta} \Bigg[& \frac{1}{2} d_\alpha h_\beta dS_{66}^{(\alpha\beta\gamma)} \sigma_{12}^{(\alpha\beta\gamma)} \\ & + \frac{1}{2} \left(h_\beta dR_{0_{12}}^{(\alpha\beta\gamma)} \sigma_{12}^{(\alpha\beta\gamma)} + d_\alpha dR_{0_{21}}^{(\alpha\beta\gamma)} \sigma_{21}^{(\alpha\beta\gamma)} \right) \Bigg], \gamma = 1, \ldots, N_\gamma \end{aligned} \tag{B.55}$$

Using the derivative chain rule for $d\sigma_{12}^{(\alpha\beta\gamma)}$

$$\begin{aligned} d\bar{\epsilon}_{12} = \frac{1}{\bar{dh}} \sum_{\alpha=1}^{N_\alpha} \sum_{\beta=1}^{N_\beta} \Bigg[& \frac{1}{2} d_\alpha h_\beta dS_{66}^{(\alpha\beta\gamma)} \frac{\partial \sigma_{12}^{(\alpha\beta\gamma)}}{\partial \bar{\epsilon}_{12}} d\bar{\epsilon}_{12} \\ & + \frac{1}{2} \left(h_\beta dR_{0_{12}}^{(\alpha\beta\gamma)} \sigma_{12}^{(\alpha\beta\gamma)} + d_\alpha dR_{0_{21}}^{(\alpha\beta\gamma)} \sigma_{21}^{(\alpha\beta\gamma)} \right) \Bigg], \gamma = 1, \ldots, N_\gamma \end{aligned} \tag{B.56}$$

Differentiating Equation (B.6) with respect to $\bar{\epsilon}_{12}$ will result in an equation that can

be solved for $\partial\sigma_{12}^{(\alpha\beta\gamma)}/\partial\bar{\epsilon}_{12}$,

$$d\bar{\epsilon}_{12} = \frac{1}{\bar{d}h}\sum_{\alpha=1}^{N_\alpha}\sum_{\beta=1}^{N_\beta}\left[\frac{1}{2}d_\alpha h_\beta dS_{66}^{(\alpha\beta\gamma)}\frac{\partial\sigma_{12}^{(\alpha\beta\gamma)}}{\partial\bar{\epsilon}_{12}}d\bar{\epsilon}_{12} + \frac{1}{2}\left(h_\beta\frac{\partial\left[u_{12}\right]^{(\alpha\beta\gamma)}}{\partial\bar{\epsilon}_{12}}d\bar{\epsilon}_{12} + \frac{\partial\left[u_{21}\right]^{(\alpha\beta\gamma)}}{\partial\bar{\epsilon}_{21}}d\bar{\epsilon}_{21}\right)\right], \gamma = 1,\ldots,N_\gamma \tag{B.57}$$

noting that

$$\begin{aligned} \frac{\partial\sigma_{12}^{(\alpha\beta\gamma)}}{\partial\bar{\epsilon}_{12}} &= \frac{\partial\sigma_{12}^{(\alpha\beta\gamma)}}{\partial\left[u_{12}\right]^{(\alpha\beta\gamma)}}\frac{\partial\left[u_{12}\right]^{(\alpha\beta\gamma)}}{\partial\bar{\epsilon}_{12}} \qquad & \alpha &= 1,\ldots,N_\alpha \\ & & \beta &= 1,\ldots,N_\beta \\ \frac{\partial\sigma_{21}^{(\alpha\beta\gamma)}}{\partial\bar{\epsilon}_{21}} &= \frac{\partial\sigma_{21}^{(\alpha\beta\gamma)}}{\partial\left[u_{21}\right]^{(\alpha\beta\gamma)}}\frac{\partial\left[u_{21}\right]^{(\alpha\beta\gamma)}}{\partial\bar{\epsilon}_{21}} \qquad & \gamma &= 1,\ldots,N_\gamma \end{aligned} \tag{B.58}$$

which leads to

$$\begin{aligned} \frac{\partial\left[u_{12}\right]^{(\alpha\beta\gamma)}}{\partial\bar{\epsilon}_{12}} &= \frac{1}{K_{T_{12}}^{(\alpha\beta\gamma)}}\frac{\partial\sigma_{12}^{(\alpha\beta\gamma)}}{\partial\bar{\epsilon}_{12}} \qquad & \alpha &= 1,\ldots,N_\alpha \\ & & \beta &= 1,\ldots,N_\beta \\ \frac{\partial\left[u_{21}\right]^{(\alpha\beta\gamma)}}{\partial\bar{\epsilon}_{12}} &= \frac{1}{K_{T_{21}}^{(\alpha\beta\gamma)}}\frac{\partial\sigma_{21}^{(\alpha\beta\gamma)}}{\partial\bar{\epsilon}_{21}} \qquad & \gamma &= 1,\ldots,N_\gamma \end{aligned} \tag{B.59}$$

where $K_{T_{12}}^{(\alpha\beta\gamma)}$ is the tangent slope of the traction $\sigma_{12}^{(\alpha\beta\gamma)}$, on interface $I = 1$, versus the displacement discontinuity in x_2-direction, and $K_{T_{21}}^{(\alpha\beta\gamma)}$ is the slope of traction $\sigma_{21}^{(\alpha\beta\gamma)}$, on interface $I = 2$, versus the displacement discontinuity in the x_1-direction. Additionally, because of traction continuity conditions and the linear displacement fields used in GMC, $\sigma_{12}^{(\alpha\beta\gamma)}$ and $\sigma_{21}^{(\alpha\beta\gamma)}$ are equal for all α and β, for a given γ.

$$\sigma_{21}^{(\alpha\beta\gamma)} = \sigma_{12}^{(\alpha\beta\gamma)} = \sigma_{12}^{(\gamma)}, \qquad \gamma = 1,\ldots,N_\gamma \tag{B.60}$$

Utilizing Equations (B.59) and (B.60) in Equation (B.57) yields

$$\frac{\partial \sigma_{12}^{(\gamma)}}{\partial \bar{\epsilon}_{12}} = \left[\frac{1}{\bar{d}h} \sum_{\alpha=1}^{N_\alpha} \sum_{\beta=1}^{N_\beta} \left(h_\beta l_\gamma S_{66}^{(\alpha\beta\gamma)} + \frac{h_\beta}{K_{T_{12}}^{(\alpha\beta\gamma)}} + \frac{d_\alpha}{K_{T_{21}}^{(\alpha\beta\gamma)}} \right) \right]^{-1}, \quad \gamma = 1, \ldots, N_\gamma \quad \text{(B.61)}$$

Substituting Equations (B.31) and (B.61) into Equation (B.56), and making use of Equation (B.60), results in a set of expressions for $A_{12}^{(\alpha\beta\gamma)}$.

$$\frac{\sigma_{12}^{(\gamma)}}{\bar{d}h} \sum_{\alpha=1}^{N_\alpha} \sum_{\beta=1}^{N_\beta} \left[\frac{1}{2} \left(\frac{A_{12}^{(\alpha\beta\gamma)}}{\mathcal{G}_{C_{12}}^{(\alpha\beta\gamma)}} + \frac{A_{21}^{(\alpha\beta\gamma)}}{\mathcal{G}_{C_{21}}^{(\alpha\beta\gamma)}} \right) \right] = \frac{\displaystyle\sum_{\alpha=1}^{N_\alpha} \sum_{\beta=1}^{N_\beta} \left(\frac{h_\beta}{K_{T_{12}}^{(\alpha\beta\gamma)}} + \frac{d_\alpha}{K_{T_{21}}^{(\alpha\beta\gamma)}} \right)}{\displaystyle\sum_{\alpha=1}^{N_\alpha} \sum_{\beta=1}^{N_\beta} \left(d_\alpha h_\beta S_{66}^{(\alpha\beta\gamma)} + \frac{h_\beta}{K_{T_{12}}^{(\alpha\beta\gamma)}} + \frac{d_\alpha}{K_{T_{21}}^{(\alpha\beta\gamma)}} \right)}, \quad \gamma = 1, \ldots, N_\gamma \quad \text{(B.62)}$$

Equation (B.62) contains N_γ relationships for $N_\alpha \times N_\beta \times N_\gamma$ unknown values of $A_{12}^{(\alpha\beta\gamma)}$ and $A_{21}^{(\alpha\beta\gamma)}$; therefore, additional equations must be established relating the scaling parameters for different α and β. Equation (B.60) can be used, along with the chain rule and a procedure similar to that used to determine Equation (B.41), to give

$$\frac{K_{T_{12}}^{(\alpha\beta\gamma)}}{\mathcal{G}_{C_{12}}^{(\alpha\beta\gamma)}} A_{12}^{(\alpha\beta\gamma)} = \frac{K_{T_{12}}^{(\hat{\alpha}\hat{\beta}\gamma)}}{\mathcal{G}_{C_{12}}^{(\hat{\alpha}\hat{\beta}\gamma)}} A_{12}^{(\hat{\alpha}\hat{\beta}\gamma)}, \qquad \begin{array}{c} \alpha = 1, \ldots, N_\alpha \\ \beta = 1, \ldots, N_\beta \\ \gamma = 1, \ldots, N_\gamma \\ \hat{\alpha} \neq \alpha \\ \hat{\beta} \neq \beta \end{array} \quad \text{(B.63)}$$

Similarly, Equation (B.60) can be manipulated

$$\frac{\partial \sigma_{12}^{(\gamma)}}{\partial \left[u_{12}\right]^{(\alpha\beta\gamma)}} d\left[u_{12}\right]^{(\alpha\beta\gamma)} = \frac{\partial \sigma_{12}^{(\gamma)}}{\partial \left[u_{21}\right]^{(\alpha\beta\gamma)}} d\left[u_{21}\right]^{(\alpha\beta\gamma)}, \qquad \begin{matrix} \alpha = 1, \ldots, N_\alpha \\ \beta = 1, \ldots, N_\beta \\ \gamma = 1, \ldots, N_\gamma \end{matrix} \tag{B.64}$$

to yield

$$\frac{K_{T_{12}}^{(\alpha\beta\gamma)}}{\mathcal{G}_{C_{12}}^{(\alpha\beta\gamma)}} A_{12}^{(\alpha\beta\gamma)} = \frac{K_{T_{21}}^{(\alpha\beta\gamma)}}{\mathcal{G}_{C_{21}}^{(\alpha\beta\gamma)}} A_{21}^{(\alpha\beta\gamma)}, \qquad \gamma = 1, \ldots, N_\gamma \tag{B.65}$$

Equations (B.65) and (B.62) can be substituted in to Equation (B.62),leading to an equation for each shear scaling parameter $A_{12}^{(\alpha\beta\gamma)}$ and $A_{21}^{(\alpha\beta\gamma)}$ for all α, β, and γ.

$$A_{12}^{(\alpha\beta\gamma)} = \frac{2\bar{d}h\mathcal{G}_{C_{12}}^{(\alpha\beta\gamma)} d\bar{\epsilon}_{12}}{\sigma_{12}^{(\gamma)} K_{T_{12}}^{(\alpha\beta\gamma)} \sum_{\hat{\alpha}=1}^{N_\alpha} \sum_{\hat{\beta}=1}^{N_\beta} \left(d_{\hat{\alpha}} h_{\hat{\beta}} S_{66}^{\left(\hat{\alpha}\hat{\beta}\gamma\right)} + \frac{h_{\hat{\beta}}}{K_{T_{12}}^{\left(\hat{\alpha}\hat{\beta}\gamma\right)}} + \frac{d_{\hat{\alpha}}}{K_{T_{21}}^{\left(\hat{\alpha}\hat{\beta}\gamma\right)}} \right)}, \qquad \gamma = 1, \ldots, N_\gamma \tag{B.66}$$

As with Equation (B.49), the denominator of Equation (B.66) must not be negative or approach zero. This leads to a constraint on the RUC dimensions and material parameters.

$$\sum_{\alpha=1}^{N_\alpha} \sum_{\beta=1}^{N_\beta} d_\alpha h_\beta S_{66}^{(\alpha\beta\gamma)} << -\sum_{\alpha=1}^{N_\alpha} \sum_{\beta=1}^{N_\beta} \left(\frac{h_\beta}{K_{T_{12}}^{(\alpha\beta\gamma)}} + \frac{d_\alpha}{K_{T_{21}}^{(\alpha\beta\gamma)}} \right), \qquad \gamma = 1, \ldots, N_\gamma \tag{B.67}$$

If the TSL is triangular, utilizing Equation (B.33), Equations (B.66) and (B.67)

become

$$A_{12}^{(\alpha\beta\gamma)} = \frac{4\bar{d}h\mathcal{G}_{C_{12}}^{(\alpha\beta\gamma)^2}d\bar{\epsilon}_{12}}{\sigma_{12}^{(\gamma)}\sigma_{C_{12}}^{(\alpha\beta\gamma)^2}\sum_{\hat{\alpha}=1}^{N_\alpha}\sum_{\hat{\beta}=1}^{N_\beta}\left(\frac{2h_{\hat{\beta}}\mathcal{G}_{C_{12}}^{\left(\hat{\alpha}\hat{\beta}\gamma\right)}}{\sigma_{C_{12}}^{\left(\hat{\alpha}\hat{\beta}\gamma\right)^2}}+\frac{2d_{\hat{\alpha}}\mathcal{G}_{C_{21}}^{\left(\hat{\alpha}\hat{\beta}\gamma\right)}}{\sigma_{C_{21}}^{\left(\hat{\alpha}\hat{\beta}\gamma\right)^2}}-d_{\hat{\alpha}}h_{\hat{\beta}}S_{66}^{\left(\hat{\alpha}\hat{\beta}\gamma\right)}\right)}, \quad \begin{matrix}\alpha=1,\ldots,N_\alpha\\ \beta=1,\ldots,N_\beta\\ \gamma=1,\ldots,N_\gamma\end{matrix} \tag{B.68}$$

and

$$\sum_{\alpha=1}^{N_\alpha}\sum_{\beta=1}^{N_\beta}d_\alpha h_\beta S_{66}^{(\alpha\beta\gamma)} << \sum_{\alpha=1}^{N_\alpha}\sum_{\beta=1}^{N_\beta}\left(\frac{2h_\beta\mathcal{G}_{C_{12}}^{(\alpha\beta\gamma)}}{\sigma_{C_{12}}^{(\alpha\beta\gamma)^2}}+\frac{2d_\alpha\mathcal{G}_{C_{21}}^{(\alpha\beta\gamma)}}{\sigma_{C_{21}}^{(\alpha\beta\gamma)^2}}\right), \quad \gamma=1,\ldots,N_\gamma \tag{B.69}$$

Similar procedures can be used to determine $A_{Ij}^{(\alpha\beta\gamma)}$ for all I and j. Summarizing these results, assuming triangular TSLs:

$$A_{11}^{(\alpha\beta\gamma)} = \frac{2\bar{d}\mathcal{G}_{C_{11}}^{(\alpha\beta\gamma)^2}d\hat{\epsilon}_{11}}{\sigma_{11}^{(\beta\gamma)}\sigma_{C_{11}}^{(\alpha\beta\gamma)^2}\sum_{\hat{\alpha}=1}^{N_\alpha}\left(\frac{2\mathcal{G}_{C_{11}}^{(\hat{\alpha}\beta\gamma)}}{\sigma_{C_{11}}^{(\hat{\alpha}\beta\gamma)^2}}-d_{\hat{\alpha}}S_{11}^{(\hat{\alpha}\beta\gamma)}\right)}, \quad \begin{matrix}\alpha=1,\ldots,N_\alpha\\ \beta=1,\ldots,N_\beta\\ \gamma=1,\ldots,N_\gamma\end{matrix} \tag{B.70}$$

$$A_{22}^{(\alpha\beta\gamma)} = \frac{2h\mathcal{G}_{C_{22}}^{(\alpha\beta\gamma)^2}d\hat{\epsilon}_{22}}{\sigma_{22}^{(\alpha\gamma)}\sigma_{C_{22}}^{(\alpha\beta\gamma)^2}\sum_{\hat{\beta}=1}^{N_\beta}\left(\frac{2\mathcal{G}_{C_{22}}^{\left(\alpha\hat{\beta}\gamma\right)}}{\sigma_{C_{22}}^{\left(\alpha\hat{\beta}\gamma\right)^2}}-h_{\hat{\beta}}S_{22}^{\left(\alpha\hat{\beta}\gamma\right)}\right)}, \quad \begin{matrix}\alpha=1,\ldots,N_\alpha\\ \beta=1,\ldots,N_\beta\\ \gamma=1,\ldots,N_\gamma\end{matrix} \tag{B.71}$$

$$A_{33}^{(\alpha\beta\gamma)} = \frac{2\ell \mathcal{G}_{C_{33}}^{(\alpha\beta\gamma)^2} d\hat{\epsilon}_{33}}{\sigma_{33}^{(\alpha\beta)} \sigma_{C_{33}}^{(\alpha\beta\gamma)^2} \sum_{\hat{\gamma}=1}^{N_\gamma} \left(\frac{2\mathcal{G}_{C_{33}}^{(\alpha\beta\hat{\gamma})}}{\sigma_{C_{33}}^{(\alpha\beta\hat{\gamma})^2}} - \ell_{\hat{\gamma}} S_{22}^{(\alpha\beta\hat{\gamma})} \right)}, \qquad \begin{matrix} \alpha = 1, \ldots, N_\alpha \\ \beta = 1, \ldots, N_\beta \\ \gamma = 1, \ldots, N_\gamma \end{matrix} \tag{B.72}$$

$$A_{23}^{(\alpha\beta\gamma)} = \frac{4h\ell \mathcal{G}_{C_{23}}^{(\alpha\beta\gamma)^2} d\bar{\epsilon}_{23}}{\sigma_{23}^{(\alpha)} \sigma_{C_{23}}^{(\alpha\beta\gamma)^2} \sum_{\hat{\beta}=1}^{N_\beta} \sum_{\hat{\gamma}=1}^{N_\gamma} \left(\frac{2l_{\hat{\gamma}} \mathcal{G}_{C_{23}}^{\left(\alpha\hat{\beta}\hat{\gamma}\right)}}{\sigma_{C_{23}}^{\left(\alpha\hat{\beta}\hat{\gamma}\right)^2}} + \frac{2h_{\hat{\beta}} \mathcal{G}_{C_{32}}^{\left(\alpha\hat{\beta}\hat{\gamma}\right)}}{\sigma_{C_{32}}^{\left(\alpha\hat{\beta}\hat{\gamma}\right)^2}} - h_{\hat{\beta}} l_{\hat{\gamma}} S_{44}^{\left(\alpha\hat{\beta}\hat{\gamma}\right)} \right)}, \qquad \begin{matrix} \alpha = 1, \ldots, N_\alpha \\ \beta = 1, \ldots, N_\beta \\ \gamma = 1, \ldots, N_\gamma \end{matrix} \tag{B.73}$$

$$A_{32}^{(\alpha\beta\gamma)} = \left(\frac{\sigma_{C_{23}}^{(\alpha\beta\gamma)} \mathcal{G}_{C_{32}}^{(\alpha\beta\gamma)}}{\sigma_{C_{32}}^{(\alpha\beta\gamma)} \mathcal{G}_{C_{23}}^{(\alpha\beta\gamma)}} \right)^2 A_{23}^{(\alpha\beta\gamma)}, \qquad \begin{matrix} \alpha = 1, \ldots, N_\alpha \\ \beta = 1, \ldots, N_\beta \\ \gamma = 1, \ldots, N_\gamma \end{matrix} \tag{B.74}$$

$$A_{13}^{(\alpha\beta\gamma)} = \frac{4\bar{d}\ell \mathcal{G}_{C_{13}}^{(\alpha\beta\gamma)^2} d\bar{\epsilon}_{13}}{\sigma_{13}^{(\beta)} \sigma_{C_{13}}^{(\alpha\beta\gamma)^2} \sum_{\hat{\alpha}=1}^{N_\alpha} \sum_{\hat{\gamma}=1}^{N_\gamma} \left(\frac{2l_{\hat{\gamma}} \mathcal{G}_{C_{13}}^{(\hat{\alpha}\beta\hat{\gamma})}}{\sigma_{C_{13}}^{(\hat{\alpha}\beta\hat{\gamma})^2}} + \frac{2d_{\hat{\alpha}} \mathcal{G}_{C_{31}}^{(\hat{\alpha}\beta\hat{\gamma})}}{\sigma_{C_{31}}^{(\hat{\alpha}\beta\hat{\gamma})^2}} - d_{\hat{\alpha}} l_{\hat{\gamma}} S_{55}^{(\hat{\alpha}\beta\hat{\gamma})} \right)}, \qquad \begin{matrix} \alpha = 1, \ldots, N_\alpha \\ \beta = 1, \ldots, N_\beta \\ \gamma = 1, \ldots, N_\gamma \end{matrix} \tag{B.75}$$

$$A_{31}^{(\alpha\beta\gamma)} = \left(\frac{\sigma_{C_{13}}^{(\alpha\beta\gamma)} \mathcal{G}_{C_{31}}^{(\alpha\beta\gamma)}}{\sigma_{C_{31}}^{(\alpha\beta\gamma)} \mathcal{G}_{C_{13}}^{(\alpha\beta\gamma)}} \right)^2 A_{13}^{(\alpha\beta\gamma)}, \qquad \begin{matrix} \alpha = 1, \ldots, N_\alpha \\ \beta = 1, \ldots, N_\beta \\ \gamma = 1, \ldots, N_\gamma \end{matrix} \tag{B.76}$$

$$A_{12}^{(\alpha\beta\gamma)} = \frac{4\bar{d}h{\mathcal{G}_{C_{12}}^{(\alpha\beta\gamma)}}^2 d\bar{\epsilon}_{12}}{\sigma_{12}^{(\gamma)}{\sigma_{C_{12}}^{(\alpha\beta\gamma)}}^2 \sum_{\hat{\alpha}=1}^{N_\alpha}\sum_{\hat{\beta}=1}^{N_\beta}\left(\frac{2h_{\hat{\beta}}\mathcal{G}_{C_{12}}^{\left(\hat{\alpha}\hat{\beta}\gamma\right)}}{{\sigma_{C_{12}}^{\left(\hat{\alpha}\hat{\beta}\gamma\right)}}^2} + \frac{2d_{\hat{\alpha}}\mathcal{G}_{C_{21}}^{\left(\hat{\alpha}\hat{\beta}\gamma\right)}}{{\sigma_{C_{21}}^{\left(\hat{\alpha}\hat{\beta}\gamma\right)}}^2} - d_{\hat{\alpha}}h_{\hat{\beta}}S_{66}^{\left(\hat{\alpha}\hat{\beta}\gamma\right)}\right)}, \quad \begin{matrix}\alpha = 1,\ldots,N_\alpha \\ \beta = 1,\ldots,N_\beta \\ \gamma = 1,\ldots,N_\gamma\end{matrix} \tag{B.77}$$

$$A_{21}^{(\alpha\beta\gamma)} = \left(\frac{\sigma_{C_{12}}^{(\alpha\beta\gamma)}\mathcal{G}_{C_{21}}^{(\alpha\beta\gamma)}}{\sigma_{C_{21}}^{(\alpha\beta\gamma)}\mathcal{G}_{C_{12}}^{(\alpha\beta\gamma)}}\right)^2 A_{12}^{(\alpha\beta\gamma)}, \quad \begin{matrix}\alpha = 1,\ldots,N_\alpha \\ \beta = 1,\ldots,N_\beta \\ \gamma = 1,\ldots,N_\gamma\end{matrix} \tag{B.78}$$

where

$$d\hat{\epsilon}_{11} = d\bar{\epsilon}_{11} - \frac{1}{\bar{d}}\sum_{\alpha=1}^{N_\alpha} d_\alpha\left(S_{12}^{(\alpha\beta\gamma)}d\sigma_{22}^{(\alpha\beta\gamma)} + S_{13}^{(\alpha\beta\gamma)}d\sigma_{33}^{(\alpha\beta\gamma)}\right), \quad \begin{matrix}\beta = 1,\ldots,N_\beta \\ \gamma = 1,\ldots,N_\gamma\end{matrix} \tag{B.79}$$

$$d\hat{\epsilon}_{22} = d\bar{\epsilon}_{22} - \frac{1}{h}\sum_{\beta=1}^{N_\beta} h_\beta\left(S_{12}^{(\alpha\beta\gamma)}d\sigma_{11}^{(\alpha\beta\gamma)} + S_{23}^{(\alpha\beta\gamma)}d\sigma_{33}^{(\alpha\beta\gamma)}\right), \quad \begin{matrix}\alpha = 1,\ldots,N_\alpha \\ \gamma = 1,\ldots,N_\gamma\end{matrix} \tag{B.80}$$

$$d\hat{\epsilon}_{33} = d\bar{\epsilon}_{33} - \frac{1}{\ell}\sum_{\gamma=1}^{N_\gamma} l_\gamma\left(S_{13}^{(\alpha\beta\gamma)}d\sigma_{11}^{(\alpha\beta\gamma)} + S_{23}^{(\alpha\beta\gamma)}d\sigma_{22}^{(\alpha\beta\gamma)}\right), \quad \begin{matrix}\alpha = 1,\ldots,N_\alpha \\ \beta = 1,\ldots,N_\beta\end{matrix} \tag{B.81}$$

The conditions on RUC size to obtain physically realistic solutions for $dR_{Ij}^{(\alpha\beta\gamma)}$ are given by:

$$\sum_{\alpha=1}^{N_\alpha} d_\alpha S_{11}^{(\alpha\beta\gamma)} << \sum_{\alpha=1}^{N_\alpha}\frac{2\mathcal{G}_{C_{11}}^{(\alpha\beta\gamma)}}{{\sigma_{C_{11}}^{(\alpha\beta\gamma)}}^2}, \quad \begin{matrix}\beta = 1,\ldots,N_\beta \\ \gamma = 1,\ldots,N_\gamma\end{matrix} \tag{B.82}$$

$$\sum_{\beta=1}^{N_\beta} h_\beta S_{22}^{(\alpha\beta\gamma)} << \sum_{\beta=1}^{N_\beta} \frac{2\mathcal{G}_{C_{22}}^{(\alpha\beta\gamma)}}{\sigma_{C_{22}}^{(\alpha\beta\gamma)^2}}, \qquad \begin{matrix} \alpha = 1, \ldots, N_\alpha \\ \gamma = 1, \ldots, N_\gamma \end{matrix} \tag{B.83}$$

$$\sum_{\gamma=1}^{N_\gamma} l_\gamma S_{33}^{(\alpha\beta\gamma)} << \sum_{\gamma=1}^{N_\gamma} \frac{2\mathcal{G}_{C_{33}}^{(\alpha\beta\gamma)}}{\sigma_{C_{33}}^{(\alpha\beta\gamma)^2}}, \qquad \begin{matrix} \alpha = 1, \ldots, N_\alpha \\ \beta = 1, \ldots, N_\beta \end{matrix} \tag{B.84}$$

$$\sum_{\beta=1}^{N_\beta}\sum_{\gamma=1}^{N_\gamma} h_\beta l_\gamma S_{44}^{(\alpha\beta\gamma)} << \sum_{\beta=1}^{N_\beta}\sum_{\gamma=1}^{N_\gamma} \left(\frac{2l_\gamma \mathcal{G}_{C_{23}}^{(\alpha\beta\gamma)}}{\sigma_{C_{23}}^{(\alpha\beta\gamma)^2}} + \frac{2h_\beta \mathcal{G}_{C_{32}}^{(\alpha\beta\gamma)}}{\sigma_{C_{32}}^{(\alpha\beta\gamma)^2}} \right), \quad \alpha = 1, \ldots, N_\alpha \tag{B.85}$$

$$\sum_{\alpha=1}^{N_\alpha}\sum_{\gamma=1}^{N_\gamma} d_\alpha l_\gamma S_{55}^{(\alpha\beta\gamma)} << \sum_{\alpha=1}^{N_\alpha}\sum_{\gamma=1}^{N_\gamma} \left(\frac{2l_\gamma \mathcal{G}_{C_{13}}^{(\alpha\beta\gamma)}}{\sigma_{C_{13}}^{(\alpha\beta\gamma)^2}} + \frac{2h_\beta \mathcal{G}_{C_{31}}^{(\alpha\beta\gamma)}}{\sigma_{C_{31}}^{(\alpha\beta\gamma)^2}} \right), \quad \beta = 1, \ldots, N_\beta \tag{B.86}$$

$$\sum_{\alpha=1}^{N_\alpha}\sum_{\beta=1}^{N_\beta} d_\alpha h_\beta S_{66}^{(\alpha\beta\gamma)} << \sum_{\alpha=1}^{N_\alpha}\sum_{\beta=1}^{N_\beta} \left(\frac{2h_\beta \mathcal{G}_{C_{12}}^{(\alpha\beta\gamma)}}{\sigma_{C_{12}}^{(\alpha\beta\gamma)^2}} + \frac{2d_\alpha \mathcal{G}_{C_{21}}^{(\alpha\beta\gamma)}}{\sigma_{C_{21}}^{(\alpha\beta\gamma)^2}} \right), \quad \gamma = 1, \ldots, N_\gamma \tag{B.87}$$

Equations (B.70)-(B.78) only need to be solved upon debonding initiation, and/or if there is a change in the global strain rate. If Equation (B.12) or (B.13) has not been satisfied for interface I, in the j-direction, of subcell $(\alpha\beta\gamma)$, then $A_{Ij}^{(\alpha\beta\gamma)} = 0$. Moreover, $\sigma_{C_{Ij}}^{(\alpha\beta\gamma)}$ and $\mathcal{G}_{C_{Ij}}^{(\alpha\beta\gamma)}$ only contribute to Equations (B.70)-(B.78) and (B.82)-(B.87) if the corresponding interface as debonded.

B.2 Effect of RUC Size on Interfacial Debonding

B.2.1 Example: 2 x 1 RUC with One Compliant Interface

Equations (B.82)-(B.87) indicate that there is a critical RUC size; above which, the cohesive parameters $A_{ij}^{(\alpha\beta\gamma)}$ will result in non-physical behavior. To demonstrate the effect of the RUC size as it approaches the critical RUC size on the debonding behavior at the interfaces, a simple, 2-D, 2 subcells $\times$ 1 subcell RUC will be used. The RUC is shown in Figure B.4. Each subcell is composed of the same isotropic

material with Young's Modulus E. Generalized plane strain is assumed in the x_1-direction. A tensile strain $\bar{\epsilon}$ is applied in the x_2-direction, and the x_3 boundaries are left stress free. Only the interface between the two subcells, with unit normal in the x_2-direction, is allowed to debond with debonding strength σ_C and critical SERR $\mathcal{G}_C$. The dimensions of the subcells are identical, and the length of the subcells in the x_2-direction are h_β, yielding a total RUC length in the x_2-direction of $h = 2h_\beta$.

Using this example, Equation (B.83) can be solved, assuming equality between the left and right-hand sides, for the critical RUC size in the x_2-direction.

$$h_C = \frac{2E\mathcal{G}_C}{{\sigma_C}^2} \tag{B.88}$$

The RUC size was then varied with respect to h_C, and the interfacial traction versus separation behavior was observed. Assuming a triangular traction separation law, the SERR should be equal to $\mathcal{G}_C$, and the interfacial traction should be zero, when the separation $[u] = \delta$, where

$$\delta = \frac{2\mathcal{G}_C}{\sigma_C} \tag{B.89}$$

The SERR when $[u] = \delta$, $\mathcal{G}_\delta$, has been calculated for multiple RUC sizes. Figure B.5 displays the error between $\mathcal{G}_\delta$ and $\mathcal{G}_C$ as a function of the percent difference between the RUC size h and the critical RUC size h_C. From this figure it can be determined that an RUC that is 1% smaller than h_C will only yield a 1% difference in the SERR when $[u] = \delta$. Therefore its is recommended that RUCs, which contain debonding interfaces, are chosen such that the left-hand sides of Equations (B.82)-(B.87) are at least less than 1% of the right-hand sides.

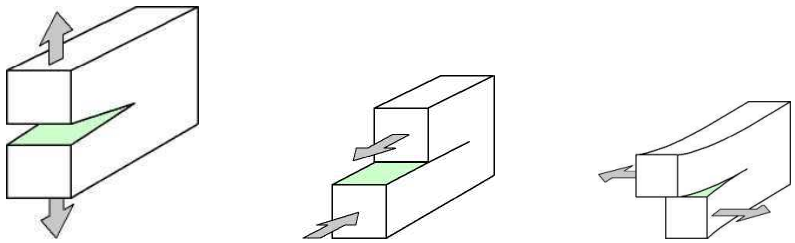

(a) Mode I (b) Mode II (c) Mode III

Figure B.1: Illustrations of three fracture modes.

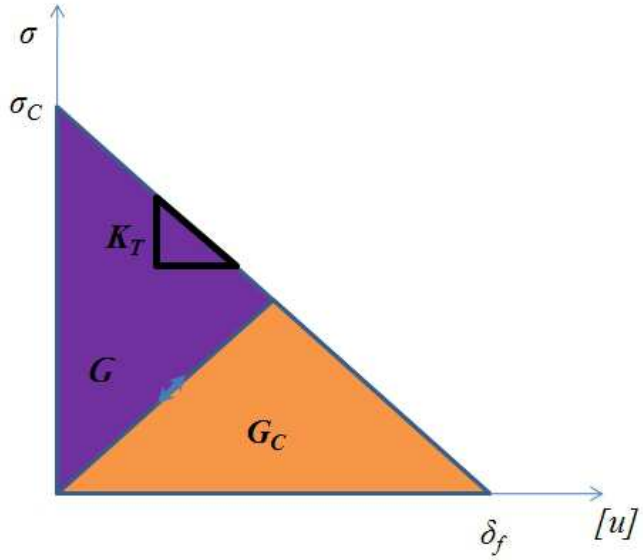

Figure B.2: Triangular traction-separation law used to relate the jump in displacement across an interface to the traction at the interface.

(a) Cracked composite RUC. (b) Cracked homogenized composite or monolithic RUC.

Figure B.3: Demonstrations of using cohesive zones within GMC to model crack growth. The red lines represent initiated cracks.

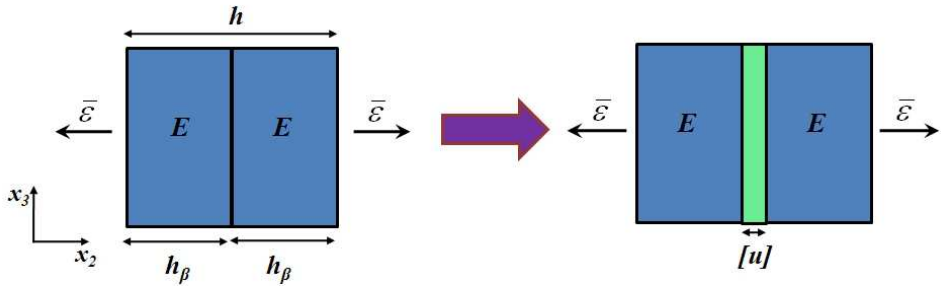

Figure B.4: Simple 2-D example used to demonstrate effect of RUC size, with respect to critical RUC size, on the resulting, interfacial traction-separation cohesive relationship. RUC containing two identical subcells, and one cohesive interface, is loaded perpendicular to the interface.

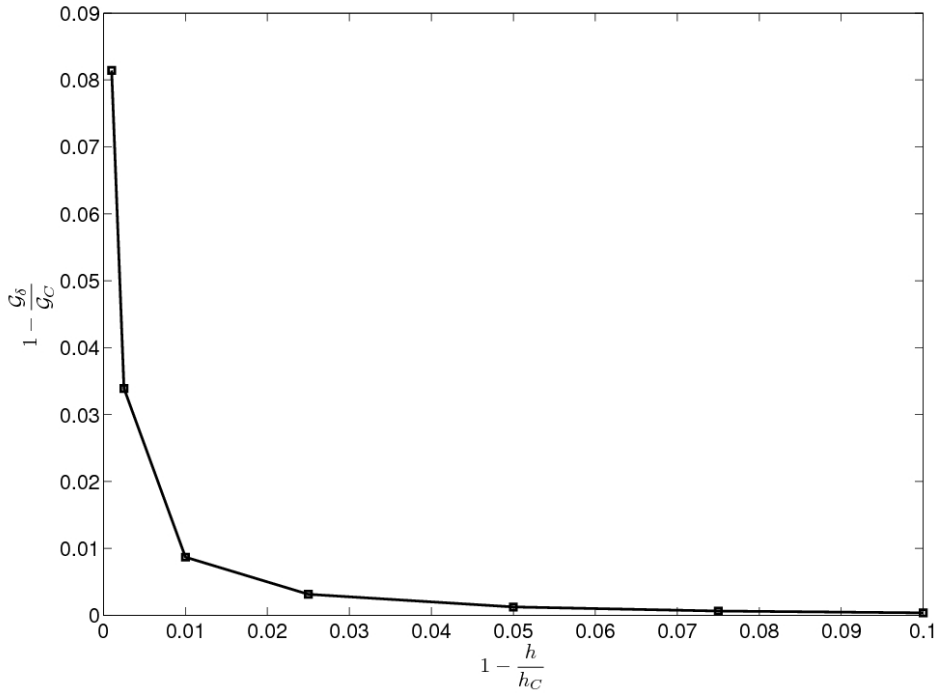

Figure B.5: Effect of RUC size h, with respect to the critical RUC size h_C on the SERR $\mathcal{G}_\delta$ when the interfacial displacement reaches δ. δ is the interfacial displacement when the SERR has reach the critical fracture energy $\mathcal{G}_C$ for a perfectly triangular traction-separation cohesive law.

Bibliography

Abaqus (2008), *Abaqus User's Manual, Vol. 1-3, Version 6.10-1*, Dassault Systèmes Simulia Corp., Providence, RI.

Aboudi, J. (1987), Damage in composite–modeling of imperfect bonding, *Compos. Sci. Technol.*, *28*, 103–128.

Aboudi, J. (1991), *Mechanics of Composite Materials: A Unified Micromechanical Approach*, Elsevier Amsterdam.

Aboudi, J. (1995), Micormechanical analysis of thermo-inelastic multiphase short-fiber composites, *Compos. Eng.*, *5*(7), 839–850.

Aboudi, J., M.-J. Pindera, and S. M. Arnold (2001), Linear thermoelastic higher-order theory for periodic multiphase materials, *J. Appl. Mech.*, *68*, 697–707.

Aboudi, J., M.-J. Pindera, and S. M. Arnold (2003), Higher-order theory for periodic multiphase materials with inelastic phases, *Int. J. Plast.*, *19*, 805–847.

Aboudi, J., S. M. Arnold, and B. A. Bednarcyk (2012), *Micromechanics of Composite Materials: A Generalized Multiscale Analysis Approach*, Elsevier, in press.

Achenbach, J. D., and H. Zhu (1989), Effect of interfacial zone on mechanical behavior of failure of fiber-reinforced composites, *J. Mech. Phys. Solids*, *37*, 381–393.

Allen, D. H., C. E. Harris, and S. E. Groves (1987a), A thermomechanical constitutive theory for elastic composites with distributed damage - i. theoretical development, *Int. J. Solids Struct.*, *23*(9), 1301–1318.

Allen, D. H., C. E. Harris, and S. E. Groves (1987b), A thermomechanical constitutive theory for elastic composites with distributed damage - ii. aplication to matrix cracking in laminated composites, *Int. J. Solids Struct.*, *23*(9), 1319–1338.

Aragonés, D. (2007), Fracture micromechanisms in c/epoxy composites under transverse compression, Ph.D. thesis, Universidad Politécnica de Madrid, Madrid, Spain.

Ashby, M. F., and C. G. Sammis (1990), The damage mechanics of brittle solids in compression, *Pure Appl. Geophys.*, *133*(3), 489–520.

Bansal, Y., and M.-J. Pindera (2004), Testing the predictive capability of the high-fidelity generalized method of cells using an efficient reformulation, *NASA/CR 2004-213043*.

Barenblatt, G. I. (1962), The mathematical theory of equilibrium cracks in brittle fracture, *Adv. Appl. Mech.*, *7*, 55–129.

Basu, S. (2005), Computational modeling of progrssive failure and damage in composite laminates, Ph.D. thesis, University of Michigan, Ann Arbor, MI.

Basu, S., A. M. Waas, and D. R. Ambur (2006), Compressive failure of fiber composites under multiaxial loading, *Int. J. Solids Structures*, *44*(9), 2648–2676.

Bažant, Z., and L. Cedolin (1979), Blunt crack band propagation in finite element analysis, *J. Eng. Mech. Div.-ASCE*, *105*, 297–315.

Bažant, Z. P. (1982), Crack band model for fracture of geomaterials, in *Proceedings of the* 4^{th} *International Conference on Numerical Methods in Geomechanics*, Edmonton, Canada.

Bažant, Z. P. (1994), Nonlocal damage theory based on micromechanics of crack interactions, *J. Eng. Mech. - ASCE*, *120*(3), 593–617.

Bažant, Z. P. (2007), Can multiscale-multiphysics methods predict softening damage and structural failure?, *Mech. Amer. Acad. Mech.*, *36*(5-6), 5–12.

Bažant, Z. P., and L. Cedolin (1983), Finite element modeling of crack band propagation, *J. of Struc. Eng.*, *109*, 69–92.

Bažant, Z. P., and L. Cedolin (1991), *Stability of Structures: Elastic, Inelastic, Fracture and Damage Theories*, Oxford University Press, New York, Oxford.

Bažant, Z. P., and B. H. Oh (1983), Crack band theory for fracture of concrete, *Mater. and Struct.*, *16*, 155–77.

Beaumont, P. W. R., R. A. Dimant, and H. R. Shercliff (2006), Failure processes in composite materials: getting physical, *J. Mater. Sci.*, *41*, 6526–6546.

Bednarcyk, B. A., and S. M. Arnold (2000), A new local debonding model with application to the transverse tensile and creep behavior of continuously reinforced titanium composites, *NASA/TM 2000-210029*.

Bednarcyk, B. A., and S. M. Arnold (2002a), Full couple micro/macro deformation, damage, and failure prediction for sic/ti-15-3 laminates, *J. Aerosp. Eng.*, *15*(3), 74–83.

Bednarcyk, B. A., and S. M. Arnold (2002b), Mac/gmc 4.0 user's manual - keywords manual, *Nasa tm-2002-212077/vol2*.

Bednarcyk, B. A., and S. M. Arnold (2002c), Mac/gmc 4.0 user's manual - example problems manual, *Nasa tm-2002-212077/vol3*.

Bednarcyk, B. A., and S. M. Arnold (2006), A framework for performing multiscale stochastic progressive failure analysis of composite structures, in *Proceedings of the 2006 ABAQUS User's Conference*.

Bednarcyk, B. A., S. M. Arnold, J. Aboudi, and M.-J. Pindera (2004), Local field effects in titanium matrix composites subject to fiber-matrix debonding, *Int. J. Plast.*, *20*, 1707–1737.

Bednarcyk, B. A., J. Aboudi, and S. M. Arnold (2010), Micromechanics modeling of composites subjected to multiaxial progressive damage in the constituents, *AIAA J.*, *48*, 1367–1378.

Belytschko, T., and K. Mish (2001), Computability in non-linear solid mechanics, *Int. J. Numer. Methods*, *52*, 3–21.

Belytschko, T., W. K. Liu, and B. Moran (2000), *Nonlinear finite elements for continua and structures*, Wiley, New York.

Belytschko, T., N. Moës, S. Usui, and C. Parimi (2001), Arbitrary discontinuities in finite elements, *Int. J. Numer. Meth. Eng.*, *50*, 993–1013.

Ben Dia, H., and G. Rateau (2005), The arlequin method as a flexible engineering design tool, *Int. J. Numer. Meth. Eng.*, *62*, 1442–1462.

Bogert, P. B., A. Satyanarayana, and P. B. Chunchu (2006), Comparison of damage path predicions for composite laminates by explicit and standard finite element analysis tool, in 47^{th} *AIAA Structures, Structural Dynamics, and Materials Conference*.

Budiansky, B., and N. A. Fleck (1993), Compressive failure of fiber composites, *J. Mech. Phys. Solids*, *41*(1), 183–211.

Camanho, P. P., P. Maimí, and C. G. Dávila (2007), Prediction of size effects in notched laminates using continuum damage mechanics, *Compos. Sci. and Technol.*, *67*, 2715–2727.

Chen, W., and G. Ravichandran (2000), Failure mode transition in creamics under dynamic multiaxial compression, *Int. J. Fract.*, *101*, 141–159.

Christensen, R. M., and K. H. Lo (1979), Solutions for effective shear properties in three phase sphere and cylinder models, *J. Mech. Phys. Solids*, *27*, 315–330.

Christensen, R. M., and F. M. Waals (1972), Effective stiffness of randomly oriented fiber composites, *J. Compos. Mater.*, *6*(3), 518.

Cid Alfaro, M. V., A. S. J. Suiker, and R. De Borst (2010), Transverse failure behavior of fiber-epoxy systems, *J. Compos. Mater.*, *44*, 1493–1516.

Cox, B., and Q. Yang (2006), In quest of virtual tests for structural composites, *Sci.*, *41*, 6526–6546.

Daniel, I. M., and O. Ishai (2006), *Engineering Mechanics of Composite Materials, 2nd Ed.*, Oxford University Press, New York, Oxford.

de Borst, R., and P. Nauta (1985), Non-orthogonal cracks in a smeared finite element model, *Eng. Comput.*, *2*, 35–46.

deBorst, R. (1987), Computation of post-bifurcation and post-failure behavior of strain-softening solids, *Comput. Struct.*, *25*, 211–224.

Dugdale, D. S. (1960), Yielding of steel sheets containing slits, *J. Mech. Phys. Solids*, *8*, 100–108.

Dvorak, G. J. (1992), Transformation field analysis of inelastic composite materials, *P. Roy. Soc. Lond. A Mat.*, *437*(1900), 311–327.

Dvorak, G. J., N. Laws, and M. Hejazi (1985), Analysis of progressive matrix cracking in composite laminates i. thermoelastic properties of a ply with cracks, *J. Compos. Mater.*, *19*, 216–234.

Eringen, A. C. (1966), A unified theory of thermomechanical materials, *Int. J. Eng. Sci.*, *4*, 179–202.

Eshelby, J. D. (1957), The determination of the elastic field of an ellipsoidal inclusion, and related problems, *P. Roy. Soc. Lond. A Mat.*, *241*(1226), 376–396.

Feyel, F. (1999), Multiscale fe^2 elastoviscoplastic analysis of composite structures, *Comput. Mater. Sci.*, *16*, 344–354.

Feyel, F., and J. L. Chaboche (2000), Fe^2 multiscale approach for modelling the elastoviscoplastic beaviour of long fibre sic/ti composite materials, *Comput. Method. Appl. Mech. Eng.*, *183*, 309–330.

Fish, J. (Ed.) (2009), *Multiscale Methods: Bridging the Scales in Science and Engineering*, Oxford University Press.

Fish, J., and Q. Yu (2001), Multiscale damage modelling for composite materials: Theory and computational framework, *Int. J. Numer. Methods Eng.*, *52*, 161–191.

Fish, J., K. Shek, M. Pandheeradi, and M. S. Shephard (1997), Computational plasticity for composite structures based on mathematical homogenization: Theory and practice, *Comput. Methods Appl. Eng.*, *148*, 53–73.

Fish, J., Q. Yu, and K. Shek (1999), Computational damage mechanics for composite materials based on mathematical homogenization, *Int. J. Numer. Methods Eng.*, *45*, 1657–1679.

Gamstedt, E. K., and B. A. Sjögren (1999), Micromechanisms in tension-compression fatigue of composite laminates containing transverse plies, *Compos. Sci. Technol.*, *59*, 167–178.

Garikipati, K. (1996), On strong discontinuities in inelastic solids and their numerical simulation, Ph.D. thesis, Stanford University, Palo Alto, CA.

Garikipati, K. (2002), A variational multiscale method to embed micromechanical surface laqs into the macromechanical continuum formulation, *Comput. Model. Eng.*, *3*, 175–184.

Garikipati, K., and T. J. R. Hughes (1998), A study of strain localization in a multiple scale framework the one dimensional problem, *Comput. Meth. Appl. Mech. Eng.*, *159*, 193–222.

Ghosh, S., and Y. Liu (1995), Voronoi cell finite element model based on micorpolar theory of thermoelasticity for heteogeneous materials, *Int. J. Numer. Methods Eng.*, *38*, 1361–1398.

Ghosh, S., and S. Moorthy (1995), Elastic-plastic analysis of arbitrary heterogeneous materials with voronoi cell finite element method, *Comput. Methods. Appl. Mech. Eng.*, *121*, 373–409.

Ghosh, S., and S. N. Mukhopadhyay (1991), A two-dimensional automatic mesh generator for finite element analysis for random composites, *Comput. Struct.*, *41*(2), 245–256.

Ghosh, S., K. Lee, and S. Moorthy (1995), Multiscale analysis of heterogeneous elastic structures using homogenization theory and voronoi cell finite element method, *Int. J. Solids and Struct.*, *32*(1), 27–62.

Gilat, R., and L. Banks-Sills (Eds.) (2010), *Advances in Mathematical Modeling and Experimental Methods for Materials and Structures: The Jacob Aboudi Volume*, *Solid Mechanics and Its Applications*, vol. 168, Springer.

Gonzaléz, C., and J. Llorca (2007a), Mechanical behavior of unidirectional fiber-reinforced polymers under transverse compression: Microscopic mechanisms and modeling, *Compos. Sci. Technol.*, *67*, 2795–2806.

Gonzaléz, C., and J. Llorca (2007b), Mechanical behavior of unidirectional fiber-reinforced polymers under transverse compression: Microscopic mechanisms and modeling, *Compos. Sci. Technol.*, *67*, 2795–2806.

Green, B. G., M. R. Wisnom, and S. R. Hallett (2007), An experimental investigation into the tensile strength scaling of notched composites, *Compos.: Part A*, *38*, 867–878.

Griffith, A. A. (1921), The pehnomena of rupture and flow in solids, *Philos. T. R. Soc. Lond.*, *221*, 163–198.

Gudmundson, P., and S. Östlund (1992), First order analysis of stiffness reduction due to matrix cracking, *J. Compos. Mater.*, *26*, 1009–1030.

Gustafson, P. A. (2008), Analytical and experimental methods for adhesively bonded joints subjected to high temperatures, Ph.D. thesis, University of Michigan, Ann Arbor, MI.

Gustafson, P. A., and A. M. Waas (2008), Efficient and robust traction laws for the modeling of adhesively bonded joints, in *49th AIAA/ASME/ASCE/AHS/ASC Structrues, Sturctural Dynamics, and Materials Conference*.

Gustafson, P. A., and A. M. Waas (2009), The influence of adhesive constitutive parameters in cohesive zone finite element models of adhesively bonded joints, *Int. J. Solids Struct.*, pp. 2201–2215.

Haj-Ali, R., and J. Aboudi (2009), Nonlinear micromechanical formulation of the high fidelity generalized method of cells, *Int. J. Solids Struct.*, *46*, 2577–2592.

Haj-Ali, R., and J. Aboudi (2010), Formulation of the high-fidelity generalized method of cells with arbitrary cell geometry for refined micromechanics and damage in composites, *Int. J. Solids Struct.*, *47*, 3447–3461.

Hallett, S. R., W.-G. Jiang, B. Khan, and M. R. Winsom (2008), Modelling the interaction between matrix cracks and delamination damage in scaled quasi-isotropic specimens, *Compos. Sci. and Technol.*, *68*, 80–89.

Hashin, Z. (1962), The elastic moduli of heterogeneous materials, *J. Appl. Mech.*, *29*, 143–150.

Hashin, Z., and A. Rotem (1973), A fatigue failure criterion for fiber reinforced composite materials, *J. Composite Materials*, *7*, 448–464.

Herakovich, C. T. (1998), *Mechanics of Fibrous Composites*, John Wiley & Sons, Inc.

Hill, R. (1952), The elastic behavior of a crystalline aggregate, *J. Appl. Mech.*, *29*, 349–352.

Hinterhoelzl, A., and R. A. Schapery (2004), Fem implementation of a three-dimensional visoelastic constitutive model for particulate composites with damage growth, *Mech. Time-Depend. Mat.*, *8*(1), 65–94.

Hinton, M. J., A. S. Kaddour, and P. D. Soden (Eds.) (2004), Elsevier, New York.

Hoek, E., and Z. T. Bieniawski (1965), Brittle rock fracture propagation in rock under compression, *Int. J. Fract.*, *1*(3), 137–155.

Horii, H., and S. Nemat-Nasser (1986), Brittle failure in compression: Splitting, faulting and brittle-ductile transition, *Philos. T. R. Soc. S.-A.*, *319*(1549), 337–374.

Hughes, T. J. R. (2000), *The Finite Element Method: Linear Static and Dynamic Finite Element Analysis*, Dover Publications, Inc.

Ji, W., A. M. Waas, W. H. Ng, P. A. Gustafson, E. J. Pineda, and R. Raveendra (2011), Computational modeling of failure in composite structures including uncertainties in material and geometrical properties, in *52nd AIAA/ASME/ASCE/AHS/ASC Structures, Structural Dynamics, and Materials Conference*.

Jirásek, M. (1998), Nonlocal models for damage and fracture: Comparision of approaches, *Int. J. Solids Struct.*, *35*(31-32).

Johnson, S. W., and P. D. Mangalgiri (1985), Influence of the resin on interlaminar mixed-mode fracture, *NASA/TM 87571*.

Jones, J. P., and J. S. Whittier (1967), Waves at flexibly bonded interfaces, *J. Appl. Mech.*, *34*, 905–909.

Jones, R. M. (1999), *Mechanics of Composite Materials, 2nd Ed.*, Taylor and Francis, Inc., Philadelphia.

Kachanov, L. M. (1958), On the creep fracture time, *Izvestiya Akademii Nauk SSSR, Otdeleniya Tekhnika Nauk*, *8*(1), 26–31.

Kachanov, L. M. (1986), *Introduction to Continuum Damage Mechanics*, Martinus-Nijhoff, Dordrecht, The Netherlands.

Kanoute, P., D. P. Boso, J. L. Chaboche, and B. A. Schrefler (2009), Multiscale methods for composites: A review, *Arch. Comput. Methods Eng.*, *16*, 31–75.

Knight, Jr., N., C. C. Rankin, and F. A. Brogan (2001), Controlling progressive failure analyes using artificial damping, in *42nd AIAA/ASME/ASCE/AHS/ASC Structures, Structural Dynamics, and Materials Conference*, Seattle, WA.

Krajcinovic, D. (1996), *Damage Mechanics*, Elsevier, New York.

Krüger, R. (2002), The virtual crack closure technique: History approach and applications, *NASA/CR 2002-211628*.

Krüger, R., M. König, and T. Schneider (1993), Computation of local energy release rates along straight and curved delamination fronts of unidirectional laminated dcb- and enf- specimens, in *34th AIAA/ASME/ASCE/AHS/ASC Structures, Structural Dynamics, and Materials Conference*, pp. 1332–1342, La Jolla, CA.

Kwon, Y. W., D. H. Allen, and R. Talreja (Eds.) (2008), *Multiscale Modeling and Simulation of Composite Materials and Structures*, Springer.

Ladeveze, P. (2004), Multiscale modelling and computation strategies for composites, *Int. J. Numer. Meth. Eng.*, *60*, 233–253.

Lamborn, M. J., and R. A. Schapery (1988), An investigation of deformation path-independence of mechanical work in fiber-reinforced plastics, in *Proceedings of the Fourth Japan-U.S. Conference on Composite Materials*, Technomic Publishing Co., Inc., Lancaster, PA.

Lamborn, M. J., and R. A. Schapery (1993), An investigation of the existence of a work potential for fiber-reinforced plastic, *J. Compos. Mater.*, *27*, 352–382.

Laws, N., and G. J. Dvorak (1988), Progressive transverse cracking in composite laminates, *J. Compos. Mater.*, *22*, 900–916.

Lee, J.-W., D. H. Allen, and C. E. Harris (1989), Internal state variable approach for predicting stiffness reductions in fibrous laminated composites with matrix cracks, *J. Compos. Mater.*, *23*, 1273–1291.

Lemaitre, J. (1996), *A Course on Damage Mechanics, 2nd Ed.*, Springer-Verlag, Berlin, Heidelberg, New York.

Lemaitre, J., and J.-L. Chaboche (1994), *Mechanics of Solid Materials*, Cambridge University Press.

Liu, P., and J. Y. Zheng (2010), Recent developments of damage modeling and finite element analysis for composite laminates: A review, *Mater. Design*, *31*, 3825–3834.

Matzenmiller, A., J. Lubliner, and R. L. Taylor (1995), A constitutive model for anisotropic damage in fiber-composites, *Mech. Mater.*, *20*(2), 125–152.

McCartney, L. N. (1987), Mechanics of marix cracking in brittle-matrix fiber-reinforced composites, in *Proceedings of the Royal Society of London. Series A, Mathematical and Physical Sciences*, vol. 409, pp. 329–350.

McCartney, L. N. (1992a), Theory of stress transfer in a 0^o-90^o-0^o cross-ply laminate containing a parallel array of transverse cracks, *J. Mech. Phys. Solids*, *40*(1), 27–68.

McCartney, L. N. (1992b), Mechanics for the growth of bridged cracks in composite materials: Part i. basic principles, *J. Compos. Technol. & Res.*, *14*(3), 133–154.

McCartney, L. N. (1998), Predicting transverse crack formation in cross-ply laminates, *Compos. Sci. Technol.*, *58*, 1069–1081.

Michel, J. C., and P. Suquet (2003), Nonuniform transformation field analysis, *Int. J. Solids Struct.*, *40*, 6937–6955.

Mishnaevsky Jr., L., and P. Brønsted (2007), Micormechanical modeling of strength and damage of fiber reinforced composites, *Risø-R 1601*.

Mori, T., and K. Tanaka (1973), Average stresses in matrix and average energy of materials with misfitting inclusions, *Acta Metall.*, *21*, 571–574.

Mura, T. (1982), *Micromechanics of Defects in Solids*, Kluwer Academic Publishers.

Nairn, J. A. (1989), Strain energy release rate of composite microcracking: A variational approach, *J. Compos. Mater.*, *23*, 1106–1129.

Nemat-Nasser, S., T. Iwakuma, and M. Hejazi (1982), On composites with periodic structure, *Mech. Mater.*, *1*, 239–267.

Ng, W. H., A. G. Salvi, and A. M. Waas (2010), Characterization of the in-situ non-linear shear response of laminated fiber-reinforced composites, *Compos. Sci. Technol.*, *70*(7), 1126–1134.

Noda, J., T. Okabe, N. Takeda, and M. Shimizu (2006), Tensile strength of cfrp cross-ply laminates containing transverse cracks, *Adv. Comps. Mater.*, *15*(1), 81–93.

Oskay, C., and J. Fish (2007), Eigendeformation-based reduced order homogenization for failure analysis of heterogeneous materials, *Comput. Methods in Appl. Mech. and Eng.*, *196*, 1216–1243.

Paas, M. H. J. W., P. J. G. Schreurs, and W. A. M. Brekelmans (1992), A continuum approach to brittle and fatigue damage: Theory and numerical procedures, *Int. J. Solids Struct.*, *30*(4), 579–599.

Paley, M., and J. Aboudi (1992), Micromechanical analysis of composites by the generalized cells model, *Mechanics of Materials*, *14*, 127–139.

Pankow, M. R. (2010), The deformation response of 3d woven composites subjected to high rates of loading, Ph.D. thesis, University of Michigan, Ann Arbor, MI.

Pietruszczak, S., and Z. Mroz (1981), Finite element analysis of deformation of strain-softening materials, *Int. J. Numer. Methods Eng.*, *17*, 327–334.

Pindera, M. J., and B. A. Bednarcyk (1999), An efficient implementation of the generalized method of cells for unidirectional, multi-phased composited with complex microstructures, *Compos.: Part B.*, *30*, 87–105.

Pineda, E. J., A. M. Waas, B. A. Bednarcyk, C. S. Collier, and P. W. Yarrington (2008), A novel multiscale physics based progrssive failure methodology for laminated composite structures, *Nasa tm-2008-215448*.

Pineda, E. J., A. M. Waas, B. A. Bednarcyk, C. S. Collier, and P. W. Yarrington (2009), Progressive damage and faiure modeling in notched laminated fiber reinforced composites, *Int. J. Fract.*, *158*, 125–143.

Pineda, E. J., A. M. Waas, B. A. Bednarcyk, and C. S. Collier (2010a), An efficient semi-analytical framework for micromechanical modeling of transverse cracks in fiber-reinforced composites, in *51st AIAA/ASME/ASCE/AHS/ASC Structures, Structural Dynamics, and Materials Conference*.

Pineda, E. J., A. M. Waas, B. A. Bednarcyk, and C. S. Collier (2010b), Computational implementation of a thermodynamically based work potential model for progressive microdamage and transverse cracking in fiber-reinforced laminates, in *51st AIAA/ASME/ASCE/AHS/ASC Structures, Structural Dynamics, and Materials Conference*, Orlando, FL.

Pineda, E. J., A. M. Waas, B. A. Bednarcyk, and C. S. Collier (2010c), Multiscale modeling of progressive microdamage and transverse cracking in fiber reinforced laminates, in *Presented at the 16^{t}h US National Conference of Theoretical and Applied Mechanics*.

Pineda, E. J., A. M. Waas, B. A. Bednarcyk, C. S. Collier, and P. W. Yarrington (2010d), A multiscale progressive damage and failure modeling approach for laminated fiber reinforced composites, in *Advances in Mathematical Modeling and Experimental Methods for Materials and Structures: The Jacob Aboudi Volume*, *Solid Mechanics and Its Applications*, vol. 168, edited by R. Gilat and L. Banks-Sills, pp. 43–56, Springer.

Pinho, S. T., C. G. Dávila, P. P. Camanho, and L. Iannucci (2005), Failure models and criteria for frp under in-plane or three-dimensional stress states including shear non-linearity, *NASA/TM 2005-213530*.

Possehl, G. L. (1996), Mehrgarh, in *Oxford Companion to Archaeology*, edited by B. M. Fagan, Oxford University Press, Oxford.

Puck, A., and H. Schürmann (1998), Failure analysis of frp laminates by means of physically based phenomenological models, *Comps. Sci. Technol.*, *58*, 1045–1067.

Puck, A., and H. Schürmann (2002), Failure analysis of frp laminates by means of physically based phenomenological models, *Comps. Sci. Technol.*, *62*, 1633–1622.

Qiao, H., Q. D. YAng, W. Q. Cheng, and C. Z. Zhang (2011), Implementation of the arlequin method into abaqus: Basic formulations and applications, *Adv. Eng. Softw.*, *42*(4), 197–207.

Ranatunga, V., B. A. Bednarcyk, and S. M. Arnold (2009), Modeling delamination in composites via continuum interfacial displacement discontinuities, in *50th AIAA/ASME/ASCE/AHS/ASC Structures, Structural Dynamics, and Materials Conference*.

Ranatunga, V., B. A. Bednarcyk, and S. M. Arnold (2010a), Modeling progressive damage using local displacement discontinuities within the feamac multiscale modeling framework, in *51st AIAA/ASME/ASCE/AHS/ASC Structures, Structural Dynamics, and Materials Conference*.

Ranatunga, V., B. A. Bednarcyk, and S. M. Arnold (2010b), Modeling progressive damage using local displacement discontinuities with the feamac multiscale modeling framework, *NASA/TM 2010-216825*.

Reuss, A. (1929), Berechnung der fließgrenze von mischkristallen auf grund der plastizitätsbedingung für einkristalle, *J. Appl. Math. Mech.*, *9*, 49–58.

Rice, J. R. (1971), Inelastic constitutive relations for solids: an internal-variable theory and its application to metal plasticity, *J. Mech. Phys. Solids*, *19*, 433–455.

Roberts, S. J. (2000), Modelling of microcracking in composite materials, Ph.D. thesis, The University of Newcastle upon Tyne, Newcastle upon Tyne, United Kingdom.

Rots, J. G., and R. de Borst (1987), Analysis of mixed-mode fracture in concrete, *J. Eng. Mech.*, *113*(11), 1739–1758.

Rudraraju, S. S. (2011), On the theory and numerical simulation of cohesive crack propagation with application to fiber-reinforced composites, Ph.D. thesis, Universtiy of Michigan, Ann Arbor, MI.

Rudraraju, S. S., R. Vignes, A. Salvi, K. Garikipati, and A. M. Waas (2008), A multiscale crack path predicting computational method for laminated fiber reinforced composites, in *49th AIAA/ASME/ASCE/AHS/ASC Structrues, Sturctural Dynamics, and Materials Conference*.

Rudraraju, S. S., A. Salvi, K. Garikipati, and A. M. Waas (2009), In-plnae fracture of laminated fiber reinforced composites with varying fracture resistance: experimental obesrvations and numerical crack propagation simulations, in *50th AIAA/ASME/ASCE/AHS/ASC Structures, Structural Dynamics, and Materials Conference*.

Rudraraju, S. S., A. Salvi, K. Garikipati, and A. M. Waas (2010), In-plane fracture of laminated fiber reinforced composites with varying fracture resistance: Experimental observations and numerical crack propagation simulations, *Int. J. Solids Struct.*, *47*, 901–911.

Sanford, R. J. (2002), *Principles of Fracture Mechanics*, Pearson Education, Inc.

Sankurathri, A., S. Baxter, and M.-J. Pindera (1996), The effect of fiber architecture on the inelastic response of metal matrix composites with interfacial and fiber damage, in *Damage and Interfacial Debonding in Composites*, edited by G. Z. Voyiadjis and D. H. Allen.

Satyanarayana, A., P. B. Bogert, and P. B. Chunchu (2007), The effect of delamination on damage path and failure load prediction for notched composite laminates, in 48^{th} *AIAA Structures, Structural Dynamics, and Materials Conference*.

Schapery, R. A. (1989), Mechanical characterization and analysis of inelastic composite laminates with growing damage, *Mechanics & Materials Center Report 5762-89-10*, Texas A & M University, College Station, TX 77804.

Schapery, R. A. (1990), A theory of mechanical behaviour of elastic media with growing damage and other changes in structure, *J. Mech. Phys. Solids*, *38*(2), 1725–1797.

Schapery, R. A. (1995), Prediction of compressive strength and kink bands in composites using a work potential, *Int. J. Solids Structures*, *32*(6), 739–765.

Schapery, R. A., and D. L. Sicking (1995), A theory of mechanical behaviour of elastic media with growing damage and other changes in structure, in *Mechanical Behaviour of Materials*, edited by A. Bakker, pp. 45–76, Delft University Press, Delft, The Netherlands.

Schuecker, C., and H. E. Pettermann (2008), Fiber reinforced laminates: progressive damage modeling based on failure mechanisms, *Arch. Comput. Methods Eng.*, *15*, 163–184.

Sicking, D. L. (1992), Mechanical characterization of nonlinear laminated composites with transverse crack growth, Ph.D. thesis, Texas A&M University, College Station, TX.

Spencer, B. W. (2002), Finite elements with embedded discontinuities for modeling reinforced concrete members, Ph.D. thesis, Brigham Young University, Provo, UT.

Sukumar, N., N. Moës, B. Moran, and T. Belytschko (2000), An extended finite element method (x-fem) for two- and three-dimensional crack modeling, *Int. J. Numer. Methods Eng.*, *48*(11), 1741–1760.

Sullivan, R. W., and S. M. Arnold (2011), An annotative review of multiscale modeling and its application to scales inherent in the field of icme, in *Models, Databases, and Simulation Tools Needed for the Realization of Integrated Computational Materials Engineering: Proceedings of the Symposium Held at Materials Science & Technology 2010*, edited by S. M. Arnold and T. T. Wong, pp. 6–23, ASM International, Houston, Texas.

Suquet, P. (1987), Elements of homogenisation for inelastic solid mechaincs, in *Homogenization Techniques for Composite Media*, *Lecture Notes in Physics*, vol. 272, edited by E. Sanchez-Palencia and A. Zaoui, Springer, New York.

Taliercio, A., and P. Sagramoso (1995), Uniaxial strength of polymeric-matrix fibrous composites predicted through a homogenization approach, *Int. J. Solids Struct.*, *32*(14), 2095–2123.

Talreja, R. (1985a), A continuum mechanics cahracterization of damage in composite materials, *P. Roy. Soc. Lond. A Mat.*, *4*, 335–375.

Talreja, R. (1985b), Transverse cracking and stiffness reduction in composite laminates, *J. Composite Materials*, *19*, 355–275.

Talreja, R. (Ed.) (1994), *Composite Materials Series*, vol. 9, Elsevier Science B.V., Amsterdam, The Netherlands.

Tan, S. C., and R. J. Nuismer (1989), A theory for progressive matrix cracking in composite laminates, *J. Compos. Mater.*, *23*, 1029–1047.

Tay, T. E., G. Liu, V. B. C., Tan, X. S. Sun, and D. C. Pham (2008), Progressive failure analysis of composites, *J. Compos. Mater.*, *42*, 1921–1966.

Timoshenko, S. P., and J. N. Goodier (1970), *Theory of Elasticity*, McGraw-Hill.

Totry, E., C. Gonzaléz, and J. Llorca (2008), Influence of the loading path on the strength of fiber-reinforced composites subjected to transverse compression and shear, *Int. J. Solids Structures*, *45*, 1663–1675.

Totry, E., C. Gonzalez, and J. Llorca (2010), Effect of fiber, matrix and interface properties on the in-plane shear deformation of carbon-fiber reinforced composites, *Compos. Sci. and Technol.*, *70*, 970–980.

Tsai, S. W. (2009), *Strength and Life of Composites*, Aero & Astro, Stanford.

Turon, A., P. P. Camanho, J. Costa, and C. G. Dávila (2006), A damage model for the simulation of delamination in advanced composites under variable-mode loading, *Mech. Mater.*, *38*(11).

Voigt, W. (1887), Theoretische studien über die elasticitätsverhältnisse der krystalle, *Abh. Kgl. Ges. Wiss. Göttingen, Math Kl.*, *34*, 3–51.

Voyiadjis, G., and P. I. Kattan (2005), *Damage Mechanics*, Taylor and Francis, Boca Raton, FL.

Waas, A. M., J. C. D. Babcock, and W. G. Knauss (1990a), An experimental study of compression failure of fibrous laminates in the presence of stress gradients, *Int. J. Solids Struct.*, *26*(9).

Waas, A. M., J. C. D. Babcock, and W. G. Knauss (1990b), An experimental study of compression failure of fibrous laminates in the presence of stress gradients, *Int. J. Solids Struct.*, *26*(9).

Walker, K. P., E. H. Jordan, and A. D. Freed (1989), Nonlinear mesomechanics of composites with periodic microstructure: First report, *NASA/TM 102051*.

Wang, J. T. (2010), Relating cohesive zone models to linear elastic fracture mechanics, *NASA/TM 2010-216692*.

Wilt, T. E. (1995), On the finite element implementation of the generalized method of cells micromechanics constitutive model, *Nasa/cr-1995-195451*.

Xie, D., and A. M. Waas (2006), Discrete cohesive zone model for mixed-mode fracture using finite element analysis, *Engineering Fracture Mechanics*, *73*(13), 1783–1796.

Xie, D. E., A. Salvi, C. E. Sun, A. M. Waas, and A. Caliskan (2006), Discrete cohesive zone model to simulate static fracture in 2-d triaxially braided carbon fiber composites, *J. Compos. Mater.*, *40*(22).

Yang, Q., and B. Cox (2005), Cohesive models for damage evolution in laminated composites, *Int. J. Frac.*, *133*, 107–137.

Yerramalli, C. S., and A. M. Waas (2003), A failure criterion for fiber reinforced polymer composites under combined compression-torsion loading, *Int. J. Solids Structures*, *40*(5), 1139–1164.